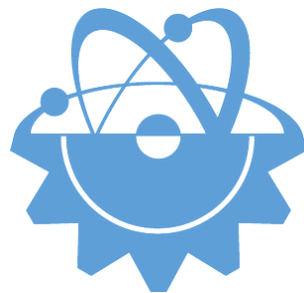


ISSN-Printed: 2536-5010
ISSN-Online: 2536-5134

Volume 10, N 1, 2020

EJT

EUROPEAN JOURNAL OF TECHNIQUE



Copyright © 2017 International Engineering, Science & Education Group

Email (for orders and customer services enquiries): info@ineseg.org, ejt@ineseg.org, ejtineseg@gmail.com

Visit our home page on www.ineseg.org or <https://dergipark.org.tr/ejt>

All Rights Reserved. No part of this publication may be reproduced, stored in a retrieval system or transmitted in any form or by any means, electronic, mechanical, photocopying, recording, scanning or otherwise, except under the terms of the Copyright, under the terms of a license issued by the Copyright International Engineering, Science & Education Group (INESEG), without the permission in writing of the Publisher. Requests to the Publisher should be addressed to the Permissions Department, International Engineering, Science & Education Group (INESEG), or emailed to info@ineseg.org

Designations used by companies to distinguish their products are often claimed as trademarks. All brand names and product names used in this journal are trade names, service marks, trademarks or registered trademarks of their respective owners. The Publisher is not associated with any product or vendor mentioned in this journal.

This publication is designed to provide accurate and authoritative information in regard to the subject matter covered. It is sold on the understanding that the Publisher is not engaged in rendering professional services. If professional advice or other expert assistance is required, the services of a competent professional should be sought.

EUROPEAN JOURNAL OF TECHNIQUE (EJT)

ISSN-Printed: 2536-5010

ISSN-Online: 2536-5134

Scope: European Journal of Technique (EJT) established in 2010. It is a peer –reviewed international journal to be of interest and use to all those concerned with research in various fields of, or closely related to, Engineering disciplines. European Journal of Technique (EJT) aims to provide a highly readable and valuable addition to the literature which will serve as an indispensable reference tool for years to come. The coverage of the journal includes all new theoretical and experimental findings in the fields of Engineering or any closely related fields. The journal also encourages the submission of critical review articles covering advances in recent research of such fields as well as technical notes.

The scopes include:

- Mechanical Engineering
- Textile Engineering
- Electrical-Electronics Engineering
- Computer and Informatics Engineering
- Civil and Architecture Engineering
- Mining Engineering
- Chemical Engineering
- Metallurgical and Materials Engineering
- Environmental Engineering
- Food Engineering
- Geological Engineering
- Industrial Engineering
- Renewable Energy

Editor-in-Chief

- Musa YILMAZ

Publisher Of Journal

- Heybet KILIÇ

ETHICS and POLICIES

European Journal of Technique (EJT) is committed to following the Code of Conduct and Best Practice Guidelines of COPE (Committee on Publication Ethics). It is a duty of our editors to follow Cope Guidance for Editors and our peer-reviewers must follow COPE Ethical Guidelines for Peer Reviewers. We expect all prospective authors to read and understand our Ethics Policy before submitting any manuscripts to our journals.

Please note that submitted manuscripts may be subject to checks using the iThenticate service, in conjunction with CrossCheck, in order to detect instances of overlapping and similar text.

The [iThenticate](#) software checks submissions against millions of published research papers, documents on the web, and other relevant sources. If plagiarism or misconduct is found, consequences are detailed in the policy.

The chief goal of our policy is threefold: to provide advice for our authors, to maintain the scholarly integrity of our journals and their content, and to detail the ethical responsibilities of EJT, our editors and authors.

We expect all authors to read and understand our ethics policy before submitting to any of our journals. This is in accordance with our commitment to the prevention of ethical misconduct, which we recognise to be a growing problem in academic and professional publications. It is important to note that most incidents of plagiarism, redundant publication, copyright infringement or similar occur because of a lack of understanding, and not through fraudulent intent. Our policy is one of prevention and not persecution.

If you have any questions, please contact the relevant editorial office, or European Journal of Technique (EJT)' ethics representative: ejtineseg@gmail.com

Download a PDF version of the Ethics and Policies [PDF,392KB].

Authors' Responsibilities

Authors should:

- Ensure that all researched work submitted is original, fully referenced and that all authors are represented accurately. The submission must be exclusive and not under consideration elsewhere.
- Provide accurate contact details for a designated corresponding author, who shall be deemed by the publisher and editor as fully responsible for the authorship of the paper and all communications concerning the ethical status and originality of the paper. This includes any queries or investigations that may arise, pre- or post publication.
- Openly disclose the source of all data and third party material, including previously unpublished work by the authors themselves. Anything that could compromise the originality of the submission should be expressly avoided and/or discussed with the editorial office in the first instance.
- Identify any third party material that they intend to include in their article, and obtain written permission for re-use in each instance from the relevant copyright holders. Such permissions should be submitted once the manuscript is accepted, or requires small changes to be accepted. For further guidance on seeking permission to use 3rd party material please see the Rights and Permissions section.
- Openly disclose any conflict of interest - for example, if publication were to benefit a company or services in which the author(s) has a vested interest.

- Expect to formally agree publication terms which defines the author and the publishers rights for the work. Visit our website for further information.
- Expect the editor to scan submissions using plagiarism detection software at [iThenticate](#) to check a paper's originality before sending out for review.
- Fully correspond and comply with the editor and publisher in any requests for source data, proof of authorship or originality in a timely manner, providing reasonable explanation for discrepancies or failures to disclose vital information.
- Fully co-operate with any consequent investigations if the editor and/or publisher are dissatisfied with the evidence available or the explanations provided.
- Expect transparency, efficiency and respect from the publisher and the editor during the submissions process.
- Remain in good communication with both the publisher and the editor.
- When necessary, submit corrigenda in a timely and responsible fashion.
- Co-operate fully with the publication of errata and with the retraction of articles found to be unethical, misleading or damaging.
- Remain in good communication with the editor(s), the publisher and any co-authors.

Editors' Responsibilities

Editors should:

- Read and understand COPE guidelines as well as EJT's ethics policy, and follow them during all editorial processes.
- Protect the reputation of their journal(s) and published work by only publishing content of the highest quality and relevance in a timely and responsible manner.
- Carry out thorough, objective and confidential peer review for original article submissions that pass the initial quality check and editorial assessment, in adherence with COPE guidelines and EJT' ethics policy.
- Detail and justify any article types which will not be peer reviewed (e.g. editorials, opinion pieces etc.).
- Provide a transparent review and publication process as far as is possible, with full respect and care paid to the author(s).
- Provide advice and give reasonable explanation and updates to authors during the submissions process and once a decision has been made.
- Allow authors the right to appeal any editorial decision.
- Only accept papers based on the original merit, quality and relevance of their content.
- Support authors in queries concerning the originality of their submissions and request the support of EJT if necessary.
- Advise the publisher of any third party material which has been included for which they do not believe sufficient permission has been cleared.

- Be ready and prepared to publish corrections, corrigenda, errata when necessary, as well as retract articles that (the editor and EJT) deem unethical, misleading or damaging.
- Remain in good communication with both the publisher and the author(s).

Reviewers' Responsibilities

Reviewers should:

- Adhere to EJT's policy of confidential peer review of their journals. This includes, but is not restricted to, keeping their identity hidden from authors and not externally distributing any work that is passed to them for their eyes only.
- Only accept invitations to review work that is relevant to their own expertise and speciality.
- Review submitted work in a responsible, impartial and timely manner.
- Report any suspected ethical misconduct as part of a thorough and honest review of the work.
- Avoid the use of unnecessarily inflammatory or offensive language in their appraisal of the work.
- Accept the commitment to review future versions of the work and provide 'follow up' advice to the editor(s), if requested.
- Seek advice from the editor if anything is unclear at the time of invitation.
- Remain in good communication with both the publisher and the editor.

EJT's Responsibilities

EJT will:

- Protect the reputation of our journals and published work by only publishing content of the highest quality and relevance in a timely and responsible manner.
- Provide detailed information concerning both our understanding of publication ethics and our implementation of the same. Emphasise a desire for prevention, not eventual detection, of ethical misconduct.
- Uphold our COPE membership (or of such similar organisations) and keep our editorial offices, publishing staff and society partners up-to-date with their guidelines and policies, adapting our own where appropriate (and publicising any update).
- When necessary, request proof of originality/accuracy from the corresponding author of any work submitted to any of our journals.
- Use plagiarism detection software when necessary for any submission to any journal at any stage of the submissions and publication process.
- Provide a transparent submissions and publication process, with full respect and care paid to the author. This includes detailed and dedicated instructions to authors for each journal, outlining referencing style, accepted article types and submission processes.

- Investigate thoroughly any suggestion of ethical misconduct detected during any stage of the submissions process. This can include, but is not restricted to, the following: plagiarism, redundant publication, fabrication or misuse of data and authorial disputes.
- When necessary, retract articles that we deem to be unethical, misleading or damaging.
- When necessary, publish errata, corrigenda and retractions in a timely and responsible fashion, detailing the decision online in an open access format and publishing in print as soon as possible.
- Remain in good communication with editors, authors, reviewers and society partners (where applicable).

Further reading

- Authorship of the paper: Authorship should be limited to those who have made a significant contribution to the conception, design, execution, or interpretation of the reported study.
- Originality and plagiarism: The authors should ensure that they have written entirely original works, and if the authors have used the work and/or words of others that this has been appropriately cited or quoted.
- Data access and retention: Authors may be asked to provide the raw data in connection with a paper for editorial review, and should be prepared to provide public access to such data.
- Multiple, redundant or concurrent publication: An author should not in general publish manuscripts describing essentially the same research in more than one journal or primary publication. EJT do not view the following uses of a work as prior publication: publication in the form of an abstract; publication as an academic thesis; publication as an electronic preprint. Information on prior publication is included within each EJT and its journal Guideline for Authors.
- Acknowledgement of sources: Proper acknowledgment.
- Disclosure and conflicts of interest: All submissions must include disclosure of all relationships that could be viewed as presenting a potential conflict of interest.
- Fundamental errors in published works: When an author discovers a significant error or inaccuracy in his/her own published work, it is the author's obligation to promptly notify the journal editor or publisher and cooperate with the editor to retract or correct the paper.
- Reporting standards: Authors of reports of original research should present an accurate account of the work performed as well as an objective discussion of its significance.
- Hazards and human or animal subjects: Statements of compliance are required if the work involves chemicals, procedures or equipment that have any unusual hazards inherent in their use, or if it involves the use of animal or human subjects.
- Use of patient images or case details: Studies on patients or volunteers require ethics committee approval and informed consent, which should be documented in the paper.

EJT has also accessed and learned from the existing policies of other publishers and leading experts as well as open access articles that detail and define ethical misconduct.

- 'Plagiarism and the law', Joss Saunders, Learned Publishing, 23:279-202: <http://www.ingentaconnect.com/content/alpsp/lp/2010/00000023/00000004/art00002>
- iThenticate Plagiarism Resources: <http://www.ithenticate.com/resources/6-consequences-of-plagiarism>

Editor-in-Chief

Musa Yilmaz, Batman University, Turkey

Vice Editor

Furkan Emre Sahin, Maxim Integrated, San Jose, CA, US

International Editorial Board

Aayush Shrivastava	University of Petroleum and Energy Studies, Dehradun, India
Adelino Pereira	Engineering Institute of Coimbra, Portugal
Ahmad Fakharian	Islamic Azad University, Qazvin, Iran
Ahmed Saber	Cairo University, Egypt
Arvind Kumar Jain	Rustam Ji Institute of Technology, India
Aydogan Ozdemir	Istanbul Technical University, Turkey
Baseem Khan	Hawassa University, Hawassa, Ethiopia
Behnam Khakhi	University of California Los Angeles, US
Behnam Mohammadi-ivatloo	University of Tabriz, Tabriz, Iran
Bharti Dwivedi	Institute of Engineering & Technology, Lucknow, UP, India
Carlos A. Castro	University of Campinas – UNICAMP, Brasil
Cafer Budak	Dicle University, Turkey
Deepak Kumar	University of Petroleum & Energy Studies (UPES), India
Ernesto Vazquez	University of Nuevo Leon, Mexico
Faisal Khan	COMSATS Institute of Information Technology, Pakistan
Farhad Shahnia	Murdoch University, Perth, Australia
Farrokh Aminifar	University of Tehran, Iran
Fatih Kocyyigit	Dicle University, Turkey
Fiaz Ahmad	National University of Computer and Emerging Sciences, Pakistan
Gouthamkumar Nadakuditi	V R Siddhartha Engineering College, India
Hafiz Ahmed	School of Mechanical, Coventry University, UK
Hamed Pourgharibshahi	Lamar University, US
Hassan Bevrani	University of Kurdistan, Iran
Hemant Kumar Gianey	Thapar University, Patiala, Punjab, India
Hessam Golmohamadi	Semnan University, Semnan, Iran
Hilmy Awad	Helwan University, Cairo, Egypt
Idris Candan	Kocaeli University, Turkey
Jamshed Ahmed Ansari	Sukkur IBA University, Pakistan
José A. Domínguez-Navarro	University of Zaragoza, Spain
Kalpna Chauhan	Galgotias College of Engineering and Technology, India
Katia Djenadi	Akli Mohand Oulhadj University of Bouira, Algeria
Khaled Ellithy	Qatar University, Doha, Qatar
Kim-Doang Nguyen	South Dakota State University, US
Kundan Kumar	KIIT University, India
Lalit Kumar	GBPIET Pauri, India
Leila Mokhnache	University of Batna 2, Algeria
Linquan Bai	ABB Inc., US
Md Shafiullah	King Fahd University of Petroleum & Minerals, Saudi Arabia
Mohamed Shaaban	Universiti Malaysia Sarawak, Malaysia
Mohammed Albadi	Sultan Qaboos University, Oman
Mohd Tariq	Aligarh Muslim University, India

Mousa Marzband	Northumbria University, Newcastle upon Tyne, United Kingdom
Neeraj Kanwar	Manipal University Jaipur, India
Nishant Kumar	Indian Institute of Technology Delhi, India
Nitin Kumar Saxena	Wolaita Sodo University, Ethiopia
Nouar Tabet	University of Sharjah, UAE
Omar Hafez	Umm Al-Qura University, Makkah, Saudi Arabia
Omveer Singh	Gautam Buddha University, India
Payam Teimourzadeh Baboli	University of Mazandaran (UMZ), Iran
Payman Dehghanian	George Washington University, US
Ragab A. El Sehiemy	Faculty of Engineering, Kafrelsheikh Univrsity, Egypt
Rajeev Kumar Chauhan	Galgotias College of Engineering and Technology, India
Rajiv Singh	G.B. Pant University of Agriculture & Technology, India
Reza Sharifi	Amir Kabir university Tehran, Iran
Rudranarayan Senapati	Kalinga Institute of Industrial Technology, India
Saleh Y. Abujarad	Universiti Teknologi Malaysia, Malaysia
Sanjay Dambhare	College of Engineering, Pune, India
Saptarshi Roy	NIT Warangal, India
Shailendra Kumar	Indian Institute of Technology Delhi, India
Shariq Riaz	The University of Sydney, Australia
Shengen Chen	University of Maine, US
Syafaruddin	Universitas Hasanuddin, Indonesia
T. Sudhakar Babu	VIT University, Vellore, India
Thamer Alquthami	King Abdulaziz University, Saudi Arabia
Theofilos Papadopoulos	Democritus University of Thrace, Greece
Uday P. Mhaskar	CSA Group, US
Vedat Veli Cay	Dicle University, Turkey
Yogesh Rohilla	K Lakshmi Pat University, Jaipur, India
Yunfeng Wen	School of Electrical Engineering, Chongqing University, China
Zbigniew M. Leonowicz	Wroclaw University of Science and Technology, Poland

Publisher of Journal

Heybey Kilic

Dicle University, Turkey / TU Delft, Netherland

CONTENTS

PERFORMANCE STUDY OF FOUR EQUALIZATION TECHNIQUES OVER A WIRELESS COMMUNICATION CHANNEL	1-12
MECHANICAL PROPERTIES OF COMPOSITE PLATES AT DIFFERENT CONDITIONS	13-24
THE EFFECTS OF HIGH DENSITY POLYETHYLENE ADDITION TO LOW DENSITY POLYETHYLENE POLYMER ON MECHANICAL, IMPACT AND PHYSICAL PROPERTIES	25-37
FEASIBILITY OF GOLD BASED HALL DEVICES FOR BIOSENSING PURPOSES ATION	38-51
MARBLE CLASSIFICATION USING DEEP NEURAL NETWORKS	52-63
A SIMULATION MODEL FOR CUSTOMER FLOW ANALYSIS IN A COMMERCIAL BANK IN NIGERIA	64-74
THE EFFECTS OF WELDING PRESSURE AND REINFORCEMENT RATIO ON WELDING STRENGTH IN DIFFUSION-BONDED AlMg ₃ /SiCp COMPOSITES	75-85
MIXING OF BIODIESELS PRODUCED FROM DIFFERENT SOURCES TO JET FUELS AND COMPARISON OF SPECIFICATIONS OF FUEL BLENDS	86-96
CRASHWORTHINESS INVESTIGATION OF VEHICLE FRONT BUMPER BEAM WITH DIFFERENT CROSS-SECTIONS UNDER AXIAL DYNAMIC LOAD	97-105
EFFECT OF WELDING PARAMETERS ON WEAR PERFORMANCE OF BORON COATING MADE WITH PTA	106-118
PERFORMANCE ANALYSIS OF COOLING SYSTEM WITH HORIZONTAL TYPE GROUND SOURCE HEAT PUMP FOR DIYARBAKIR CONDITIONS	119-130
OPTIMIZATION OF PROCESS CONDITIONS FOR ADSORPTION OF METHYLENE BLUE ON FORMALDEHYDE-MODIFIED PEANUT SHELLS USING BOX-BEHNKEN EXPERIMENTAL DESIGN AND RESPONSE SURFACE METHODOLOGY	131-142
THE ROLE OF STATIC VAR COMPENSATOR AT REACTIVE POWER COMPENSATION	143-152
IDENTIFICATION OF PARKINSON'S DISEASE BY AR MODELLING OF GAIT SIGNALS	153-159
INVESTIGATION OF ROUTE TRACKING PERFORMANCE WITH ADAPTIVE PID CONTROLLER IN QUADROTOR	160-172
EFFECT OF WC REINFORCED ON MICROSTRUCTURE AND MECHANICAL PROPERTIES OF CUALMN ALLOYS PRODUCED BY HOT PRESSING METHOD	173-183
THOROUGH ANALYSIS OF COMBUSTION AND EMISSIONS OF POWER GENERATOR DIESEL ENGINE AT HIGH IDLING OPERATIONS FUELED WITH LOW PERCENTAGE OF DIFFERENT BIODIESEL BLENDS	184-195
A STUDY ON THE EXAMINATION OF THE SINTER METALOGRAPHIC STRUCTURE	196-206

PERFORMANCE STUDY OF FOUR EQUALIZATION TECHNIQUES OVER A WIRELESS COMMUNICATION CHANNEL

Anwr ELASYRI^{1}, Dogu Cagdas ATILLA², Cagatay AYDIN³*


Abstract. Equalization techniques are commonly used in low to moderate data transmission over time varying wireless mobile channels. Their use is mainly to alleviate the detrimental effect of intersymbol interference brought about by the multipath phenomena of such channels. The wireless multipath channel is time varying which makes the use of adaptive equalization a necessity to cope with channel variations and consequently to overcome resulting intersymbol interference effects, restore the transmitted symbols, and extract the information being sent. The first part of this paper presents a comparison study of the performances of four representative methods of adaptive equalization. Linear and nonlinear structures each with both LMS and RLS adaptation algorithms are used in the investigation. In the second part of the paper, a computer simulation is carried out to investigate the relationship between the number of propagation paths of the wireless mobile channel and the number of taps in the incorporated adaptive equalizer. Four equalizer structures are used in this investigation which is based on Simulink software package to simulate a communication system incorporating these equalizers. The bit error rate (BER) performance is used as a measure for establishing this dependency.

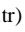
Key words: intersymbol interference (ISI); LMS and RLS algorithms; linear equalizers, decision feedback equalizers.

1. Introduction

The IT industries, over the last few decades, have significantly being revolutionized by the invention of internet and the application of the packet switching wireless networks. The former has provided a high speed information transmission via the use of optical fiber webs that virtually covers the whole world. Packet switching wireless networks, on the other hand, have modernized telecommunication systems as they made the dispatch of information possible for the people while they are on the move. The internet technologies have witnessed an extreme development to the extent that made an efficient high-speed data transmission technique over communications channels a necessity of the day. As the rate of the

¹ Department of Electrical and Computer Engineering in Graduate School of Science and Engineering, Altinbas University, Istanbul, Turkey, (anwarabdslam@gmail.com)  <https://orcid.org/0000-0001-7570-1782>

² Department of Electrical and Electronics Engineering in School of Engineering and Natural Sciences, Altinbas University, Istanbul, Turkey, (cagdas.atilla@altinbas.edu.tr)  <https://orcid.org/0000-0002-1895-0333>

³ Department of Electrical and Electronics Engineering in School of Engineering and Natural Sciences, Altinbas University, Istanbul, Turkey, (cagatay.aydin@altinbas.edu.tr)  <https://orcid.org/0000-0002-4249-6951>

data transmission increases to fulfill the needs of the users, the channel introduces distortions in data. One major cause of distortion is Inter Symbol Interference (ISI).

In digital communications, the information is coded and transmitted in the form of rectangular pulses that may assume definite number of levels. The bandwidth of such rectangular pulses is of course infinite. As a pulse propagates through a band limited communication channel, its duration will extend in time with the result of being smeared into adjacent time slots and therefore interfere with the adjacent symbols occupying such slots. This is referred as inter symbol interference (ISI) [1]. Other types of impairments encountered like thermal noise, shot noise, and cross talk will negatively affect the received symbols even further. This makes the use of signal processing techniques at the receiver inevitable in order to overcome the impairments inflicted on the transmitted pulses and consequently facilitate the recovery of their information. Such processing techniques are called “equalization”. In principle, the design of a pair of transmitting and receiving filter that can minimize the effect of ISI and the additive noise is feasible provided that the channel characteristics are precisely known [2-5]. However, in general the characteristics of channel are random in the sense that it is one of an ensemble of possible channels [6-8]. Therefore, using a fixed pair of transmitting and receiving filters will not be adequate if designed on the basis of average channel characteristics as far as ISI is concerned. To overcome this problem adaptive equalization, as shown in Fig. 1, is widely used. The role of equalization is to exercise a precise control so that the channel time response behaves appropriately [3], [9-11].

Adaptive equalizers may be of many different kinds depending on their structure and the adaptation algorithm being implemented. The most commonly used ones are; symbol spaced equalizer, fractionally spaced equalizer, decision-feedback equalizer, and blind equalizer [10].

2. Related work

Reference [1] gives good analytical and conceptual information which constitute solid bases for wireless communications in general and networks in particular.

A good overview of the most adaptive techniques is briefly presented in [2], [8], [12]. In [8] FPGA was recommended to replace DSP as more flexibility is provided. Researchers in [3] proposed and investigated an adaptive spatio-temporal equalization for MIMO channels. The proposed solution was tested on a MIMO system and found to give a good adaptation to varying channels resulting in improved performance. The authors in [13] analyzed the use of adaptive filters for equalizing the underwater acoustic channel and compared its behavior when implementing LMS to that when RLS adaptation algorithm is used. In [14] LMS, RLS and PSO (particle swarm optimization) algorithms were used to implement the adaptive channel equalizer. Results measured in terms of mean square error (MSE) and bit error rate (BER) versus number of iterations were obtained. A block minimum mean-squared error equalizer for orthogonal frequency-division multiplexing (OFDM) systems over TV time-varying multipath channels was proposed in [15]. The proposed algorithm used was shown to be less complex and smaller than for other MMSE approaches.

Optimizing the overall impulse response of transmit and receive filters to reduce the frequency selective fading channel to a flat fading one was discussed in [3]. This technique effectively equalizes the received samples as the simulation results had shown. Efficient calculation of the average BER of particular equalization techniques for QPSK transmission over static and quasi-static fading channels was proposed in [9] using an approximate Fourier series method. In [4] a maximum likelihood sequence

estimation (MLSE) equalizer implemented by the generalized Viterbi algorithm (GVA) was shown to be effective in cancelling both ISI and cochannel interference. A channel-sampling scheme to estimate the channel transitions into and out of the fade state was investigated in [10]. An approach for speeding up the convergence rate and reducing the complexity of equalization was investigated in [5]. This approach is based on combining RLS and LMS algorithms. In [16], a low-complexity per-subcarrier channel equalizer for high-rate wideband transceiver over doubly-dispersive channel was analyzed and its performance was evaluated. Local minima problem during the training mode of most standard adaptive algorithms was addressed in [7], [17] and techniques such as neural network, was recommended to alleviate such limitations. The effect of filter tap-length on the performance of equalized communication system as a function of the number of transmission paths in a multipath environment was tackled in [11].

3. Rayleigh channel equalization Models

A multipath, nonstationary communication channel could adequately be represented by a Rayleigh channel model [1], [6], [9]. To alleviate both; the detrimental effects of ISI which arises from the multipath phenomena and the Doppler effects arising from mobility, an adaptive equalizer should be implemented by the receiver as depicted in Fig. 1. Two types of Equalizer structure each with two different adaptation algorithms are investigated in this work.

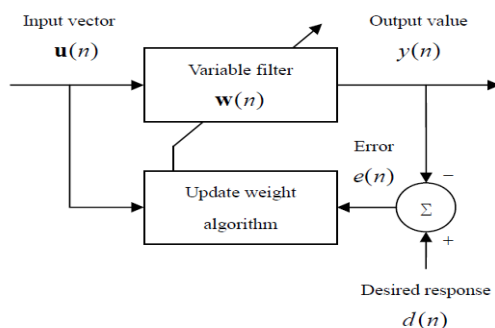


Fig.1. a block diagram of general adaptive filter

3.1 Linear equalizers

According to their structures, filters normally distinguish themselves in the context of an adaptive filter with finite memory [2], [8], [11]. A transversal filter is practically implemented using three basic elements, as depicted in Fig. 2: (a) a unit-delay element, (b) multiplication element, and (c) a summing component. The duration of the filter time response is determined by its length, i.e. the number of delay elements used in its structure. Also, the number of delay elements, M in the figure, defines the filter order. The unit-delay operator Z^{-1} is defined by the unit delay element. The operator, Z^{-1} , operates on the input $u(n)$ giving the output $u(n-1)$. The multiplier element in the filter multiplies the tap input by a filter tap weight or filter coefficient.

Thus, a multiplier connected to the k^{th} tap input $u(n-k)$ produces $W_k * u(n-k)$, where W_k is the respective tap weight and $k = 0, 1, \dots, M$.

The asterisk denotes complex conjugation, which accounts for complex valued tap weights. Individual multiplier outputs are summed producing the overall filter output. For the transversal filter shown, the output is given by

$$y(n) = \sum_{k=0}^M w_n^* u(n - k) \tag{1}$$

The process defined by equation 1 above merely convolves the finite duration impulse response of the filter, W_n^* , with the filter input $u(n)$ to produce the filter output $y(n)$. This is commonly referred to as a finite convolution.

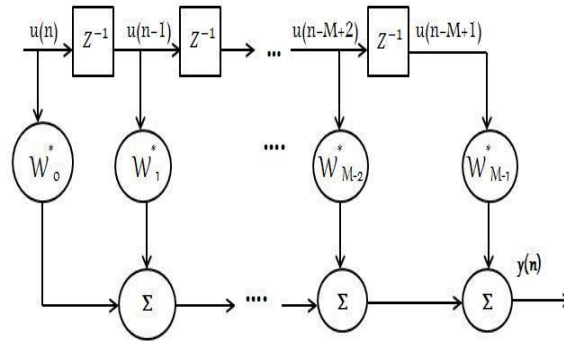


Fig.2. Structural constituent of transversal filter

3.2 Feedback Equalizers

The decision-feedback equalizer (DFE) is the nonlinear adaptive filter. A decision-feedback equalizer consists of two sections; a feedforward section and a feedback section. Both sections are implemented using transversal filters whose taps are spaced at the reciprocal of the symbol rate. The data sequence to be equalized is applied to the input of the feedforward section. Fig. 3 gives an illustration of this type of structure.

Previously detected symbols produce intersymbol interferences. The role of the feedback section is to subtract out the ISI from the estimates of future symbols. This cancellation is an old idea known as the bootstrap technique [14].

A decision-feedback equalizer yields good performance in the presence of severe intersymbol interference, as is experienced in fading radio channels. Fig. 3 shows the block diagram of DFE [3].

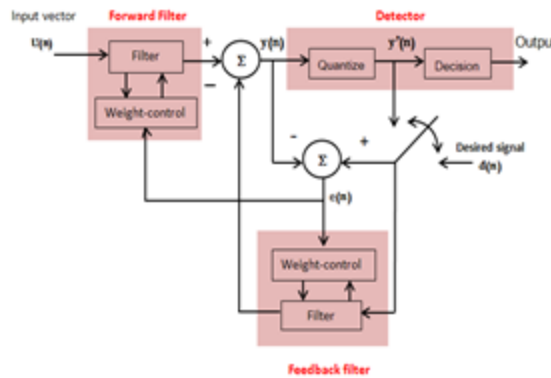


Fig. 3: A functional block diagram of general DFE

4. Phase one; Simulation Results and Discussions

Two types of equalizers were used in this investigation; a linear equalizer and a decision feedback type of equalizer. With each equalizer two kinds of adaptation algorithm, as mentioned previously, were used. The experimental sets up parameters were almost kept the same throughout the experimentation and a table of each is given beside the corresponding result for each experiment. In phase one of experimentations the number of taps is kept fixed and the performance, in terms of bit error rate, is recorded as the energy per bit to noise power ratio is varied. In phase two, the number of propagation paths of the simulated wireless channel is fixed for a given scenario and the number of taps for the equalizer used is varied. The performance in terms of bit error rate is similarly recorded for a range of SNR values. The results obtained will be presented next in the form of graphs. Discussions, explanations and suggestions are given appropriately.

4.1 Linear Equalizer with LMS Adaptation Algorithm

Fig.4 clearly shows that at low to moderate SNR (up to about 12 dBs) the number of taps of the equalizer has no effect on the performance of the system, but beyond 12 dB we found that increasing the taps will adversely affect the performance. This is justified on the bases that only three paths were considered in the scenario and at higher SNR increasing the complexity of the equalizer will decrease its rate of convergence and consequently increases the bit error rate.

Table 4.1: Operating parameters for linear equalizer with LMS algorithm

Component	Parameters	Value
Variable in Matlab model	M	2
	Tsym	0.0001
	EbNo Vec	0 : 1 : 18
Random Integer Generator	Set size	M
	Sample time	Tsym
	Samples per frame	1000
BPSK Modulator Base Band	Phase offset (rad)	0
	Output data type	Double
Rayleigh Fading	Maximum Doppler shift	0.04
	Discrete path delay vector	[0 , 0.00000002 , 0.00000003]
	Average path gain Vector	[0, -8 , -12]
AWGN Channel	Number of bits per symbol	$\log_2(M)$
Equalizer	Symbol period	Tsym
	Number of taps (10,20,30,40)	10, 20, 30, 40
	Number of samples per symbol	1
	Reference tap to (10,20,30,40)	3, 6, 7, 11
BPSK Demodulator Baseband	Step size	0.0009
	Decision type	Hard decision
Error Rate Calculation	Phase offset	0
	Receive delay to (10,20,30,40) tap	3, 6, 7, 11
	Target number of error	10000
	Maximum number of symbols	10000000

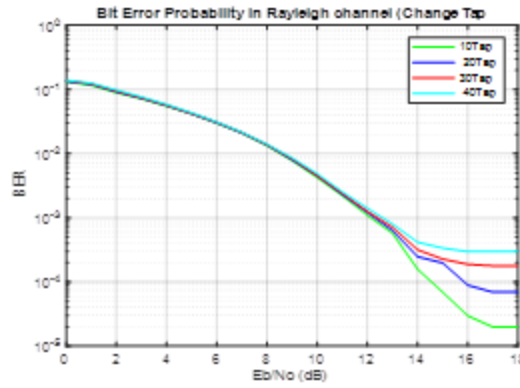


Fig. 4: BER performance for linear equalizer with LMS algorithm

4.2 Linear equalizer with RLS adaptation algorithm

For this algorithm the behavior of the system shows a little effect when increasing the equalizer taps. Fig. 5 clearly illustrates the finding already deduced for the linear equalizer with LMS algorithm. At SNRs beyond 14 dB, it is found that higher SNR shows an adverse relationship between the bit error rate and the number of taps of the equalizer as was found with the LMS algorithm and as was deduced earlier. The system implementing linear equalizer with RLS algorithm performs relatively better, in terms of BER than that with LMS algorithm as the graphs in Figs.4 and 5 indicates.

Table 4.2: Operating parameters for linear equalizer with LMS algorithm (Other parameters are set as in Table 4. 1)

Component	Parameters	value
Equalizer	Number of taps (10,20,30,40)	10, 20, 30, 40
	Number of samples per symbol	1
	Reference tap to (10,20,30,40)	3, 6, 9, 12
	Forgetting factor	0.99

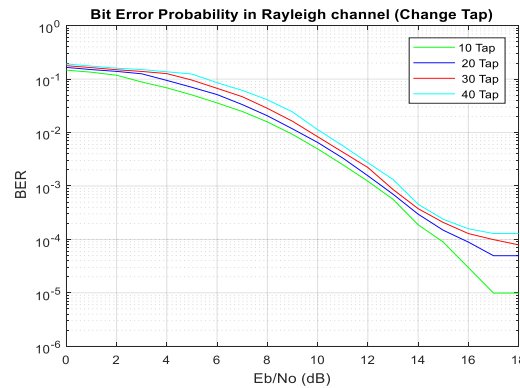


Fig. 5: BER performance for linear equalizer with RLS algorithm

4.3 DFB equalizer with LMS adaptation algorithm

The functional components of a general decision feedback equalizer (DFE), is illustrated by the block diagram of Fig. 3. The equalizer in the last experimental set was replaced by a DFE implementing LMS adaptation algorithm. Fig. 6 illustrates the BER rate performance of the decision feedback equalizer for

four different tap-lengths; 10 taps, 20 taps, 30 taps, and finally 40 taps. The Figure clearly shows that at low SNR (up to about 6 dB) the performance of the system is very poor. Over the range 6 to 13 dB, the performance improves significantly. However, over this range varying the tap lengths has no effect as well. Beyond 13 dB, we notice that increasing the tap-lengths will have a negative impact on the system performance, this behavior comes in consistence with the finding already obtained for the linear equalizer.

Table 4.3: Operating parameters for decision feedback equalizer with LMS algorithm (Other parameters are set as in Table 4.1)

Component	Parameters	value
Equalizer	Num of forward tap is (10,20,30,40)	4, 9, 14, 19
	Num of feedback tap is (10,20,30,40)	6, 11, 16, 21
	Num of samples per symbol	1
	Reference tap is (10,20,30,40)	3, 6, 9, 12
	Step size	0.0009

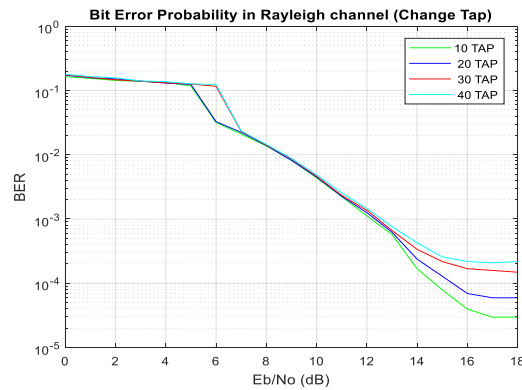


Fig. 6: BER performance for a decision feedback equalizer with LMS algorithm

4.4 DFB equalizer with RLS adaptation algorithm

The performance of the system incorporating this type of equalizer that employs RLS adaptation algorithm shows similar behavior to the last system. The graphs in figs. 3, 4, 6 and 7 indicates that about 0.5 dB is gained by implementing a DFE over the linear equalizer regardless the adaptation algorithm being employed

Table 4.4: Operating parameters for decision feedback equalizer with RLS algorithm (Other parameters are set as in Table 4.1)

Component	parameters	value
Equalized	Num of forward tap is (10,20,30,40)	4, 9, 14, 19
	Num of feedback tap is (10,20,30,40)	6, 11, 16, 21
	Num of samples per symbol	1
	Reference tap is (10,20,30,40)	3, 6, 9, 12
	Forgetting factor	0.99

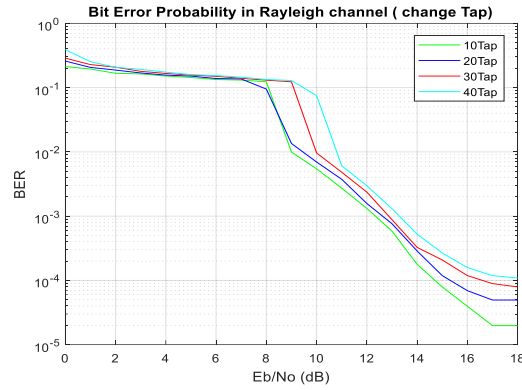


Fig. 7: BER performance for decision feedback equalizer with RLS algorithm

5. Phase Two; Simulation Results and Discussions

In this part of investigation, the effect of the number of paths (along which the transmitted signal propagates in the wireless channel) on the performance of a system implementing equalization is investigated. The system is modeled using Simulink software package. The performance is measured in terms of bit error rate (BER). Two different equalizer's structures are used, as in the first part; linear (tapped line) equalizer and decision feedback (nonlinear) equalizer. With each one of them, two adaptation algorithms (the most commonly used ones) are employed. They are; the least mean squares (LMS) algorithm and the recursive least square (RLS) algorithm. The scenario is to have up to seven paths in the channel model with corresponding gains and phase delays. The length of the equalizer (number of taps) is fixed for both structures, and for each particular number of paths; a bit error rate graph is evaluated. The procedure is repeated for the four different models. The results obtained are presented as follow:

5.1 Linear equalizer with LMS adaptation algorithm

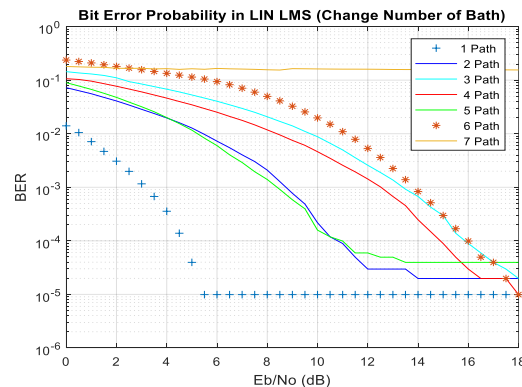


Fig. 8: BER performance for linear equalizer with LMS algorithm

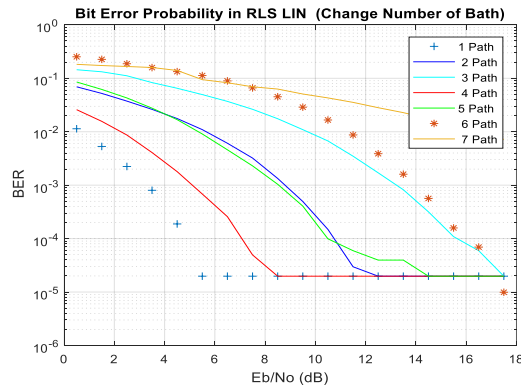
Table 5.1: Operating parameters for linear equalizer with LMS algorithm

Component	parameters	Value
Variable in Matlab model	M	2
	Tsym	0.0001
	EbNoVec	0 : 1 : 18
Random Integer Generator	Set size	M
	Sample time	Tsym
	Samples per frame	1000
BPSK Modulator Base Band	Phase offset (rad)	0
	Output data type	double
Rayleigh Fading	Maximum Doppler shift	0.04
	Discrete path delay vector to number of Path (1 , 2 , 3 , 4 , 5 ,6 , 7)	[0 0.00000002 0.00000003 0.00000004 0.00000005 0.00000006 0.00000007]
	Average path gain Vector to number of Path (1 , 2 , 3 , 4 , 5 ,6 , 7)	[0 -6 -9 -12 -13 -17 -19]
AWGN Channel	Number of bits per symbol	$\log_2(M)$
	Symbol period	Tsym
Equalized	Number of taps	5
	Number of samples per symbol	1
	Reference tap	2
	Step size	0.0009
BPSK Demodulator Baseband	Decision type	Hard decision
	Phase offset	0
Error Rate Calculation	Receive delay	2
	Target number of error	10000
	Maximum number of symbols	10000000

5.2 Linear equalizer with RLS adaptation algorithm

Table 5.2: Operating parameters for linear equalizer with RLS algorithm (Other parameters are set as in Table 5. 1).

Component	parameters	value
Equalized	Number of taps	5
	Number of samples per symbol	1
	Reference tap	2
	Forgetting factor	0.99

**Fig. 9: BER performance for linear equalizer with RLS algorithm**

5.3 DFB equalizer with LMS adaptation algorithm

Table 5.3: Operating parameters for DFB equalizer with LMS algorithm (Other parameters are set as in Table 5.1).

Component	parameters	value
Equalized	Number of forward taps	2
	Number of feedback taps	3
	Number of samples per symbol	1
	Reference tap	2
	Step size	0.0009

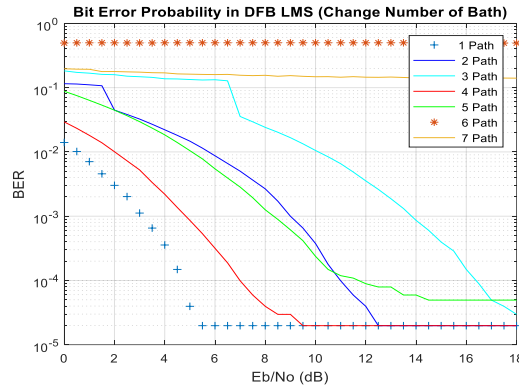


Fig. 10: BER performance for DFB equalizer with LMS algorithm

5.4 DFB equalizer implementing RLS adaptation algorithm

Table 5.4: Operating parameters for DFB equalizer with RLS algorithm (Other parameters are set as in Table 5.1).

Component	parameters	Value
Equalized	Number of forward taps	2
	Number of feedback taps	3
	Number of samples per symbol	1
	Reference tap	2
	Forgetting factor	0.99

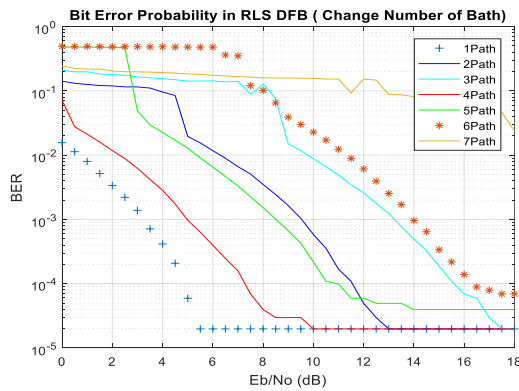


Fig. 11: BER performance for DFB equalizer with RLS algorithm

CONCLUSION

The simulation conducted in the first part of this work and the associated results obtained clearly indicate that in such time-varying environment there can be no definite relationship(s) among the structure (complexity or tap-length) of the equalizer, the adaptation algorithm and their impact on the performance of the communication system that uses equalization technique to alleviate the detrimental effect (i.e. ISI) which results due to multipath phenomena. The number of dominant multipath in a particular scenario intuitively recommend a particular number of taps in the implemented equalizer, however the nature of the environment (i.e. being nonstationary) keeps such dominating paths not fixed in number. It is also noted that the linear equalizer with RLS algorithm offers about 0.5 dB gain over the same equalizer when employs LMS algorithm. Also it noted that the FBE provides about 0.5 dB advantage over the linear equalizer.

In the second phase of experimentations, the results for the four models show that the best performance is obtained when the number of the multipath (excluding) the main (LOS) path is equal to the number of taps of the equalizer. For a single path, we found best performance for all scenarios. This is intuitive since a single path means that a single copy of the message signal arrives at the receiver and hence no ISI is present. These findings encourage a further investigation in implementing suitable techniques of sensing the channel to establish the number of significant multipath and devising a way of adaptively changing the number of taps in the implemented equalizer. The effect of the reference tap in the transversal structure and the number of proportional taps in the forward and backward in addition to the reference tap in DFB structure are to be determined when varying the tap-lengths of the implemented equalizer.

REFERENCES

- [1] Proakis, J., Salehi, M., *Digital Communications*, McGraw-Hill Companies, Inc., Fifth Edition, New York, 2008.
- [2] Malik, G., Sappal, A. (2011). Adaptive Equalization Algorithms: an Overview. *International journal of advanced computer science and applications*, vol. 2, no. 3.
- [3] Leon, W., Mengali, U., Taylor, D. (1997). Equalization of Linearly Frequency-Selective Fading Channels. *IEEE Transaction on Communication*. vol. 45.
- [4] Wah Lo, B., Ben Letaief, K. (1999). Adaptive Equalization and Interference Cancellation for Wireless Communication Systems. *IEEE Transaction on Communication*. vol. 47.
- [5] Mosleh, M., AL-Nakkash, A. (2010). Combination of LMS and RLS Adaptive Equalizer for Selective Fading Channel. *European Journal of Scientific Research*. Vol. 43.
- [6] Tehrani, A., Hassibi, B., Cioffi, J. (1999). Adaptive Equalization of Multiple-input Multiple-output (mimo) Frequency Selective Channels. *IEEE*.
- [7] Kundu, D., Nijhawan, G. (2017). Performance Analysis of Adaptive Channel Equalizer Using LMS, Various Architecture of ANN and GA. *International Journal of Applied Engineering Research*.
- [8] Patel, S., Panchal, S., Mewada, H. (2014). Comparative Study of LMS & RLS Algorithms for Adaptive Filter Design with FPGA. *Progress In Science in Engineering Research Journal (PISER)*.

- [9] Smee, J., Beaulieu, N., (1998). Error-Rate Evaluation of Linear Equalization and Decision Feedback Equalization with Error Propagation. *IEEE Transaction on Communication.* vol. 46.
- [10] Sharma, P., Chandra, K. Prediction of State Transitions in Rayleigh Fading Channels. *IEEE Transaction on Vehicular Technology.* vol. 56.
- [11] Asim, F., Bashir, S., Salman, M. (2015). Effect of Variation in Filter Length on Adaptive Equalization in Frequency Selective Channels. *International Bhurban Conference on Applied Sciences & Technology (IBCAST), Islamabad, Pakistan.*
- [12] Khajababu, Md., Padma Sree, Y., Sridha, G V. (2015). Channel Equalization of Adaptive Filters Using LMS and RLS Algorithms. *International Journal of Advanced Technology in Engineering and Science,* vol. 03.
- [13] Dileep, S., Naidu, G B S R., Naveen, V. (2013). Adaptive Channel Equalizer for Wireless Communication System. *International journal of electronics and communication engineering (ijece).* vol. 2, 159-166.
- [14] Sireesha, N., Chithra, K., Tata, S. (2015). Performance Analysis of Linear Recursive Least Squares Adaptive Filter to Mitigate Multipath Effect. *Proceedings of Sympol.*
- [15] Rugini, L., R., Banelli, P., Leus, G. (2005). Simple Equalization of Time-Varying Channels for OFDM. *IEEE Communication Letters.* vol. 9.
- [16] Sharma, P., Chandra, K. Prediction of State Transitions in Rayleigh Fading Channels. *IEEE Transaction on Vehicular Technology.* vol. 56.
- [17] Ihalainen, T., Stitz, T. (2007). Channel Equalization in Filter Bank Based Multicarrier Modulation for Wireless Communications. *EURASIP Journal on Advances in Signal Processing.*
- [18] Khajababu, Md., Padma Sree, Y., Sridha, G V. (2015). Channel Equalization of Adaptive Filters Using LMS and RLS Algorithms. *International Journal of Advanced Technology in Engineering and Science,* vol. 03.
- [19] Dhiman, J., Ahmad, S., Gulia, K. (2013). Comparison between Adaptive filter Algorithms (LMS, NLMS and RLS). *International Journal of Science, Engineering and Technology Research (IJSETR)* Vol.2.

MECHANICAL PROPERTIES OF COMPOSITE PLATES AT DIFFERENT CONDITIONS

Gurbet ÖRÇEN^{1}, Kadir TURAN², Sedat BİNGÖL³*


In this study; the effects of thermal aging on the mechanical properties of composite materials were investigated. In study, eight layered woven glass fiber reinforced epoxy composite plates were used. Thermal aging was performed in an electric furnace using time and temperature change parameters. The time changes were 1, 3 and 5 hours, and 50 °C, 100 °C, and 150 °C were used for temperature changes. Thermally aged composite plates, at specified time and temperature values; modulus of elasticity, poisson ratio, tensile strength, compression strength, shear modulus and shear strength were determined in fiber reinforcement direction. The results obtained were compared with the results obtained from the specimens waited at room temperature. At the end of the study, it was determined that the mechanical properties of the composite plates changed when the thermal aging temperature and temperature increased.


Key words: Thermal Aged, Composite Plates, Mechanical Properties, Environmental Effects.


1. Introduction

The need for materials with advanced mechanical properties is now met by using composite materials. One of the most important features of composite materials is that they can be designed. The design requires that the loads and temperatures at which the product is used be predetermined. This is not the case for composite materials, although it has been identified for conventional materials. In this meaning, the effect of thermal aging on mechanical behavior requires a good analysis and appropriate design.

Many studies have been conducted in the literature, especially on the effects of thermal aging on composite plates. Mouzakis et al. [1] investigated the damage behavior of glass fiber / polyester composite materials exposed to different environmental conditions. They studied changes in ambient temperature, humidity and UV radiation on mechanical properties. In the study, they determined that the tensile strength of the specimens decreased by 2.5 %, the modulus of elasticity increased by 7% and the elongation rate increased by 13%. Leveque et al. [2] investigated the effects of thermal aging on the strength and mechanical behavior of polymer matrix composites. In the study, they stated that the mechanical properties of carbon epoxy composites with different reinforcement angles changed

¹ Department of Mechanical Engineering, University of Dicle, Diyarbakır, Turkey, (gurbetorcen@dicle.edu.tr)  <https://orcid.org/0000-0002-8329-8142>

² Department of Mechanical Engineering, University of Dicle, Diyarbakır, Turkey, (kturan@dicle.edu.tr)  <https://orcid.org/0000-0002-4065-9649>

³ Department of Mechanical Engineering, University of Dicle, Diyarbakır, Turkey, (sbingol@dicle.edu.tr)  <https://orcid.org/0000-0002-4290-4193>

when exposed to thermal aging under a constant temperature of 120 °C in the range of 720 to 4400 hours. Ktsotsi et al. [3] investigated the mechanical behavior of aged carbon/epoxy composite sheets at different pressures and temperatures. They determined that the aging process affects mechanical behavior. Mulina et al. [4] examined the effects of glass fiber/vinylester and glass fiber/epoxy composite sheets on thermo-mechanical properties. As a result of the study, they determined that the creep elongation increases due to the increase in temperature. Alcock et al. [5] investigated changes in the mechanical performance of polypropylene tapes exposed to different temperatures. They found that increasing temperatures adversely affect tensile strength. Brinson and Gates [6] investigated the effects of thermal aging on the creep behavior of polymer matrix composites. Specifically, they determined that temperatures above glass transition temperatures adversely affect mechanical behavior. Dlouhy et al. [7] investigated the effects of thermal aging on fracture toughness and mechanical properties of glass matrix composite sheets reinforced with short carbon fibers. They found that the thermal aging process reduced the tensile strength by 44% to 77% and that the fracture toughness of the samples aged at 700 °C decreased by 84%. Ray [8], investigated the effects of thermal shock on the interface shear stresses of glass fiber/epoxy composite plates. They calculated that interfacial shear strength decreased for 5 minutes and increased for later periods. Hu and Sun [9], investigated the creep behavior of carbon/epoxy composite plates exposed to thermal aging at certain times. Belaid et al. [10] investigated the effects of thermal aging on the mechanical behavior of glass fiber / polyester composite plates. They stated that as time increases, modulus of elasticity decreases by approximately 50% and tensile strength decreases by 22%. Cao et al. [11,12] investigated the effect of temperature on carbon fiber reinforced polymer (CFRP) layered, hybrid carbon/glass fiber reinforced polymer layered (C/GFRP), hybrid carbon / basalt fiber reinforced polymer layered (C/BFRP) composites. The authors stated that carbon fibers containing different fiber-reinforced polymer layers significantly decreased their tensile strength with increasing temperature. However, it is stated that the tensile strength of FRP sheets is still a constant value after reaching the polymer glass transition temperature (T_g) and this value is higher than the tensile strength of the impregnated fiber sheets [12]. Sauder et al. [13] measured the fundamental mechanical properties of various carbon fibers up to 2400 °C by tensile testing. In this study, it was stated that Young's modulus decreased with increasing temperature and tensile strength increased to a maximum value. Nikolaev et al. [14] investigated the effect of temperature on stationary and cycles ranging from 120 °C to 196 °C on CFRP-produced samples. Giannadakis and Varna [15] investigated the effect of thermal fatigue and thermal aging on CF/EP composites. The authors stated that the mechanical properties of specimens exposed to thermal aging over long periods of time decreased mainly as a result of matrix degradation. Eric et al. [16], investigated the changes in the mechanical properties of porous-Matrix Ceramic composites which were kept at 1000 °C, 1100 °C, 1200 °C for 1000 hours. $[0^0/90^0]$ composite, 1200 °C after heat treatment; they stated that the value of 60 GPa increased to 70 GPa, thus increasing the modulus of elasticity with a small increase. Plecnik [17] investigated the strength of epoxy resin at elevated temperatures by performing compression, tensile and shear tests. They stated that the strength decreased at temperatures close to the glass transition temperature and reached a fixed value when the glass transition temperature was exceeded. Rami et al. [18] investigated the mechanical properties of carbon, glass and glass-carbon hybrid composite plates under different temperatures. They stated that the tensile strength and elastic modulus value of carbon, glass and carbon-glass hybrid composite decreased when the temperature was increased.

This study; it is important to observe the effects of temperature and time changes on the mechanical properties of composite plates. For this purpose, in order to clearly observe the effects and changes of temperature change and time change, the test results of thermally aged specimens were compared with the results of samples waited at room temperature (25 °C). Mechanical properties obtained in fiber reinforcement direction were investigated. The change of these mechanical properties is an important area in terms of reconsidering the convenient design conditions with reference to temperature and time changes of the composites.

2. Experimental Study

In this study, the tests on glass fiber reinforced epoxy composite plates were divided into three groups. In group 1; Tensile tests were performed to determine modulus of elasticity, tensile strength and poisson ratio. In 2rd group, compression tests were performed. In the 3rd group, tests were performed to determine the shear modulus and shear failure load. Specimens were prepared from 1.6 mm thick composite plate according to ASTM standards. The prepared specimens were subjected to thermal aging at 50 °C, 100 °C, 150 °C for 1 hour, 3 hours and 5 hours in an electric oven where ambient humidity was neglected. For the consistency of the experimental study, three samples were produced for each parameter and experiment. The specimens were allowed to cool after being removed from the furnace and tested after cooling. The arithmetic mean of the obtained results were taken and transferred to tables and graphs.

2.1. Tensile Test

Elasticity modulus (E_{11}), poisson ratio and tensile strength were determined by tensile tests in the direction of fiber reinforcement. Strain gauges were used to determine the modulus of elasticity and poisson ratio. Specimens were used 14 mm width, 200 mm length and 1 mm thickness and 0° fiber reinforcement angle. Since woven glass fiber is used, the mechanical properties parallel to the fiber reinforcement direction and perpendicular to the fiber reinforcement are equal.

Modulus of elasticity and poisson ratio were determined according to ASTM D3039-76 standard [19]. Specimens were tested in the tensile device at a rate of 1 mm / min. The axial normal tension of the specimens in the fiber direction (σ_{11}) was obtained by dividing the tensile load (F) by the cross-sectional area (A). The elongation values in the fiber reinforcement direction (ϵ_{11}) were determined by the values obtained from the strain-gauge. The modulus of elasticity (E_{11}) in the fiber reinforcement direction was calculated by substituting the obtained values in the formula (1).

$$\sigma_{11} = \frac{F}{A}; \epsilon_{11} = \frac{\Delta l}{l} \Rightarrow E_{11} = \frac{\sigma_{11}}{\epsilon_{11}} \quad (\text{MPa}) \quad (1)$$

To determine the Poisson ratio, strain gauge was used to calculate the transverse shrinkage ratio perpendicular to the fiber (ϵ_{22}). The poisson ratio was also determined using the formula (2).

$$\nu_{12} = - \frac{\epsilon_{22}}{\epsilon_{11}} \quad (2)$$

In the determination of the tensile failure load, the tensile load is increased until the specimens breaks. The tensile damage load in the fiber reinforcement direction was determined by the formula (3) by dividing the obtained maximum load (P_{ult}), into the cross-sectional area (A).

$$X_t = \frac{P_{ult}}{A} \text{ (MPa)} \quad (3)$$

In tensile test, three specimens were made from each geometry and load-extension graphs were obtained by using the data obtained from these specimens. Figure 1 presents the results obtained from specimens waiting at 100 °C for 1 hour.

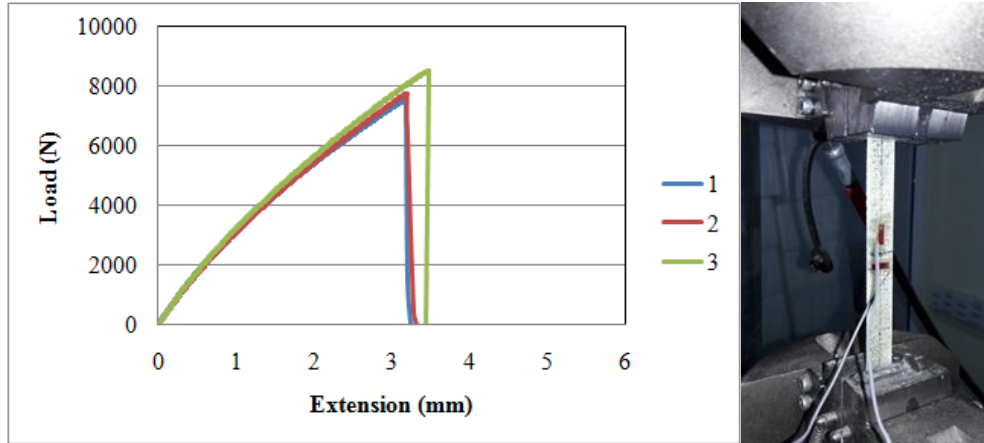


Figure 1. Tensile test set up and tensile test results of three specimens thermal aging for 1 hour at 100 °C.

2.2. Compression Test

The specimens whose geometry is specified in Figure 2 for determination of compression failure load were prepared according to ASTM 3410-75 [19]. The test was carried out by increasing the compressive load until the specimens were broken.

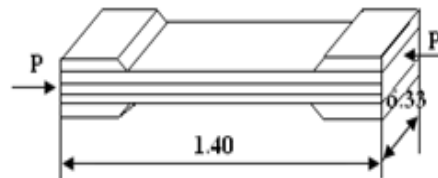


Figure 2. The geometry of the test specimen prepared for the determination of compressive strength [20].

The compressive strength is obtained by the formula 4, that is, by dividing the maximum compressive failure load (P_{ult}) by the cross-sectional area (A).

$$X_c = \frac{P_{ult}}{A} \text{ (MPa)} \quad (4)$$

In Figure 3, the load-extension graph of three specimens prepared at 100 °C for 1 hour is given as an example.

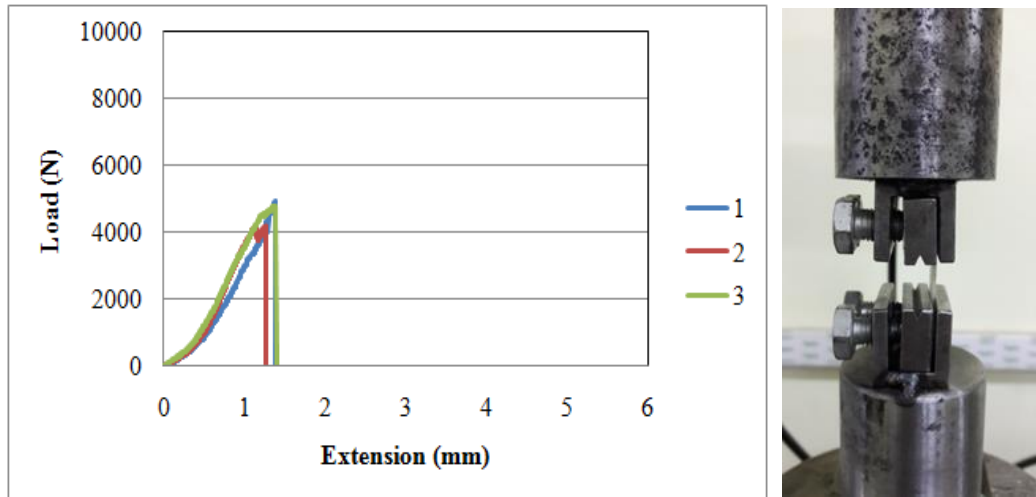


Figure 3. Results of compression test and compression test set of thermally aged sample for 1 hour at 100 ° C.

2.3. Shear Test

Specimens were prepared according to ASTM 5379 standard [19] to determine the shear modulus and shear failure load. The specimen geometry shown in Figure 4 was used in the shear test.

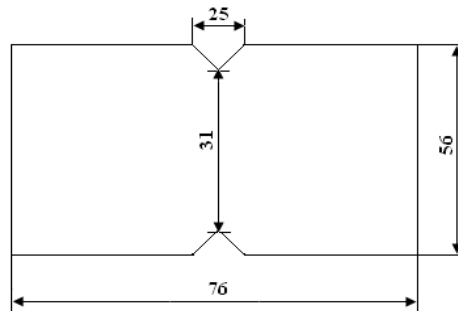


Figure 4. Specimens geometry for shear testing [20].

The shear failure load (S_{12}) was calculated by the formula (5) and the shear modulus (G_{12}) was calculated by the formula (6) from the linear region of the graph indicated in Figure 5.

$$S_{12} = \tau = \frac{P_{ort}}{A} \quad (5)$$

$$G_{12} = \frac{P}{2.A.\varepsilon} \quad (6)$$

In Figure 5, the load-extension graph of the three specimens prepared for 1 hour at 100 °C is given as an example.

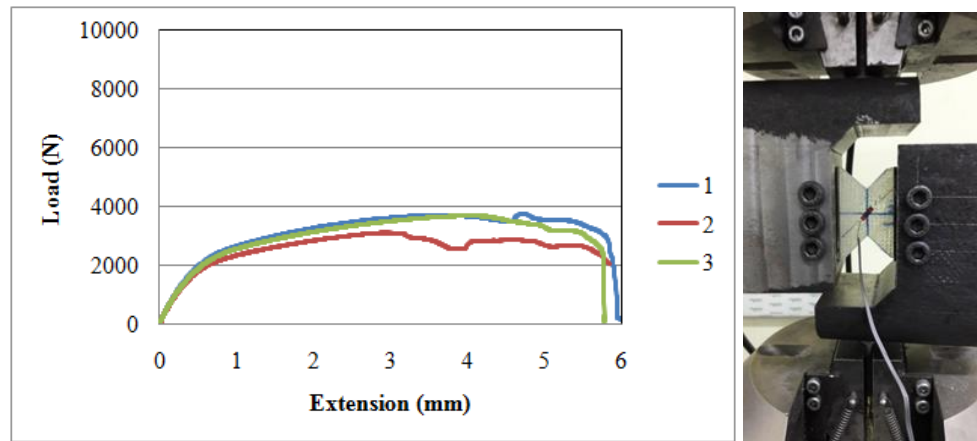


Figure 5. Shear test results and shear test set of thermally aged specimens for 1 hour at 100 ° C.

3. Experimental results and discussion

3.1. The effect of thermal temperature on strength and comparison

For the determination of tensile strength of glass fiber reinforced epoxy composite specimens, the values obtained from the test results were averaged and transferred to Figure 6 and Table 1.

When Figure 6 and Table 1 are examined; it is seen that the tensile strength values obtained at 50 °C, 100 °C and 150 °C are actually close to each other, but these values are higher than those obtained from specimens kept at room temperature (25 °C). It is seen that the temperature has an increasing effect on the tensile strength of the composite material, but it decreases as the waiting time increases. While it reaches maximum value at 100 °C for all three waiting dwell times, it is seen that these values decrease at 150 °C and close values are obtained. It was found that the tensile strength of the specimens which was kept at 150 °C for 1 hour increased by 9.58% compared to the value obtained from the specimens kept at room temperature, and decreased by 6.35% according to the value obtained from specimens kept at 100 °C for 1 hour.

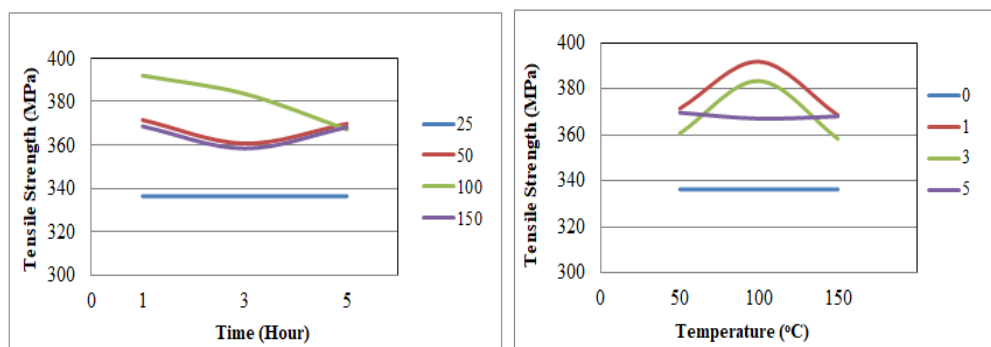


Figure 6. Graphs of tensile strengths obtained from thermally aged specimens based on time and temperature.

Shear strength values obtained from glass fiber reinforced epoxy composite specimens are shown in Figure 7 and Table 1. It is seen that maximum values are obtained from specimens exposed to thermal aging at 100 °C. The shear strength values obtained from the specimens kept at 50 °C, 100 °C and 150 °C for 5 hours, respectively, according to the value obtained from the specimens kept at room temperature; 7.61%, 16.32% and 4.99% were found to be low.

Table 1. Temperature-time effect on strength values obtained from specimens.

Strength Type	Time (h)	Temperature parameters (°C)			
		25	50	100	150
Tensile Strength (MPa)	1	336.4	371.5937	392.06	368.6633
	3	336.4	360.7363	383.6367	358.43
	5	336.4	369.8293	367.2233	368.2127
Compressive Strength (MPa)	1	250.815	202.2787	209.6153	171.2823
	3	250.815	176.703	192.091	154.636
	5	250.815	215.1523	229.8763	179.3153
Shear Strength (MPa)	1	80.8835	78.451	85.8115	74.72
	3	80.8835	76.271	80.6225	67.6835
	5	80.8835	84.434	95.9625	76.8405

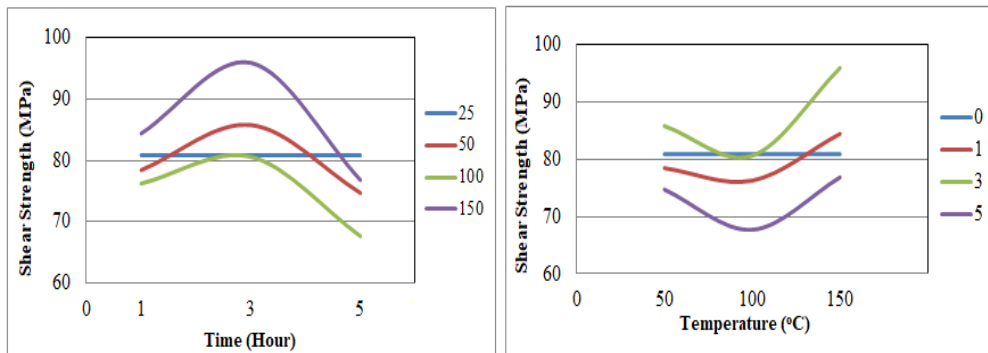


Figure 7. Graphs of shear strengths obtained from thermally aged specimens based on time and temperature.

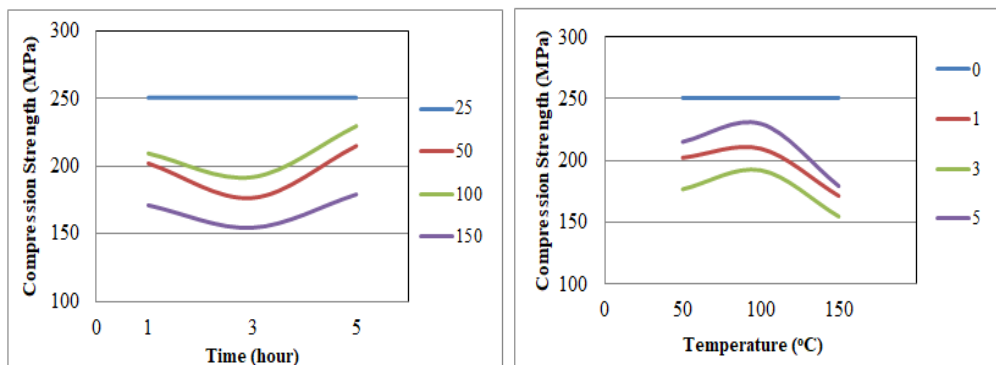


Figure 8. Graphs of compressive strengths obtained from thermally aged specimens based on time and temperature.

The compressive strength of glass fiber reinforced epoxy composite specimens is shown in Figure 8 and Table 1. The highest compressive strength values were obtained from the specimens kept at room temperature (25 °C). Maximum values were obtained from specimens exposed to thermal aging at 100 °C. The lowest values were obtained from the specimens subjected to thermal aging at 150 °C for 1 hour, 3 hours and 5 hours. According to the values obtained from the specimens at room temperature, it was calculated that they decreased by 31.70%, 38.70% and 28.50% respectively.

3.2. The effect of thermal temperature on poisson ratio, elasticity and shear modulus and comparison

The average values obtained in the determination of the modulus of elasticity of glass fiber reinforced epoxy composite specimens were transferred to Figure 9 and Table 2.

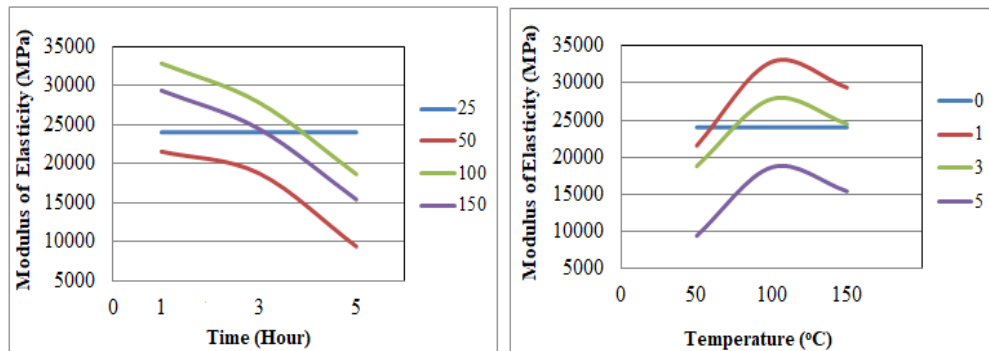


Figure 9. Graphs of Elasticity modulus obtained from thermally aged specimens based on time and temperature.

The highest elastic modulus value; it is obtained from specimens exposed to thermal aging at 100 °C for 1 hour. However, it was found that these values decreased when the waiting time was 5 hours. It was found that the elasticity modules obtained from the specimens kept at 50 °C, 100 °C and 150 °C decreased according to the values obtained from the specimens kept at room temperature (25 °C) in the ratios of %60.89, %22.32 ve %35.72, respectively (Figure 9, Table 2).

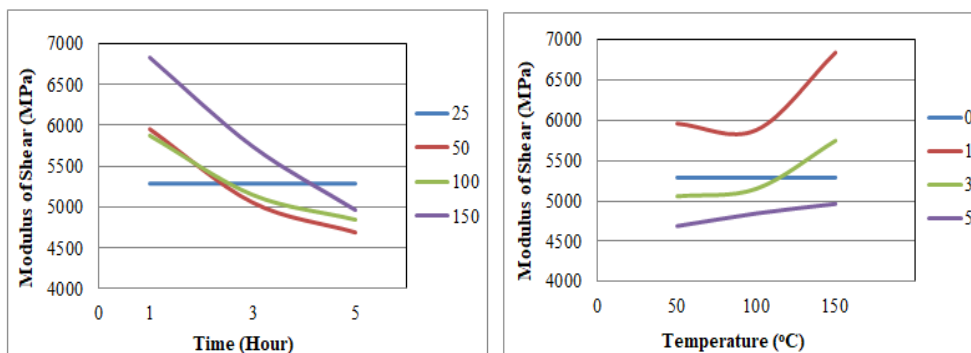


Figure 10. Graphs of Shear modulus obtained from thermally aged specimens based on time and temperature.

Shear modulus values of glass fiber reinforced epoxy composites were determined and indicated in Figure 10 and Table 2. The shear modulus values obtained when the specimens were exposed to thermal temperature for 1 hour at 50 °C, 100 °C and 150 °C increased compared with the values obtained from the specimens at room temperature; 12.62%, 11.13%, 29.21% respectively. This situation has a positive effect on the composite material, but it has been found that these values

decrease when the waiting time increases. This situation; It also shows that the values obtained when kept at each temperature parameter for 5 hours decreased by 11,30%, 8,35% and 6,11%, respectively, when compared to the values obtained from the specimens kept at room temperature (Figure 10).

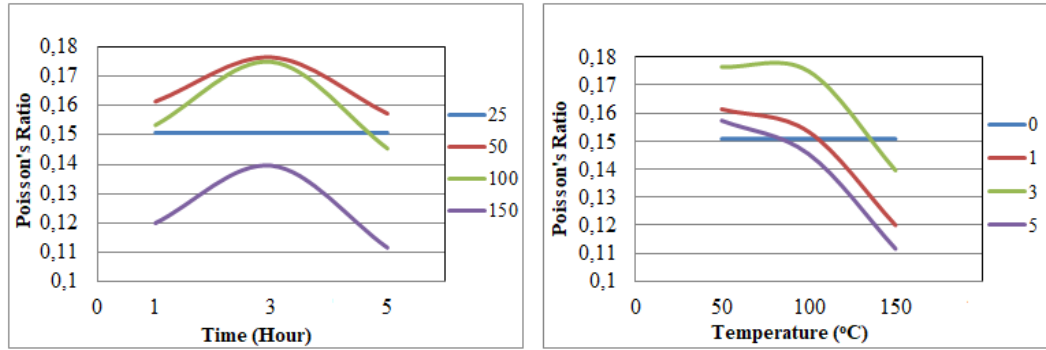


Figure 11. Graphs of Poisson's ratio obtained from thermally aged specimens based on time and temperature.

The values obtained after the test for determining Poisson's ratio were transferred to Figure 11 and Table 2. It is seen that the lowest poisson ratio values are obtained from the specimens aged at 150 °C. At 50 °C; poisson ratio increased between 6.7% - 13.3%, while the temperature at 150 °C caused a decrease between 13.33% - 26.66%.

Table 2. Temperature-time effect on the values obtained from the specimens

	Time (h)	Temperature Parameters (°C)			
		25	50	100	150
Elasticity Modulus (MPa)	1	24026.17	21558.81	32867.83	29387.40
	3	24026.17	18792.44	27860.46	24488.14
	5	24026.17	9396.221	18662.31	15422.41
Shear Modulus (MPa)	1	5288.10	5955.875	5876.702	6833.148
	3	5288.10	5057.419	5150.782	5744.90
	5	5288.10	4690.348	4846.253	4964.485
Poisson's Ratio	1	0.150797	0.161431	0.153397	0.12
	3	0.150797	0.176535	0.175	0.139587
	5	0.150797	0.157344	0.145453	0.111614

3.3. Determination of the glass transition temperature of the composite plate

The glass transition temperature of the glass fiber reinforced epoxy composite plate was determined by DSC tests to effectively understand thermal aging. Glass transition temperature tests were performed with Shimadzu DSC-60 device by increasing 10 °C every minute. As a result of the experiments, the glass transition temperature of the composite plate was found to be 107.95 °C (Figure 12).

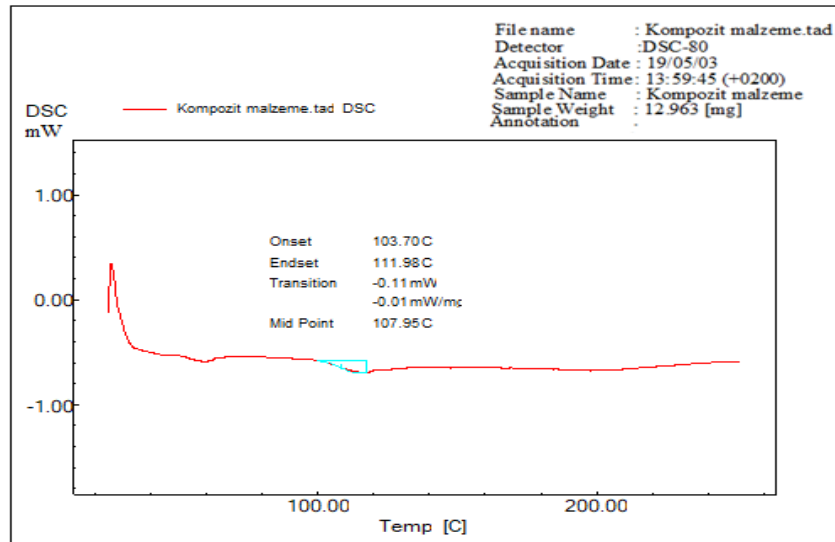


Figure 12. Graph of glass transition temperature of glass fiber reinforced woven epoxy composite plate.

4. Results

The values obtained in the study re-demonstrated the importance of the relationship between temperature and composite plates. Because it is known that if the glass transition temperature of the glass fiber reinforced epoxy composite plate is exceeded, the fiber-resin interfaces of the composites will deteriorate and consequently their strength is expected to decrease. The damage to the integrity of the matrix material [15] appears to be more pronounced above the glass transition temperature of the composites. It also increases the viscosity of polymers when the temperature exceeds the glass transition temperature. In this meaning, the glass transition temperature is a critical threshold [11]. However, in the experiment, it has been found that with the increase of temperature, it causes an increase in tensile strength, even if it is low, and other mechanical properties decrease.

In this study, it was determined that the tensile strength of the composite increased by 6.55% and 16.5%, especially with the increase of thermal temperature. It is seen that the composite specimen reaches the maximum value at 100 °C at the value close to the glass transition temperature. It was observed that the maximum values obtained at 150 °C were decreased /steady progress when Tg temperature was exceeded. This progress is noted in the study by Cao et al. [12] and Plecnik [17]. In addition, Sauder et al. reported that they reached maximum strength value with increasing temperature due to fiber texture [13]. If the temperature exceeds 150 °C, these values are expected to decrease further. In addition, an increase was observed in shear strength (5 hours at 50 °C, 1-5 hours at 100 °C), poisson ratio (1.3, 5 hours at 50 °C), elasticity (1 to 3 hours at 100 °C to 150 °C) and shear modulus (1 hour at 50,100 and 150 °C) values. However, it was found that these values decreased when waiting time and temperature increased. As can be seen in the literature [10,11,12,14,18].

5. Conclusions

In this study, the effects of thermal temperature on the glass fiber reinforced epoxy composite plate were investigated experimentally. Specimens were kept at 50 °C, 100 °C and 150 °C for 1, 3 and 5 hours. Then tensile test was performed and the results were evaluated.

As a result of this experimental study;

- It was found that the compressive strength values of the specimens exposed to thermal aging were lower.
- The lowest values of modulus of elasticity, poisson ratio, shear modulus and shear strength were obtained from the specimens kept at 150 °C for 5 hours.
- It was found that mechanical properties of the specimens decreased with increasing temperature and waiting time except tensile strength.

Acknowledgment

This work, it was supported by DÜBAP ENGINEERING-15.010 project.

References

- [1] Mouzakis, D.E., Zoga, H., Galiotis, C., Accelerated Environmental Ageing Study of Polyester/Glass Fiber Reinforced Composites (GFRPCs), *Composites: Part B*, 39 (2008),pp. 467–475.
- [2] Leveque, D., Schieffer, A., Mavel, A., Maire, J.F., Analysis of How Thermal Aging Affects The Long-Term Mechanical Behavior and Strength of Polymer–Matrix Composites, *Composites Science and Technology* ,65 (2005), pp.395–401.
- [3] Tsotsis, T.K., Keller, S., Lee ,K., Bardis, J., Bish J., Aging of Polymeric Composite Specimens for 5000 Hours at Elevated Pressure and Temperature, *Composites Science and Technology*, 61 (2001), pp. 75-86.
- [4] Muliana, A., Nair, A., Khan, KL.A., Wagner, S., Characterization of Thermo-Mechanical and Long-Term Behaviors of Multi-Layered Composite Materials, *Composites Science and Technology*, 66 (2006),pp. 2907–2924.
- [5] Alcock, B., Cabrera, N.O., Barkoula, N.M., Reynolds, C.T., Govaert, L.E., Peijs, T., The Effect of Temperature and Strain Rate on the Mechanical Properties of Highly Oriented Polypropylene Tapes and All-Polypropylene Composites, *Composites Science and Technology*, 67 (2007), pp. 2061–2070.
- [6] Brinson, L.C., Gates, T.S., Effects of Physical Aging on Long Term Creep of Polymers and Polymer Matrix Composites , *Inf. J. Solids Structures*, 32(1995), pp. 827-846.
- [7] Dlouhy, I., Chlup, Z., Boccaccini, D.N., Atiq, S., Boccaccini, A.R., Fracture Behaviour of Hybrid Glass Matrix Composites: Thermal Ageing Effects, *Composites: Part A*, 34 (2003), pp.1177–1185.
- [8] Ray, B.C., Thermal Shock on Interfacial Adhesion of Thermally Conditioned Glass Fiber/Epoxy Composites, *Materials Letters*, 58 (2004), pp.2175–2177.

- [9] Hu, H., Sun, C.T., The Characterization of Physical Aging in Polymeric Composites, *Composites Science and Technology* , 60 (2000), pp. 2693-2698.
- [10] Belaid, S., Chabira, S.F., Balland, S.P., Sebaa, M., Belhouideg, S., Thermal Aging Effect on The Mechanical Properties of Polyester Fiberglass Composites, *J. Mater. Environ. Sci.*, 6 (2015) ,10, pp.2795-2803
- [11] Cao, S., Wu, Z., Wang, X., Tensile Properties of CFRP and Hybrid FRP Composites at Elevated Temperatures, *Journal of composite materials*,43(2009), 4.
- [12] Cao, S., Wu, Z., Tensile Properties of FRP Composites at Elevated and High Temperatures, *Journal of applied mechanics* , 11(2008),pp. 963-970.
- [13] Sauder, C., Lamon, J., Paille, R., The Tensile Behavior of Carbon Fibers at High Temperatures up to 2400 °C, *Carbon*, 42 (2004),pp. 715–725.
- [14] Nikolaev, V.P., Myshenkova, E.V., Pichugin, V.S., Sinitsyn, E.N., Khoroshev, A. N., Temperature Effect on the Mechanical Properties of Composite Materials, *Inorganic Materials*, 50(2014), 15, pp. 1511–1513.
- [15] Giannadakis, K., Varna, J., (2009). Effect of Thermal Aging and Fatigue on Failure Resistance of Aerospace Composite Materials, *IOP Conf. Series: Materials Science and Engineering*, 5, doi:10.1088/1757-899X/5/1/012020.
- [16] Eric, A., Carelli, V., Effects of Thermal Aging on the Mechanical Properties of a Porous-Matrix Ceramic Composite, *J. Am. Ceram. Soc.*, 85(2002), 3, pp.595–602.
- [17] Plecnik, J., Temperature Effects on Epoxy Adhesives, *Journal of Structural Division*, 106 (1980), 106(1), pp. 99-113.
- [18] Rami, A. H., Adi, A.O., Jamal, A. A., Adil A.T., Temperature Effect on the Mechanical Properties of Carbon, Glass and Carbon–Glass FRP Laminates, *Construction and Building Materials* , 75 (2015), pp. 342–348.
- [19] Carlsson, L.A, Pipes, R.B., *Experimental Characterization of Advanced Composite Materials-Second Edition*, Technomic Publishing Company book,(1997).
- [20] Okutan, B., *Stress and Failure Analysis of Laminated Composite Pinned Joints*, Ph. D. thesis, Science Institute of Dokuz Eylül University, İzmir. 2001.

THE EFFECTS OF HIGH DENSITY POLYETHYLENE ADDITION TO LOW DENSITY POLYETHYLENE POLYMER ON MECHANICAL, IMPACT AND PHYSICAL PROPERTIES

Erkin AKDOĞAN^{1*}


Polyethylene materials are the most widely used polymers which we encountered everywhere in our daily life. Some of the advantages of the polyethylenes are the diversity of production types, corrosion resistance, electrical insulation and recyclability. The main production methods are compression molding, transfer molding, rotational molding, injection molding, gas-assisted injection molding, extrusion and blown film extrusion techniques. It is possible to increase the mechanical properties of low density polyethylene materials by addition of high density polyethylene materials. Both polymer has same monomers but their chemical structure and bonding properties are different. Their physical properties can change with their chemical structure and bonding properties. In this study, 25%, 50% and 75% by weight of high density polyethylene were added to low density polyethylene. Granules were pre-mixed with a mechanical mixer before production of the samples. Plastic injection molding machine was used for specimen preparation. Density, hardness, tensile test, three-point bend test, compression test, tear test and Izod impact tests were performed. Densities and hardness values of the polymer blends decrease by the increasing amount of low density polyethylene. In general, it was observed that the mechanical properties of the polymer blends increase as the high density polyethylene content increase.

Key words: Low density polyethylene, High density polyethylene, Density, Hardness, Tensile test, Three point bend test, Compression test, Tear test, Izod impact test

1. Introduction

Polymeric materials, light weight, cheapness, insulation, sufficient mechanical properties, easy formability, decorative and ergonomic usage, chemically resistant and can be used for different purposes. Due to these properties, it has wide usage fields such as machinery, chemistry, physics, textile, industry, medicine, biochemistry and biophysics. Polymer as a word which derives from the origin of poly means multiple and mer(meros) means structure from two Greek words. Polymers consist of monomers. Monomers are the structures that can be connected to each other by covalent bonds to form large molecules. The production methods of polymers includes first the polymerisation of polymer as a

^{1*} Department of Mechanical Engineering, University of Karamanoğlu Mehmetbey, Karaman, Turkey, (eakdogan@kmu.edu.tr)

 <https://orcid.org/0000-0001-6993-6972>

chemical process, after producing the desired part with mechanical and thermal process. Thermoplastic materials are in the subgroup of polymers and can be finalized by being shaped by heat and mechanical treatment. These process can be performed again and again on these materials. But their physical properties can change against heat, remolding and forming process. Injection molding, gas-assisted injection molding, extrusion, blown film extrusion, rotational molding, pressure molding and transfer molding are the main production methods of thermoplastic polymer products [1, 2]. Polyethylene is a polymer with a broad range application areas in plastics industry. Polyethylene is a group in polyolefin family. Its chemical structure includes methylene (CH_2) monomers. Polyethylene materials are classified according to their density and bonding type. Low density polyethylene (LDPE), linear bonded low density polyethylene (LLDPE), medium density polyethylene (MDPE), high density polyethylene (HDPE), ultra high molecular weight polyethylene (UHMWPE) and cross-linked polyethylene (XLPE) are the six different types of polyethylenes. Some of the wide range application areas of polyethylenes are chemical containers, detergent cups, tubes, pressurized water and gas pipes, cable insulation, some automotive parts, various food storage containers, shopping bags, pochette and plastic bags, entertainment and toys. HDPE and LDPE are the most widely used polyethylene types. Both thermoplastics are suitable for injection and extrusion productions.

Polymer blends which have called as polymer alloys have been performed by researchers with mixing different polymers from many years. Productions and physical tests of HDPE-polypropylene (PP), HDPE-LLDPE and LDPE-polyamide 6 (PA6)-ethylene vinyl acetate (EVA) alloys were carried out [4]. Shebani et al. 2018 added 20%, 40%, 60%, and 80% LDPE polymer to the HDPE polymer. They performed tensile test, charpy impact test, hardness measurement and differential scanning calorimeter (DSC) tests. They found out that with the addition of LDPE, tensile strength and hardness values decreased, but the elongation at break and the toughness values increased [5]. Sarkhel et al. 2006, in their study, HDPE blended LDPE in 80/20, 60/40, 40/60 and 20/80 ratios respectively to obtain polymer mixtures. They found that the melt viscosity of these mixtures decreases with the increased concentration of LDPE. Besides, they found out that increased amount of LDPE causes the deterioration in mechanical properties from the results of tensile tests. However they determined that the increasing amount of LDPE in mixture, increased the Izod impact strength values. As a result, they observed that as the LDPE ratio in HDPE polymer increased, the crystal ratio decreased in DSC analysis [6, 7].

In this study, 25%, 50% and 75% by mass of HDPE polymer was added to LDPE polymer. Density, hardness, Izod impact, tear, tensile, three point bending and compression tests were performed.

2. Material and Method

2.1. Materials

Two different polymer were mixed in different ratios in this study. A new polymer alloy was produced by mixing these two different polymers. LDPE polymer was used as a granular form Petilen I22-19T commercial product with a melt flow rate of 22 g/10 min (190 °C / 2.16 kg) of PETKIM. HDPE polymer was used as a granular form Petilen I668 commercial product with a melt flow rate of 5.5 g/10 min (190 °C / 2.16 kg) from PETKIM. Both polymers are suitable for injection molding.

2.2. Preparation of Samples

The production of LDPE-HDPE mixtures, granular materials were pre-mixed with Heidolph brand, RZR 2021 model mechanical mixer. 25%, 50% and 75% by mass of HDPE was added to the

LDPE polymer. Each formula was mixed at 200 rpm for 10 minutes. The samples were dried in the oven at 60 °C for 4 hours to remove moisture. Specimens were prepared in a single screw plastic injection molding machine (diameter: 35 mm, L/D ratio: 30, clamping force: 700 kN). Mixtures were injected into mold at 170-180-190-200 °C temperatures from feeding zone to nozzle zone. Mechanical mixer, oven and plastic injection molding machine are shown in Figure 1.



Figure 1. Equipment and machines used in production a) mechanical mixer, b) oven and c) plastic injection machine

Mixing ratios by weight of the samples are given in Table 1. Thirty specimen groups were produced from each formulas. The specimen group includes tensile test, flexural test, tear test, conical calorimeter test, compression test, notched and unnotched Izod impact test specimens (Figure 2).

Table 1. Mixing ratios of HDPE-LDPE blends

Specimen	Code	LDPE (%)	HDPE (%)	Total (%)
LDPE	LDPE	100	-	100
LDPE3-HDPE1	L3H1	75	25	100
LDPE1-HDPE1	L1H1	50	50	100
LDPE1-HDPE3	L1H3	25	75	100
HDPE	HDPE	-	100	100

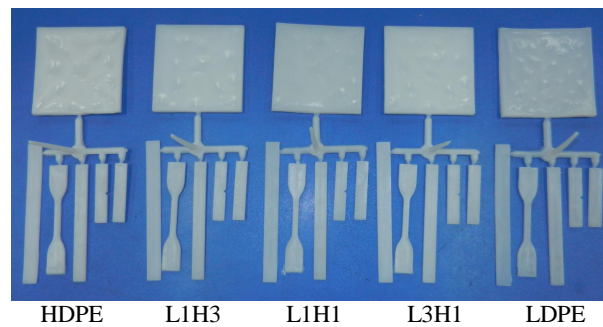


Figure 2. The produced samples in the plastic injection molding machine

2.3. Tests and Characterizations

All samples were stored in Nüve brand TK252 model conditioning cabinet at 23 °C and 50% relative humidity for 40 hours according to ASTM D618 standard before tests (Figure 3). Tests were performed at 23 °C and 50% relative humidity.



Figure 3. Nüve TK 252 conditioning unit

The density measurement was made from 6 samples from each formulas. The mass and volumes were measured and the density of the samples were calculated by dividing the mass by volume according to ASTM D792 standard. Three-point bending samples were used for density measurement (Figure 4). Hardness measurements were carried out on 6 samples in X.F Shore-D hardness tester (Figure 5) according to ASTM D2240 standard.

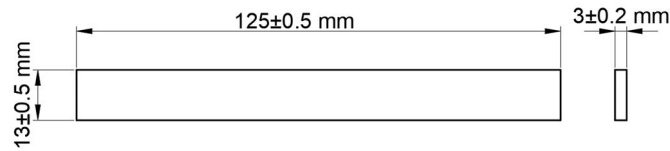


Figure 4. The dimensions of three-point bending specimen [3]



Figure 5. X.F Shore-D durometer

Impact strength properties were determined with pendulum impact test machine. Izod impact resistance test was performed at Ceast Resil Impactor device (Figure 6) according to ASTM D256 standard. 6 samples were tested from each mixture with 7.5 J to 25 J. The dimensions of the specimens are shown in Figure 7. The size of notch is 2.54 mm depth with an angle of 45° according to ASTM D256 standard.



Figure 6. Ceast Resil impactor test device [3]

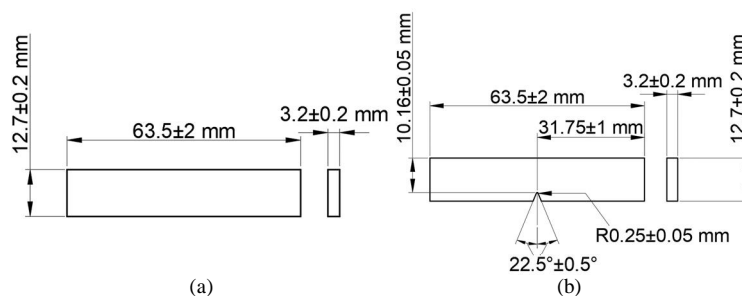


Figure 7. The dimensions of Izod impact test specimens (a) unnotched and (b) notched [3]

Tear strength test was performed on 6 samples from each mixture according to ASTM D624 (Type-T) standard. The tests were performed on Shimadzu brand AGS-X 100 kN model 100 kN load cell equipped static tensile-compression tester (Figure 8) with a tensile speed of 50 ± 5 mm/min. The dimensions of the tear test specimens were given in Figure 9. Tear strengths of mixtures were calculated from tear tests.



Figure 8. Shimadzu AGS-X 100 kN tensile-compression test device

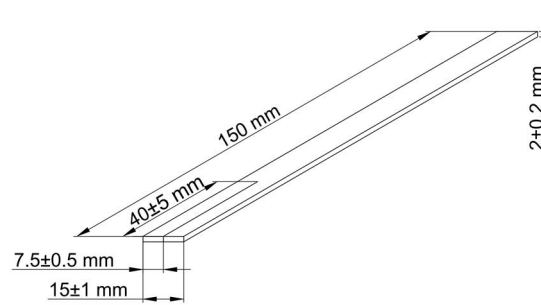


Figure 9. The dimensions of tear test specimen [3]

Tensile tests were performed in Shimadzu brand AGS-X 100 kN model 100 kN load cell equipped static tensile-compression test device at 50 ± 5 mm / min tensile speed according to ASTM D638 (Type-IV) standard. The dimensions of the tensile test specimens are given in Figure 10. Six tensile test specimen were tested from each formulas. Tensile strength, rupture strength, modulus of elasticity according to tensile condition, elongation at break and toughness values of the material were calculated from the tensile tests.

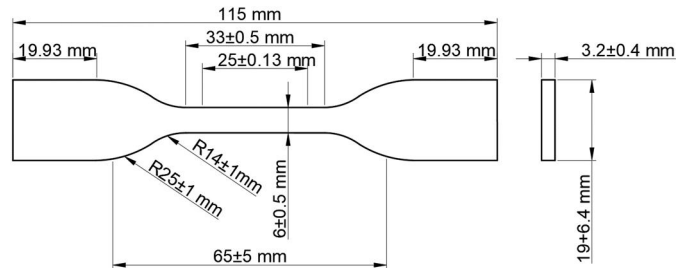


Figure 10. The dimensions of tensile test specimen [3]

Three-point bend tests were performed in Instron 8801 model 50 kN load capacity dynamic tensile and compression test device according to ASTM D790 standard with crosshead speed of 1.4564 mm/min (Figure 11). The sizes of the three point bend test specimen is given in Figure 4 and six specimen were tested from each formula. Bending strength and flexural modulus according to bending condition values were calculated from the tests. 5% strain were taken into account to find the flexural strength values.

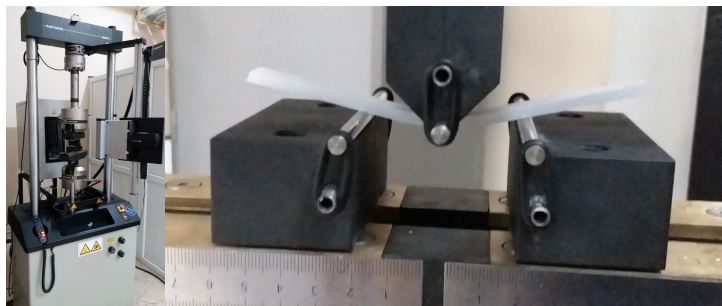


Figure 11. Instron 8801 dynamic tensile-compression test device

Compressive tests were performed in Shimadzu brand AGS-X 100 kN model 100 kN load cell equipped static tensile testing machine was used with crosshead speed at 1.3 mm/min according to ASTM D695 standard. The compressive test plates were shown in Figure 8. The sizes of the compression test specimen less than 3.2 mm thickness is given in Figure 12 and six specimen were tested from each formulas. Compressive strength, yield stress in compression and compressive modulus values were calculated according to the compression state. 10% deformation values were taken into account of the specimens for compressive strength values. The compressive modulus of HDPE and LDPE were calculated from the slope of the linear region in stress-strain curve.

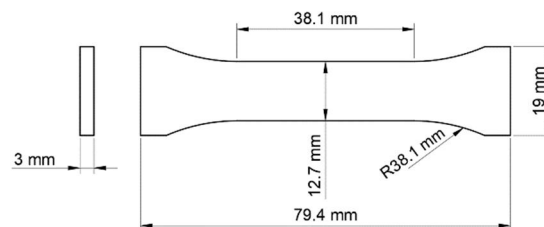


Figure 12. The dimensions of compressive test specimen

3. Experimental Results and Discussion

3.1. Density

The results of the density measurements; mean values, maximum and minimum ranges were given in Figure 13(a). The mean and standard deviation of the density values were given in Table 2. The addition of LDPE to the HDPE polymer increase the density values. The density of pure LDPE was 0.888 g/cm^3 while the density of pure HDPE was 0.951 g/cm^3 . The addition of 25% mass of HDPE to LDPE polymer increases the density by 2% to 0.905 g/cm^3 . Increasing amount of HDPE addition to LDPE polymer 50% and %75 mass increases the density by %3 and %4 to 0.913 g/cm^3 and 0.922 g/cm^3 respectively.

3.2. Hardness

Hardness value of the polymers plays key role in their usage areas. The meaning of the hardness is resistance of a material to deformation, indentation, penetration and scratching. The hardness values of polymers vary depending on their crystal phases. HDPE is more crystalline polymer (51%) than LDPE polymer (38%) [8]. The more crystalline phases bring more rigid and hard physical properties. [5]. This results are the evidence of this explanation. It has been observed that LDPE polymer hardness about 42.9 Shore-D and HDPE was 63.9 Shore-D in the hardness test. Figure 13(b) shows the average hardness values, the highest and the lowest ranges. Mean hardness and standard deviation values are given in Table 2. 25% mass of HDPE addition significantly increase the hardness values of LDPE by 34% to 57.4 Shore-D. %50 mass of HDPE addition increase the hardness values of HDPE by 35% to 57.9 Shore-D. Further addition of 75% mass of HDPE to LDPE polymer increase the hardness values by 44% to 61.6 Shore-D. The hardness value of the LDPE polymer was much lower than HDPE polymer. It was observed that significant change in the hardness values by adding HDPE to LDPE polymer.

3.3. Izod Impact Test

In spite of hammer value reached 25 J, unnotched Izod impact specimens couldn't be broken. The hammer tilted the sample and passed the other side. In the notched Izod impact experiments, no breakage was observed 25% by mass of HDPE in LDPE polymer and pure LDPE. That's because of the soft and more flexible segments of LDPE in LDPE-HDPE blend. 25% LDPE and 50% LDPE were added to the specimens were broken with a 7.5 J hammer (Figure 13(c)). Due to HDPE more crystalline than LDPE polymer and more co-monomer decrease the crystal orientation. This disrupts the impact properties of the polymer [9]. The Izod impact strength of notched pure HDPE was found 8.5 kJ/m². The addition of 75% and 50% mass of HDPE to LDPE polymer decrease the Izod impact strength values compared to HDPE polymer by %11 and %20 to 7.6 kJ/m² and 6.8 kJ/m² respectively. Mean Izod impact strength values and standard deviation values are given in Table 2.

3.4. Tear Test

The highest and lowest ranges of tear strength values of the blends are given in Figure 13(d). Mean tear strength and standard deviation values are given in Table 2. The tear strength value of pure LDPE was found 45 N/mm and pure HDPE was found 132 N/mm. The addition of 25% HDPE by mass to LDPE polymer increase tear strength values by 16% to 52 N/mm compared to LDPE. It was observed by the addition of %75 HDPE to LDPE polymer increased by 28% to 57 N/mm. The addition of 50% HDPE by mass to the LDPE polymer decreased to the lowest tear strength value by 52% to 21 N/mm. In general, it has been observed that HDPE addition to LDPE polymer increase the tear strength values. In contrast to this the addition of LDPE to HDPE polymer decreases the tear strength values remarkable except the addition of both polymer 50% weight percentage significantly decreases the tear strength values. Because of the branching network of LDPE more complicated than HDPE polymer [5-9]. This deteriorates the tearing properties.

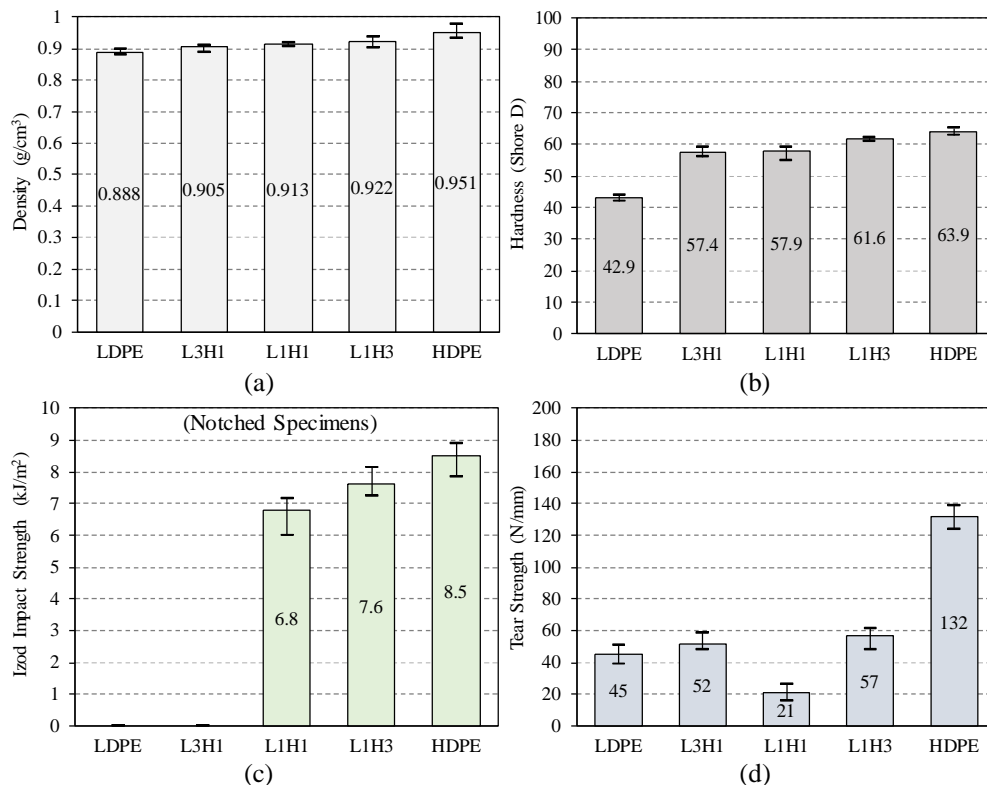


Figure 13. (a) Density, (b) hardness, (c) Izod impact strength and (d) tear strength values of LDPE-HDPE blends

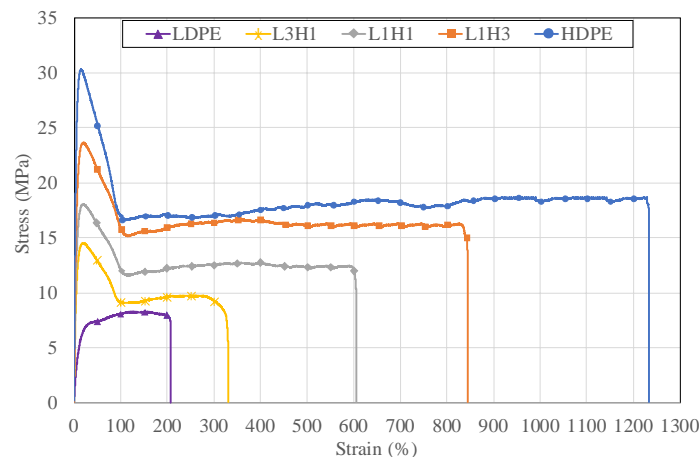
Table 2. Density, hardness, Izod impact strength and tear strength values of LDPE-HDPE blends

Code	Density (g/cm ³)	Hardness (Shore D)	Izod Impact Strength (kJ/m ²)		Tear Strength (N/mm)
			Unnotched	Notched	
LDPE	0.888±0.007	42.9±0.8	-	-	45±5
L3H1	0.905±0.008	57.4±1.1	-	-	52±4
L1H1	0.913±0.004	57.9±1.7	-	6.8±0.5	21±5
L1H3	0.922±0.014	61.6±0.5	-	7.6±0.4	57±7
HDPE	0.951±0.016	63.9±0.9	-	8.5±0.4	132±7

3.5. Tensile Test

Tensile test is important to characterize the material mechanical behaviors from the stress-strain curves under tension state. This test was revealed to find suitable application and optimum usage ratio of LDPE and HDPE polymer blends. The tensile test curves of the LDPE-HDPE samples were given in Figure 14. Mean values and standard deviation values of tensile strength, rupture strength, modulus of elasticity, elongation at break and toughness values of the composites were given in Table 3.

The average, highest and lowest range values of tensile strengths were shown in Figure 15(a). It was observed that the tensile strength of LDPE polymer was found 7.7 MPa and HDPE polymer was 30.6 MPa. The addition of 25% mass of HDPE to LDPE polymer increases the tensile strength by 121% to 17 MPa. Furthermore, it was seen that 50% and 75% addition of HDPE to LDPE polymer decreases tensile strength by 142% and 213% to 18.6 MPa and 24.1 MPa values respectively.

**Figure 14. Stress-Strain curves of LDPE-HDPE blends****Table 3. Tensile test results of LDPE-HDPE blends**

Code	Tensile Strength (MPa)	Rupture Strength (MPa)	Elasticity Modulus (MPa)	Elongation at Break (%)	Toughness (J/mm ³)
LDPE	7.7±0.4	7.1±0.3	102±12	208±12	1.6±0.2
L3H1	17±1.5	8.7±0.6	305±20	346±28	3.3±0.4
L1H1	18.6±0.6	12.5±0.3	448±38	670±40	6.9±0.6
L1H3	24.1±1.1	14.8±0.7	523±31	878±57	10.1±0.6
HDPE	30.6±1.3	17.7±0.6	920±46	1249±42	23.1±1.2

Same manner was observed in rupture strengths, the addition of HDPE to LDPE polymer were significantly increased the rupture strengths (Figure 15(b)). It has been determined that the rupture strength of LDPE was 7.1 MPa and HDPE was 17.7 MPa. The addition of HDPE by 25% mass to LDPE polymer increased the rupture strength by 23% to 8.7 MPa. 50% and 75% mass of HDPE addition to LDPE polymer were increased this value by 76% and 108% to 12.5 MPa and 14.8 MPa values respectively.

The elasticity modulus of LDPE and HDPE polymer were observed 102 MPa and 920 MPa respectively. 25% addition of HDPE to LDPE polymer was increased the elasticity modulus

significantly by 199% to 305 MPa. It was observed that 50% of HDPE addition to LDPE polymer was increased by 339% to 448 MPa. Furthermore, the addition of 75% HDPE to LDPE polymer increased the elasticity modulus by 413% to 523 MPa (Figure 15(c)).

The elongation at break values of LDPE polymer was around 208%, while the elongation at break of HDPE polymer was 1249% (Figure 15(d)). By the addition of 25% HDPE to LDPE polymer, this value was seen to increase by 66% to 346%. The addition of 50% and 75% HDPE to LDPE polymer increased the elongation at break values by 222% and 322% to 670% and 878% respectively.

The toughness values were observed from the tensile test curves. The areas under curves were calculated. The highest and the lowest ranges and mean values were given in Figure 15(e). Pure LDPE polymer toughness value was calculated 1.6 J/mm³ and HDPE polymer was 23.1 J/mm³. It was observed that the addition of 25% mass of HDPE to LDPE polymer increase by 106% to 3.3 J/mm³, 50% of HDPE to LDPE increases by 331% to 6.9 J/mm³ and 75% of HDPE to LDPE increase by 531% to 10.1 J/mm³.

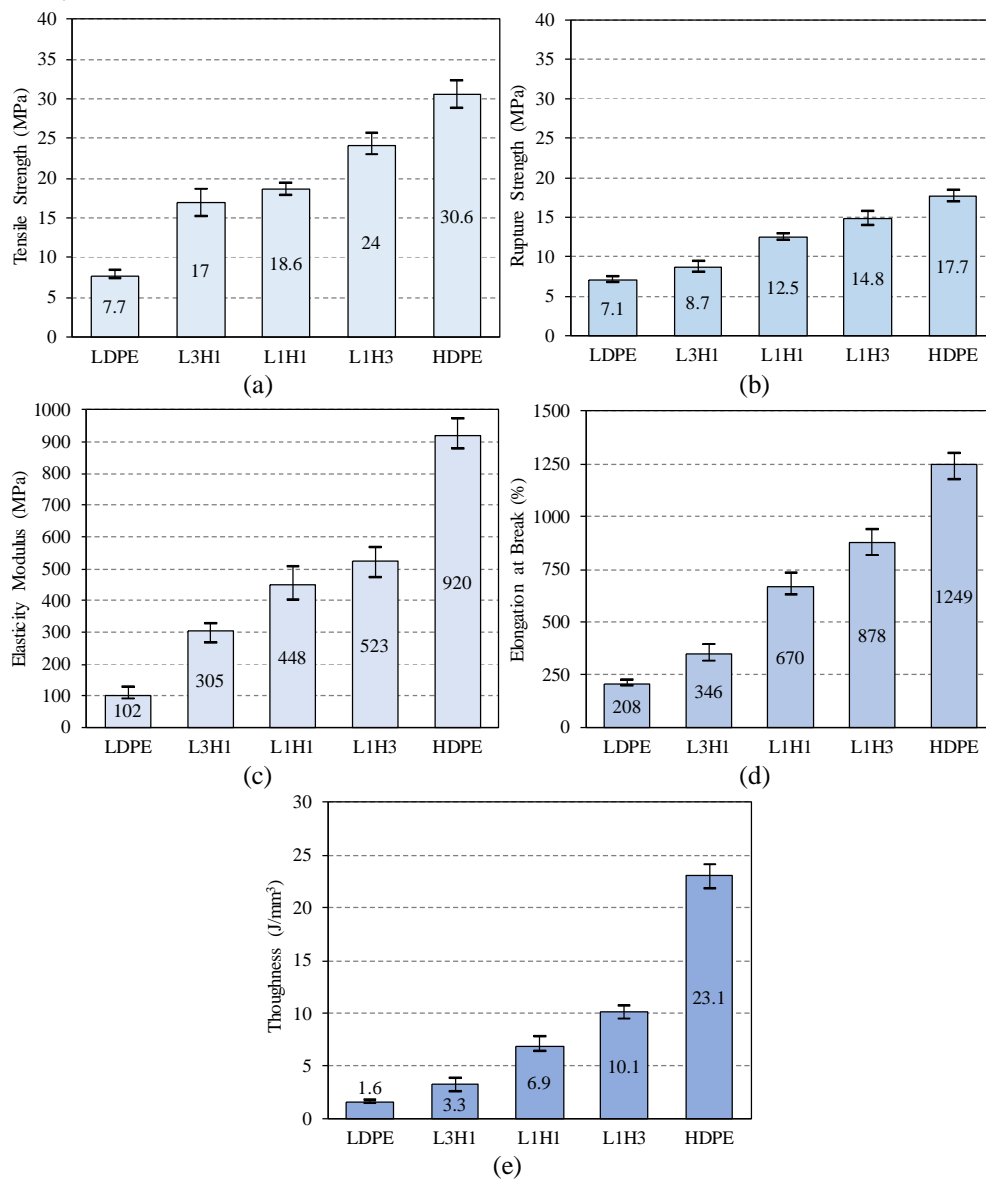


Figure 15. (a) Tensile strength, (b) rupture strength, (c) elasticity modulus, (d) elongation at break and (e) toughness values of LDPE-HDPE blends

3.6. Three Point Bend Test

The mean and standard deviation values of flexural strength and flexural modulus of composites were given in Table 4. The addition of HDPE to LDPE polymer increased the flexural strength and flexural modulus values according to bending state.

Table 4. Three point bend test results of LDPE-HDPE blends

Code	Flexural Strength (MPa)	Flexural Modulus (MPa)
LDPE	7.8±0.5	345±19
L3H1	10.9±0.7	455±34
L1H1	13.3±0.8	558±29
L1H3	17.1±1.2	875±28
HDPE	24.3±0.9	1109±51

The average, highest and lowest range values of flexural strengths are shown in Figure 16(a). The flexural strength value of LDPE polymer was observed 7.8 MPa and HDPE polymer was 24.3 MPa. 25% by mass of HDPE addition to LDPE polymer was increased flexural strength value by 40% to 10.9 MPa. By mass of 50% and 75% addition of HDPE to LDPE polymer increased flexural strength by 71% and 119% to 13.3 and 17.1 MPa respectively.

The flexural modulus of LDPE polymer was calculated 345 MPa and HDPE polymer was 1109 MPa. The addition 25% by mass of HDPE to LDPE polymer increased the flexural modulus by 50% to 455 MPa, 50% mass of HDPE addition increased by 97% to 558 MPa and 75% addition increased by 241% to 875 MPa (Figure 16(b)). It was found that increasing amount of HDPE addition to LDPE polymer were increased the flexural strength and flexural modulus.

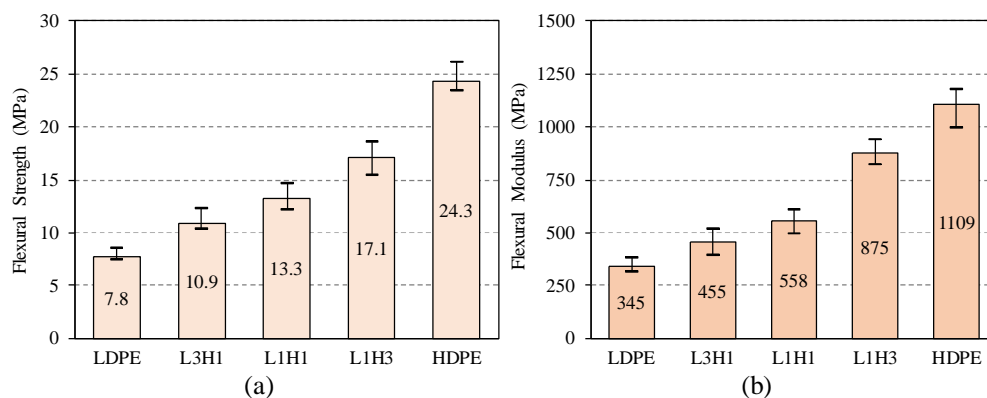


Figure 16. (a) Flexural strength and (b) flexural modulus values of LDPE-HDPE blends

3.7. Compressive Strength Test

Compressive strength, compressive yield strength and compressive modulus of LDPE-HDPE blends mean and standard deviation values were given in Table 5. The compressive strength value of LDPE was found 10.7 MPa and HDPE was 23 MPa. The addition of 25% HDPE to LDPE polymer was increased the compressive strength values of composite by 50% to 16.1 MPa. 50% and 75% addition of HDPE polymer to LDPE polymer were increased by 60% and 63% to 17.1 MPa and 17.4 MPa respectively (Figure 17(a)).

Compressive yield strength values of LDPE and HDPE were calculated 4.2 MPa and 9 MPa respectively. The addition of 25% HDPE to LDPE polymer increased by 126% to 9.5 MPa. 50% HDPE increased 76% to 7.4 MPa and 75% HDPE increased by 157% to 10.8 MPa (Figure 17(b)).

The highest and lowest ranges and mean values of compressive modulus were shown in Figure 17(c). The compressive modulus of LDPE and HDPE were found 185 MPa and 710 MPa respectively. Addition of 25% mass of HDPE to LDPE polymer increased the compressive modulus by 66% to 307 MPa. 50% HDPE addition increased by 107% to 383 MPa. Furthermore 75% addition of HDPE to LDPE polymer increased by % 130 to 426 MPa.

Table 5. Compression test results of LDPE-HDPE blends

Code	Compressive Strength (MPa)	Compressive Yield Strength (MPa)	Compressive Modulus (MPa)
LDPE	10.7±0.7	4.2±0.4	185±12
L3H1	16.1±0.3	9.5±0.6	307±37
L1H1	17.1±0.7	7.4±0.5	383±36
L1H3	17.4±0.8	10.8±0.6	426±27
HDPE	23±0.8	9±0.3	710±40

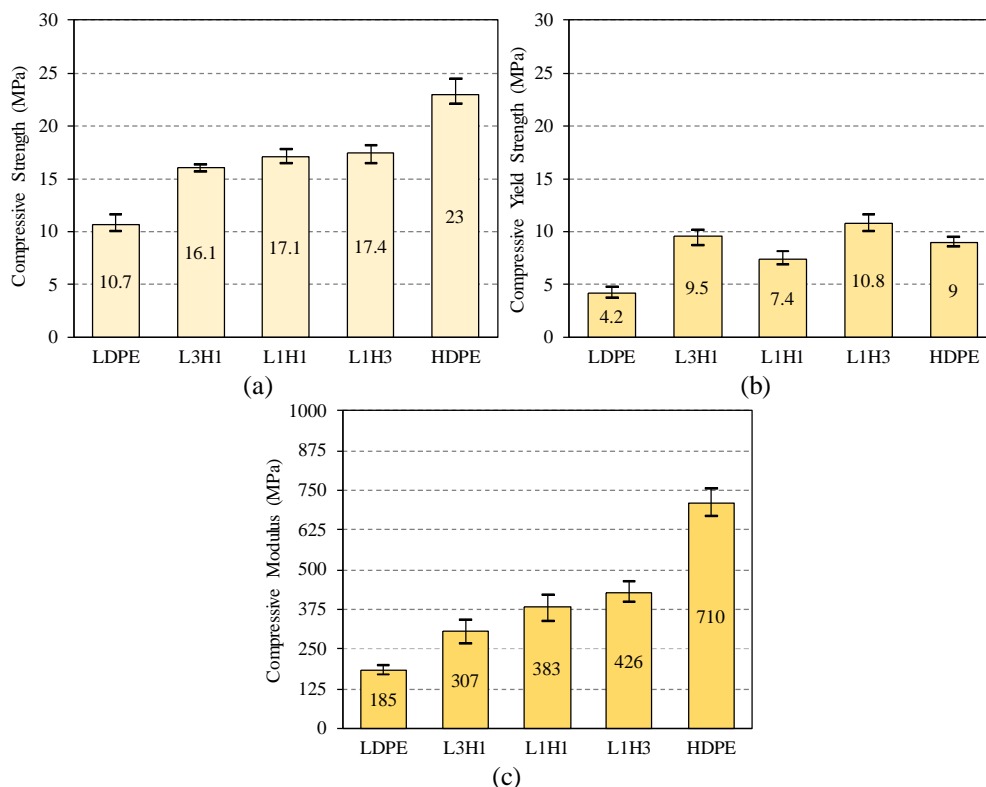


Figure 17. (a) Compressive strength, (b) compressive yield strength and (c) compressive modulus values of LDPE-HDPE blends

4. Conclusions

In this study, it was carried out that mixing the low density and high density polyethylene in different ratios. The production method of the samples were performed by plastic injection machine. HDPE polymers were added to LDPE polymers in 25%, 50%, 75% by mass and some physical and mechanical tests were performed. As a result of the studies, the following conclusions were drawn.

- It was found out that the addition of HDPE to LDPE polymer increase the density, hardness and tear strength values. In contrast, the addition of the LDPE to HDPE polymer decrease these values.
- In Izod impact tests, although the hammer energy increased to 25 J, all unnotched specimens couldn't be broken. HDPE, L1H3 and L1H1 specimens were broken in notched Izod impact tests. The addition of 75% and 50% HDPE to LDPE polymer decrease the Izod impact strength values compared to pure HDPE polymer.

- It was found that the tensile curves obtained from the tensile test were in accordance with the pure LDPE and pure HDPE polymer tensile characteristics.
- Tensile strength, rupture strength, elongation at break, toughness and modulus of elasticity values were increased by adding HDPE to LDPE polymer from the results of the tensile tests.
- Flexural strength and flexural modulus values of the composites increased by the addition of HDPE polymer to LDPE polymer.
- It was observed that the addition of HDPE to LDPE polymer increases the compressive strength, compressive yield strength and compressive modulus. 25% and 75% of LDPE addition increase the compressive yield strength values above pure HDPE.
- In contrast to all results the addition of LDPE to HDPE polymer decreases the physical and mechanical properties of HDPE polymer.
- Thermal and combustion tests of these polymer blends will be performed in the next study.

Acknowledgement

Author would like to thank both institutions for using Pamukkale University, Mechanical Engineering Laboratories and Karamanoğlu Mehmetbey University, Mechanical Engineering Laboratories. This study was oral presented proceeding in UMTK 2019 congress.

References

- [1] Saçak, M., *Polimer Kimyası (Polymer Chemistry)*, Gazi Kitabevi, Ankara, TR, 2008.
- [2] Akkurt, S., *Plastik Malzeme Bilimi Teknolojisi ve Kalıp Tasarımı (Plastic Material Science Technology and Mold Design)*, Birsen Yayınevi, İstanbul, TR, 2007.
- [3] Akdoğan, E. and Yurtseven, R. (2016). The Effects of Ammonium Polyphosphate and Boron Containing Flame Retardants on Mechanical Properties of Thermoplastic Polyurethane Materials. *16th International Materials Symposium (IMSP'2016)*, Denizli, TR, 262-270.
- [4] Taşdemir, M., *Polimer Karışımları ve Uygulamaları (Polymer Blends and Applications)*, Seçkin Yayıncılık, Ankara, TR, 2016.
- [5] Shebani, A., Klash, A., Elhabishi, R., Abdsalam, S., Elbreki, H. and Elhrari, W., (2018). The Influence of LDPE Content on the Mechanical Properties of HDPE/LDPE Blends, *Research & Development in Material Science*, 7(5), 1-7.
- [6] Sarkhel, G., Banerjee, A. and Bhattacharya, P., (2006). Rheological and Mechanical Properties of LDPE/HDPE Blend, *Polymer-Plastics Technology and Engineering*, 45, 713-718.
- [7] Cho, K., Lee, B.H., Hwang, K., Lee, H., and Choe, S., (1998). Rheological and Mechanical Properties in Polyethylene Blends, *Polymer Engineering and Science*, 38(12), 1969-1975.
- [8] Li, D., Zhou, L., Wang, X., and Yang, X., (2019). Effect of Crystallinity of Polyethylene with Different Densities on Breakdown Strength and Conductance Property, *Materials*, 12(11), 1746-1758.
- [9] Ren, Y., Shi, Y., Yao, X., Tang, Y., and Liu, L.Z., (2019). Different dependence of tear strength on film orientation of LLDPE made with different co-monomer. *Polymers*, 11(3), doi:10.3390/polym11030434.

- [10] ASTM D256, Standard Test Methods for Determining the Izod Pendulum Impact Resistance of Plastics, ASTM International, West Conshohocken, PA, U.S.A., (2013).
- [11] ASTM D618, Standard Practice for Conditioning Plastics for Testing, ASTM International, West Conshohocken, PA, U.S.A., (2013).
- [12] ASTM D624, Standard Test Method for Tear Strength of Conventional Vulcanized Rubber and Thermoplastic Elastomers, ASTM International, West Conshohocken, PA, U.S.A., (2012).
- [13] ASTM D638, Standard Test Method for Tensile Properties of Plastics, ASTM International, West Conshohocken, PA, U.S.A., (2014).
- [14] ASTM D790, Standard Test Methods for Flexural Properties of Unreinforced and Reinforced Plastics and Electrical Insulating Materials, ASTM International, West Conshohocken, PA, U.S.A., (2017).
- [15] ASTM D792, Standard Test Methods for Density and Specific Gravity (Relative Density) of Plastics by Displacement, ASTM International, West Conshohocken, PA, U.S.A., (2013).
- [16] ASTM D2240, Standard Test Method for Rubber Property-Durometer Hardness, ASTM International, West Conshohocken, PA, U.S.A., (2015).

FEASIBILITY OF GOLD BASED HALL DEVICES FOR BIOSENSING PURPOSES

Davut IZCI^{1}, John HEDLEY²*


Hall sensors widely dominates the field of magnetic sensing. Basically, they produce information in terms of voltage with respect to applied field. The produced output depends on several parameters such as carrier mobility, carrier concentration, thickness and device geometries. In brief, materials with higher mobility and less thickness provides better candidates for such purposes. Looking at those parameters; gold-based Hall devices may not be thought of as the best candidate for magnetic field sensing. However, this does not suggest that it cannot be used for biosensing purposes. Gold presents an advantage of potential label-free biosensing device development since it can easily be functionalized for biosensing purposes. In this study, the feasibility of gold-based Hall devices was investigated through different fabrication techniques with and without adding separate layers including materials such as copper, nickel and chromium. The characterization has revealed that devices with smaller dimensions produce better output. The results showed that using gold to fabricate Hall sensors has merit for potential label-free biosensing purposes by designing a suitable geometry and following relevant microfabrication techniques.


Key words: *Hall sensors, microfabrication, gold-based Hall devices*

1. Introduction

Biosensors are analytical devices that are used in various fields such as food safety, environmental monitoring and medical diagnostics. A biosensor is combined of bioreceptor and transducer. Those two elements are integrated in such a way that the detection of specific target molecules are allowed. A bioreceptor is a specific recognition element for detecting desired chemicals and biomolecules whereas the transducer is used to convert the detection event into a meaningful description by means of electrical, mechanical or optical signals.

Historically, the field of biosensor research traces back to 1962 with enzyme electrode development by Lenard C. Clark [1] for testing glucose levels in blood and since then the bio-sensing field has been contributed by scientists from different research backgrounds. In 1970s, the first generation of biosensors was commercialized [2]. Further developments followed by describing a bio-recognition system for the use of whole cell. Research and developments on the field has continued, particularly over the last decade. It is likely that the biosensors will have a huge impact on point of care diagnostics [3] because they have potential to be simplified and reduced in size, thus providing

¹ Vocational School of Technical Sciences, Batman University, Batman, Turkey, (davut.izci@batman.edu.tr)
 <https://orcid.org/0000-0001-8359-0875>

² School of Engineering, Newcastle University, Newcastle upon Tyne, UK, (john.hedley@newcastle.ac.uk)
 <https://orcid.org/0000-0002-2893-8776>

easy to use products. Therefore, this field needs to be improved based on new materials and design implementations to achieve a detection range of very small concentrations.

In order to detect a specific desired biological element, the sensor surface should be functionalised and this is usually done with complementary molecule [1]. In the presence of desired biological element, a capture process occurs. This process refers to the recognition step. A transducer is then used for converting the recognition event into a measurable electrical signal. A desired target molecule is captured by bio-receptor and this event creates a physical change in the transducer. The physical change can be measured as electrical, mechanical, optical or electrochemical based on transducer type. This change is converted to an electrical signal for a meaningful interpretation of the detection. The signal from output of the transducer is usually very small and needs to be amplified. In addition to amplification, any noisy harmonics should also be removed. Figure 1 represents a complete bio-sensing system depicting recognition (a), transducing (b), signal amplification (c) and processing (d) with recording/displaying (e) steps.

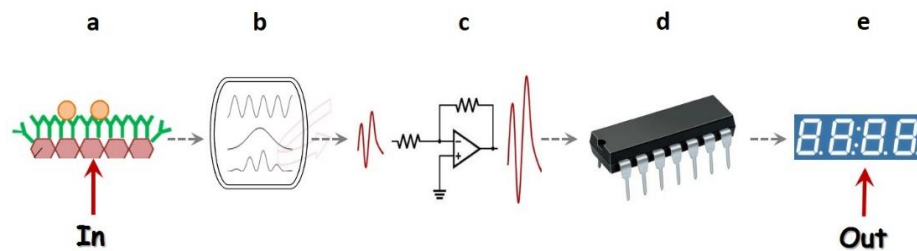


Figure 1. Recognition (a), conversion (b), signal amplification (c), processing (d), recording and displaying (e) steps.

Biosensors field is one of the fields that requires more improvements and currently an enormous amount of work is undertaken [4], [5]. Using magnetism is one of the techniques that was widely used to form detection platforms for biosensing purposes since it has a huge promise [6]–[8]. Apart from its key role in daily life from electric production to data storage and from quantitative explanation of physical properties of materials to particle acceleration [9], magnetic field has a huge potential of providing non-destructive and highly efficient detection platforms in biosensing field [6]. It provides a low intrinsic background in biological systems since those systems have no comparable biological signal [10]. Several mechanisms were reported based on different applications of magnetism such as magnetoresistance [11], planar Hall effect [12], spin valve [13], superconducting quantum interference devices (SQUID) [14], and Hall effect [15]. Amongst them, the Hall effect principle is the easiest way of achieving a magnetic sensor although it may not reach the sensitivity limits offered by some of those structures, e.g. SQUID sensors. Although each application has some certain advantages in terms of sensitivity, the specific requirements for operation such as low temperature demand in SQUID sensors, or fabrication complexity could make them unpractical. Thus, a considerable effort can be observed in biosensing applications that employ the Hall effect principle [16]–[18]. The Hall effect principle can briefly be explained as the transverse voltage that occurs due to Lorentz force. This force is appeared due to deviation in flow of electrons which can be observed under the presence of perpendicularly applied magnetic field. The obtained voltage depends on several parameters such as applied current and field, thickness and geometrical structure along with carrier mobility and density of a particular material.

Any thin layer of metal or semiconductor in a simple rectangular shape with four contacts could be considered as a Hall device although they would suffer from significant small potential difference produced at the output due to their electric transport parameters. Because, certain requirements such as

carrier mobility, density of charge carriers etc., should be satisfied in materials to have effective and sensitive Hall devices. Several structures have been reported such as silicon, bismuth, indium antimonite thin films and two-dimensional electron gas heterostructures for fabrication of Hall devices [15]. Commercially available Hall sensors are dominated by silicon, due to well-developed CMOS manufacturing process [19]. However, in applications requiring higher sensitivity, heterostructures from III-V compounds are required because of superior electron transport properties they have [20]. In the latter type of devices, manufacturing cost can be high and integration with signal processing circuitry may be difficult [19]. Indium antimonite [21], bismuth [22] and graphene [23] thin films are also used in Hall applications due to the high electron mobility properties they retain and the linear response they demonstrate for a wide range of field strengths. However, gold based sensors have been designed and manufactured for this study as an alternative route. The aim was to explore a cheaper and easier way of implementation for Hall based biosensors as gold can easily be functionalised for biosensing purposes [24]–[26] if a label-free approach is implemented.

2. Design

Hall devices are basically devices that are producing information as an output voltage taking the applied field into account. Hall voltage output is proportional with carrier mobility and inversely proportional with carrier concentration, however, the geometrical structure has certain effects in terms of produced output [27]. Therefore, designing a suitable geometrical structure has a huge influence in terms of produced output. Scaling those structures are also affecting the output voltage [28]. Several devices with different geometrical structures and dimensions was designed for this study. Figure 2 is a sketch of basic geometrical structures with corresponding dimensions (in terms of length and width) on the masks. Active areas that were ranging from 1 mm to 3 mm were designed to be used for devices on FR4 substrate. The reason of designing devices with relatively large sizes (millimetre range) was due to PCB fabrication limits.

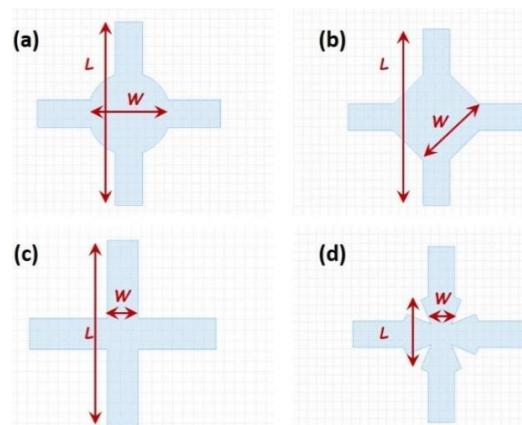


Figure 2. Representation of circle (a), square (b), cross (c) and cauliflower (d) geometries (L: Length, W: Width).

A second design including cross structures with relatively smaller sizes (500 μm) was also designed for this study. The second design was used to operate laser machine (HPC Laserscript) to create masks for gold sputtering on a glass substrate. The reason of choosing the latter dimension was because of the limit that the laser cutting machine can reach to obtain a clear mask from acrylic. Due to thermal distortion in acrylic, smaller dimensions with clear shapes were not feasible.

To fabricate micro-scale gold devices on a silicon substrate, a mask was designed with several geometrical forms along with various length to width ratios (l/w) greater than 3, in order to avoid

weakening the Hall effect due to geometrical factor [15], and made on a 4-inch quartz to form devices having active areas of 10 μm , 20 μm , 40 μm and 60 μm . Figure 3 shows the designed mask for the latter purpose.

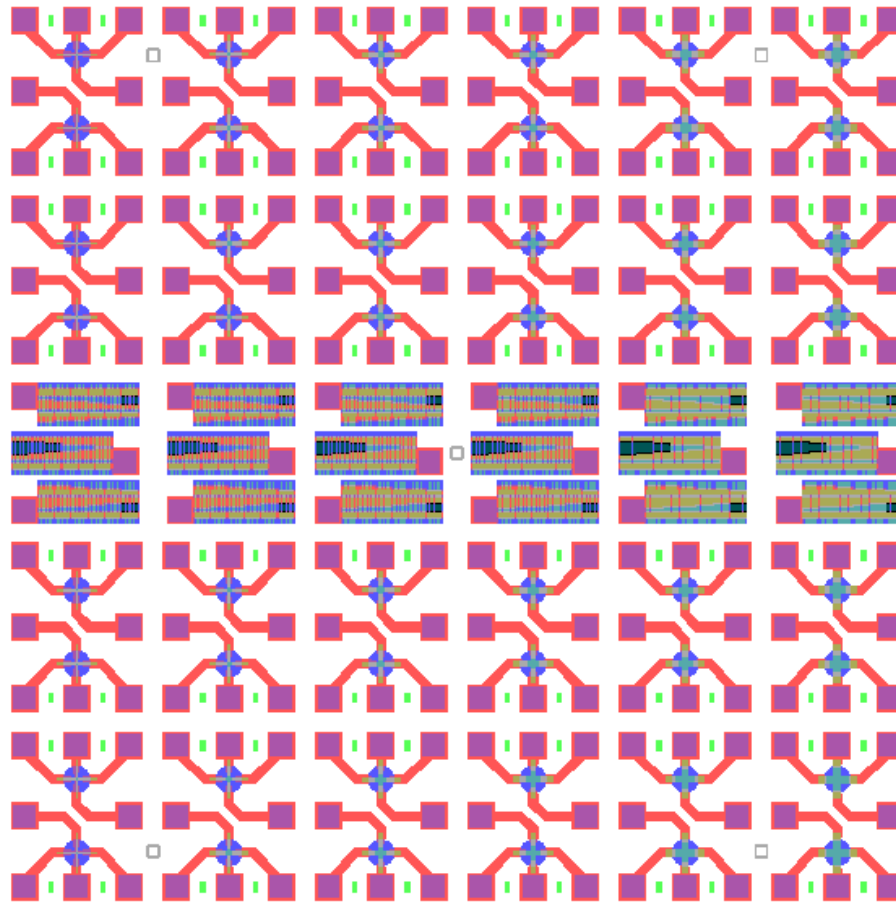


Figure 3. Designed mask with Hall device structures from 10 microns to 60 microns.

3. Materials

Thin films [29], 2DEG heterostructures [30] or single layer atomic structures such as graphene and its derivatives [31] are the excellent choices since they meet the required criteria for better Hall devices. However, working with those materials requires familiarity of microfabrication processes which could be expensive to a certain extent and could cost time. Therefore, this study focused on devices that are relatively easy to fabricate. Three different routes were followed to manufacture gold based Hall devices. Firstly, gold devices, in combination with nickel and copper, were used to be made on an FR4 substrate following traditional PCB fabrication routes. Secondly, pure gold structures were employed to be directly used on a glass substrate. This approach was simple in terms of fabrication with feasibility as Hall sensors. The last approach was to use gold based micro-Hall devices in combination of chromium on a silicon die by implementing microfabrication steps. This method of fabrication was more complicated to fabricate devices and leading to slightly less sensitive sensors for relatively bigger sizes, yet, can be applied to biosensing applications.

4. Fabrication

4.1. Fabrication on FR4 Substrate

In this approach, the aim was to use an alternative and easier way of device fabrication and practically observe the response of an inhomogeneous combination of metals along with different shapes and sizes. The devices were made of single-sided PCB with no plated-through holes and were built on 1.6 mm FR4 epoxy glass fibre substrate along with three layers of different materials using PCB fabrication techniques. It consisted of 35 μm of copper (Cu) layer, 3-5 μm nickel (Ni) layer, and 0.3 μm of gold (Au) layer. A cross-sectional view of the design is given in Figure 4.

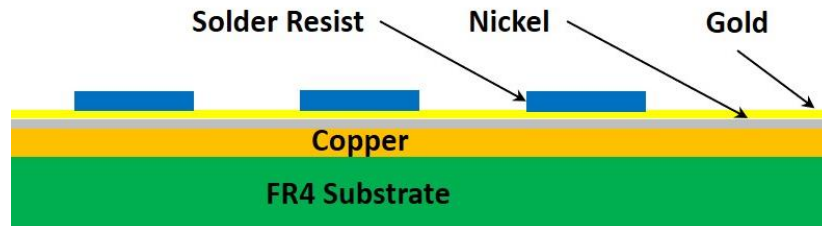


Figure 4. Cross-sectional view of designed Hall devices on PCB.

Several devices with different geometrical structures (Greek cross, square, cauliflower, round etc.) and dimensions ranging from 1 mm to 3 mm were fabricated for each shape – see Figure 5. The reason of designing devices with relatively large sizes was due to PCB fabrication limits. Most of the devices consisted of 4 contact points; 2 for biasing and other 2 for reading, respectively. The devices with 6 contacts (Figure 5(e) and Figure 5(f)) were aimed to be used for quantum Hall effect or magnetoresistance effects for future works. The areas covered by solder resist was designed for potentially limiting any bead attachment to the required areas of devices meaning that the functionalisation process can be performed only on active areas of the devices.

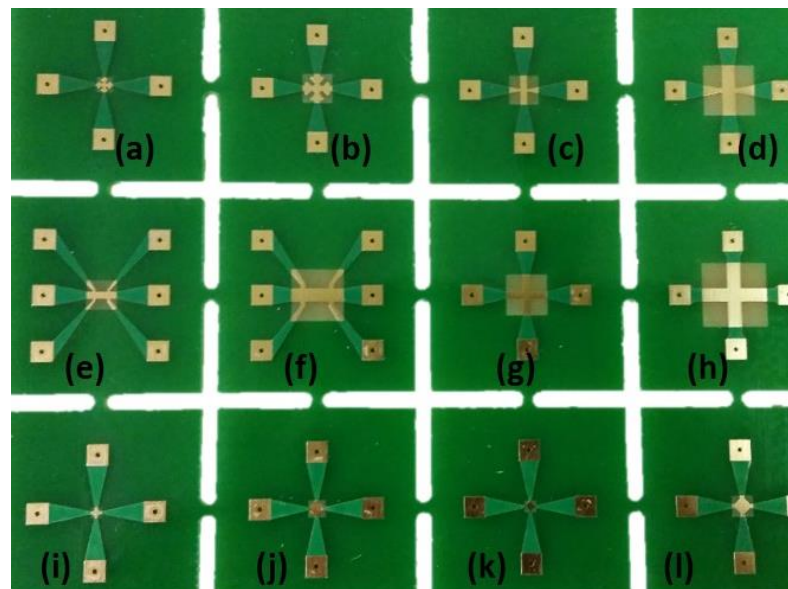


Figure 5. Actual view of fabricated Hall devices on an FR4 substrate.

4.2. Fabrication on Glass Substrate

Devices that are explained in previous section had non-homogeneous structures since they included three different layers of materials. Additionally, surface roughness was not as smooth as desired. Therefore, additional structures were designed and made on a thin acrylic mask by cutting relevant structures with laser cutting machine. Then a gold layer of around 30 nm were formed by sputtering technique using a Bio-Rad Microscience Division SC500 sputter machine. Those devices had relatively large sizes (500 μm and more) due to the limitation in laser beam size and thermal distortion issue in the acrylic. Figure 6 shows the sputter machine used for forming gold structures (a) along with the created acrylic masks on glass slides (b) and one of the slides with formed Hall devices (c).

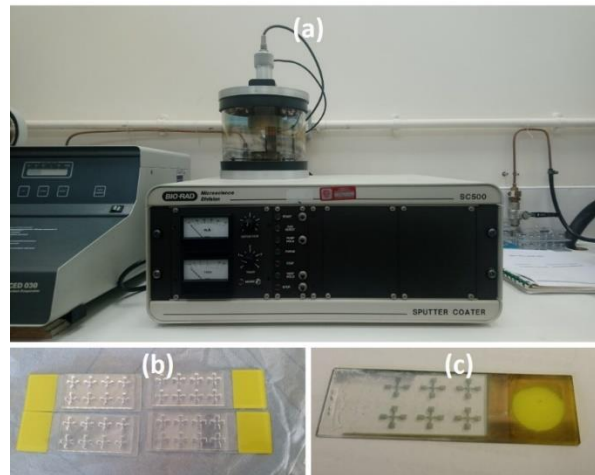


Figure 6. Gold sputter coater (a) with designed acrylic masks (b) and actual fabricated devices on glass substrate (c).

4.3. Fabrication on Si Substrate

This approach was implemented to fabricate gold devices with an adhesion layer. Micro-Hall devices from 10 μm to 60 μm were also fabricated using microfabrication techniques including lithography and lift-off processes by employing a SiO_2/Si substrate. A chromium layer was used to aid the adhesion. Figure 7 demonstrates the microfabrication steps designed for device manufacturing.

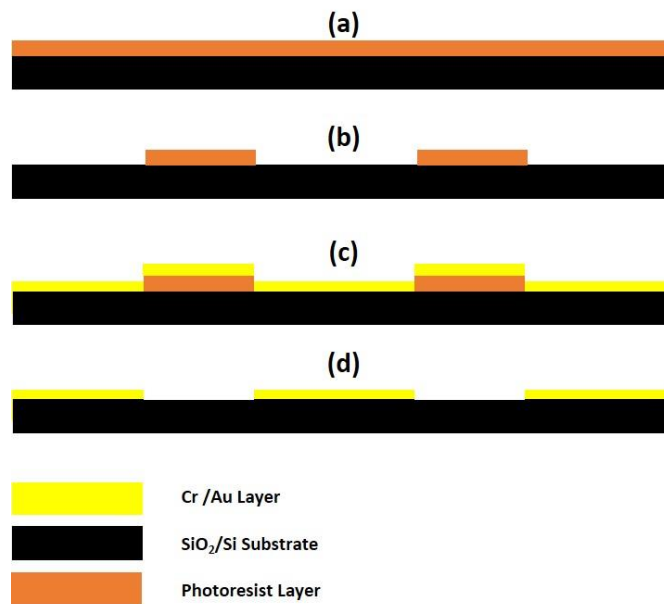


Figure 7. Lithography and lift-off process for micro-Hall gold devices. Positive photoresist cover (a), lithography and developing resist stages for constructing the pattern (b), chromium (Cr) and gold (Au) evaporation using e-beam evaporator (c), and lift-off process (d).

The fabrication started with cutting silicon substrates of around $10 \times 10 \text{ mm}^2$ and cleaned before any process. The cleaning procedure took place initially by doing ultrasonic bath at $80 \text{ }^\circ\text{C}$ using NMP (N-methyl-2-pyrrolidone) and IPA (propan-2-ol) for 10 and 5 minutes, respectively, followed by rinsing with ultra-pure water. This was carried out as an initial step for organic clean. Then, further cleaning process was taken place using piranha solution (a mixture of H_2O_2 (hydrogen peroxide) and H_2SO_4 (sulphuric acid)) to remove any residue. The last step in cleaning was to employ RCA cleaning method (steps including NH_4OH (ammonium solution), H_2O_2 and BHF (buffered hydrofluoric acid)). After wet-chemical cleaning procedure, the substrate was dried using nitrogen gun. The substrate was covered with negative photoresist (AZ5214E) by using a spin coater (EMS 6000 spin coater) and pre-baked at $90 \text{ }^\circ\text{C}$ for 10 minutes, following the cleaning procedure. Then, the lithography process was performed with the aid of patterned glass mask. The sample was exposed to UV for 4 seconds using KarlSuss MJB-3 mask aligner. A post-bake stage took place by using a hot plate (Electronic Micro Systems Ltd Model 1000-1 Precision Hot Plate) at $120 \text{ }^\circ\text{C}$ for 30 seconds followed by a blank UV exposure for 8 seconds. The latter process was performed to use the photoresist as an image reversal. After lithography, patterns were obtained by developing the photoresist using AZ 326 MIF developer. A chromium layer of 7 nm and gold layer of 35 nm were evaporated using e-beam evaporator (Edwards 306 e-beam evaporator) after developing relevant structure. These thicknesses were decided to be adequate for visibility and adhesion. In addition, the stated thicknesses were decided to be sufficient for potential biosensing applications in liquid medium. The last step was to do lift-off process in order to remove unnecessary parts. Figure 8 shows the obtained device structures after following the steps explained above.

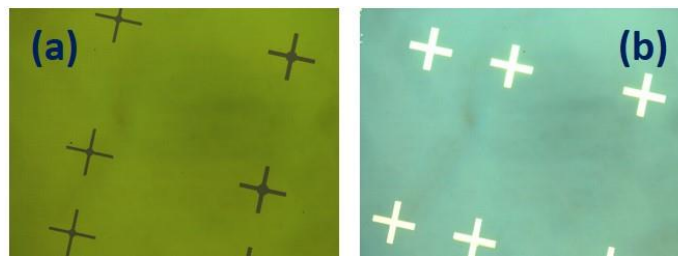


Figure 8. Patterned photoresist after lithography and developer (a), obtained device structures after lift-off (b).

A similar process was carried out to form contacts on the obtained structures. Meanwhile, it is worth to note that the steps given in Figure 8 are for forming the Hall features using negative photoresist. To obtain contacts, positive resist was used instead of negative resist due to feature arrangements on the mask. Therefore, the process took place in the reverse meaning that the features were formed on the areas where exposed to UV directly. In this case, the same photoresist was used, however, it was pre-baked at 90 °C for 15 minutes and the exposure time was 4 seconds without performing post-bake and blank exposure. The same developer was used to develop the resist and a layer of chromium with 30 nm along with a layer of gold with 250 nm were evaporated using e-beam evaporator. The fabrication was completed by doing the second lithography. Figure 9 shows the developed features aligned with previously formed Hall structures (a) and the devices with contacts after lithography process (b) along with the fabricated devices on a $10 \times 10 \text{ mm}^2$ die (c).

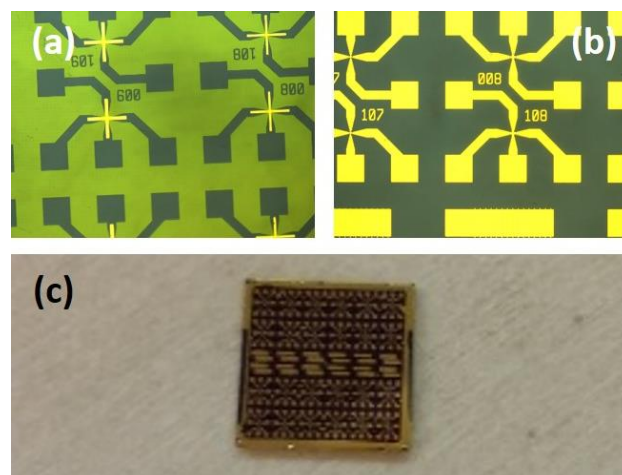


Figure 9. Patterning and forming contacts along with a silicon die used as a substrate with the fabricated devices on.

5. Measurements, Results and Discussion

5.1. Devices on FR4 Substrate

Devices on FR4 substrate had non-homogeneous material combination along with relatively thick and large structures. Initially, a low noise linear DC power supply (Farnell E30-28T) was used to drive the devices. The reason of not using a switching power supply was to minimize any noise caused by biasing source. Apart from this power supply, a Keithley 6221 AC and DC current source was also used for operating devices. To allow current flow, the contacts of the device were soldered using a screened cable. The reason of using the screened cable was to eliminate external noise effects. The PCB Hall device was placed in between designed c-core structure as shown in Figure 10 in order to apply a perpendicular magnetic field.

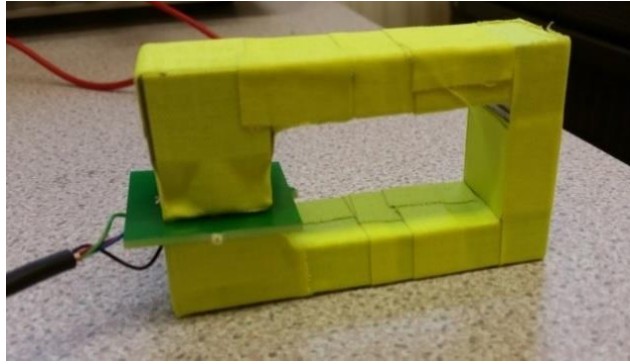


Figure 10. Performing Hall measurements using a designed structure consisting of a rare earth magnet and pure iron.

A custom made integrated circuitry [10] was used to perform measurements. The output voltages in few hundreds of nanovolts were obtained from PCB based Hall devices. Figure 11 presents a typical output obtained from gold devices on an FR4 substrate. A current-related sensitivity of $3 \mu\text{V}/\text{AT}$ was calculated which proved that the sensitivity of those type of Hall sensors are not in a desired range as was estimated due to its relatively large and thick structure along with its non-homogeneous structure.

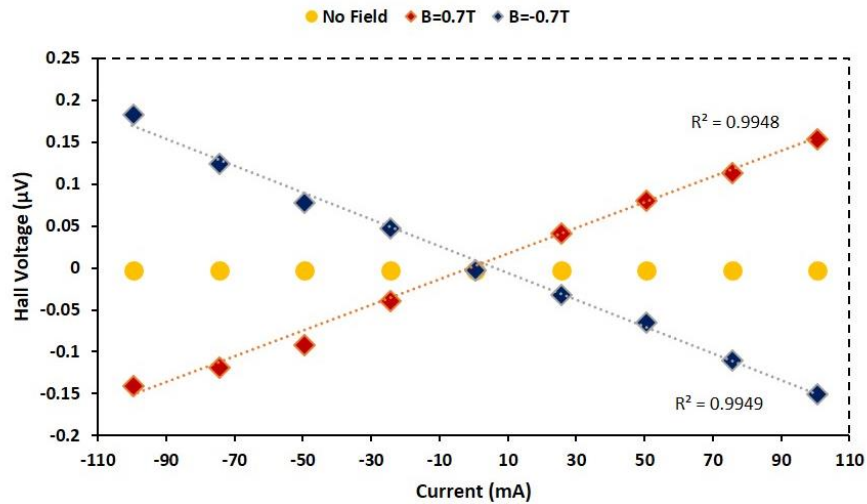


Figure 11. A typical Hall output from gold devices on FR4 substrate.

5.2. Devices on Glass Substrate

The gold devices on a glass substrate were designed and fabricated to eliminate the non-homogeneous structure issue so that the sensitivity could be improved. To perform measurements, a screened cable was connected to the device's contacts with the aid of silver paint (RS Pro Silver Conductive Adhesive Paint). Similar to the case in the devices on FR4 substrate, the magnetic field was provided using the same iron core and rare earth magnet as shown in Figure 12.

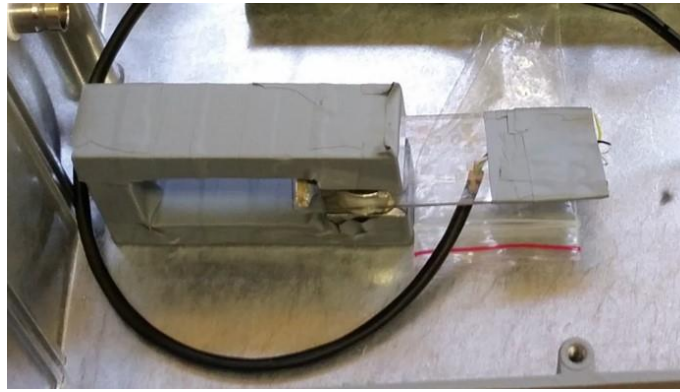


Figure 12. Au Hall device on glass substrate placed in magnetic field.

As was expected, this type of devices showed better sensitivity characteristics compared to devices on FR4. Because, it did not include different material combination and had thinner gold layer. They also presented a good linearity behaviour. Outputs in microvolt range were obtained from those devices as shown in Figure 13. The obtained values were better than the devices on FR4 substrate by about an order of magnitude. The behaviour they presented suggests that they can be adopted for applications where high sensitivity is not required. A current-related sensitivity of $5 \text{ mV} / \text{AT}$ was obtained which confirms the improvement of the performance comparing FR4 based Hall sensors. However, in terms of biosensing applications, they are not suitable due to lack of adhesion to the substrate which consequently causes delamination when a liquid inserted on them.

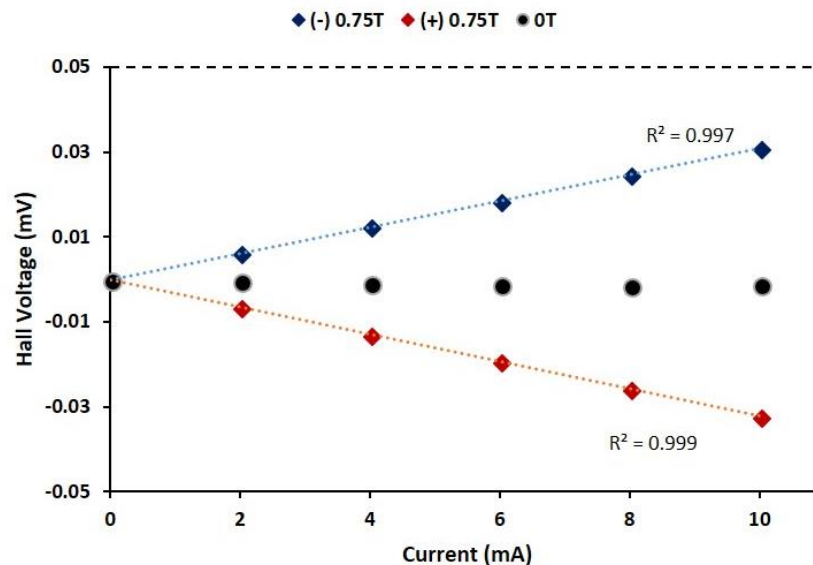


Figure 13. Response of a Au Hall device on glass substrate to magnetic fields under varying current.

5.3. Devices on Si Substrate

Micro-fabricated gold devices were employed as an alternative to gold-based Hall devices on glass substrate to improve the adhesion. To do so, a layer of chromium was used, however, addition of this extra layer means that the performance of the device would decrease. To overcome this issue, the size of the sensors was decreased to compensate the reduction of the performance due to adhesion layer. The fabricated devices were wire-bonded to a 28-pin DIP chip, as demonstrated in Figure 14, using a wire bonder (Kulicke & Soffa Industries Model 4700 Wire Bonder).

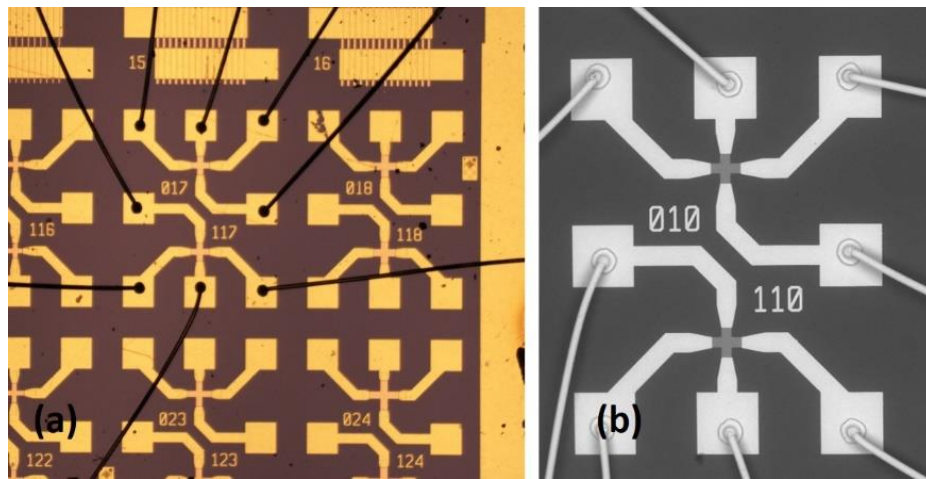


Figure 14. An optical (a) and SEM (b) image of wire-bonded contacts to a chip.

The initial measurements were performed on devices with $60\ \mu\text{m}$ sizes. The performance parameters with those devices were no better than gold devices on glass substrate. This was an expected reduction since micro-Hall gold devices were fabricated with an additional layer of chromium. A current-related sensitivity of $3\ \text{mV}/\text{AT}$ was obtained from those devices which verified the reduction in performance. Figure 15 shows the output change of a $60\ \mu\text{m}$ device with respect to magnetic field.

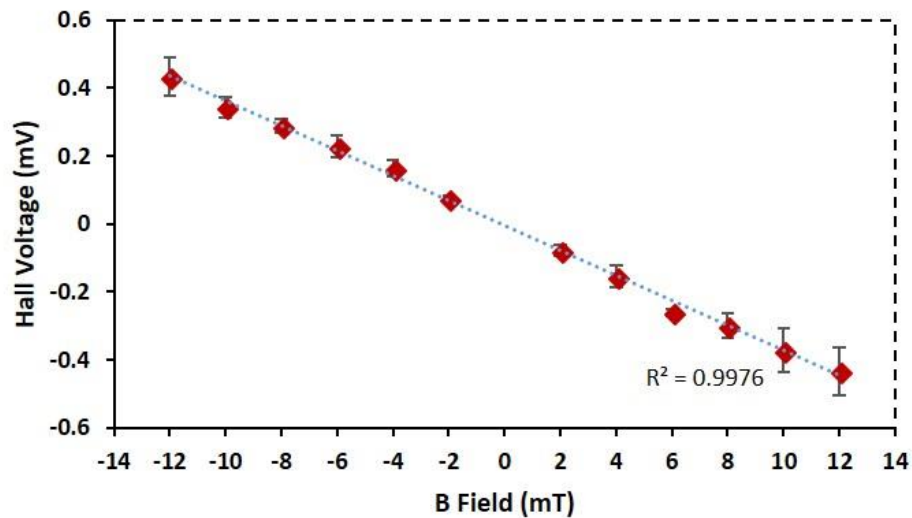


Figure 15. The output of a Cr/Au device on silicon substrate with $60\ \mu\text{m}$ active area.

However, the following measurements on devices with $10\ \mu\text{m}$ active areas presented a considerably better performance. This was attributed to the size effect [28] meaning that the smaller the size the better the performance. A current-related sensitivity of $27\ \text{mV}/\text{AT}$ was calculated for those devices. In Figure 16, the output characteristic of a $10\ \mu\text{m}$ device is presented with respect to varying current (a) and magnetic field (b). The device output with respect to varying current for positive and negative magnetic fields was demonstrated to be highly linear and repeatable. Similarly, the output of the device with respect to varying magnetic field with a constant biasing current has also showed promising figures.

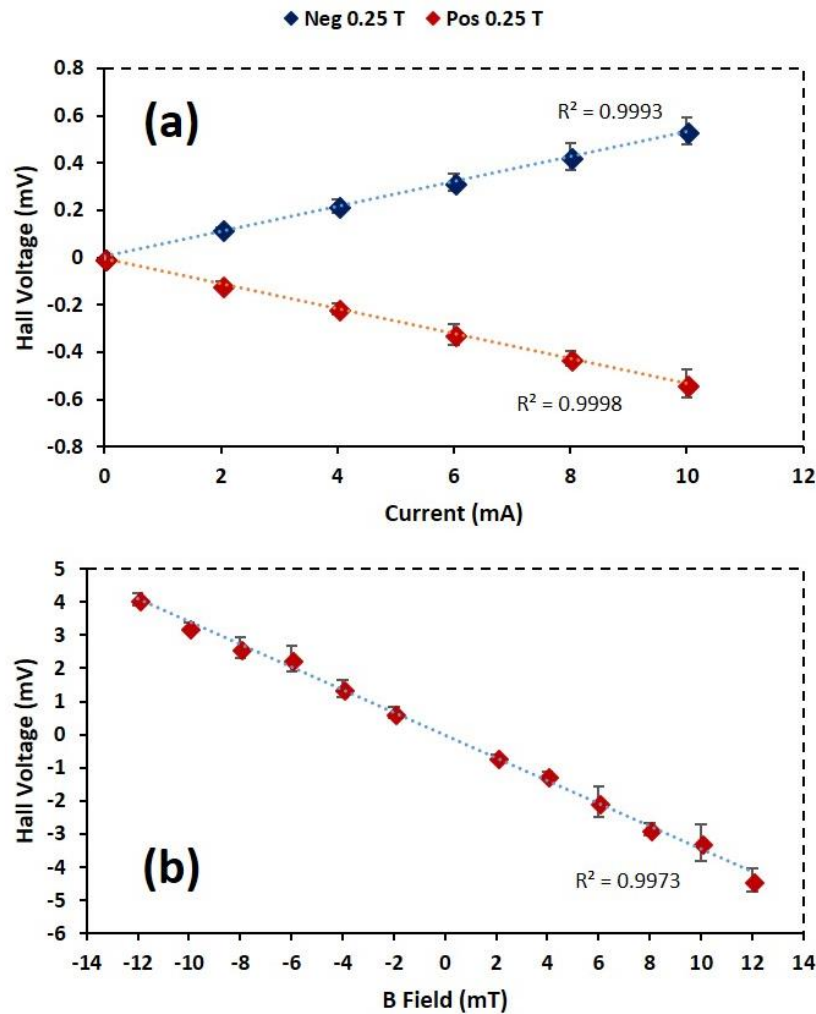


Figure 16. The output of a Cr/Au device on silicon substrate with 10 μm active area.

The performance parameters for gold based devices manufactured via different routes is summarized in Table 1. As can be seen, eliminating non-homogeneous structure, reducing layer number and the size of the device has significant effect on performance parameters.

Table 1. Comparison of performance parameters for gold-based devices

Devices	Current-related Sensitivity
Au / Cu / Ni on PCB (1 mm size)	3 μV/AT
Au on Glass Substrate (500 μm size)	5 mV/AT
Au / Cr on SiO ₂ /Si Substrate (60 μm size)	3 mV/AT
Au / Cr on SiO ₂ /Si Substrate (10 μm size)	27 mV/AT

6. Conclusion

In general, gold-based Hall devices on FR4 substrate cannot be considered for high sensitivity applications due to their electric material properties and non-homogeneous structure. However, reducing the layer sizes has merit for applications not requiring high sensitivity as was shown with gold devices on glass substrate. In reality, the performance parameters for the latter type of Hall sensors can significantly be improved if they can be made in smaller sizes as confirmed by gold devices on silicon substrate with 10 μm active areas. In this work, the aim was to discover a cheaper and easier fabrication method, thus, the devices on glass substrate were made with larger sizes, due to

limitation of laser size and distortion in acrylic because of thermal heat effect. Moreover, sputtering technique is not convenient for creating a smooth surface as it is bombarding the gold all around the surface. Therefore, employing an appropriate glass mask with smaller features and implementing lithographical processes would allow smaller sizes. Using electron beam evaporation can improve the surface smoothness which will consequently lead to devices with much better performances. Meanwhile, it is worth to note that creating devices with only a thin gold layer will not be suitable for biosensing applications although they might be used for applications requiring dry air. Because, the material is removed from the surface when it is introduced in liquid environment. This is due to the lack of the adhesion layer. In the meantime, employing an adhesion layer will cause distortion in the performance as was shown by Cr/Au devices with 60 μm active sizes. Nevertheless, this issue can be overcome by decreasing the feature size as was confirmed by Cr/Au devices with 10 μm active areas.

References

- [1] S. P. Mohanty and E. Kouciasanos, "Biosensors: A tutorial review," *IEEE Potentials*, vol. 25, no. 2, pp. 35–40, 2006, doi: 10.1109/MP.2006.1649009.
- [2] S. Song, H. Xu, and C. Fan, "Potential diagnostic applications of biosensors: Current and future directions," *Int. J. Nanomedicine*, vol. 1, no. 4, pp. 433–440, 2006, doi: 10.2147/nano.2006.1.4.433.
- [3] S. K. Vashist, "Point-of-care diagnostics: Recent advances and trends," *Biosensors*, vol. 7, no. 4, 2017, doi: 10.3390/bios7040062.
- [4] S. Vigneshvar, C. C. Sudhakumari, B. Senthilkumaran, and H. Prakash, "Recent advances in biosensor technology for potential applications - an overview," *Front. Bioeng. Biotechnol.*, vol. 4, no. FEB, p. 11, 2016, doi: 10.3389/fbioe.2016.00011.
- [5] B. Wang, U. Akiba, and J. I. Anzai, "Recent progress in nanomaterial-based electrochemical biosensors for cancer biomarkers: A review," *Molecules*, vol. 22, no. 7, p. 1048, 2017, doi: 10.3390/molecules22071048.
- [6] D. Issadore *et al.*, "Magnetic sensing technology for molecular analyses," *Lab Chip*, vol. 14, no. 14, pp. 2385–2397, 2014, doi: 10.1039/c4lc00314d.
- [7] T. Takamura, P. J. Ko, J. Sharma, R. Yukino, S. Ishizawa, and A. Sandhu, "Magnetic-particle-sensing based diagnostic protocols and applications," *Sensors (Switzerland)*, vol. 15, no. 6, pp. 12983–12998, 2015, doi: 10.3390/s150612983.
- [8] J. Llandro, J. J. Palfreyman, A. Ionescu, and C. H. W. Barnes, "Magnetic biosensor technologies for medical applications: A review," *Med. Biol. Eng. Comput.*, vol. 48, no. 10, pp. 977–998, 2010, doi: 10.1007/s11517-010-0649-3.
- [9] R. S. Popović, *Hall effect devices*, 2nd ed. Philadelphia : Institute of Physics Pub., 2004.
- [10] D. İzci, "Constructing an Electronic Circuitry for Label-free Hall Biosensors," *Balk. J. Electr. Comput. Eng.*, vol. 7, no. 4, pp. 366–372, Oct. 2019, doi: 10.17694/bajece.633908.
- [11] G. Rizzi, F. W. Osterberg, A. D. Henriksen, M. Dufva, and M. F. Hansen, "On-chip magnetic bead-based DNA melting curve analysis using a magnetoresistive sensor," *J. Magn. Magn. Mater.*, vol. 380, pp. 215–220, 2015, doi: 10.1016/j.jmmm.2014.09.004.
- [12] M. Volmer and M. Avram, "Using permalloy based planar hall effect sensors to capture and detect superparamagnetic beads for lab on a chip applications," *J. Magn. Magn. Mater.*, vol. 381, pp. 481–487, 2015, doi: 10.1016/j.jmmm.2014.10.172.
- [13] T. Q. Hung, S. Oh, J. R. Jeong, and C. G. Kim, "Spin-valve planar Hall sensor for single bead detection," *Sensors Actuators, A Phys.*, vol. 157, no. 1, pp. 42–46, 2010, doi: 10.1016/j.sna.2009.11.033.
- [14] D. Drung *et al.*, "Highly sensitive and easy-to-use SQUID sensors," *IEEE Trans. Appl. Supercond.*, vol. 17, no. 2, pp. 699–704, 2007, doi: 10.1109/TASC.2007.897403.
- [15] D. İzci, C. Dale, N. Keegan, and J. Hedley, "The Construction of a Graphene Hall Effect Magnetometer," *IEEE Sens. J.*, vol. 18, no. 23, pp. 9534–9541, Dec. 2018, doi: 10.1109/JSEN.2018.2872604.
- [16] A. Sandhu, Y. Kumagai, A. Lapicki, S. Sakamoto, M. Abe, and H. Handa, "High efficiency

- Hall effect micro-biosensor platform for detection of magnetically labeled biomolecules,” *Biosens. Bioelectron.*, vol. 22, no. 9–10, pp. 2115–2120, 2007, doi: 10.1016/j.bios.2006.09.021.
- [17] K. Togawa *et al.*, “Detection of magnetically labeled DNA using pseudomorphic AlGaAs/InGaAs/GaAs heterostructure micro-Hall biosensors,” *J. Appl. Phys.*, vol. 99, no. 8, 2006, doi: 10.1063/1.2162041.
- [18] G. Mihajlović *et al.*, “Detection of single magnetic bead for biological applications using an InAs quantum-well micro-Hall sensor,” *Appl. Phys. Lett.*, vol. 87, no. 11, 2005, doi: 10.1063/1.2043238.
- [19] H. Xu *et al.*, “Batch-fabricated high-performance graphene Hall elements,” *Sci. Rep.*, vol. 3, p. 1207, 2013, doi: 10.1038/srep01207.
- [20] M. Bando *et al.*, “High sensitivity and multifunctional micro-Hall sensors fabricated using InAlSb/InAsSb/InAlSb heterostructures,” *J. Appl. Phys.*, vol. 105, no. 7, p. 07E909, 2009, doi: 10.1063/1.3074513.
- [21] O. Kazakova *et al.*, “Detection of a micron-sized magnetic particle using insb hall sensor,” *IEEE Trans. Magn.*, vol. 45, no. 10, pp. 4499–4502, 2009, doi: 10.1109/TMAG.2009.2025513.
- [22] D. Petit, D. Atkinson, S. Johnston, D. Wood, and R. P. Cowburn, “Room temperature performance of submicron bismuth Hall probes,” *IEE Proc. Sci. Meas. Technol.*, vol. 151, no. 2, pp. 127–130, 2004, doi: 10.1049/ip-smt:20040167.
- [23] B. Chen, L. Huang, X. Ma, L. Dong, Z. Zhang, and L. M. Peng, “Exploration of sensitivity limit for graphene magnetic sensors,” *Carbon N. Y.*, vol. 94, pp. 585–589, 2015, doi: 10.1016/j.carbon.2015.07.040.
- [24] J. M. Pingarrón, P. Yáñez-Sedeño, and A. González-Cortés, “Gold nanoparticle-based electrochemical biosensors,” *Electrochim. Acta*, vol. 53, no. 19, pp. 5848–5866, 2008, doi: 10.1016/j.electacta.2008.03.005.
- [25] K. Saha, S. S. Agasti, C. Kim, X. Li, and V. M. Rotello, “Gold nanoparticles in chemical and biological sensing,” *Chem. Rev.*, vol. 112, no. 5, pp. 2739–2779, 2012, doi: 10.1021/cr2001178.
- [26] N. Khlebtsov and L. Dykman, “Biodistribution and toxicity of engineered gold nanoparticles: A review of in vitro and in vivo studies,” *Chem. Soc. Rev.*, vol. 40, no. 3, pp. 1647–1671, 2011, doi: 10.1039/c0cs00018c.
- [27] M. A. Paun, J. M. Sallese, and M. Kayal, “Hall effect sensors design, integration and behavior analysis,” *J. Sens. Actuator Networks*, vol. 2, no. 1, pp. 85–97, 2013, doi: 10.3390/jsan2010085.
- [28] M. A. Paun, J. M. Sallese, and M. Kayal, “Comparative study on the performance of five different hall effect devices,” *Sensors (Switzerland)*, vol. 13, no. 2, pp. 2093–2112, 2013, doi: 10.3390/s130202093.
- [29] V. P. Kunets *et al.*, “InSb quantum-well-based micro-hall devices: Potential for pT Detectivity,” *IEEE Trans. Electron Devices*, vol. 56, no. 4, pp. 683–687, 2009, doi: 10.1109/TED.2009.2014187.
- [30] N. Haned and M. Missous, “Nano-tesla magnetic field magnetometry using an InGaAs-AlGaAs-GaAs 2DEG Hall sensor,” *Sensors Actuators, A Phys.*, vol. 102, no. 3, pp. 216–222, 2003, doi: 10.1016/S0924-4247(02)00386-2.
- [31] L. Huang, Z. Zhang, B. Chen, X. Ma, H. Zhong, and L. M. Peng, “Ultra-sensitive graphene Hall elements,” *Appl. Phys. Lett.*, vol. 104, no. 18, 2014, doi: 10.1063/1.4875597.

MARBLE CLASSIFICATION USING DEEP NEURAL NETWORKS

Murat CANAYAZ^{1*}, *Fatih ULUDAĞ*²


Deep learning, which has been described as the processing and interpretation of data, is now widely used. In this study, deep neural networks are used for the classification of marbles which can be used in the industry. For this purpose most used marbles images were obtained from companies in Turkey and 28-class dataset was created. Then VGG16, ResNet and LeNet models were trained on this dataset. Data augmentation was performed to have class balance. To evaluate the models performance accuracy metric is used. In the VGG16 model, fine tuning was applied and %97 accuracy was achieved. In experimental studies, models were trained with different parameter settings. The performances of the models are given comparatively. The fact that both new dataset and deep neural networks are used for the first time in marble classification are among the positive aspects of this study. It is planned to integrate the models produced in the future studies into mobile based expert systems.

Key words: Marble Classification, Deep Neural Networks, VGG16, ResNet, LeNet

1. Introduction

The increase in the use of natural stones in architecture and decoration, the simplicity in the processing of them as a result of technological developments and the obtaining of them in a more economical way has caused more marble production worldwide. Turkey is located in the Alpine-Himalayan belt the richest marble deposits in the world. Turkey's total marble reserves are estimated to be about 5.1 billion cubic meters, which corresponds to approximately 33 percent of the world reserves [1]. Marble industry has an important role in Turkey's economy. Overall marbles can be divided into eight major groups in Turkey. These marble groups are Marmara types, beige, blacks, whites, cherry colors, onyxes, pinks and greens [2]. In 2016, approximately 860 million dollars of exports were made [3]. Turkey, in 2016, took the first place by achieving %45,7 of world stone exports as marble, travertine etc.

Marble can be found in different colors and textures in nature due to the minerals in it and differences in its formation. In Turkey, more than 80 in different structures and more than 120 in different colors and patterns of marble reserves are determined. Although there is no general standard

¹ Computer Engineering Department, Engineering Faculty, Van Yuzuncu Yil University, 65000, Van, Turkey, (mcanayaz@yyu.edu.tr)  <https://orcid.org/0000-0001-8120-5101>

² Econometrics Department, Faculty Of Economics And Administrative Sciences, Van Yuzuncu Yil University, 65000, Van, Turkey, (fatihuludag@yyu.edu.tr)

for naming marble types, the color in general or the region where they are extracted or both are considered together Elazig Cherry, Mugla White, Burdur Beige etc.

Even marble types have with the same name, there may be color and texture differences. Even field experts have difficulty identifying the type of marble they encounter. This situation may cause problems between suppliers and customers[4].

The classification of the marble species and the determination of the product quality are generally made by experts in the field. Based on the variability of marble types from country to country and from region to region and the range of the color scale, companies need automatic systems.

In the literature, many studies have been done to classify marble species. Hernandez et al. compared the classification success of artificial neural networks with deterministic statistical classification algorithms for control of marble slabs[5]. Machine learning based computer vision applications have recently been used in the classification of marble types and determination of quality levels[6-9].

Doğan and Akay proposed a method based on the AdaBoost algorithm and histogram differences and totals for the classification of marble slabs and achieved a high success for four different marble classes[10]. Lopez et al. used functional support vector machine and functional neural network using data obtained from spectrometer for classification of ornamental Stones[11]. Topalova and Tzokev used multilayered artificial neural networks to classify marble textures in real time[12]. Selver et al. classify the marble slabs using hierarchical clustering algorithm to increase the quality control standards[9].

In the field of computer vision, Deep Learning models have been quite successful [13]. Since the artificial neural networks are insufficient to extract information from the pictures, the Convolutional Neural Networks have been developed[14]. The architecture of convolutional neural networks is inspired by the biological vision system. Compared to standard artificial neural networks with similar layer size, CNNs have less connection, lower number of parameters to be trained [13]. The success of these networks in vision applications is due to two important features: spatially shared weights and spatial pooling[15]. CNN is the more complex form of neural networks. In this multi-layered network, for feature extraction there are 3 main layers, such as convolution layer, pool layer, fully connected layer. Normally in the neural networks, each neuron in the input layer is bound to the next layer by the output neuron. This is called fully connected. In the CNN structure, the FC structure is not used until the last layer [20,21]. In the literature, the most popular area in which CNN is used is image classification.

In this study, LeNet, Visual Geometry Group Convolutional Neural Networks (VGG16) and Residual Neural Network(ResNet) architectures which are frequently used in the literature are used for the classification of marble slabs and their success is compared. The main aim of the study is to investigate models for the automatic identification systems needed in the sector and to integrate effective models with mobile platforms.

The contributions of this paper are as follows:

- It is the first multi-class study in marble classification using Deep Neural Networks.
- It provides new dataset for marble classification
- Models obtained at the end of the study can be used as decision support mechanism
- The models can be easily integrated into mobile applications

2. Related Work

When image classification problems for marble samples are examined, we see that geometric and morphological transformation, color and textures of the image are obtained by using image processing applications before CNN networks. Most of the works are designed to be operated on the production line based on marble industry. From these studies;

Alajarin et al. has designed a system to classify marbles in the production line at the marble industry. In the prototype he used, he analyzed the color texture of the marble surfaces and classified them according to the corresponding group. RGB, XYZ, YIQ, and K-L for image analysis. Color spaces are used, and then feature extraction is provided by basic component analysis. The extracted features and the artificial neural network were used to classify the marbles[8].

Selver et al. followed a two-stage method for marble classification. First, features were extracted using textures and color spaces. These features have been tested with many artificial neural networks. Then classification was made by using hierarchical radial basis function network (HRBFN)[9].

Benavente and Pina presented a mathematical method based on morphology, dividing and classifying polished marble samples. In this method, separate textural regions were determined by watershed method. Morphological procedures were applied to find 3 elements on image (vein, background and transition) and classification was made according to these properties[16].

Akkoyun performed a program to be used in marble classification. This program makes marble quality classification by using image processing applications on marble images obtained from production band[17].

In their study, Doğan and Akay suggested a new hierarchical classification method based on the use of AdaBoost classification algorithms of various types for automatic classification of marble slab images. Features obtained by total and difference histograms method are classified by using Adaboost algorithms. This classification was compared with neural networks and SVM[10].

Selver et al. have developed an automated industrial conveyor belt system using image processing and hierarchical clustering for classifying marble slabs in their study[18].

We could not find a marble classification multi-class study using CNN networks in the literature. However, Ferreira and colleagues used CNN to classify granite tiles[19] and Torun et al. [22] have trained 600 images in 3 classes by Alexnet and Local Binary Pattern method in their study.

3. Experiments

3.1. Experimental Setup

CNN networks such as LeNet, VGGNet16, ResNet were used for the application. Two methods were used in the use of these networks. In the first method, the existing network structures for LeNet and ResNet were preserved. The training was provided by the transfer learning method for the VGG16 network. A Geforce Gtx 1070 GPU graphic card was used for applications on the Ubuntu 16.04 operating system. This reduces the calculation time for each iteration. The application is coded in python language using the Keras library. The used network architectures and dataset will briefly be introduced.

3.1.1 LeNet

LeNet[23] is a CNN structure which is designed to recognize handwriting and machine-printed character recognition by Yann LeCun. The structure of LeNet is simple and small. LeNet as consisting of two parts: (i) a block of convolutional layers; and (ii) a block of fully-connected layers. The LeNet architecture consists of two sets of convolutional, activation, and pooling layers, followed by a fully-connected layer, activation, another fully-connected layer, and finally a softmax classifier.

3.1.2 VGG16

VGGNET [24] developed by Simonyan and Zisserman was first used in ILSVRC 2014. VGG16, consisting of 16 layers deep (13 convolutional layer), is the most preferred network structure for the extraction of attributes from images due to its homogeneous structure. It includes $3 * 3$ filters. The VGGNET structure is publicly available. It requires high calculation costs with 138 million parameters.

3.1.3 ResNet

This model[25], created by the Microsoft team, was developed to eliminate the problem of the convergence of gradient values to 0 in multi-layered deep networks. Thanks to this structure, which is known as residual now, it is possible to get successful results in deep layer networks.

3.1.4 Transfer Learning

Transfer learning is a method used for feature extraction from data set by using VGGNet, Alexnet[13], GoogleNet[26] etc. In this method, the attributes of the images are subtracted without using the upper layers of the network. In addition, in a method called Fine-tuning, upper layers are removed and replaced by other layers in this method. In transfer learning method, firstly, the existing layers must be frozen until the appropriate layers are found. After the network is trained in certain iterations, the existing layers are released and the network is continued with the new layers. In this study, this method is applied to VGGNet. Initially, new layers were added instead of the upper layers, then the existing layers were frozen up to 25 epoch. In the VGG16 model, Flatten, Dense (256), Dropout (256), Dense (classes = 28) layers are added instead of the upper layers that are extracted in the fine tuning process. With this training, the network reaches a certain accuracy rate. A new training process is continued as much as the desired epoch. Fig. 1 shows the transfer learning process.

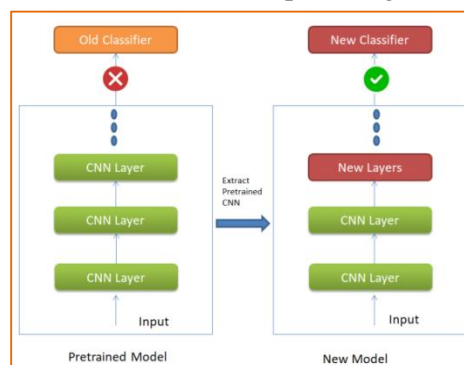


Figure 1. Transfer learning process

3.1.5 Dataset

In Turkey there are more than 300 varieties of marble. In terms of industry, there are 28 marble types which are the most widely used among these types of marble. A data set has been created from marble images obtained from the firms operating in the sector. These images were resized to 224 * 224 by using OpenCV[27] library based on the size of the image used in the CNN network. The number of images is increased via the data agumentation method. The data set consists of nearly 5600 marble images. The number of images in each class is set to be equal to 200. 150 of them were used for training and testing. The remaining 50 is used in the validation process for the first time by the network. Our dataset, which contains a sample from each class, is shown in Fig. 2. The original dataset we have created can be reached below link publicly available [Google Drive Link](#).

In the data agumentation process which we use to increase our data set, class ImageDataGenerator in the Keras library is used. The methods and ratios used are as follows; rotation_range=40,width_shift_range=0.2, height_shift_range=0.2, shear_range=0.2, zoom_range=0.2,horizontal_flip=True, fill_mode='nearest'.

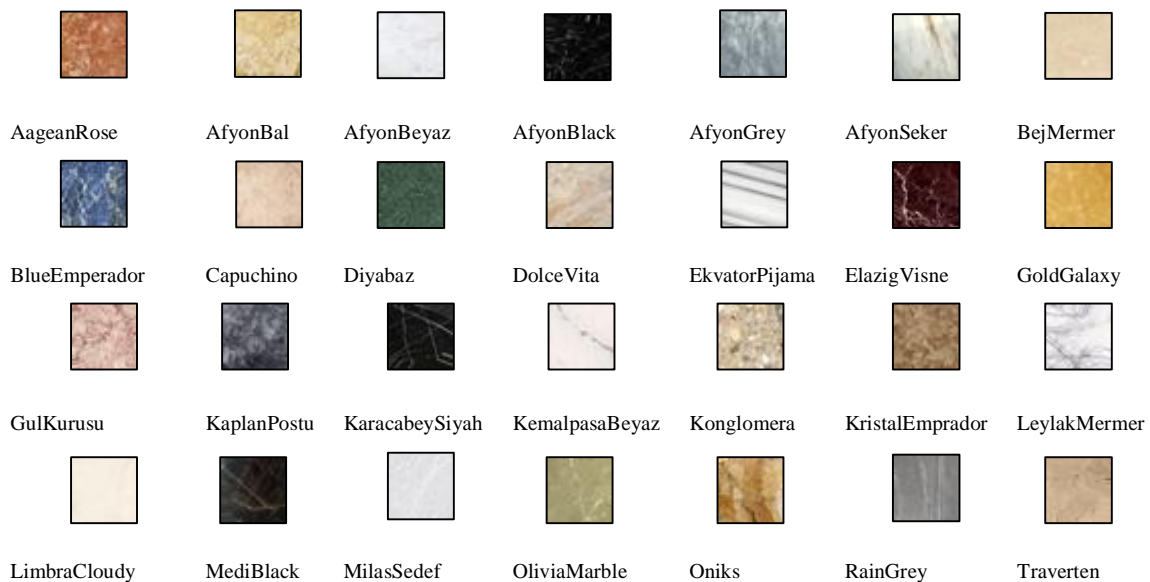


Figure 2. Marble images of 28 class

3.2. Evaluation Metric

After completing the model trainings, accuracy, precision, recall and f1 score metrics are used in the model estimation process. A brief description of these is given below. These metrics are easily obtained with the scikit-learn and keras library in python programming language.

Accuracy(acc) compares the index of the maximum true value to the index of the predicted maximum value, indicating how often the estimates are at the same point as the true values.

Precision (P) is defined as the number of true positives(Tp) over the number of true positives plus the number of false positives(Fp)

$$P = \frac{T_p}{T_p + F_p} \quad (14)$$

Recall (R) is defined as the number of true positives(Tp) over the number of true positives plus the number of false negatives(Fn)

$$R = \frac{T_p}{T_p + F_n} \quad (15)$$

The quantities are also related to the (F1) score, which is defined as the harmonic mean of precision and recall

$$F1 = 2 \frac{P \times R}{P + R} \quad (16)$$

A macro-average calculates the metric independently for each class, and then takes the average, whereas a micro average collects contributions to measure the average measurement of all classes[28].

3.3. Experimental results under different parameter settings

This section shows the results from the models. The models were run until they reached 100 and 1000 epochs. The parameter values used in these models are given in Tab. 1.

Working steps in summary;

- In the study, firstly marble images were collected to create dataset.
- These images were resized to 224 * 224 through OpenCV
- These images are enhanced by data augmentation
- Data set is divided into train, test.
- Marbles are classified by using CNN networks.

In the experiments, 2 pathways were observed in the use of CNN networks. Firstly, the data set that we have created has been trained in CNN networks and the appropriate weight values and high accuracy model have been saved. The second way was the classification of marble by using VGG16 model with the method called fine tuning. The results in the tables were obtained from the test data.

Table 1. Parameter values

Models	Optimizer	Loss Function	Metrics	Batch_Size	Test_Split_Size
LeNet	SGD learning rate:0.01 Adam learning rate:0.001	Categorical_Cross_entropy	Accuracy	128	0.25
VGGNet	RMSprop learning rate:0.001* SGD learning rate:0.001	Categorical_Cross_entropy	Accuracy	32	0.25
ResNet	SGD learning rate:0.1** Momentum:0.9 Adam learning rate:0.001	Categorical_Cross_entropy	Accuracy	128	0.25

*This optimizer is used for the first 25 epoch of training where the layers are frozen. SGD optimizer was used for further training. **In the ResNet model, overfitting was prevented by using L2 norm regularization. For this purpose, the coefficient of regularization for weight reduction is 0.0005

Table 2. Models with SGD optimizer(100 epochs)

Models		precision	recall	f1-score
LeNet	Micro Avg	0.73	0.73	0.73
	Macro Avg	0.75	0.75	0.72
	WeightedAvg	0.75	0.73	0.71
VGG16	Micro Avg	0.96	0.96	0.96
	Macro Avg	0.97	0.96	0.96
	WeightedAvg	0.96	0.96	0.96
ResNet	Micro Avg	0.82	0.82	0.82
	Macro Avg	0.85	0.83	0.82
	WeightedAvg	0.86	0.82	0.81

Table 3. Models with SGD optimizer(1000 epochs)

Models		precision	recall	f1-score
LeNet	Micro Avg	0.93	0.93	0.93
	Macro Avg	0.94	0.94	0.93
	Weighted Avg	0.93	0.93	0.93
VGG16	Micro Avg	0.97	0.97	0.97
	Macro Avg	0.98	0.98	0.98
	Weighted Avg	0.98	0.97	0.97
ResNet	Micro Avg	0.96	0.96	0.96
	Macro Avg	0.97	0.97	0.97
	Weighted Avg	0.97	0.96	0.96

When we look at the results in Tab. 2 of 100 epoch using SGD optimizer, it is seen that VGG16 achieves a better result with approximately 96% precision performance. LeNet model needs more iteration due to its simple structure.

It is possible to see a better performance of VGG16 in Tab. 3 where 1000 epoch is used. ResNet achieved a result close to VGG16 with a performance of 96%. Thanks to its high epoch value, the LeNet model provided a significant performance improvement over the results of 100 epochs.

Tab. 4 shows only the results of LeNet and ResNet models obtained with Adam optimizer. The reason why the VGG16 model is not in this table is that the data set we use with Adam optimizer is worse than the LeNet model in the experimental observations. Looking at the table, it seems that the ResNet model performs well from the Lenet model, but this is not a very satisfactory result for a model.

When we examine Tab. 5, it is possible to say that the Lenet model, which performs 92%, will be suitable for the data set that we use with Adam optimizer. Fig. 3 shows the confusion matrix obtained with validation data on the VGG16 model which provides the highest performance.

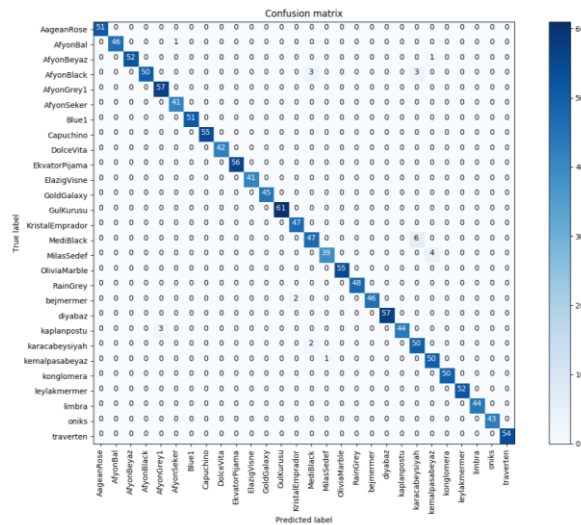


Figure 3. Confusion matrix of validation data on VGG16

Table 4. Models with Adam optimizer(100 epochs)

Models		precision	recall	f1-score
LeNet	Micro Avg	0.77	0.77	0.77
	Macro Avg	0.78	0.77	0.77
	WeightedAvg	0.78	0.77	0.77
ResNet	Micro Avg	0.88	0.88	0.88
	Macro Avg	0.90	0.89	0.87
	WeightedAvg	0.89	0.88	0.86

Table 5. Models with Adam optimizer(1000 epochs)

Models		precision	recall	f1-score
LeNet	Micro Avg	0.92	0.92	0.92
	Macro Avg	0.92	0.92	0.92
	WeightedAvg	0.92	0.92	0.92
ResNet	Micro Avg	0.89	0.89	0.89
	Macro Avg	0.90	0.90	0.90
	WeightedAvg	0.90	0.89	0.89

When the performance of the models are evaluated, it is possible to say that the VGG16 model is better than the other models when it is used with SGD optimizer on the marble data set. In the second performance criterion in which Adam Optimizer is used, LeNet performed better than ResNet in the high epoch number. It was observed that the VGG16 gave even worse results than LeNet when it is used with Adam optimizer. Fig. 4 shows the visualization of activation maps for the first 5 blocks in VGG16. Fig. 5 shows experimental studies on the model obtained by performing transfer learning on VGG16. The red label indicates the estimated label and the green label indicates the actual label value.

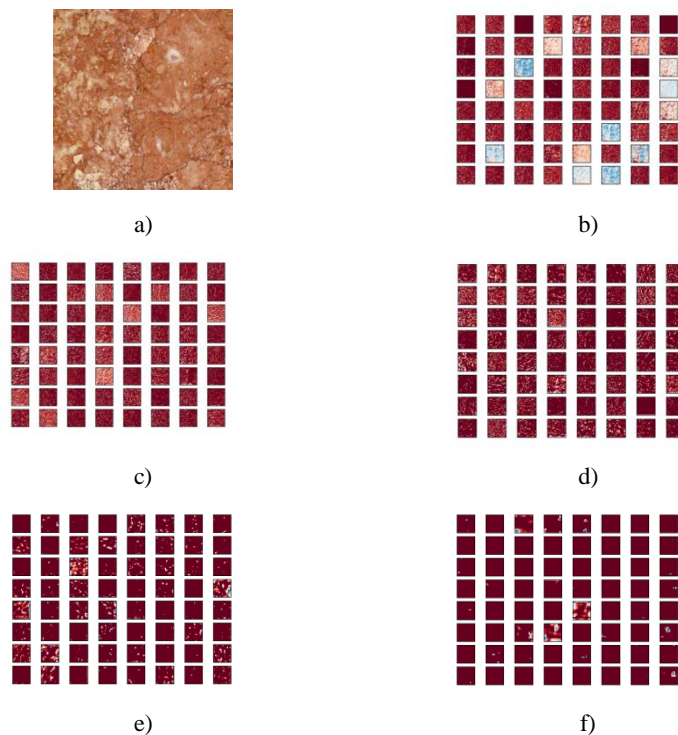


Figure 4. a) Original Image b) Visualization of the feature maps extracted from block 1 c) Visualization of the feature maps extracted from block 2 d) Visualization of the feature maps extracted from block 3 e) Visualization of the feature maps extracted from block 4 f) Visualization of the feature maps extracted from block 5

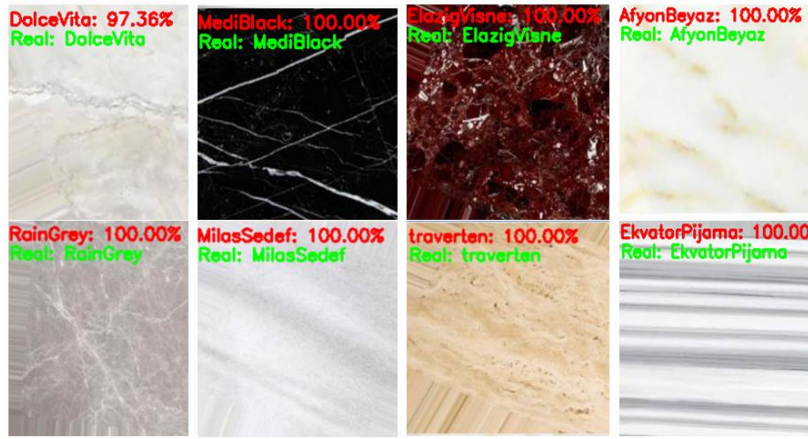


Figure 5. Experimental results of validation data on VGG16

4. Conclusion

The aim of this study, which we used to classify marble images with CNN networks, is preparing dataset for expert systems which can be used in marble industry and presenting our trained model with these datasets to the service of researchers. Within the framework of the research, 28 most familiar images of marble were obtained and these images were extended by data augmentation method and data set was created. The dataset is trained with LeNet, ResNet, VGGNet16, which is one of the most known CNN network architectures. Looking at the results of the training, it is observed that high accuracy rate is achieved. Because some networks used require computational costs, the GPU requirement was created and this requirement was met with the Geforce GTX 1070 GPU. VGGNet16 and ResNet models were completed on an epoch with an average of 18 seconds with this GPU. In LeNet model, this rate was 2 seconds. The evaluation metrics are not only satisfied with accuracy, but also the results are given in metrics such as f score, precision, recall in model estimation process. Since the use of CNN in the multi-class marble classification field was first tried in this study, it is suggested that researchers will give an idea for future studies. The dataset were published as public. The mobile expert system is designed to be developed for future applications.

Acknowledgment

This study is supported Scientific Research Projects Department Project No. FBA-2018-6915 by Van Yuzuncu Yıl University.

References

- [1] Yalçın, S., Uyanık, T. (2001). Dünya mermer ticaretinde Türkiye'nin yeri. *Türkiye III. Mermer Sempozyumu*, Afyon, Türkiye, 397-416.
- [2] Gökay, M. K., Gundogdu, I. B. (2008). Color identification of some Turkish marbles. *Construction and Building Materials*, 22(7), 1342-1349.
- [3] TURKSTAT, Turkey Marble Export, Turkey, 2016
- [4] Bianconi, F., González, E., Fernández, A., Saetta, S. A. (2012). Automatic classification of granite tiles through colour and texture features. *Expert Systems with Applications*, 39(12), 11212-11218.

- [5] Hernández, V. G., Perez, P. C., Pérez, L. G. G., Balibrea, L. M. T., Pina, H. P. (1995). Traditional and neural networks algorithms: applications to the inspection of marble slab. *In Systems, Man and Cybernetics, Intelligent Systems for the 21st Century., IEEE International Conference on*, 5, 3960-3965.
- [6] Martinez-Alajarin, J. (2004). Supervised classification of marble textures using support vector machines. *Electronics Letters*, 40(11), 664-666.
- [7] Juan, M.C.V.A., Balibrea, T., Manuel, L.(1999). Marble Slabs Quality Classification System using Texture Recognition and Neural Networks Methodology. *European Symposium on Artificial Neural Networks Bruges*,Belgium, 75-80.
- [8] Martinez-Alajarin, J., Luis-Delgado J. D., Tomas-Balibrea, L. M. (2005). Automatic system for quality-based classification of marble textures. *In IEEE Transactions on Systems, Man, and Cybernetics, Part C (Applications and Reviews)*, 35(4), 488-497, doi: 10.1109/TSMCC.2004.843236
- [9] Selver, M. A., Akay, O., Ardali, E., Bahad, A., Onal, O., Ozden, G. (2009). Cascaded and hierarchical neural networks for classifying surface images of marble slabs. *IEEE Transactions on Systems, Man, and Cybernetics, Part C (Applications and Reviews)*, 39(4), 426-439.
- [10] Doğan, H., Akay, O. (2010). Using AdaBoost classifiers in a hierarchical framework for classifying surface images of marble slabs. *Expert Systems with Applications*, 37(12), 8814-8821.
- [11] López, M., Martínez, J., Matías, J. M., Taboada, J., Vilán, J. A. (2010). Functional classification of ornamental stone using machine learning techniques. *Journal of Computational and Applied Mathematics*, 234(4), 1338-1345.
- [12] Topalova, C., Tzokev, A. *Adaptive marble plate classification system based on neural network and Plc Implementation*, Annals of DAAAM & Proceedings, 2011.
- [13] Krizhevsky, A., Sutskever, I., Hinton, G. E. (2012). ImageNet classification with deep convolutional neural networks. *In Proceedings of the 25th International Conference on Neural Information Processing Systems*, USA, 1097-1105.
- [14] LeCun, Y. Generalization and network design strategies. Technical Report CRG-TR-89-4, Department of Computer Science, University of Toronto, 1989.
- [15] Kim, Y. (2014). Convolutional neural networks for sentence classification. *In Proceedings of the 2014 Conference on Empirical Methods in Natural Language Processing*, Doha, Qatar, 1746–1751.
- [16] Benavente, N., Pina, P. (2009). Morphological segmentation and classification of marble textures at macroscopical scale. *Computers & Geosciences*, 35(6), 1194-1204.
- [17] Akkoyun, O. (2010). An evaluation of image processing methods applied to marble quality classification. *2nd International Conference on Computer Technology and Development*, Cairo, 158-162. doi: 10.1109/ICCTD.2010.5646128
- [18] Selver, M. A., Akay, O., Alim, F., Bardakçı, S., Ölmez, M. (2011). An automated industrial conveyor belt system using image processing and hierarchical clustering for classifying marble slabs. *Robotics and Computer-Integrated Manufacturing*, 27(1), 164-176.
- [19] Ferreira, A., Giraldi, G. (2017). Convolutional Neural Network approaches to granite tiles classification. *Expert Systems with Applications*, 84, 1-11. <https://doi.org/10.1016/j.eswa.2017.04.053>.
- [20] Rosebrock, A. *Deep Learning for Computer Vision*, PyImageSearch, 2017.
- [21] Goodfellow, I., Bengio, Y., Courville, A. *Deep Learning*, MIT Press, 2016.
- [22] Torun, Y., Akbaş, M. R., Çelik M. A., Kaynar, O. (2019). Development a Machine Vision System For Marble Classification. *27th Signal Processing and Communications Applications Conference (SIU)*, Sivas, Turkey, 1-4. doi: 10.1109/SIU.2019.8806419

- [23] LeCun, Y., Bottou, L., Bengio, Y., Haffner, P. (1998). Gradient-based learning applied to document recognition. *In Proceedings of the IEEE*, 86(11), 2278-2324.
- [24] Simonyan K., Zisserman, A. (2014). Very deep convolutional networks for large-scale image recognition. *In: CoRR abs/1409.1556*
- [25] He, K., Zhang, X., Ren, S., Sun, J. (2015). Deep residual learning for image recognition. *CoRR, abs/1512.03385*.
- [26] Szegedy C. et al. (2015). Going deeper with convolutions. *2015 IEEE Conference on Computer Vision and Pattern Recognition (CVPR)*, Boston, MA, 1-9.
- [27] OpenCV, (2019). <https://opencv.org/>
- [28] Scikit-Learn Documentation, (2019).

A SIMULATION MODEL FOR CUSTOMER FLOW ANALYSIS IN A COMMERCIAL BANK IN NIGERIA

Mayowa Rafiat AJIBOYE^{1*}, Isiaka ISMAIL², Temitope Olubanjo KEHINDE³, Adewale ABE⁴


In view of competitiveness and increasing search for improved services in Nigerian commercial banks, there are some organizational changes necessary to facilitate this fate. Recently, the possibility of applying operational research techniques, more specifically computer simulation, was raised to address the problem of customer queues at bank branches. No bank has been punished with a fine if there are customers waiting for more than a certain period of time in the queues to be served. The solution to the problem sought to offer customer-care to the crowd in all bank branches in Nigeria. In view of this, the present work proposes a computer simulation model to study the flow of customers in a branch of the bank. This model simulates service capacity and time in the face of various hypothetical scenarios to which a bank branch may be subject using the Rockwell Automation Arena[®] v15 software. The results make it possible to evaluate new policies for increasing the quality of service and compliance with easy customer-care operational service. The generated scenarios were evidence alternatives that would reduce waiting times with only a few minor alterations. Thereby allowing the service with maximum waiting time the standards required.


Key words: *Simulation, commercial-banks, queuing, Arena, customer-care*


1. Introduction

Waiting lines have always characterized a problem at commercial banks. Initially, parallel lines were used, one for each service desk. Subsequently, these parallel lines were replaced by a single line, where all customers wait in a single line for the first available window. Currently, in addition to the single line, bank branches provide customers with a wide variety of alternative services and in an automated way, either at branches or over the internet, but they have not, however, been able to eliminate the long lines inside the bank branches.

With the emergence of new products and services offered by the banking sector, banking institutions, aware of their responsibilities, have invested significantly in actions aimed at offering personalized and high-quality service to all their customers and users.

¹ Department of Accounting, Al-Hikmah University, Ilorin, Nigeria (rafiat.ajiboye@yahoo.com)  <https://orcid.org/0000-0003-01777-4799>

² Department of Electrical & Electronic Engineering, Ekiti State University, Ado-Ekiti, Nigeria, (isiaka.ismail@eksu.edu.ng)  <https://orcid.org/0000-0003-2428-2383>

³ Department of Industrial & Production Engineering, University of Ibadan, Ibadan, Nigeria, (kehindeolubanjo@gmail.com)  <https://orcid.org/0000-0001-7703-7395>

⁴ Department of Electrical & Electronic Engineering, Ekiti State University, Ado-Ekiti, Nigeria, (adewale.abe@eksu.edu.ng)  <https://orcid.org/0000-0002-3285-1833>

Due to modernization and increasing population, the number of people served by banks grow daily and the services offered are increasing in numbers. To further aggravate this problem, there is a seasonality inherent in banking operations, such as payday for civil servants, the eve of holidays, end and beginning of the month, lunchtime and close to the closing of the branch, etc.

These issues generate changes in the dynamics of the client flow and make it difficult to predict resources allocation and, consequently, control the time of the agency's operations. It is often common for a customer to wait for more than 30 minutes to be served or perform an operation at an ATM. This is a typical problem and is repeated in many agencies in the country. Following the worldwide trend of expanding electronic service as a cost reducer, the banking sector has been gradually expanding investment in electronic equipment to increase the range of services, facilitate the service and convenience of its customers.

According to Abensur [1], the need for the banking network to reduce administrative and operational costs without prejudice to the quality of service has raised the segment to greater investment. New technologies such as ATMs allow banks to offer their customers service channels such as withdrawals, deposits, bill payments, transfers, and investments.

However, many customers still prefer traditional service, directly at the counter, as they believe that personal contact is essential. Therefore, offering a quality service means adjusting consumer expectations on a consistent basis, that is, if the perceived service reaches or exceeds the expected service, customers feel able to use the service provider again [2-4]. The search for process improvement is an important factor for the institutional success of any organization, regardless of its size, whether public or private, as long as it is carried out in a structured way and is understood by everyone in the organization. Therefore, if, on the one hand, there is an increase in technology to reduce the queues in the attendance at the counters, and on the other hand, there is a reduction in the number of attendants, the problem will persist if there are still queues at conventional ATMs.

Recently, this problem was studied by Favaretto and proposed the approach from the perspective of operational research [5]. He identified the complexity inherent to the dynamics of customer flow in bank branches and characterized it as a typical problem to be addressed by computer simulation. In these works, it was concluded, among other things, that considering the usual costs of banking operations, the stipulated time is compatible with the amount of the fine adopted, forcing the bank to operate within the law. In the work of Paradi and Zhu, basic procedures were presented for data sampling and the construction of a simulation model for a bank branch [6].

In view of this, it becomes necessary to build a model that allows studying the performance of the process under certain conditions, allowing the observation of behaviour and enabling the comparison of different scenarios. Thus, the present work aimed to create a computer simulation model from data collected directly at a bank branch to assess the flow of customers in critical periods of operation. From the developed model, several hypotheses were presented that could minimize or even solve the issue. The scenarios were simulated according to different situations that the agency could be subject to at different times of operation.

2. Description of the Bank Branch

The X branch chosen for this study has the services of manual cashiers (conventional service) and ATMs (automatic teller machines or self-service) with independent single lines, thus characterizing it as a typical agency with the services under study. At the request of management, the agency was not identified.

The branch has two floors, as shown in Figures 1 and 2. As seen in Figure 1, the lower floor, the entrance to the branch and right after the ATM windows. After the revolving door are the information and general assistance desks, where customers take their passwords and head for the stairs. On the lower floor, there are also seven tables for managers. There are seven ATMs for self-service (two of which were inactive). Two employees assist customers with difficulties in operating the machines. Next to the stairs, there are two information and general assistance windows, where the customer also takes the password for assistance from the manual boxes on the upper floor.

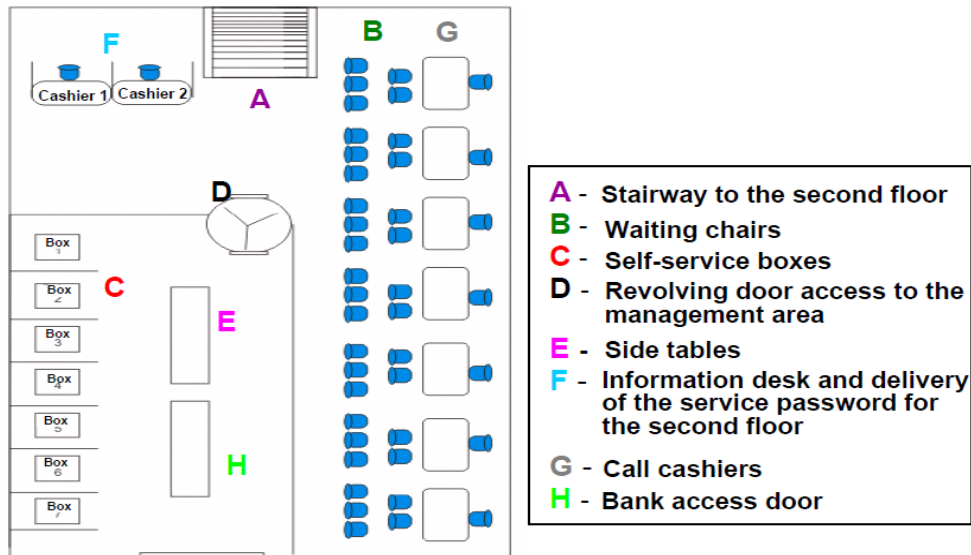


Figure 1. Ground floor of the Agency.

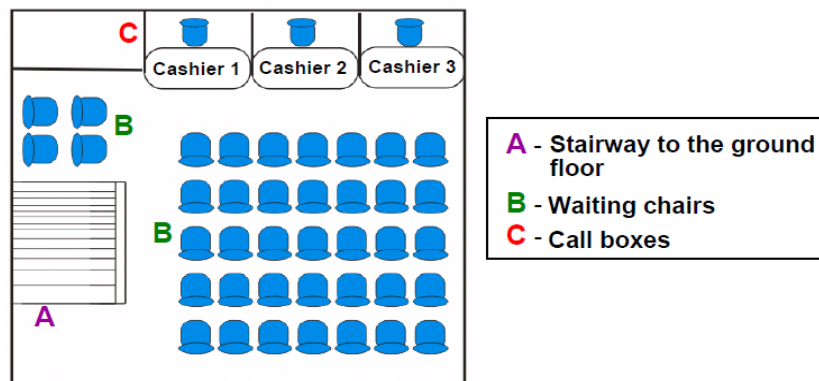


Figure 2. Top floor of the Agency.

On the upper floor, shown in Figure 2, there are manual assistance windows and chairs for waiting for assistance. Of these windows, two operated regularly and one was inactive. One attendant is designed specifically for conventional customers and the other is designed to serve preferred customers (elderly, pregnant women, etc.). If this type of customer is not on hold, he also serves conventional service customers.

At the agency, the queuing and password system, that is, the customer arrives, picks up the password, waits on the chairs destined for that purpose, and is attended to by the order of arrival.

The service points are:

- Manual assistance: 2 boxes, open from 10 am to 4 pm.
- Self-service: 5 ATMs, open from 8 am to 8 pm.

During the observation of the system, three types of assistance were identified:

- i. Customer service execution - preferential (manual service);
- ii. Customer service execution - conventional (manual service);
- iii. Customer self-service (ATM service).

3. Description of the Simulation Model

For the development of the model presented in this work, the methodology was proposed by [7, 8], composed of problem formulation and analysis; project planning; formulation of the conceptual model; macro-information and data collection; model translation; verification and validation; experimental design; comparison of systems and identification of the best solutions; documentation and presentation of results and implementation. The verification and validation were carried out also using the methodology proposed by Sargent [9, 10]. The conceptual model was developed using the logical elements proposed by Montevechi, *et al.* [11].

The translation of the conceptual model of the system to the computer simulation model was performed using the Rockwell Automation Arena[®] v15 software. The data were collected between September 1 and September 30, 2019, as they are typical days of high demand in bank branches and from this, it was possible to observe that of the 4523 customers who used conventional cash, 82 % were of normal service and 18 % were in priority service.

Two people with stopwatches were positioned in strategic places for data collection. One person was located next to the ATMs and the other to the executive ATMs, collecting customer arrival times independently. On the second day, service times were collected, where, once again, one person was located next to the ATMs and the other one next to the executive ATMs.

Figures 3 and 4 show the arrival times of customers at the agency for executive and automatic assistance, throughout the working day (10 am to 4 pm) and at 15 minute intervals.

It can be seen in these graphs that the behaviour of the flow of customers arriving at the bank branch is very irregular, presenting strong fluctuations, sharply and throughout the period. In this way, the difficulty of finding a possible distribution of probabilities that adequately represents the stochastic behaviour of the variables under analysis is characterized. Thus, it was decided to insert this data into the computational model through resources for generating shifts, the *Schedule*. This feature establishes rules that will be in effect for certain periods of time. Thus, it is possible to generate values very close to those presented in the respective Figures 3 and 4.

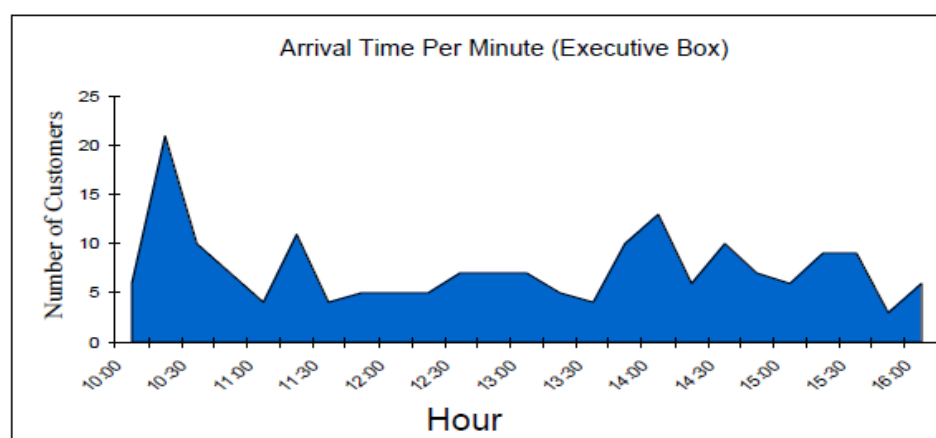


Figure 3. Customer arrival times per minute for manual service.

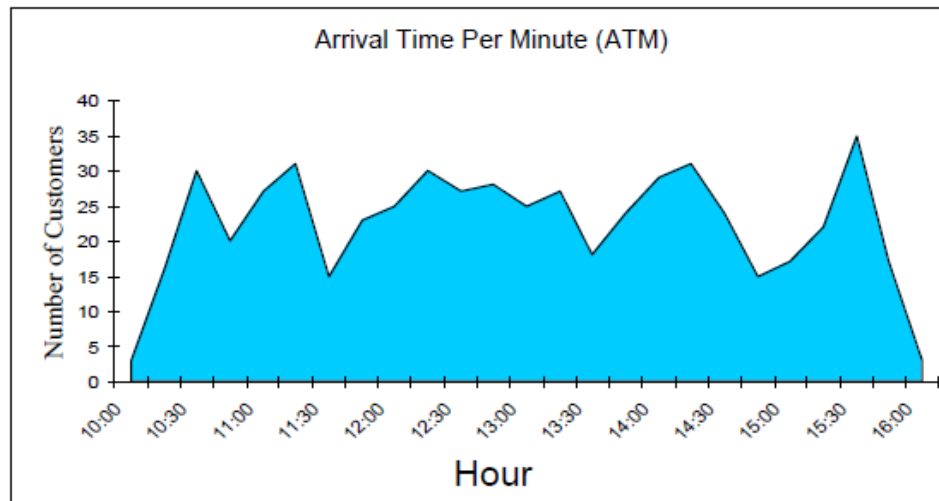


Figure 4. Customer arrival times per minute for automated service.

Regarding service times, the behaviour was more homogeneous, oscillating more smoothly around an average. This result was already expected, as it is an operation carried out in a more regular and systematic way, by one person, who performs the service. These data were processed by the *Input Analyzer* software, complementary to Rockwell Automation Arena[®] v15 software, to determine the best probability distribution that adheres to the set of values. The elements F_2 , F_3 and F_4 , in the legend of Figure 5, show the theoretical distributions of probabilities that best adhere to the stochastic behaviour of the variables.

The main purpose of the *Input Analyzer* software is to identify the best theoretical probability distribution, using the following adherence tests, namely: Chi-square and K-S [12].

After collecting data and identifying the behaviour of the variables that represent the dynamics of the customer flow at the bank branch, the conceptual model of the system was then shown, shown in Figure 5.

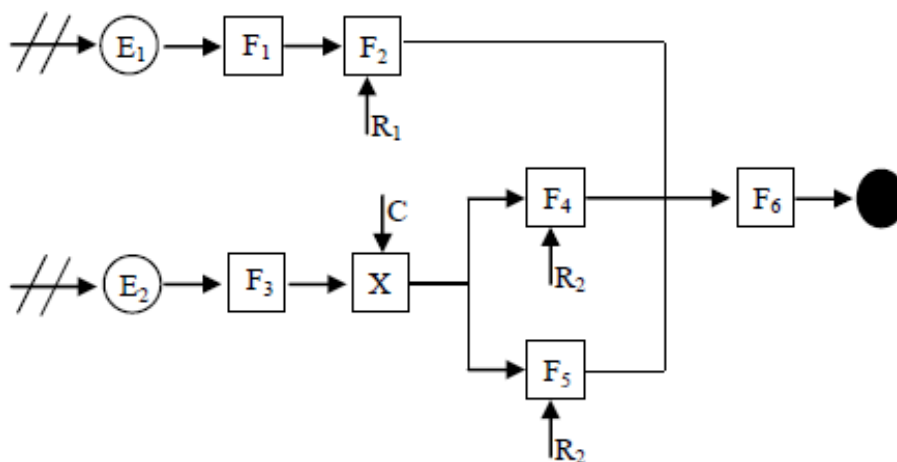


Figure 5. Conceptual model of customer flow at the bank branch.

The description of the parameters used in the banking service operation are stated in **Table 1** below. Two Arena[®] v15 *schedule* modules (referring: E_1 and E_2 , in Figure 5) were used to input data regarding the arrival of customers who were destined for ATMs and executive cashiers.

Table 1. Banking service operation parameters.

	Description	Parameter
E ₁	Arrival of Customers for Automatic Service	<i>Schedule</i> - referring to Figure 4 (one customer at a time)
E ₂	Arrival of Customers for Manual Service	<i>Schedule</i> - referring to Figure 3 (one customer at a time)
F ₁	Automatic Answering Queue Location	Infinite capacity
F ₂	Auto Answer	Normal log (average: 0.0725 and deviation: 0.0656) min
F ₃	Manual Service Queue Location	Infinite capacity
F ₄	Conventional Manual Service	0.5 + Normal log (average: 3.1 and deviation: 2.76) min
F ₅	Manual Attendance Preference	0.5 + Normal log (average: 3.1 and deviation: 2.76) min
F ₆	Exit Location	Infinite capacity
R ₁	Electronic Cashier	5 Answering Machines
R ₂	Execution Cashier	3 Service windows
C	¹ Preferential Service Control	15 % of Preferred Customers

¹If there is no preferred customer, the first in line is served. .

This procedure was adopted, because although all clients use the same access door when the agency arrives, the behaviour of the two services is different, justifying the collection made separately.

The customer who goes to the ATM, after performing self-service, leaves the system. The customer who goes to the cashier after his arrival is characterized by his type of service, whether preferential or conventional. If the customer has a preferential service, he goes to his specific cashier and is served. In the same way, the conventional customer is addressed to the conventional execution cashier and is served, if the customer of this service is in the queue and the preferred execution cashier is idle, the conventional customer goes to the preferred cashier to be served. Then, after the service, this type of customer leaves the system.

After the translation of the conceptual model to the simulation model in Arena[®] v15, verification, and validation were performed, following the methodology proposed by Sargent [9, 10]. In this stage, the model was monitored step by step, that is, all incoming customers were accompanied to their service and checked out. It was also found that the results obtained matched those of the real system, through an agency employee.

4. Analysis and Discussion of Results

Six hypothetical scenarios were designed, in order to allow the assessment of different situations in relation to the flow of clients that the agency maybe subject to, in typical situations of its daily life. These scenarios are described below and consider both a situation of increase with a reduction in the arrival rate, as well as an increase in resources.

The reduction in the arrival rate makes it possible to evaluate days with a less intense flow, characteristic of the system's seasonality.

- Scenario 1 - Increasing the capacity of the manual gearbox from one to two, in addition to the preferred gearbox.
- Scenario 2 – 10 % increase in the number of customers arriving at the agency.
- Scenario 3 - Increase of 20 % in the number of customers arriving at the agency.
- Scenario 4 - Increase in the number of preferred customers from 15 % to 25 %.
- Scenario 5 - Increase in the number of ATMs from 5 to 6 resources.
- Scenario 6 – 50 % reduction in the number of customers arriving at the agency.

50 replications were used in the simulations of the respective scenarios. In the analysis of these scenarios, the average and the maximum number of customers waiting in the queues, the average and the maximum waiting times in the queues and the average and maximum occupancy rates of the service resources were considered. The results of the simulations of the respective scenarios are presented in **Tables 2 to 7**.

Scenario 1:

The increase in the number of conventional execution boxes from one to two boxes was simulated. The results show only the rates and times that have changed.

Table 2. Representation of results for scenario 1.

	Actual situation		Scenario 1	
	Medium	Maximum	Medium	Maximum
CONVENTIONAL Execution Box				
Number of customers in the queue	7	34	2	22
Waiting time	15.45 min	78.13 min	2.87 min	33.31 min
Cashier occupancy rate	92.62 %	99.99 %	66.30 %	83.83 %
PREFERENCIAL Execution Box				
Number of customers in the queue	1	6	1	9
Waiting time	3.84 min	51.09 min	2.41 min	47.17 min
Cashier occupancy rate	81.72 %	99.93 %	44.64 %	66.44 %

Results and observations:

From the results obtained in the simulation of this scenario, it was possible to observe that the number of customers in the conventional executive cashier queue, service time and cash occupancy rate decreased. And in the preferred cash register, despite having undergone changes, its impact was minimal. However, in both situations in scenario 1, the law was sometimes not enforced. However, the occupancy rate of the conventional cashier resource went from 99.9 % to 83.8 % in maximum situations. Thus, moving to a more adequate occupancy rate for a human being.

Scenario 2:

A proportional increase in the data collected for the agency arrival rate by 10 % was simulated. The arrival rate increased from 738 to 801 customers, maintaining the same behavior of the data collected for both arrivals.

Table 3. Representation of results for scenario 2.

	Actual situation		Scenario 2	
	Medium	Maximum	Medium	Maximum
CONVENTIONAL Execution Cashier				
Number of customers in the queue	7	34	11	49
Waiting time	15.47 min	78.11 min	21.64 min	99.16 min
Cashier occupancy rate	92.62 %	99.99 %	95.60 %	100 %
PREFERENCIAL Execution Cashier				
Number of customers in the queue	1	6	1	9
Waiting time	3.84 min	51.09 min	4.23 min	45.34 min
Cashier occupancy rate	92.62 %	99.93 %	89.30 %	99.90 %
ELECTRONIC Cashier				
Number of customers in the queue	3	36	5	45
Waiting time	1.31 min	16.90 min	2.40 min	23.33 min
Cashier occupancy rate	76.56 %	85.22 %	83.92 %	94.17 %

Results and observations:

It was observed that in the conventional executive cashier, the number of customers in the queue, the service time and the cash occupancy rate increased a lot. In the preferred executive cash register, the increase was smaller. At the ATM, the impact was great, and there was an increase in all items.

Scenario 3:

In this scenario, the number of customers who arrived was 858, due to the 20 % rate increase.

Table 4. Representation of results for scenario 3.

	Actual situation		Scenorio 3	
	Medium	Maximum	Medium	Maximum
CONVENTIONAL Execution Cashier				
Number of customers in the queue	7	34	16	75
Waiting time	15.46 min	78.12 min	31.51 min	120.70 min
Cashier occupancy rate	92.62 %	99.99 %	98.08 %	100 %
PREFERENCIAL Execution Cashier				
Number of customers in the queue	1	6	2	9
Waiting time	3.83 min	51.08 min	4.65 min	50.05 min
Cashier occupancy rate	81.72 %	99.93 %	95.12 %	100 %
ELECTRONIC Cashier				
Number of customers in the queue	3	36	11	82
Waiting time	1.30 min	16.91 min	5.60 min	40.26 min
Cashier occupancy rate	76.56 %	85.22 %	91.43 %	96.10 %

Results and observations:

As in the previous scenario, the queues increased, but with greater intensity.

Scenorio 4:

This scenario was simulated with the same rate of arrival of customers at the branch, with the percentage of preferred customers increasing from 15 % to 25 %.

Table 5. Representation of results for scenario 4.

	Actual situation		Scenorio 4	
	Medium	Maximum	Medium	Maximum
CONVENTIONAL Execution Cashier				
Number of customers in the queue	7	34	6	34
Waiting time	15.46 min	78.12 min	14.76 min	83.36 min
Cashier occupancy rate	92.62 %	99.99 %	89.61 %	99.98 %
PREFERENCIAL Execution Cashier				
Number of customers in the queue	1	6	2	14
Waiting time	3.83 min	51.08 min	5.36 min	60.99 min
Cashier occupancy rate	81.72 %	99.93 %	85.06 %	99.93 %

Results and observations:

In this scenario, the preferred executive cash register had an increase in all criteria, whereas in the conventional executive cash register there was a decrease in the number of customers in the queue, in the service time and occupancy rate, but not enough to comply with the law.

Scenorio 5:

In this scenario, the behavior of the system was analyzed by increasing the number of ATMs, from 5 to 6 machines.

Table 6. Representation of results for scenario 5.

	Actual situation		Scenorio 4	
	Medium	Maximum	Medium	Maximum
ELECTRONIC Cashier				
Number of customers in the queue	3	36	1	21
Waiting time	1.31 min	16.90 min	0.39 min	10.26 min
Cashier occupancy rate	76.56 %	85.22 %	64.06 %	73.89 %

Results and observations:

In this scenario, it was noticed that there was a drop in all the evaluated points, due to the increase in the resource's capacity.

Scenario 6:

In the last simulated scenario, the situation with which the agency spends during non-peak days was analyzed, so a 50 % drop in arrival rate was estimated. Soon it was possible to analyze what the agency's idleness these days. The number of clients who arrived at the agency to simulate this scenario was 372.

Table 7. Representation of results for scenario 6.

	Actual situation		Scenario 6	
	Medium	Maximum	Medium	Maximum
CONVENTIONAL Execution Cashier				
Number of customers in the queue	7	34	1	18
Waiting time	15.46 min	78.12 min	4.20 min	52.19 min
Cashier occupancy rate	92.62 %	99.99 %	63.82 %	83.47 %
PREFERENCIAL Execution Cashier				
Number of customers in the queue	1	6	0	5
Waiting time	3.83 min	51.08 min	1.23 min	30.43 min
Cashier occupancy rate	81.72 %	99.93 %	26.37 %	49.05 %
ELECTRONIC Cashier				
Number of customers in the queue	3	36	0	5
Waiting time	1.30 min	16.91 min	0.01 min	2.62 min
Cashier occupancy rate	76.56 %	85.22 %	31.95 %	38.18 %

Results and observations:

In this analysis the expected occurred. On normal days, the agency's resource capacity met the needs of the demand, but in the waiting time for conventional and preferred cash, they still exceeded the limit determined by law in some moments of the simulations.

5. Analysis of Scenario

In scenario 1, when there was an increase in the resource capacity of conventional executive cash, the flow of clients improved considerably at the branch, through the reduction of queues and service time. Through this result, the agency is practically complying with the law, but in the preferred cashier the waiting time is still long, so a fourth cashier is needed during peak hours. The occupancy rate also decreased, giving the agency's employee time off to provide better quality care.

In scenario 2, the 10 % increase in the arrival rate influenced the increase in the number of customers who arrived at the branch, so the number of customers in the queues and the occupancy rate also increased in all cashiers, but not significantly, due to these already high. However, in scenario 3, with the 20 % increase, this impact was greater, as the number of customers increased significantly and the cashiers had their occupancy rate of 100 %.

In scenario 4, with the increase in the percentage of preferred customers, the cash flow of this type of service was overloaded, but the load of the conventional service box decreased.

In scenario 5, the number of ATMs was increased from 5 to 6 counters, in this situation the machine occupancy rate decreased even though it was not necessary, since the machines can have their occupancy rate up to 100 %. But due to the arrival rate being very dispersed, in some moments small and in others very large, the addition of this window reduced the queues for this service, which can be seen in Figure 3, providing more satisfaction to the customer in self-service.

In scenario 6, the customer arrival rate decreased by 50 %, to analyze what the agency's situation would be like on non-peak days. For this situation, the capacity of the agency's current resources meets its needs.

The analyzed scenarios can be divided into two classes. First, the scenarios that propose an improvement in the current situation of the agency, such as, for example, the increased capacity for appeal and, later, the scenarios that simulate situations that may occur to worsen the current situation of the agency, such as the increase in the rate of arrival of customers.

However, as observed in the analysis of the scenarios, on peak days changes are needed in the real situation of the agency, so that it is complying with the “queue law” and providing more quality in the service of its clients.

Through the comparisons made between the scenarios presented, those that improved the service conditions at the agency, represented in scenarios 4, 5 and 6, stood out. From these comparisons, it was possible to analyze how the average service time would be, the average number of queued customers and the average occupancy rate according to the best scenarios as proposed by the agency.

6. Conclusions

The model adequately described the behavior of the system under study and proved to be an important tool to assist bank branch managers in making decisions about the operation of resources and to better control the behavior of queues. From the computer simulations, it was possible to evaluate that, in peak days, there is a need to increase the capacity of resources in the studied agency, so that it can be fulfilling the requirements determined by the “queuing law”.

From the initial moment of data collection, it was possible to observe that the occupancy rate of the agency's employees was high and, from the results of the simulations, it was possible to verify that the employees had their occupancy rate beyond normal. If the rate of arrival of customers increases further, as analyzed in some scenarios, it was found that the attendants, in manual cashiers would further increase their respective occupancy rates to extremely high rates, compromising the performance of functions.

It is also worth mentioning the application of Integrated DEFinition Methods of simulation (IDEF-SIM) in conceptual modeling. As indicated in the article by Montevechi, *et al.* [11], the creation of the conceptual model, using appropriate syntax and semantics, makes the computational model translation stage more agile, improving the development of the simulation project as a whole.

References

- [1] Abensur, E.O. (2011). Banking operations using queuing theory and genetic algorithms," *Produto & Produção*, 12(2), 69 - 86.
- [2] Kelton W., Sadowski, R., Sturrock, D.T. *Simulation with Arena*, 4th Edition, McGraw-Hill, New York, USA, 2007.
- [3] Cardoen, B., Demeulemeester, E., Beliën, J. (2010). Operating room planning and scheduling: A literature review, *European journal of operational research*, 201(3), 921-932.
- [4] VanBerkel, P.T., Blake, J.T. (2007). A comprehensive simulation for wait time reduction and capacity planning applied in general surgery, *Health care management Science*, 10(4), 373-385.
- [5] Favaretto, F. (2018). Management of Queues Assisted by Two Servers With Different Assistance Rates, *Sistemas & Gestao*, 13(1), 2-9.

- [6] Paradi, J.C., Zhu, H. (2013). A survey on bank branch efficiency and performance research with data envelopment analysis, *Omega*, 41(1), 61-79.
- [7] Banks, J., Carson II, J., Nelson, B., Nicol, D. *Discrete-event system simulation*, 5th Edition, Prentice Hall, USA, 2009.
- [8] Banks, J. *Handbook of simulation: principles, methodology, advances, applications, and practice*. John Wiley & Sons, 1998.
- [9] Sargent, R.G. (2010). Verification and validation of simulation models," *In Proceedings of the 2010 IEEE winter simulation conference*, Baltimore, MD, USA, 166-183.
- [10] Sargent, R.G. (2013). Verification and validation of simulation models, *Journal of simulation*, 7(1), 12-24.
- [11] Montevechi, J., Leal, F., de Pinho, A., da Silva Costa, R., de Oliveira, M., da Silva, A. (2010). Conceptual modeling in simulation projects by mean adapted IDEF: an application in a Brazilian tech company," *In Proceedings of the 2010 IEEE winter simulation conference*, Baltimore, MD, USA, 1624-1635.
- [12] Gibbons, J.D., Olkin, I., Sobel, M. (1999). *Selecting and Ordering Populations: A New Statistical Methodology*, 2nd Edition, SIAM, USA, 1999.

THE EFFECTS OF WELDING PRESSURE AND REINFORCEMENT RATIO ON WELDING STRENGTH IN DIFFUSION-BONDED AlMg₃/SiCp COMPOSITES


Nilhan ÜRKMEZ TAŞKIN¹, Rifat YAKUT^{2}, Engin ALP³*


In this study, using the diffusion welding method, welded joints were created with AlMg₃/SiCp composite materials, and the mechanical strengths of these joints were examined. The AlMg₃/SiCp composite specimens were cut out of plates produced directly with the semi-solid stir-squeeze casting method and contained 10% SiCp and 20% SiCp reinforcement. To examine the effects of reinforcement ratios on joint strength, specimen couples with the same and different reinforcement ratios were created. To examine the effects of different welding pressures on joint strength, by keeping the welding temperature constant at 580°C, welding was performed under 3 different pressures as 1.5 MPa, 2.5 MPa and 3.5 MPa. By determining the mechanical strengths of the welded joints that were formed by shear test, the effects of reinforcement ratios and welding pressures on joint strength were investigated. As a result of the shear tests applied on the welded specimens, in the specimens that were diffusion-welded, welding quality decreased based on increasing reinforcement ratios, but as the amount of pressure and application duration increased, joint strength increased. As the SiC ratio increased in the joint zones, diffusion became difficult, and weak joints were obtained. The microscopic structure of the joint zone was examined by using optical microscopy and scanning electron microscopy (SEM). It was seen that diffusion welding could be successfully performed in bonding SiCp-reinforced aluminium composites if the suitable welding pressure and duration are selected.


Key words: *Diffusion Welding, Aluminium, SiC, Metal Matrix Composites, Shear Test.*

1. Introduction

Metal matrix composite (MMC) materials are advanced materials that have increasing usage rates in almost all industrial fields, especially defence, automotive and aviation [1-3]. A selected metal or metal alloy matrix material may not only be strengthened with reinforcements in micro/nano dimensions and different forms, but all thermal processes and cold forming methods that can be

¹ Department of Mechanical Engineering, University of Trakya, Edirne, Turkey, (nilhanurkmez@gmail.com)
 <https://orcid.org/0000-0003-2251-3889>

² Department of Energy Systems Engineering, University of Batman, Batman, Turkey, (rifat.yakut@batman.edu.tr)
 <https://orcid.org/0000-0003-0059-3785>

³ Department of Mechanical Engineering, University of Trakya, Edirne, Turkey, (enginalp@hotmail.com)
 <https://orcid.org/0000-0002-1881-1675>

applied on the metal or metal alloy selected as the main matrix material may also be performed [4]. Although MMCs continue to be used and developed in almost every sector, it is one of the main problems that need to be overcome that, in bonding applications of these materials with different metals or themselves, the superior technical properties gained in production cannot be transferred to the joint zone [5-7]. Especially in bonding applications of particle-reinforced composite materials with fusion welding, different densities of the reinforcement material and the matrix material lead to separation of the matrix material that goes into a liquid form and the reinforcement materials in various forms, failure of achieving the reinforcement distribution before the welding process and formation of segregation zones [8, 9]. Besides this, problems such as formation of unwanted reaction products due to processing temperatures higher than the melting temperature, uncontrolled solidifications that form during cooling or cracking of welding zones by excessive reduction of the ductility of the material are also frequently encountered [10-14]. In solid-state welding methods where melting does not take place, it is aimed for the materials to be bonded to preserve their structures and properties before the welding process, while the welding parameters in the diffusion bonding/welding method are temperature, pressure, duration of pressure application and atmosphere, welding zones with adequate mechanical properties may be obtained by providing the optimum values, and this method may also be used to bond MMCs according to the reports in the literature [15-23]. However, welding particle-reinforced aluminium composites is difficult and requires taking special precautions. Systematic work on this issue has been encountered in very few studies, and in this study, the weldability of MMC materials containing different reinforcement ratios was examined. Composite specimen couples with the same and different reinforcement ratios were prepared from AlMg3/SiCp composite blocks, and the prepared specimens were subjected to diffusion welding at the temperature of 580°C and under pressures of 1.5 MPa, 2.5 MPa and 3.5 MPa. To determine the effects of reinforcement ratios on joint strength, shear and microhardness tests were applied, and the microstructures of the bonded-welded joints were examined by optical microscopy and SEM.

2. Experiments

2.1. Materials

The specimen material consisted of AlMg3/SiCp composite material obtained by the semi-solid stir and squeeze casting method. This method is described in a patent held by Urkmez Taskin and Taskin [23, 24]. As the matrix material in the composite materials to be subjected to diffusion welding, the AlMg3 (EN AW 5754) aluminium alloy, which has good weldability, ductility and toughness properties and excellent corrosion resistance especially against seawater, was used. The chemical, mechanical and physical properties of AlMg3 are shown in Tables 1 and 2. As the reinforcement material, SiCp particles with grain sizes of 500 Mesh (~12 µm) were utilized. With semi-solid stirring, the reinforcement material can be homogeneously stirred into the matrix alloy in the desired ratio, and during stirring, problems such as flocculation of the reinforcement, separation from the mixture or precipitation are not encountered. Additionally, as reinforcement addition takes place at a relatively lower temperature than liquid stirring methods, formation of unwanted reaction products is minimized [20, 23, 25].

Table 1. Chemical composition of the AlMg3 alloy [23]

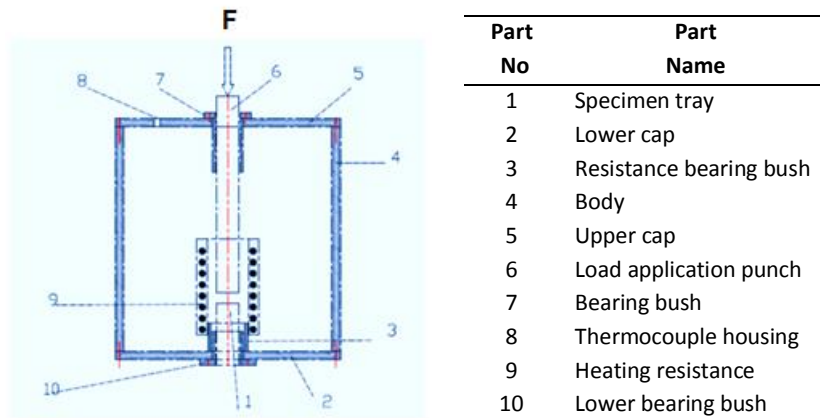
Fe	Si	Mn	Cr	Ti	Cu	Be	Mg	Zn	-
max 0.4	max 0.4	max 0.5	max 0.3	max 0.15	max 0.1	max 0.0003	2.6-3.6	max 0.2	0.1<Mn+Cr<0.6 Al-remainder

Table 2. Mechanical and physical properties of the AlMg3 alloy and composite specimens [23]

	AlMg3	AlMg3/SiCp (vol 10%)	AlMg3/SiCp (vol 20%)
Brinell hardness (HBW): (O) (H111)	45	100	148
Tensile strength (MPa) (F) (H112)	180	210	245
Proof strength (MPa) (F) (H112)	70-80	190	210
Density, g/cm ³	2.66	2.91	2.99
Young Modulus, GPa	68-72	70	76
Shear Modulus, GPa	27	-	-
Melting Temperature, °C	600-640	-	-
A-Min. elongation at fracture (%) (F) (H112)	13-14	12	10

2.2. Diffusion welding furnace and shear test apparatuses

For the diffusion welding process, the diffusion welding furnace whose picture is seen in Figure 1 was designed and produced. The picture of the apparatus that was designed for placing the specimens into the diffusion welding furnace and forming welded joints is shown in Figure 2, while the specimen dimensions are shown in Figure 3.

**Figure 1. Schematic drawing of Diffusion bonding apparatus [25]**

Diffusion welding apparatuses were designed and produced out of steel material with the machining method. The welded specimens [28] had dimensions of 25 mm x 12 mm x 3 mm, while the shear specimens were obtained by cutting these specimens into 3 parts with dimensions of 8 mm x 12 mm x 3 mm (Figure 3). For applying the shear test, a shear apparatus was designed in compliance with the jaws of the INSTRON 1501 universal device and produced (Figure 4).

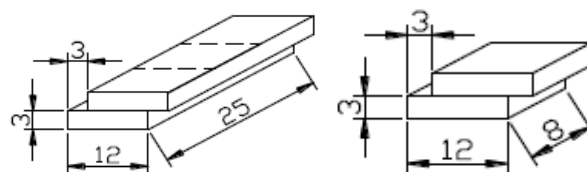
**Figure 2. Diffusion bonding fixture [25]****Figure 3. Dimensions of diffusion and shear test specimens [25]**



Figure 4. Apparatus for the shear test and the diffusion bonded shear test specimen photo [25]

2.3. Diffusion Welding

The diffusion welding specimens were cut out of AlMg3 composite blocks with dimensions of 25 mm x 12 mm x 3 mm using the wire erosion method. The cut specimens were placed onto each other in the welding apparatus shown in Figure 2 and joined. In the diffusion welding process, welding temperature, duration and pressure values were selected by considering studies in the literature. In the trial welding processes, welding was performed when the welding temperature was in the range of 560 - 590°C, and thus, the welding temperature was selected as 580°C. The diffusion welding process was performed under normal atmosphere and without using an intermediate layer. Two different times as 120 min and 180 min were selected as the welding durations. The welding duration started as soon as the temperature of the specimens reached 580°C. During the process, the temperature was constantly controlled. The specimens were cooled by themselves inside the furnace and under a fixed load. The literature was taken as a basis for the pressure values to be applied in the diffusion welding process. For the diffusion welding of Al-based SiC particle-reinforcement composite materials, by conducting trials in the interval of 1-5 MPa, the lower pressure value for bonding to start was determined as 1.5 MPa, while the upper pressure value where plastic deformation started was determined as 3.5 MPa. In the same conditions, by performing welding procedures with the specified parametric values on the unreinforced matrix alloy, the reference specimens were prepared. Using three different pressure values and two different durations, 2 specimens for each case were joined by diffusion welding. The welding pressures and times used in this study are shown in Table 3 [23, 26].

Table 3. Diffusion bonding parameters used in this study

Material Combination	Temperature (°C)	Welding Pressure (MPa)	Welding Time (min)
AlMg3- AlMg3	580	1.5 2.5 3.5	120 180
AlMg3-AlMg3/SiCp, (vol 10%)			
AlMg3-AlMg3/SiCp, (vol 20%)			
AlMg3/SiCp, (vol 10%)-AlMg3/SiCp, (vol 10%)			
AlMg3/SiCp, (vol 20%)-AlMg3/SiCp, (vol 20%)			

2.4. Characterisation

Each of the welded specimens was divided into three equal parts, and a total of 6 shear test specimens with the same conditions were prepared. The surfaces of the specimens to be welded were prepared with 100, 200 and 400 mesh sandpapers, and they were left in pure alcohol before the procedure. To determine the bond strength of the diffusion welded specimens, shear and hardness tests were applied. The shear tests were performed at a progression rate of 0.5 mm/min with an INSTRON 8501 Universal test device by applying force in the compression direction. The microhardness tests were performed on the basis of the DIN EN ISO 6507-1 standard.

The welded specimens were firstly divided lengthwise into two and embedded in Bakelite. The specimens that were subjected to standard sanding and polishing procedures were finally subjected to

etching. The metallographic examinations of the welded specimens were carried out by an optical microscope and by SEM.

3. Results and Discussion

The specimens that were bonded by diffusion welding were firstly macroscopically examined, and whether or not the welding pressure caused a deformation was determined. As seen in Table 4, a preliminary study was carried out under 1.5 MPa, 2.5 MPa and 3.5 MPa of pressure and 120 min and 180 min of welding duration to determine the suitable pressure and duration. As the results obtained at the welding durations of 120 min and 180 min in the preliminary study were in parallel to each other, it was found appropriate in this study to use the welding duration of 180 min. Whether or not joint formation took place and whether or not deformation was observed are shown in Table 4 regarding the material couples' welding procedure in the preliminary study. No deformation was observed in any of the specimen couples that were welded under the pressures of 1.5 MPa and 2.5 MPa.

Table 4. Diffusion bond and deformation formation according to the applied pressure and time

Material couple	Temperature (°C)	Pressure (MPa)	Time (dk)	Deformation	Bonding
AlMg3 - Al Mg3	580	1.5	120	-	-
			180	No	+
		2.5	120	No	-
			180	No	+
		3.5	120	Yes	+
			180	Yes	+
Al Mg3 - AlMg3/SiCp (10%)	580	1.5	120	No	-
			180	No	-
		2.5	120	No	-
			180	No	+
		3.5	120	Partially	+
			180	Partially	+
AlMg3 - AlMg3/SiCp (20%)	580	1.5	120	No	-
			180	No	-
		2.5	120	No	-
			180	No	+
		3.5	120	Partially	+
			180	Partially	+
AlMg3/SiCp (10%) - AlMg3/SiCp (10%)	580	1.5	120	No	-
			180	No	-
		2.5	120	No	-
			180	No	+
		3.5	120	No	+
			180	Yes	+
AlMg3/SiCp (20%) - AlMg3/SiCp (20%)	580	1.5	120	No	-
			180	No	-
		2.5	120	No	-
			180	No	+
		3.5	120	No	+
			180	No	+

Deformation took place in the non-reinforced specimen couples and on the non-reinforced side in cases of welding with 10% and 20% SiCp-reinforced composites under the pressure of 3.5 MPa. No

deformation was observed on the reinforced sides. Under the same pressure, deformation did not occur after the welding process of 20% SiCp and 10% SiCp-reinforced composites. No deformation was observed in the 20-20% AlMg3/SiCp specimen couple under 2.5 MPa. There was negligible deformation in the 10-10% AlMg3/SiCp specimen couple under 3.5 MPa. The pressure value of 3.5 MPa was determined as the upper boundary of pressure in the diffusion welding process of 10% SiCp-reinforced specimens. There was no deformation in the 20-20% AlMg3/SiCp specimens under 3.5 MPa.

The welded joints were examined under an optical microscope and by SEM. Figure 5 shows that, in the optical microscopic examinations of the specimens processed under a pressure of 1.5 MPa for 120 min, the welding zone lines were noticeable, and gaps and welding lines could not be eliminated in this zone.

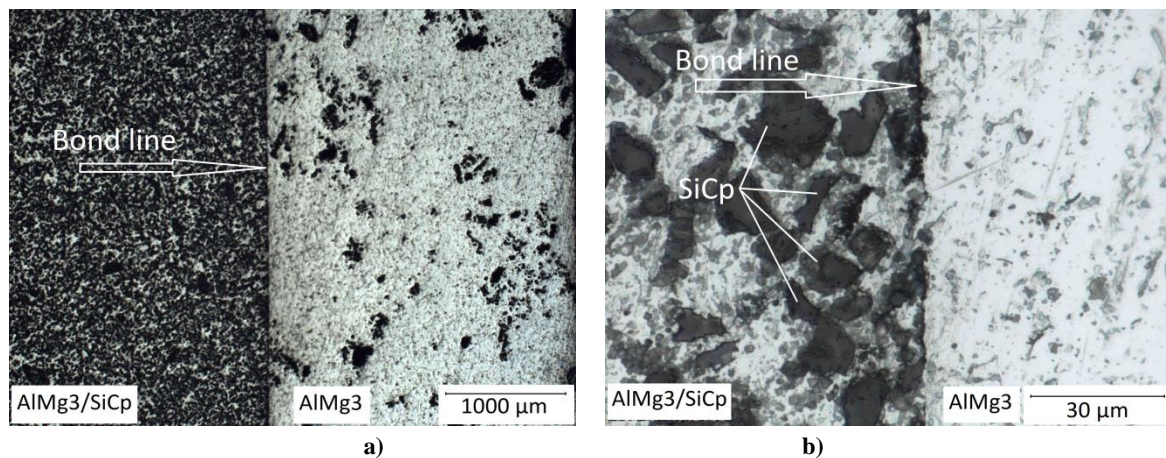


Figure 5. Optical microscope images of the AlMg3/SiCp (20%)- AlMg3 couple diffusion welded for 180 min under 1.5 MPa. a) x2.5, b) x100

Figure 6a shows that there were gaps and pores of $\sim 1-5 \mu\text{m}$ dimensions on the joint line in the bonding zones of the AlMg3/SiCp (vol.20%) - AlMg3specimens that were bonded under a pressure of 2.5 MPa for 120 min, whereas Figure 6b shows that gaps and pores decreased on the joint line in the bonding zones of the AlMg3/SiCp (vol.20%) - AlMg3specimens that were bonded under a pressure of 2.5 MPa for 180 min.

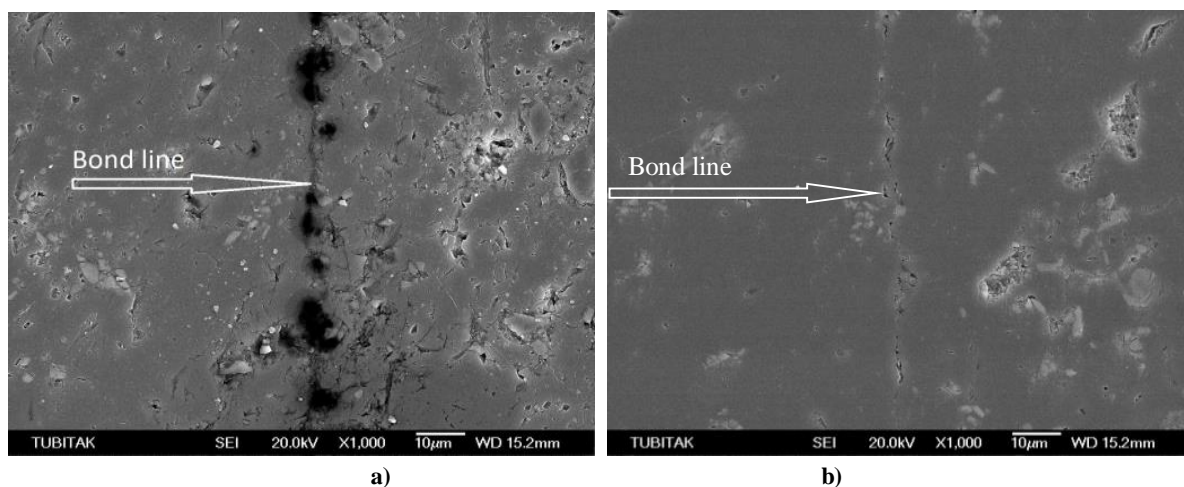


Figure 6. SEM images of the bonded joints of AlMg3/SiCp (20%) - AlMg3 samples under a) 2.5 MPa pressure and 120 min. b) 2.5 MPa pressure and 180 min.

Figures 7a and 7b show the bonding zones of the AlMg3 / SiCp (vol.20%)-AlMg3 couple that were bonded for 180 min under a pressure of 3.5 MPa. Bonding occurred in the welding zone, and the line in the interface mostly became unnoticeable.

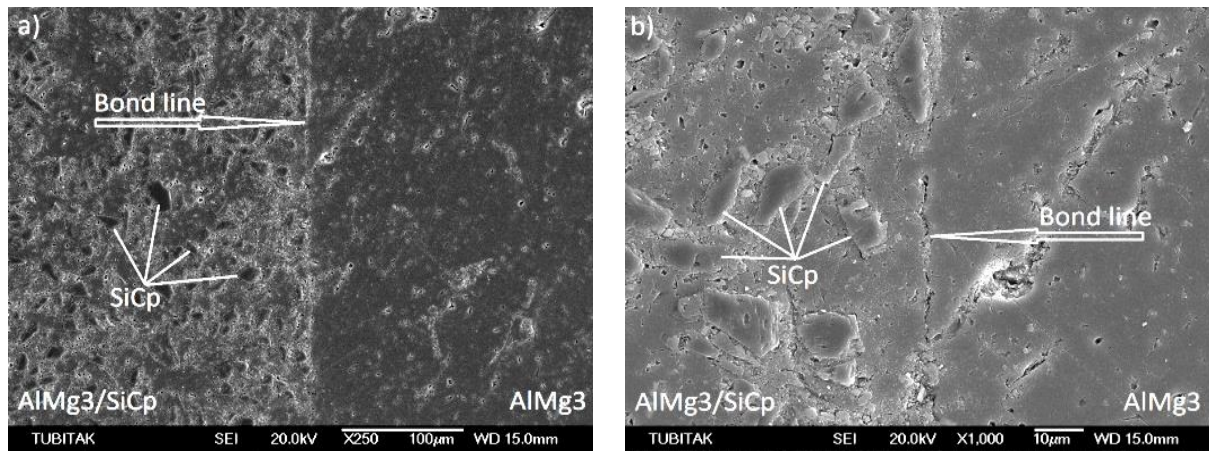


Figure 7. Optical microscope and SEM images of the AlMg3/SiCp (20%) - AlMg3 couple diffusion-welded for 180 min under a pressure of 3.5 MPa. a) X250, b) X1000

As the diffusion welding pressure increased, there were increases in the shear strength of all specimens where bonding occurred. Moreover, in the welding process of the composites with a high reinforcement ratio, the reinforcement particles probably posed an obstacle to diffusion, and lower results were obtained in comparison to the shear strength of the non-reinforced material. When the joined specimens included a high ratio of reinforcement, for example, in the case that both parts included 20% of reinforcement, and 1.5 MPa of pressure and 120 min of time were applied, bonding did not occur completely, and very low shear strength values were obtained. With the increase in the welding time and pressure, bonding occurred in the composite materials with high reinforcement ratios, and the shear strength values increased. The highest shear strength values were obtained in the diffusion welding process of the non-reinforced specimens, while as the welding pressure that was applied increased, the shear strength values showed an increase. These results were in good agreement with the studies by Cooke et al. (2012) and Zhang et al. (1999). In both these studies, it was stated that the strength of diffusion bonded joints decreases with increasing SiCp volume percentage. In the welding of the composite materials with the welding parameters in this study, the highest shear strength was obtained in the specimen couple where AlMg3 / SiCp(vol.10%)-AlMg3 were bonded for 180 min under a pressure of 3.5 MPa. If the shear test results are interpreted, it is seen that the reinforcement rate affected the quality of welding in the diffusion welding process of the particle-reinforced composite materials. In this study that was in parallel with similar studies in the literature, the SiCp particles in the bonding zone affected the success of diffusion welding negatively, and joints with low strengths were obtained. Increased welding pressure and time led to an increase in joint strength [26, 27]. The lowest shear strength was obtained at a 1.5 MPa bonding pressure in the AlMg3 / SiCp (volume 20%) composite couples, and the highest shear strength was obtained at a 3.5 MPa bonding pressure in the AlMg3 / SiCp(vol.10%)-AlMg3 couples. For the bonded joints produced at the bonding time of 120 minutes, not enough diffusion bond was provided for all samples. Figure 8 shows the plot of the change in the shear strength of the samples with the diffusion bonding pressures in 180 minutes of bonding time.

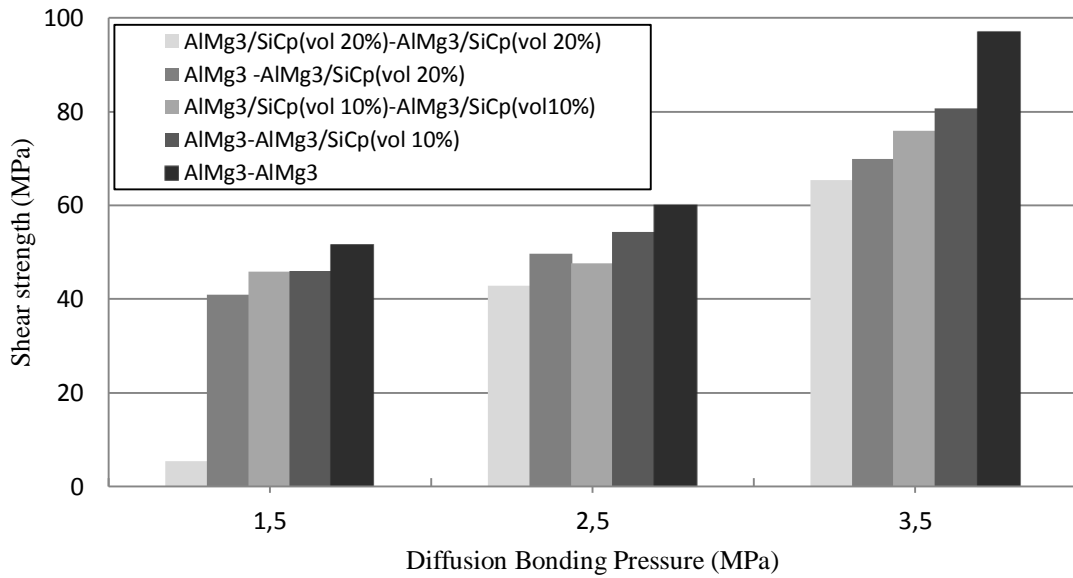
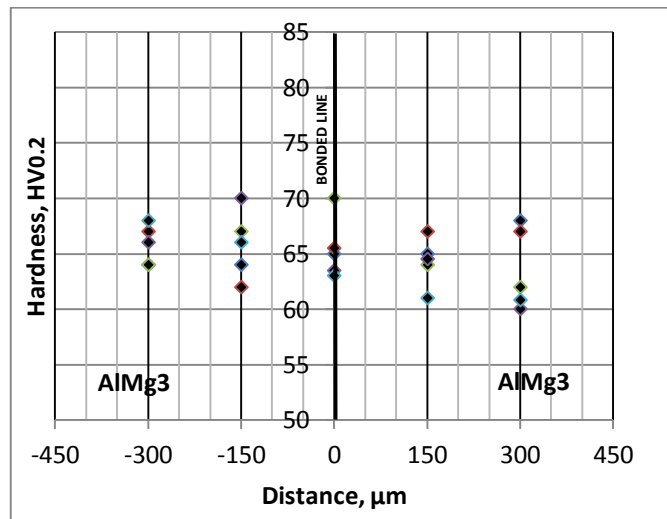
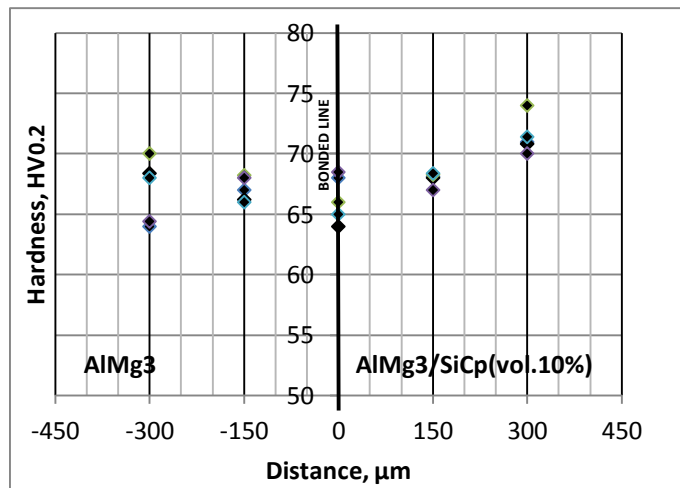


Figure 8. Shear test results at different bonding pressures and the welding duration of 180 min



(a)



(b)

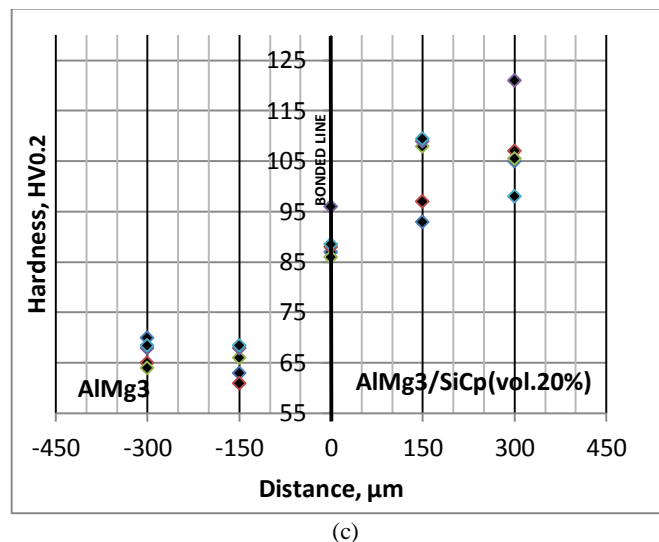


Fig.9. Hardness profiles across the bonded line, (a) AlMg3-AlMg3 (b) AlMg3-AlMg3/SiCp (vol.10%) (c) AlMg3-AlMg3/SiCp (vol.20%)

The microhardness profiles for across the bond line for the AlMg3/AlMg3 and AlMg3/SiCp-AlMg3 couples (3.5 MPa/180min) are shown in Fig. 9. In all conditions, the hardness values in all regions were higher than the hardness values of the base (AlMg3) materials. Fig. 9a shows the cross-section of the bond line of the AlMg3-AlMg3 couple. The hardness profile shows the almost homogeneous distribution in the bond regions of these samples. The highest hardness value as 70 HV0.2 was measured in this sample. In welded joints formed used the AlMg3/SiCp composites and the AlMg3 matrix alloys, the hardness values in the bond region were measured as higher than the matrix material's hardness values. The highest hardness value on the side of the AlMg3/SiCp (vol.10%) composite was found as 74 HV0.2, and the hardness value on bonded line was 68 HV0.2 (Fig. 9b). Fig. 9c shows the cross-section of the bond line of the AlMg3-AlMg3/SiCp (vol%20) couple. In this sample, a hardness peak was observed close to the interface on the composite side. When the holding time was increased from 120 min to 180 min, hardness was also increased. Likewise, by increasing the welding pressure from 2.5 MPa to 3.5 MPa, hardness was also increased. It was found that the side of the AlMg3/SiCp (vol.20%) composite at a 3.5 MPa pressure had the maximum hardness value as 124 HV0.2. Moreover, the hardness value on the AlMg3 matrix alloy was 68.5 HV0.2, and the hardness value on the bonded zone was nearly the same values. These results were in good agreement with the studies by Muratoglu et al. (2006) and Mollaoglu et al. (2006). In both these studies, it was stated that the hardness values of diffusion bonded joints increase by increasing SiCp volume percentage, and when the bonding time increases, the bonding strength increases, too. Bonding time has a significant effect on the diffusion bonding process.

4. Conclusions

The following conclusions may be drawn from this study:

- The AlMg3 / SiCp - AlMg3 couples were successfully diffusion-bonded for all welding pressures at a 580°C bonding temperature for 180 min holding times. The AlMg3 couples

were bonded with diffusion at lower pressures in comparison to the composite samples. It was observed that their shear strength was higher than the composite couples.

- b) The shear strength of the AlMg₃ / SiCp (vol.20%) composite couples was lower than the AlMg₃ / SiCp (vol.10%) and AlMg₃ couples at all pressures. As the reinforcement rate was increased in the composite samples, deformation decreased at all bonding pressures.
- c) As the diffusion pressure and bonding time increased, the shear strength increased in all samples.
- d) The strength of the diffusion-bonded joints decreased with increasing SiCp volume percentage. The hardness values of the diffusion bonded joints increased with increasing the SiCp volume percentage. Moreover, bonding time had a significant effect on the diffusion bonding process.

5. References

- [1] Zhang X.P., Ye I., Mai W.Y., et.al., Investigation on Diffusion Bonding Characteristics of SiC Particle Reinforced Aluminum Metal Matrix Composites (Al/SiCp MMC) Composites. Part A: Appl. Sci.Manuf. 30, 12, 1415-1421, 1999.
- [2] Garg, P., Jamwal, A., Kumar, D., Sadasivuni, K. K., Hussain, C. M., Gupta, P. (2019). Advance research progresses in aluminium matrix composites: Manufacturing & applications, *Journal of Materials Research and Technology*, 8 (5), 4924–4939.
- [3] Rosso, M. (2006). Ceramic and metal matrix composites: Routes and properties, *Journal of Materials Processing Technology*, 175 (1-3), 364–375.
- [4] Kaczmar, J. W., Pietrzak, K., Wlosinski, W. (2000). The production and application of metal matrix composite materials, *Journal of Materials Processing Technology*, 106 (2000), 58–67.
- [5] Ellis, M. B. D. (2007). Joining of Al-based metal matrix composites - A review, *Materials and Manufacturing Processes* 11 (1), 45–66.
- [6] Arık, H., Aydın, M., Kurt, A., Türker M. (2005). Weldability of Al₄C₃-Al composites via diffusion welding technique, *Materials and Design*, 26 (6), 555-560.
- [7] Uluköy, A., Onar V., Kaplan, Y. (2015). The microstructure and hardness properties analysis of welded aluminum matrix material reinforced with sic using different currents and forms of welding” *Pamukkale University Journal of Engineering Sciences*, 21 (8), 365-370.
- [8] Karakoç, H., Çıtak, R., (2017). Study on weldability of b₄c reinforced aluminium composite materials with TIG welding, *El-Cezeri Journal of Science and Engineering*, 4 (3), 584-592.
- [9] Storjohann, D., Barabash, O.M., Babu, S.S., David, S.A., Sklad, P.S., Bloom, E.E., (2005). Fusion and friction stir welding of aluminum-metal-matrix composites, *Metallurgical and Materials Transactions A-Physical Metallurgy and Materials Science*, 36 (11), 3237–3247.
- [10] Lean, P. P., Gil, L., Urena, A., (2003). Dissimilar welds between unreinforced AA6082 and AA6092/SiC/25p composite by pulsed-MIG arc welding using unreinforced filler alloys (Al-5Mg and Al-5Si), *Journal of Materials Processing Technology* 143–144 (2003), 846–850.
- [11] Mollaoğlu, H., Diffusion bonding of SiC particulate reinforced Al metal matrix composites, Yildiz Technical University, Institute of Science and Technology, Master of Science Thesis, İstanbul, 2004.
- [12] Buytoz, S., The investigation of weldability of al matrix - Al₂O₃ reinforced composite materials with solid state bonding methods, Fırat University, Institute of Science and Technology, Master of Science Thesis, Elazığ, 1999.

- [13] Çalgılı, U., The investigation of joinability of with hot pressing manufactured AlSiMg-SiCp reinforced composites, Fırat University, Institute of Science and Technology, Master of Science Thesis, Elazığ, (2005).
- [14] Çelik, S., An investigation of diffusion welding parameters for pure aluminum and copper in inert gas, Balıkesir University, Institute of Science and Technology, Ph.D. Thesis, Balıkesir, 1996.
- [15] Kaya, M., Kılıç, M., Kırık, I., Karakurt, E. M., Gülenç, B., (2017). Diffusion bonding between Ti-6Al-4V alloy and interstitial free steel, *Mat.-wiss. u. Werkstofftech.*, 48, 1–5.
- [16] Dikbaş, H., The investigation of bondability of Ni-Ti alloys by powder metallurgy method with the diffusion bonding, Fırat University, Institute of Science and Technology, Master of Science Thesis, Elazığ, (2005).
- [17] Erden, İ. O., Investigation of weldability of Al-Si₃N₄ composite materials by diffusion welding, Gazi University, Institute of Science and Technology, Master of Science Thesis, Ankara, 2005.
- [18] Mollaoğlu, H., Diffusion bonding of SiC particulate reinforced Al metal matrix composites, Yıldız Technical University, Institute of Science and Technology, Master of Science Thesis, İstanbul, 2004.
- [19] Çelik, Y. H., Kılıçkap, E., Yenigün, B. (2018). The effect of contact pressure and B₄C ratio on hardness and wear behaviours in Al-matrix composites produced by PM method, *Science and Eng. J of Fırat Univ.*, 30 (1), 33-40.
- [20] Yakut R., Ürkmez Taşkın, N. (2019). Production of AA7075/B₄C composite materials by the semi-solid stirring method, *European Journal of Technique (EJT)*, 9 (2), 230–240.
- [21] Adin, H., Seven, B., Çakar, F., Yıldırım, H., Ataş, İ. (2017). Experimental determination of the mechanical properties of composite materials produced with particle reinforced adhesives, *European Journal of Technique (EJT)*, 7 (2), 158–164.
- [22] Yakut R., Ürkmez Taşkın, N. (2018). Production of AA7075 / B₄C / SiC hybrid composite materials by semi-solid stirring method, *1st International Engineering And Technology Symposium (1st Iets) 03–05 May, Batman / Turkey*
- [23] Ürkmez, N., Production of AlMg₃/SiCp composites and investigations of variations in mechanical properties, Yıldız Technical University, Institute of Science And Technology, Ph.D. Thesis, İstanbul, 2004.
- [24] Ürkmez Taşkın, N., Taşkın, V. (2015). Continuous Composite Metal Foam production and method and device for stirring particle reinforced composite metal, *European Patent Office, Espacenet Patent Publication Number: WO2015094139A2*
- [25] Alp, E., Investigation of weldability of AlMg₃/SiCp composites, Trakya University, Institute of Science and Technology, Master of Science Thesis, Edirne, 2008.
- [26] Muratoğlu, M., Yılmaz, O., Aksoy, M. (2006). Investigation on diffusion bonding characteristics of aluminum metal matrix composites (Al/SiCp) with pure aluminum for different heat treatments, *Journal of Materials Processing Technology*, 178, 211-217.
- [27] Özdemir, U., Microstructural and mechanical characterization of diffusion bonded TiAl and Ti6Al4V alloys, Mustafa Kemal University, Institute of Science and Technology, Master of Science Thesis, Hatay, 2003.
- [28] Cooke, Kavian & Khan, Tahir & Oliver, Gossett. (2012). Transient liquid phase diffusion bonding Al-6061 using nano-dispersed Ni coatings. *Materials & Design*. 33. 469-475. 10.1016/j.matdes.2011.04.051.

MIXING OF BODIESELS PRODUCED FROM DIFFERENT SOURCES WITH JET FUEL AND COMPARISON OF FUEL PROPERTIES OF THE BLENDS


Fevzi YAŞAR^{1*}

Air quality standards set forth by the Clean Air Act and its amendments have established guidelines for the reduction of harmful ground-level emissions from the aviation sector. The aviation industry raises environmental concerns as it is vulnerable in the event of an energy crisis and also consumes fossil fuels. In this sector, when using biomass based fuels instead of fossil fuels, possible energy crises will be prevented and greenhouse gas emissions will also be reduced. This is a kind of biomass energy (bioenergy), biodiesel, can be used in diesel engines as an alternative fuel. Biodiesel is produced from renewable resources such as vegetable and animal fats. Biodiesel is sustainable, environmentally friendly, non-toxic, an alternative fuel for diesel engines. In this study, biodiesel fuels were produced from different feedstocks (canola oil, algae oil, sunflower oil, cottonseed oil, and waste cooking oil) and then blended with jet fuel (JP-8) at various ratios including 5-10-15-20% (on volume basis, v/v). The some critical fuel properties of the blends were compared with each other and those of the jet fuel. Considering the properties of the biodiesel used, it is seen that the fuel with the highest density, viscosity, flash point and freezing point was waste cooking oil (WCO) (892 kg/m³, 4.66 mm/s², 180 °C, -8 °C). Accordingly, WCO biodiesel blends were found to be higher than others. In addition, it was determined that the algae biodiesel used in the study had the best density (881 kg/m³), flash point (150 °C) and freezing point (-14 °C), and cotton biodiesel met the most suitable viscosity value.

Key words: *Jet fuel, biodiesel, blend, fuel properties*

1. Introduction

Energy, which is of primary importance in ensuring the development, and welfare of countries, has recently become one of the most strategic tools in the international system. Energy policies address issues such as the safe access of energy resources to international markets in the short term, supply and pricing, and development plans and policies in the long term. Although there are no problems in terms of reserves in oil and natural gas supply for the next few decades, issues such as searching, producing, and delivering new reserves seem to remain the main problem areas affecting international relations. Population and income growth are the main factors that cause increase in energy consumption. The recent population growth, especially in non-Western countries, and the rapid industrialization and

¹ Vocational School of Technical Sciences, Department of Chemistry and Chemical Process Technology, Batman University, 72100, Batman, Turkey, (fevzi.yasar@batman.edu.tr),  <https://orcid.org/0000-0003-3504-9157>

urbanization of these countries have led to major increases in primary energy demand such as oil and natural gas. As the world economy grows, the desire for fast delivery of products for trade countries has made it important to use the existing energy resources effectively and then to obtain cheap and clean energy resources. In order to meet the energy needs, imported energy sources have been used, and high-cost investments based on fossil-based fuel imports have been made, and foreign dependency in energy has reached serious levels for many countries. The aviation industry is a fast growing sector, which is the only network that provides the possibility of rapid worldwide transport. Air transport is becoming more popular in world trade, tourism and travelling, the connection of companies for meetings and conferences, and many other businesses. It is a convenient way of bridging large distances in relatively short time [1]. One of the most important factors that determines the transportation cost in the aviation sector is the fuels used in planes. On the other hand, as a result of the increase in fossil fuel consumption in the aviation sector, it causes environmental problems due to the harmful and toxic gases such as CO₂, SO₂ and NO_x [2, 3]. By 2020, global international aviation emissions are projected to be around 70% higher than that of 2005; and the International Civil Aviation Organization (ICAO) forecasts that by 2050 they could grow by a further 300-700% [4]. The International Energy Agency (IEA) has reported that the world will need 50% more energy in 2030 than it needs today due to the transportation sector becoming as the second largest energy consuming sector after the industrial sector. Mostly, transportation sector sourced from fossil fuels consumes more than 90% of petroleum while a small amount is sourced from natural gas and renewable energy sources [9, 10]. As the demand for energy increases, the conventional oil and natural gas reserves that can be commercially exploited will diminish after approximately 41.8 and 60.3 years, respectively [11]. Therefore, in order to limit the negative consequences of climate change, priority and significance should be given to new and renewable energy sources, not fossil fuels [12]. For many years, efforts have been made to use alternative fuels to eliminate these problems in road vehicles, and countries encourage the use of biofuels both to protect the environment and to reduce their dependence on import petroleum. Similarly, in the aviation sector, this has led to the need to identify this potential and examine the availability of alternative fuels. In the studies carried out for this purpose, the necessity of the use of biofuels in the aviation industry and the characteristics of alternative fuel types that can be used were examined. As a result, thanks to the fuel systems and unique designs of the aircraft to be produced in the future, it is evaluated that alternative fuels that can be used in internal combustion engines and gas turbines may have similar properties, and this will contribute to economic development and environmental protection by creating a fuel union in road and air transport [13]. However, it is a known fact that fuel also significantly affects the potential of reducing greenhouse gas emissions. Four certified pathways to produce bio-jet fuels are described here and shown in Fig.1.

Among these alternative methods and fuels, blending and using biodiesel with different proportions of jet fuels has become very popular recently. Commercial aviation fuel is fossil-sourced, and the concern that fuels may perish over time raises a number of concerns regarding the safety of fuels. In addition, jet fuel production studies from solar energy and carbon dioxide are thought to take quite a long time. This requires aviation industry stakeholders to have cost-effective, environmentally friendly and sufficient fuel supplies that can be used in existing and future fleets. As a result, various airline companies, aircraft manufacturers and engine manufacturers, as well as other industry participants, are collaborating with biofuel suppliers to test renewable jet fuel mixtures in existing engines both on the ground and in the sky [15].

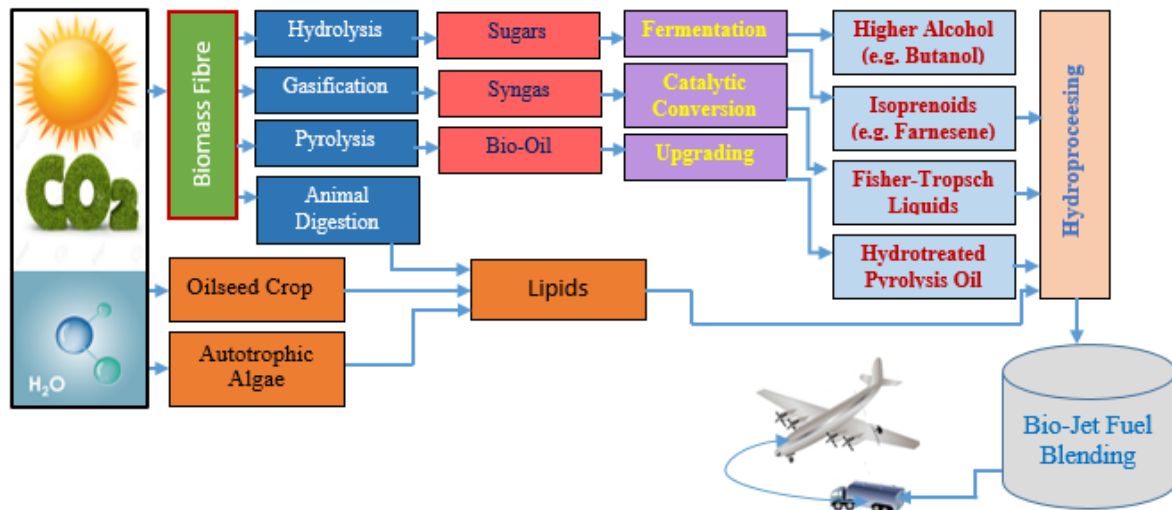


Figure 1. A simplified schematic diagram of different technology pathways to bio-jet fuel [14]

Over the past five years, several commercial routes have been flown using blends of biofuels and conventional jet fuel. For instance, in 2008, Air New Zealand flew a Boeing 747 from Auckland to Wellington with one of its four engine fuelled with a blend of 50% hydro-processed jatropha seeds and 50% Jet A1. In late 2011, KLM Royal Dutch Airlines launched a series of 100 flights from Amsterdam to Paris powered by a 50% blend of camelina-derived biofuel, followed by 100 more flights in February 2012 using cooking oil-derived biofuel. Similarly, between July and December 2012, Lufthansa performed a long-term evaluation of Hydro-processed Esters and Fatty Acids (HEFA) kerosene on 1187 flights from Hamburg to Frankfurt [16]. The International Air Transport Association aspires to use 6% biofuel blends in aircraft by 2020 and several test flights have already been performed using blends of conventional jet fuel and bio-jet fuel from algae, camelina, jatropha and other plant-based feedstocks for both commercial airliners and military aircraft. Sustainability remains the main concern in order for biofuels to become the source of jet fuel; notably, the ability for the biofuel to conserve ecological balance, productivity, biodiversity and natural resources. Use of biofuels with jet fuels is undoubtedly expected to be an improvement in reducing emissions [17]. Payan et al. [18] addressed environmental studies of alternative fuels and analysed the relative greenhouse gas (GHG) emission reduction for biomass sources compared to conventional jet fuel based on fossil sources and its blend. The results are summarized in Table 1.

As can be seen in Table 2, when compared to conventional fossil fuel sources, while raw material having the highest GHG emission is Jatropha with 42%, the raw material having the lowest emission is found to be Wood Residues with 148%. The increase in trade, through both inter-region and inter-country, demonstrates the importance of the transportation sector in terms of country economy with globalization. Airway is one of the means, which is used for carrying and transporting both people and products or services from one place to another with various purposes. The global fuel consumption by commercial airlines has increased each year since 2009, and is predicted to reach an all-time high of 98 billion gallons in 2020. While the great recession created a slight decrease in consumption over 2008 and 2009,

by 2011 consumption levels had recovered to exceed pre-recession levels. Fig. 2 shows the total fuel consumption of commercial airlines worldwide between 2005 and 2020 [19]

Table 1. Relative GHG emission reductions for biomass sources compared to fossil sources [18].

Biomass Feedstock	GHG Emission Reduction Compared to Conventional Jet Fuel (%)
Jatropha	42
Canola	44
Corn Stover	55
Switchgrass	63
Miscanthus	72
Camelina	86
Waste Fat	87
Algae	124
Sweet Sorghum	133
SRCW	145
Wood Residues	148

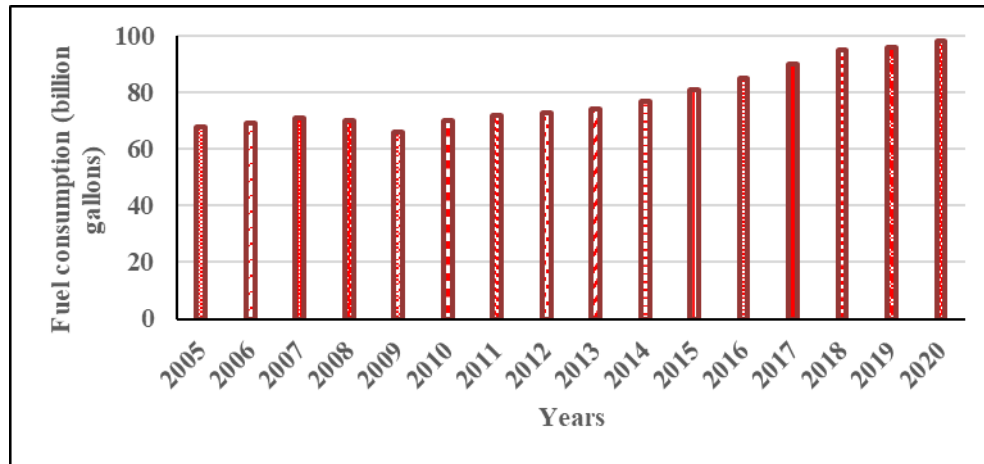


Figure.2. Total fuel consumption of commercial airlines worldwide between 2005 and 2020 (in billion gallons)

2. Materials and Methods

The fuel properties of biodiesel vary greatly depending on the fatty acid distribution [20]. The most important features are ignition ability, cold flow properties and oxidative stability. Although saturation and fatty acid distribution in lipids do not have a significant effect on the production of biodiesel by the transesterification method, it is directly associated with the properties of the fuel. For example, biodiesel fuels produced from saturated oils have a high cetane number and very strong oxidative stability, while exhibiting lower combustion properties. Biodiesel fuels produced from saturated fat tend to gel at ambient temperatures. Biodiesel produced from long chain unsaturated fatty acid rich raw material has good cold flow property. However, the tendency of these fatty acids to oxidize is very high when compared to others. Therefore, problems may arise during the long-term storage of biodiesel [21].

The analyses of fatty acid composition of the oils were conducted by Dicle University Science and Technology Application and Research Centre (DÜBTAM). The fatty acid profile of the vegetable oils used in this study is summarized in Table 2.

Table 2. Fatty acid compositions of oils (wt.%)

Fatty acid	C:D	Closed Formula	Algae	Sunflower	Cotton	Canola	WCO
Lauric	C12:0	C ₁₂ H ₂₄ O ₂	---	---	---	---	---
Myristic	C14:0	C ₁₄ H ₂₈ O ₂	---	0.075	0.686	0.045	0.13
Palmitic	C16:0	C ₁₆ H ₃₂ O ₂	15.64	5.933	21.468	6.234	8.80
Palmitoleic	C16:1	C ₁₆ H ₃₀ O ₂	0.324	0.144	0.556	0.342	---
Stearic	C18:0	C ₁₈ H ₃₆ O ₂	2.108	3.442	2.607	2.486	4.20
Oleic	C18:1	C ₁₈ H ₃₄ O	54.89	36.224	18.214	61.455	45.15
Linoleic	C18:2	C ₁₈ H ₃₂ O ₂	19.56	52.945	55.446	22.124	39.74
Linolenic	C18:3	C ₁₈ H ₃₀ O ₂	4.876	0.383	0.145	5.108	0.20
Arachidic	C20:0	C ₂₀ H ₄₀ O ₂	2.240	0.230	0.062	1.432	0.43
Behenic	C22:0	C ₂₂ H ₄₄ O ₂	0.334	0.456	0.144	0.366	0.75

The algae oil used in the study was obtained from a commercial company (Soley Biotechnology, Istanbul, Turkey) and the other oils were purchased from a local supermarket. In order to produce fuel suitable for the standard, Sigma-Aldrich's 99.7% purity methyl alcohol and as a catalyst Merck brand 99.9% purity potassium hydroxide (KOH) were purchased from commercial companies. In accordance with our previous studies and literature information, 65 °C temperature, 60min reaction time, 1% catalyst and 20% of methyl alcohol were determined as optimum conditions; and transesterification reactions of all oils were performed under these conditions. The properties of the biodiesel fuels produced were analysed at TÜPRAŞ Batman Refinery fuel analysis laboratory and Batman University Technical Sciences Vocational School Refinery and Petro-Chemistry Technology Program Laboratory.

3. Results and Discussion

Fuel properties of jet fuel (JP-8) and biodiesel blends mixed in different proportions are given in Table 3. Density is an important fuel property directly related to aircraft performance. Some fuel-gauging systems give readings proportional to the speed of sound; therefore, this property is also an important fuel parameter. The speed of sound in a material characterizes its susceptibility to pressure changes at constant entropy. Therefore, while density is a static property, the speed of sound provides information about effects relating to the distribution of energy on a molecular scale [22]. When biodiesel produced from different oils at the rates of 5%, 10%, 15% and 20% is added to jet fuel, the density values of the blends change as in Figure 3.

Table 3. Fuel properties of jet fuel, biodiesel fuels and their blends at various blends

FUELS		PROPERTIES			
		Density 15°C (kg/m ³)	Kinematic Viscosity 40 °C (mm ² /s)	Flash Point (°C)	Freezing Point (°C)
Raw	Jet Fuel	795	1.17	43.0	-55.1
	Canola	883	4.48	172.0	-11
	Algae	881	4.55	150.0	-14
	Sunflower	885	4.28	178.0	-7
	Cotton	881	4.22	175.0	-13
	WCO*	892	4.66	180.0	-8
%5B	Canola	800	1.23	55.5	-29.7
	Algae	801	1.25	48.0	-25.7
	Sunflower	803	1.23	53.5	-32.6
	Cotton	812	1.34	55.5	-21.4
	WCO*	818	1.54	60.1	-16.5
% 10B	Canola	803	1.33	60.2	-25.3
	Algae	805	1.36	49.5	-21.2
	Sunflower	809	1.32	56.2	-28.4
	Cotton	816	1.38	60.3	-18.5
	WCO*	823	1.58	65.5	-13.7
%15B	Canola	809	1.42	64.8	-21.4
	Algae	811	1.44	50.5	-18.6
	Sunflower	816	1.43	59.5	-24.3
	Cotton	825	1.52	62.7	-15.2
	WCO*	836	1.77	68.3	-9.7
% 20B	Canola	816	1.56	68.4	-17.8
	Algae	818	1.59	51.5	-15.2
	Sunflower	824	1.55	63.7	-17.1
	Cotton	830	1.64	68.5	-11.3
	WCO*	840	1.95	70.7	-5.8

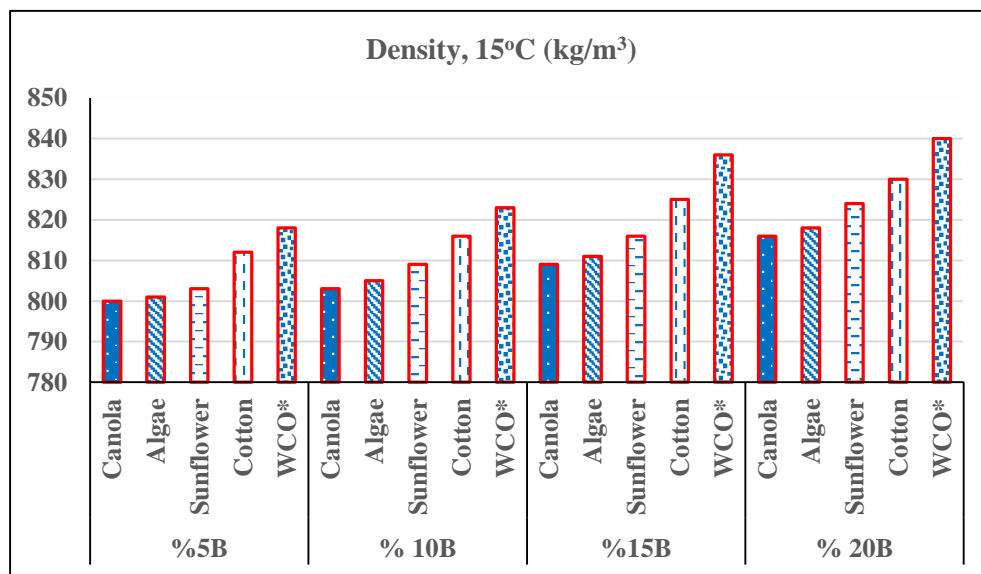


Fig. 3. Density changes of biodiesels mixed with jet fuel in different proportions

As seen in Figure 3, it is seen that when biodiesel fuels with higher density than jet fuel are mixed with jet fuel, they show a relative increase in density compared to the amount of biodiesel (%). However, all measured values appear to be within the scope of ASTM D 1298. Jet fuels are a mixture of hydrocarbons, the molecular weights of these hydrocarbons vary depending on their chain length. Therefore, it is known that the melting point and the smoke point, which have a significant effect on the quality of aviation fuel, change with the chain length of the hydrocarbon [23]. One of the important features that determine the quality of the fuels used in the aviation industry is the viscosity of the fuel. It is desirable that the fuel viscosity is quite low, since low viscosity means that the fuel comes to the engine combustion chamber without problems [24]. Apart from these features, jet fuels must not have any water other than the amount specified in the standards. If there is too much water in the fuel, the risk of freezing of the fuel will increase as the aircraft rises high. Freezing of the fuel will disrupt or interrupt the fuel flow to the turbines. This can cause turbines to malfunction. The high viscosity of jet fuels is an important problem for the injection nozzles of the turbines. In such a case, during fuel injection, the nozzles need to use more energy to spray the fuel. If this problem is not resolved, it will shorten the working life of the injection nozzles, resulting in higher maintenance costs and re-ignition the engine in the event of a malfunction during flight. It also affects the pressure drop in high viscosity fuel lines [25]. As a consequence, the fuel pump must work harder to guarantee a constant flow rate so that the turbines can continue working as required [26, 27]. In Figure 4, there are the viscosity values of jet fuel + biodiesel blends obtained with biodiesel mixed with jet fuel at different rates measured at 40 °C. It is seen that all of the determined values are below 2 mm²/s. This predicts that the mixture obtained by adding up to 20% of biodiesel into jet fuel will not be a problem in terms of viscosity.

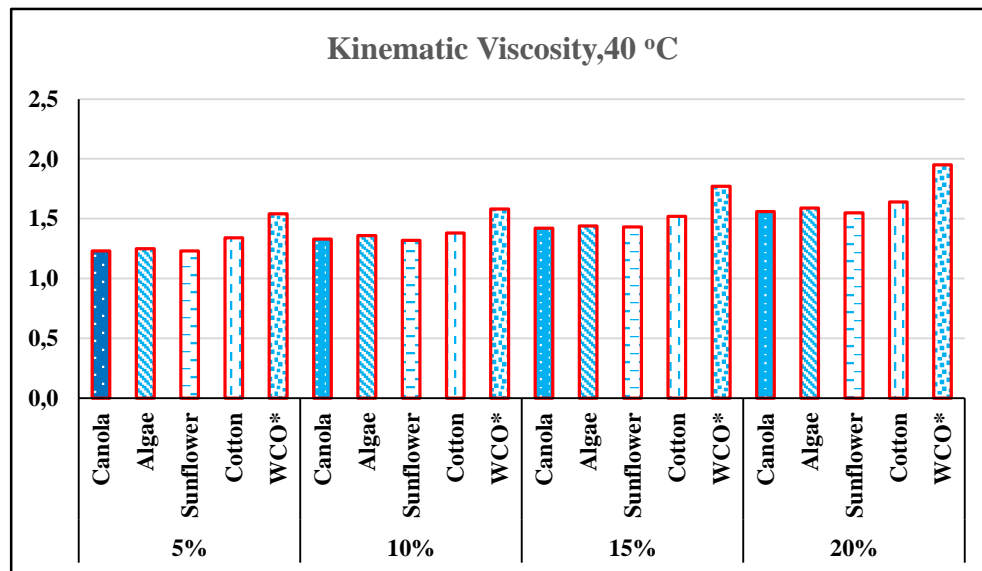


Fig. 4. Viscosity changes of biodiesels mixed with jet fuel in different proportions

The flash point of a volatile material is the lowest temperature at which its vapours ignite if given an ignition source [28, 29]. The flash point is sometimes confused with the auto-ignition temperature, the temperature that causes spontaneous ignition. The fire point is the lowest temperature at which the vapours keep burning after the ignition source is removed. It is higher than the flash point, because at the flash point more vapour may not be produced fast enough to sustain combustion [30].

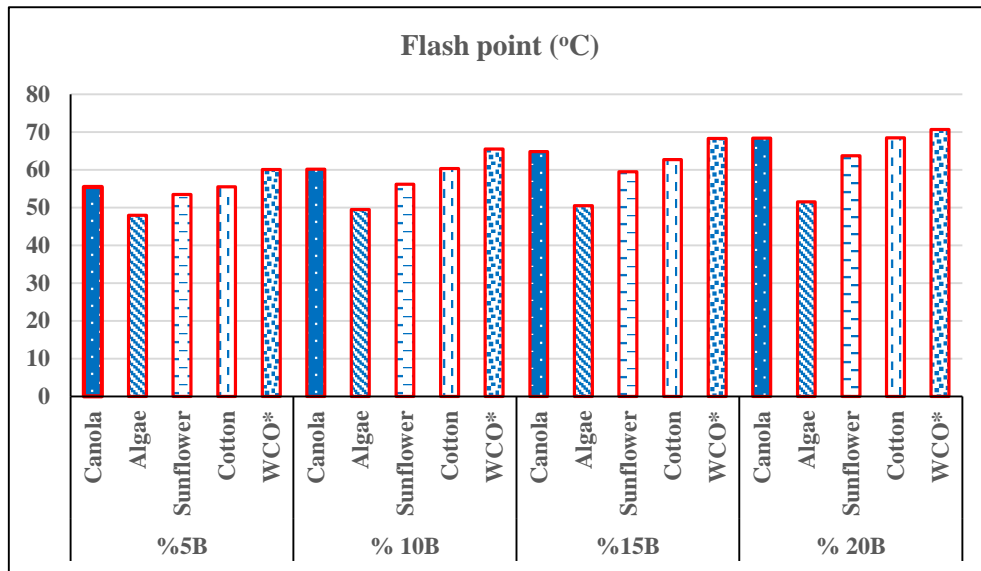


Fig. 5. Flash point changes of biodiesels mixed with jet fuel in different proportions

When biodiesel produced from different oils at 5%, 10%, 15% and 20% ratios is added to the jet fuel, the flash point values of the mixtures change as in figure 5. It is seen that all of the obtained results are within the scope of ASTM D 3828 values. Therefore, it is thought that when 20% of the biodiesel used in this study is added to the jet fuel, it will not be a problem in terms of the Flash Point feature.

Freezing point is an important quality specification for jet fuel [31]. This is the temperature at which components in the fuel start to solidify into wax crystal [32]. Freezing point is measured as the temperature at which the last wax crystal melts when warming a fuel that has previously been cooled until wax crystals formed [33]. At very low temperatures, aviation fuels will develop solid hydrocarbon crystals. The freezing point test for aviation fuels was developed to determine the temperature at which these crystals completely disappear. The freezing point test is important for aviation fuels since impeding fuel flow can have catastrophic effects for aircraft such as interfering with the atomisation of the fuel [34].

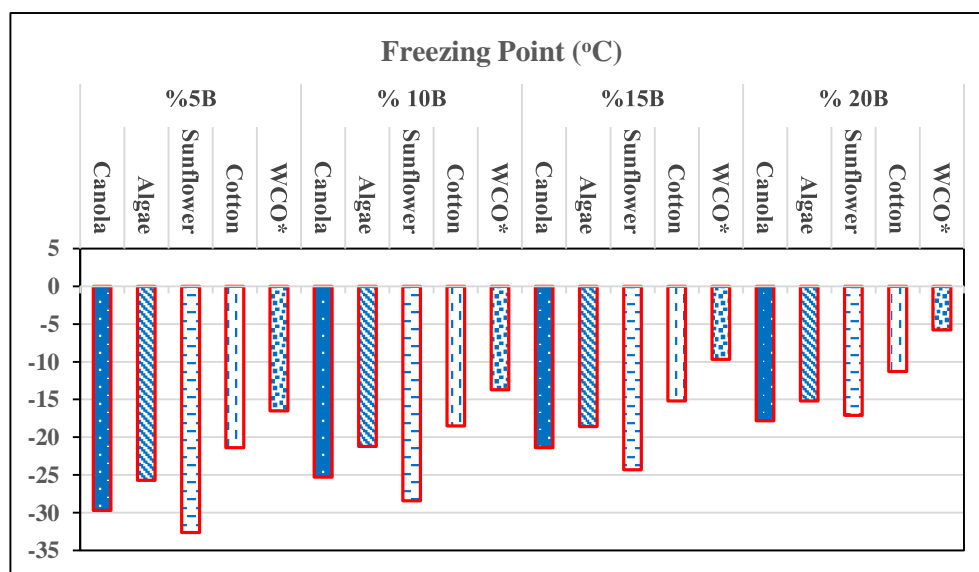


Fig. 6. Freezing point changes of biodiesels mixed with jet fuel in different proportions

As seen in Figure 6, when the biodiesel used in the study was added to the jet fuel in different proportions (5%, 10%, 15% and 20%) and freezing points of the mixtures were measured, a significant increase was found in the values. This suggests that fuel mixtures may cause some problems in the engine as the aircraft height increases. However, it is anticipated that this problem can be solved with additional freezing point reducing additives and appropriate amount of biodiesel.

4. Conclusions

The main purpose of this study is to determine the density, viscosity, flash point and freezing point values of the fuel mixtures obtained by adding 5%, 10%, 15% and 20% ratios (v/v) of different biodiesel blends into jet fuel. The fatty acid compositions of the oils used in the study were measured and the effects of the biodiesel fuels produced from various oils on the fuel quality were determined. Considering the properties of the biodiesel used, it is seen that the fuel with the highest density, viscosity, flash point and freezing point is WCO (892 kg/m³, 4.66 mm²/s, 180 °C, -8 °C). As a result, values of WCO biodiesel blends were found to be higher than other blends. In addition, it was determined that the Algae biodiesel used in the study has the best density (881 kg/m³), Flash point (150 °C) and Freezing point (-14 °C), and the cotton biodiesel meets the most suitable viscosity value. When we look at the mixtures we used in this study, it is seen that all values except freezing point values comply with the standards. It is thought that the freezing point problem in the blends can be overcome by using suitable additives and appropriate proportions.

References:

- [1] Zajac, G., The role of air transport in the development of international tourism, *Journal of International Trade, Logistics and Law*, Vol. 2, (2016), (1), pp,1-8.
- [2] Kumbur, H., Özer, Z., Özsoy, H.D., Avcı, E.D., Comparison of the potential environmental impact of conventional and renewable energy sources and in Turkey, *III. Renewable Energy Resources Symposium and Exhibition*, Mersin, (2005).
- [3] McCollum, D., Gould, G., Greene, D., Greenhouse gas emissions from aviation and marine transportation: mitigation potential and policies, *Solutions White Paper Series*, (2009).
- [4] Reducing emissions from aviation. (2020). <https://ec.europa.eu/clima/policies/transport/aviation>
- [5] Kousoulidou, K., Lonza, L., Biofuels in aviation: Fuel demand and CO₂ emissions evolution in Europe toward 2030, *Transportation Research Part D*, 46, (2016), pp,166–181.
- [6] Azami, M.H., Amin, S., Comparative study of alternative biofuels on aircraft engine performance, *Proceedings of the Institution of Mechanical Engineers, Part G: Journal of Aerospace Engineering*, 231, (2017), 8, pp, 1509-1521.
- [7] Azami, M.H., Savill, M., Modelling of spray evaporation and penetration for alternative fuels, *Fuel* 180, (2016), pp, 514–520.
- [8] Ashraful, A.M., Masjuki, H.H., Kalam, M.A., Fattah, I.M.R., Imtenan, S., Shahir, S.A., Mobarak, H.M., Production and comparison of fuel properties , engine performance , and emission characteristics of biodiesel from various non-edible vegetable oils : A review, *Energy Conversion and Management*, 80, (2014), pp,202–228.
- [9] Atabani, A.E., Silitonga, A.S., Badruddin, I.A., Mahlia, T.M.I., Masjuki, H.H., Mekhilef, S., A comprehensive review on biodiesel as an alternative energy resource and its characteristics, *Renewable and Sustainable Energy Reviews*, 16, (2012), 2070–2093.

- [10] Maity, J.P., Bundschuh, J., Chen, C.Y., Bhattacharya, P., Microalgae for third generation biofuel production, mitigation of greenhouse gas emissions and wastewater treatment: Present and future perspectives – A mini review, *Energy*, 78, (2014), pp,104-113.
- [11] Mohammadnejad, M., Ghazvini, M., Mahlia, T.M.I., Andriyana, A., A review on energy scenario and sustainable energy in Iran, *Renewable and Sustainable Energy Reviews*, 15, (2011), 9, pp, 4652-4658.
- [12] Edenhofer, O., Pichs-Madruga, R., Sokona, Y., Special Report on Renewable Energy Sources and Climate Change Mitigation, *Special Report of the Intergovernmental Panel on Climate Change (IPCC)*, (2012).
- [13] Yilmaz, N., Atmanlı, A., Sustainable alternative fuels in aviation, *Energy*, 140, (2017), pp, 1378-1386.
- [14] Biofuels for aviation technology brief, International Renewable Energy Agency, (2017).
- [15] <https://www.energy.gov/eere/bioenergy>, U.S. Department of Energy, Energy Efficiency & Renewable Energy, Alternative Aviation Fuels: Overview of Challenges, Opportunities, and Next Steps, (2016).
- [16] Fortier, M.O.P., Roberts, G.W., Stagg-Williams, S.M., Sturm, B.S.M., Life cycle assessment of bio-jet fuel from hydrothermal liquefaction of microalgae, *Applied Energy*, 122, (2014), pp, 73-82.
- [17] Wormslev, E.C., Pedersen, J.L., Eriksen, C., Bugge, R., Skou, N., Sustainable Jet Fuel for Aviation: Nordic perspectives on the use of advanced sustainable jet fuel for aviation, *Nordic Energy Research*, (2016), pp, 1-253.
- [18] Payan, A.P., Kirby, M., Justin, C.Y., Mavris, D.Y., Meeting emissions reduction targets: A probabilistic lifecycle assessment of the production of alternative jet fuels, *AIAA/3AF Aircraft Noise and Emissions Reduction Symposium*, 16-20 June (2014), pp, 1-18.
- [19] Fuel consumption of airlines worldwide: <https://www.statista.com/statistics/655057/>, (2020).
- [20] Knothe, G., Dependence of Biodiesel Fuel Properties on The Structure of Fatty Acid Alkyl Esters, *Fuel Processing Technology*, 86, (2005), pp, 1059 – 1070.
- [21] Hu, Z., Tan, P., Yan, X., Lou, D., Life Cycle Energy, Environment and Economic Assessment of Soybean-Based Biodiesel as an Alternative Automotive Fuel in China, *Energy*, 33, (2008), pp, 1654–1658.
- [22] Outcalt, S.L., Laesecke, A., Brumback, K.J., Comparison of Jet Fuels by Measurements of Density and Speed of Sound of a Flightline JP-8. *Energy Fuels*, 24, (2010), pp, 5573–5578.
- [23] Hocking, M.B., Handbook of Chemical Technology and Pollution Control (Third Edition), 2005, pp, 593-636.
- [24] Rulemaking, A., Aviation Rulemaking Advisory Committee, Fuel Properties - Effect on Aircraft and Infrastructure, Task Group 6/7 on Fuel Properties Report to the Fuel Tank Harmonization Working Group of the FAA Aviation Rulemaking Advisory Committee, (1998), pp, 1-37.
- [25] Robertson, B. Baumgarten G.P. Evaluation of Automotive Fuel Flowmeters, Book. 13. Cilt, (1977).
- [26] Mark, S. Ramsey, P. E., In Practical Wellbore Hydraulics and Hole Cleaning, *Book*, (2019).
- [27] M. Imam, M.M., Basha, M. Shaahid, S.M., Ahmad, A. Al-Hadhramia, L.M., Effect of Viscosity on the Pressure Gradient in 4-inch Pipe. 2014 ASME International Mechanical Engineering Congress and Exposition, (2014), Montreal, Canada.
- [28] Durkee, J., Management of Industrial Cleaning Technology and Processes, *Book*, (2006).
- [29] Silla, E., Wypych, G., Fundamental Principles Governing Solvents Use. Handbook of Solvents (Third Edition), *Book*, (2019).
- [30] Dimian, A.C., Kiss, A.A., Integrated Design and Simulation of Chemical Processes Computer Aided Chemical Engineering, *Book*, (2003).

- [31] Coetzer, R. L. J., Joubert, T. S., Viljoen, C. L., Nel, R. J. J., Strydom, C. A., Response surface models for synthetic jet fuel properties. *Applied Petrochemical Research*, 8, (2018), pp, 39–53.
- [32] Dahlquist, E., Biomass as Energy Source: Resources, Systems and Applications. *Book*. (2013).
- [33] Al Sabagh, A. M. Azzam, E., Nasser, N. M., Abdel Haliem, F. T., El-Shafey, A. M., Using ethoxylated polyalkylphenol formaldehyde as additive to enhance some physical properties of Egyptian jet fuel A1, *African Journal of Engineering Research*, 4, (2016), 2, pp, 11-25
- [34] Drews, A.W., Manual on Hydrocarbon Analysis (6th Edition): (MNL 3), *Book*, (1998).

CRASHWORTHINESS INVESTIGATION OF VEHICLE FRONT BUMPER BEAM WITH DIFFERENT CROSS-SECTIONS UNDER AXIAL DYNAMIC LOAD

Hüseyin BEYTÜT¹, Selçuk KARAGÖZ^{2*}, Serkan ÖZEL³


Bumper beam, is one of the first structures exposed to impact at the time of an accident. Therefore, how it behaves at the time of an accident is extremely important in terms of passenger safety, cargo and other critical parts of the vehicle. What is expected from a bumper beam is to absorb the kinetic energy of the vehicle through plastic deformation, particularly at low and medium speeds. In this study, finite element models of the crash situations of the bumper beams with five different cross-sectional geometries and equal weights were created by using the HyperMesh software and crash analyses were carried out. Since the bumper beams may behave differently in different barrier types, pole and wall barrier impact test was investigated. AA6061-T6 Aluminum alloy was used as the material and Johnson-Cook was used as the material model. The results revealed that the cross-sectional geometry had significant effect on crashworthiness and the models exhibited different crashworthiness on wall and pole barriers. RADIOSS/explicit and non-linear finite element codes were used.


Keywords: Vehicle bumper beam; energy absorption; finite element method; crashworthiness.


1. Introduction

In today's vehicle designs, vehicle crashworthiness and vehicle mitigation have become attractive matters for both automobile manufacturers and researchers [1, 2]. Crashworthiness is an engineering term used to describe the ability of a vehicle structure to protect its occupants during a crash [3]. The importance of vehicle crashworthiness is constantly increasing due to strict safety norms, high competition and increasing safety concerns.

Bumper beams, which are among the passive safety systems in vehicles, are important structural elements for vehicle crashworthiness. Since the bumper beam is one of the main parts that absorbs vehicle crash energy, its design and production are extremely critical for an efficient energy absorption

¹ Department of Mechanical Engineering, Bitlis Eren University, Bitlis, Turkey, (hbeytut@beu.edu.tr)  <https://orcid.org/0000-0001-8751-2225>

^{2*} Department of Mechanical Engineering, Bursa Technical University, Bursa, Turkey, (selcuk.karagoz@btu.edu.tr)  <https://orcid.org/0000-0002-1987-5750>

³ Department of Mechanical Engineering, Bitlis Eren University, Bitlis, Turkey, (sozel@beu.edu.tr)  <https://orcid.org/0000-0003-0700-1295>

[4]. Bumper beams are impact absorber structures located in the front and rear of the vehicle and whose primary function is to protect critical parts of the vehicle and occupants. Bumper beams are applied to today's vehicles by being designed with different materials in various geometries with crash boxes.

The main purpose of this dual system is to absorb the kinetic energy of vehicle and to ensure that occupants survive the accident with minimum damage. Since the cross-section of the bumper has effect on the crash performance, it can be designed in different cross-sections [5] (fig. 1).

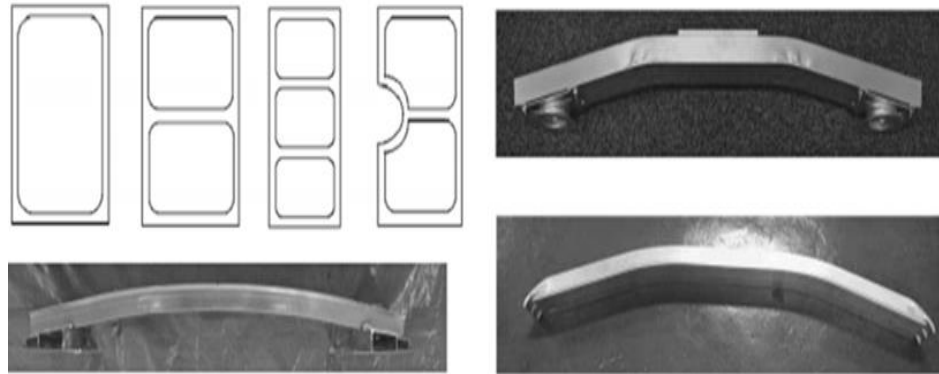


Figure 1. Bumper beam cross-section examples and models [5].

The main physical phenomenon, where the structures used for energy absorption absorb energy, is plastic deformation. Keeping plastic deformation at maximum level is important in terms of the amount of energy that is absorbed. Therefore, the material used needs to be stiff but deformable [6-8]. A non-deformable structure will act as rigid and transmit the force to the other parts without performing its essential task which is energy absorption.

Cross-section [9, 10], material [11, 12], wall thickness [13], loading conditions [14], which are the main parameters that significantly affect crashworthiness of bumper beam, are the most studied subjects by researchers. Certain parameters have been determined in the determination of crashworthiness of energy absorbing structures. The most important ones are the amount of absorbed energy, peak crushing force, mean crushing force, crash force efficiency and specific energy absorption.

1.1 Absorbed Energy (AE)

The amount of absorbed energy by bumper beam can be found in the area below the force-displacement curve (Equation 1).

$$AE = \int_0^d P(x)dx \quad (1)$$

Where; d refers to displacement and $P(x)$ refers to the force in the axial direction.

1.2 Peak Crushing Force (PCF)

Peak crushing force generally occurs on the first reaction force if the trigger mechanism (groove, hollow, hole) is not used. It is expected to be low in terms of the force to be transmitted to the occupants at the time of an accident.

1.3 Mean Crushing Force (MCF)

The mean crushing force value is found by the ratio of AE to displacement (Equation 2). In order to keep the AE at the maximum level, it is a desired situation that the forces after the first reaction force are close to the mean crushing force.

$$P_o = \frac{AE}{d} \quad (2)$$

1.4 Crash Force Efficiency (CFE)

Crash force efficiency (η) is calculated by the ratio of the MCF to the PCF (Equation 3). It is an important parameter in evaluating the crashworthiness of the structure since it depends on both the AE and PCF (P_{max}).

$$\eta = \frac{P_o}{P_{max}} \quad (3)$$

1.5 Specific Energy Absorption (SEA)

It is calculated by the ratio of the AE to the mass of the structure (Equation 4). Since all models in this study have equal weights, the absorbed energy rates will be equal to the specific energy absorption rates.

$$SEA = \frac{AE}{m} \quad (4)$$

2. Material and Method

In addition to the energy absorption property of bumper designs, lightness, ease of production and being economic are also expected. Steel, aluminum, magnesium alloys and polymeric-based composites are main materials used as bumper beam material [15]. In this study, Aluminum 6061-T6 alloy was used as the bumper material. Johnson-Cook material model [16], which represents the isotropic elasto-plastic material was used due to the fact that the vehicle front structure components used for energy absorption are subjected to significant plastic deformations in a very short time at the time of an accident and due to the effect of strain rate on crashworthiness. Johnson-Cook material model is often used in dynamic analyses since it pays attention to the strain rate, hardening and temperature effect [17-19]. In this study, temperature influence was neglected. The mechanical properties and Johnson-Cook parameters belonging to aluminum 6061-T6 alloy are given in Table 1.

Table 1. Mechanical properties of AL6061-T6 alloy and Johnson-Cook parameters [20].

$E(GPa)$	$\rho(gr/cm^3)$	ν	$A(GPa)$	$B(GPa)$	n	C
70	2.7	0.33	324	114	0.42	0.002

Where A is the yield stress, B is hardening parameter, n is hardening exponent and C is strain-rate coefficient. Bumper models was designed as surface on CATIA software in a way to have the same surface area (0.357 m^2) in 5 different geometries (Figure 2). In model 2, model 3 and model 4 designs, outward or inward hollows were formed. In this way, it was aimed to reduce the peak crushing force by allowing easier folding.

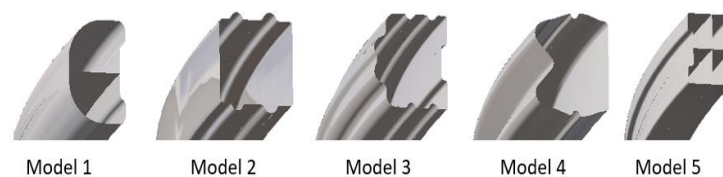


Figure 2. Bumper beam models designed in 5 different cross-sectional geometries and in the same weight.

Each bumper weight is calculated as approximately 1155 g for 1.2 mm wall thickness and 2700 kg/m³ density. Shell elements in the size of 2.5x2.5 were used for mesh by using HyperMesh software. As contact definition, "Nodes to Surface Contact", which ideally represents the model in dynamic analyses and uses penalty method, was used [21, 22]. During folding, the friction coefficient between the surfaces of the bumper beams and between the bumper beam and the wall and pole barriers was accepted as 0.2 and Coulomb's law of friction was used [23, 24]. The created pole and wall barriers were defined as rigid to prevent deformation. 1225 kg mass was added to the bumper beams to provide a real crash environment and they were crashed to straight wall and pole barriers with 56 km/h. In addition, all models were restricted from other degrees of freedom except the axis to which the speed was provided (Figure 3).

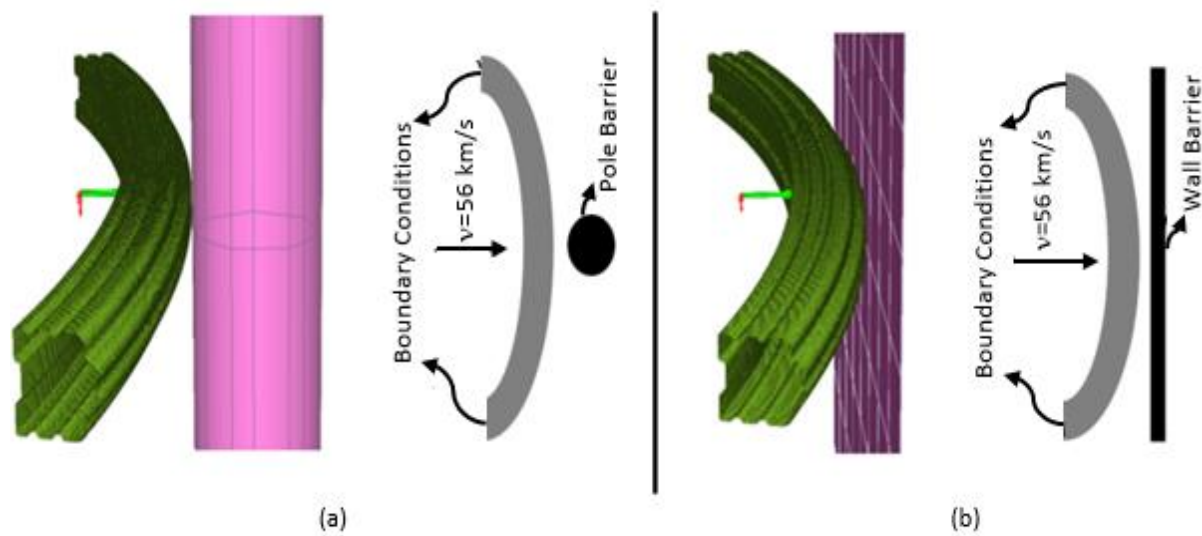


Figure 3. Model 3's finite element model and schematic representation regarding a) pole barrier b) wall barrier.

Since the bumper beam under dynamic load was subjected to very high plastic deformation in a very short time, explicit method was used. In the explicit method, the total analysis time is divided into much smaller time intervals which are named as time steps. The statement regarding the time step is given in Equation 5 and Equation 6.

$$\Delta t_e = \frac{l}{c} \quad (5)$$

$$c = \sqrt{\frac{E}{\rho}} \quad (6)$$

Here; l represents the smallest distance between the 2 nodal points of the element, c represents the sound velocity of the material, E represents the elasticity modulus of the material and ρ represents the density of the material. As the size of the element used in the formation of the mesh becomes smaller and the elasticity modulus of the material increases, the time step will become smaller and thus, the solution time will extend. In this study, the time step varies between 1.966 E-4 and 3.321 E-4 depending on the model.

3. Results and Discussion

The deformation conditions occurring on the wall and pole barriers of the bumper beam models designed for each geometry at the end of the crash analyses are shown in Figure 4. While off-center

deformation was observed on the pole barrier, deformations also occurred on the sides on the wall barrier. In addition, stresses were at maximum level on these areas because the end parts of all models were restricted to other degrees of freedom except the axis in which the speed was provided.

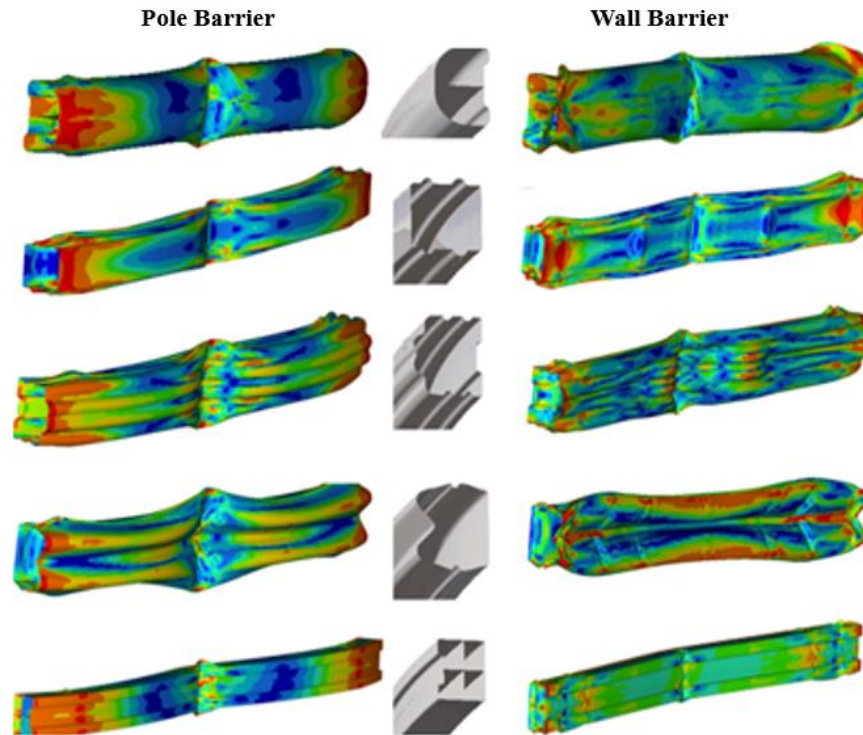


Figure 4. Models' deformation conditions on rigid pole and wall barriers and Von Mises stress distributions.

It is a desired situation that the reaction force, which is an important criterion in the evaluation of crashworthiness, is low in terms of occupant and transported cargo safety. In order to reduce the peak crushing force that usually occurs in the first reaction force, hollows were added to Model 2, Model 3 and Model 4. Thanks to the added hollows, the peak crushing force in these models was found to be lower than in other models. On the rigid wall barrier, the highest crushing force was achieved in Model 5 and the lowest in Model 1 (fig. 5).

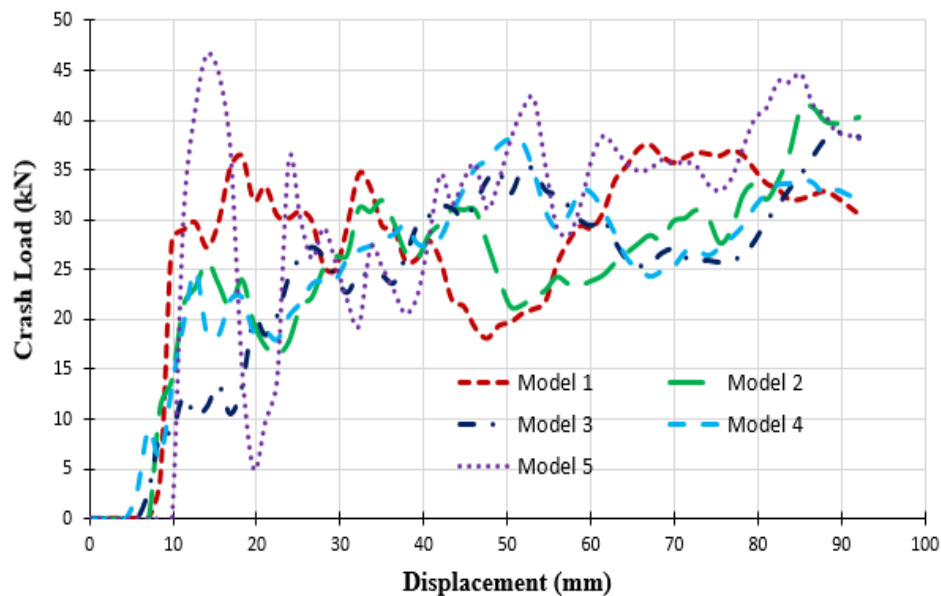


Figure 5. Crash load versus displacement curves for rigid wall barrier.

Peak crushing forces on the pole barrier of the models with hollows were also lower as on the wall barrier. In terms of both wall barrier and pole barrier, the first reaction force of the Model 3 was found to be the lowest and the Model 5 was found to be the highest. This situation is thought to be caused by the fact that the Model 5 did not have any hollow and its cross-sectional geometry was straighter than other models.

For all models, the peak crushing force on the wall barrier was higher than the pole barrier. The reaction forces of the models occurring on the rigid pole barrier are given in Figure 6. In the Model 1 with no hollow, the peak crushing force occurred at the first reaction force, while it occurred at the next reaction forces in other models. On the rigid pole barrier, the highest crash load was obtained in the Model 5 and the lowest in the Model 2.

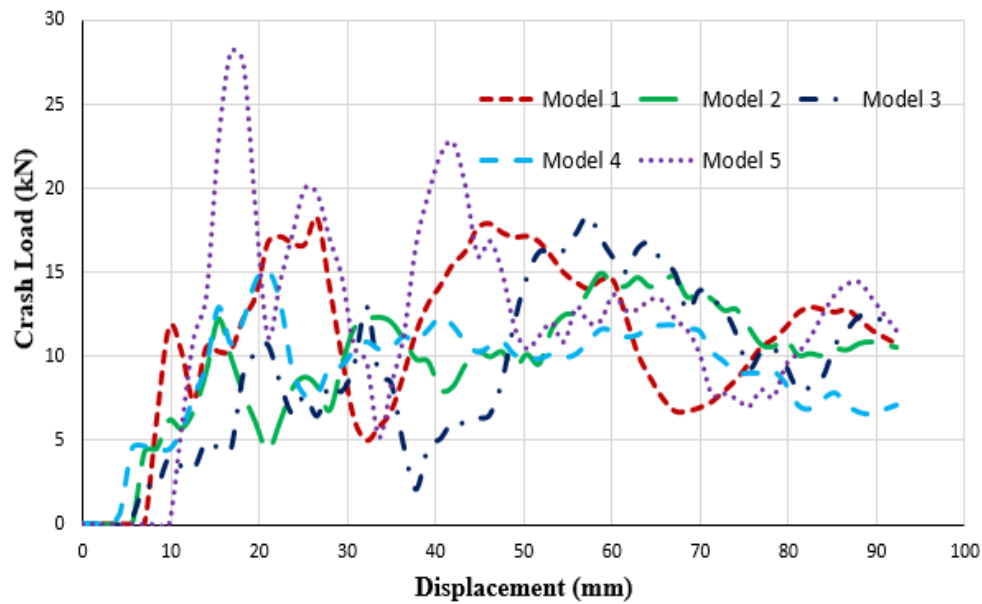


Figure 6. Crash load versus displacement curves for rigid pole barrier.

The amount of absorbed energy by the models on the wall barrier is given in Figure 7. The Model 5 has the most energy absorption, while the Model 3 has the lowest energy absorption.

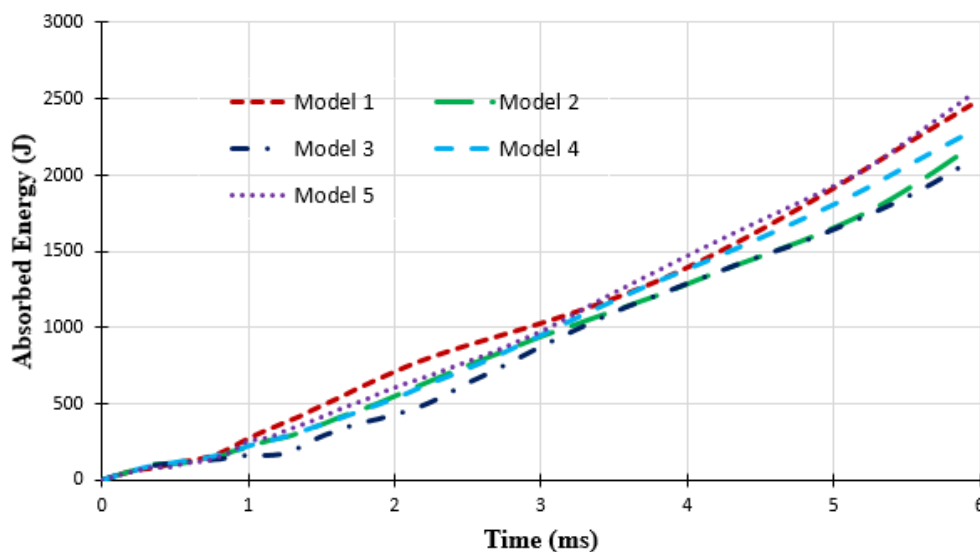


Figure 7. Absorbed energy versus time curves for rigid wall barrier.

The amount of absorbed energy by the models on the pole barrier is given in Figure 8. The Model 5 has the highest energy absorption, while the Model 4 has the lowest energy absorption.

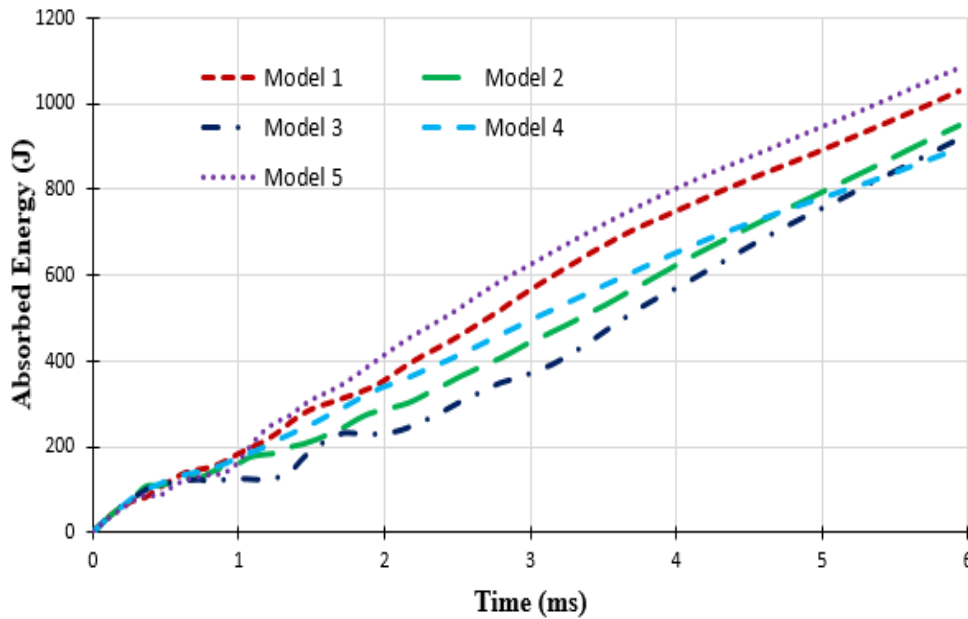


Figure 8. Absorbed energy versus time curves for rigid pole barrier.

Since all bumper beam models had a more homogeneous plastic deformation on the wall barrier, they achieved more energy absorption compared to the pole barrier. At the same time, their peak crushing forces were also higher. When the analysis results are evaluated, it is seen that the highest absorbed energy (AE) value was obtained in the Model 5 in terms of both pole and wall barrier. The lowest peak crushing force (PCF) was obtained in the Model 1 for rigid wall barrier and Model 4 for rigid pole barrier. When the results are evaluated in terms of crash force efficiency (CFE) depending on both AE and MCF, the best result was obtained in the Model 1 for rigid wall barrier and Model 2 for rigid pole barrier. Dynamic analysis results for all models are given in Table 2.

Table 2. Dynamic analysis results for all models.

Model No	Rigid Wall Barrier				Rigid Pole Barrier			
	AE (J)	PCF (kN)	MCF (kN)	CFE	AE (J)	PCF (kN)	MCF (kN)	CFE
Model 1	2456.70	37.56	26.65	0.709	1029.33	18.20	11.15	0.612
Model 2	2189.75	41.22	23.75	0.576	949.51	14.94	10.28	0.688
Model 3	2094.02	38.79	22.72	0.586	920.08	18.44	9.96	0.540
Model 4	2282.18	38.14	24.76	0.649	895.58	15.10	9.70	0.642
Model 5	2524.40	46.74	27.39	0.586	1082.20	28.19	11.72	0.415

4. Conclusion

The peak crushing force is expected to be low and the absorbed energy is expected to be high in the values obtained as a result of crash analyses. 5 different bumper beams having the same weight were modeled and crashworthiness under dynamic load was investigated. In order to reduce the peak crushing force that usually occurs at the first reaction force, hollows were added to some models. It was observed that the first reaction force was lower in the models with hollow and it was concluded that the first reaction force could be reduced by adding hollow.

When finite element analysis of the models is evaluated, it is seen that the highest energy absorption was achieved in the Model 5 with 2524.40 J for rigid wall barrier and 1082.2 J for rigid pole barrier. However, in the Model 5, the peak crushing force values were 46.74 kN for the rigid wall barrier and 28.19 kN for the rigid pole barrier, and these are the highest values for all models. This situation is thought to be caused by the fact that the Model 5 did not have any hollow and its cross-sectional geometry was straighter than other models. Although the Model 5 has the highest energy absorption value, it is considered negative because the peak crushing force is much higher than other designs. When the results are evaluated in terms of crash force efficiency depending on both absorbed energy amount and peak crushing force, it was obtained in the Model 1 with 0.709 for rigid wall barrier and in Model 2 with 0.688 for rigid pole barrier. Since the Model 1 has more stable reaction forces for rigid wall barrier and Model 2 for rigid pole barrier, these designs come to the forefront compared to other designs.

The results reveal that the minor changes made in the cross-sectional geometry of bumper beam affect crashworthiness and the first reaction force can be reduced by adding hollows to bumper beam. Furthermore, the models showed different crashworthiness on rigid wall and pole barriers. Therefore, it is important to perform analyses not only for a barrier type but also all possible barrier types of the bumper beam to be mounted to the vehicle in terms of the vehicle crashworthiness.

References

- [1] Sun, G.Y., G.Y. Li, S.W. Zhou, H.Z. Li, S.J. Hou, and Q. Li,(2011) *Crashworthiness design of vehicle by using multiobjective robust optimization*. Structural and Multidisciplinary Optimization. 44(1): p. 99-110, doi:10.1007/s00158-010-0601-z.
- [2] Yang, R.J., N. Wang, C.H. Tho, and J.P. Bobineau,(2005) *Metamodeling development for vehicle frontal impact simulation*. Journal of Mechanical Design. 127(5): p. 1014-1020, doi:10.1115/1.1906264.
- [3] Jones, N., *Structural impact*. Cambridge: Cambridge university press. 2011
- [4] Cheon, S.S. and J.H. Choi,(1995) *Development of the composite bumper beam for passenger cars*. Composite Structures. 32(1-4): p. 491-499, doi:10.1016/0263-8223(95)00078-X.
- [5] Hashimoto, N.,(2017) *Application of Aluminum Extrusions to Automotive Parts*. Kobelco Technology Review, (35): p. 69-75.
- [6] Safari, H., H. Nahvi, and M. Esfahanian,(2018) *Improving automotive crashworthiness using advanced high strength steels*. International Journal of Crashworthiness. 23(6): p. 645-659, doi:10.1080/13588265.2017.1389624.
- [7] Wierzbicki, T. and W. Abramowicz,(1983) *On the Crushing Mechanics of Thin-Walled Structures*. Journal of Applied Mechanics-Transactions of the Asme. 50(4a): p. 727-734, doi:Doi 10.1115/1.3167137.
- [8] Khatri, N.A., H. Shaikh, Z.A. Maher, A. Shah, and S.F. Ahmed,(2018) *A Review on Optimization of Vehicle Frontal Crashworthiness for Passenger Safety*. International Journal of Engineering & Technology. 7(2.34): p. 1-4, doi:10.14419/ijet.v7i2.34.13894.
- [9] Patil, S.A., R. Moradi, and H.M. Lankarani. *Vehicle mass optimization for frontal structure using I-sight and study of weld parameterization for mass improvement*. in *ASME 2014 International Mechanical Engineering Congress and Exposition*. 2014. American Society of Mechanical Engineers.
- [10] Zhang, Z.H., S.T. Liu, and Z.L. Tang,(2009) *Design optimization of cross-sectional configuration of rib-reinforced thin-walled beam*. Thin-Walled Structures. 47(8-9): p. 868-878,

- doi:10.1016/j.tws.2009.02.009.
- [11] Belingardi, G., A.T. Beyene, E.G. Koricho, and B. Martorana,(2015) *Alternative lightweight materials and component manufacturing technologies for vehicle frontal bumper beam*. Composite Structures. 120: p. 483-495, doi:10.1016/j.compstruct.2014.10.007.
- [12] Ding, M., J. Liu, B. Liu, X. Wang, T. Li, and D. Cao. *On the development of automotive composite material rear bumper beam*. in *Proceedings of SAE-China Congress 2015: Selected Papers*. 2016. Springer.
- [13] Wang, G., J. Zhou, Z. Liu, L. Li, B. Liu, X. Li, et al.,(2012) *Lightweight design and crash performance analysis of automotive aluminum bumper*. The Chinese Journal of Nonferrous Metals. 22(1): p. 90-98.
- [14] Hosseinzadeh, R., M.M. Shokrieh, and L.B. Lessard,(2005) *Parametric study of automotive composite bumper beams subjected to low-velocity impacts*. Composite Structures. 68(4): p. 419-427, doi:10.1016/j.compstruct.2004.04.008.
- [15] Tanlak, N., F.O. Sonmez, and M. Senaltun,(2015) *Shape optimization of bumper beams under high-velocity impact loads*. Engineering Structures. 95: p. 49-60, doi:10.1016/j.engstruct.2015.03.046.
- [16] Johnson, G.R.,(1983) *A constitutive model and data for materials subjected to large strains, high strain rates, and high temperatures*. Proc. 7th Inf. Sympo. Ballistics: p. 541-547.
- [17] Wang, Q., F. Wu, B. Tang, and C. Li. *Damage Behavior of Boron Steels with Various Hardness Using the GTN and the Johnson-Cook Model*. in *Advanced High Strength Steel And Press Hardening-Proceedings Of The 4th International Conference On Advanced High Strength Steel And Press Hardening (Ichs2018)*. 2018. World Scientific.
- [18] Raman, R., K. Jayanth, I. Sarkar, and K. Ravi. *Analyzing the effect of carbon fiber reinforced polymer on the crashworthiness of aluminum square hollow beam for crash box application*. in *IOP Conference Series: Materials Science and Engineering*. 2017. IOP Publishing.
- [19] Estrada, Q., D. Szwedowicz, A. Rodriguez-Mendez, M. Elías-Espinosa, J. Silva-Aceves, J. Bedolla-Hernández, et al.,(2019) *Effect of radial clearance and holes as crush initiators on the crashworthiness performance of bi-tubular profiles*. Thin-Walled Structures. 140: p. 43-59, doi:10.1016/j.tws.2019.02.039.
- [20] Lesuer, D.R., G. Kay, and M. LeBlanc, *Modeling large-strain, high-rate deformation in metals*. 2001, Lawrence Livermore National Lab., CA (US).
- [21] Gumruk, R. and S. Karadeniz,(2009) *The influences of the residual forming data on the quasi-static axial crash response of a top-hat section*. International Journal of Mechanical Sciences. 51(5): p. 350-362, doi:10.1016/j.ijmecsci.2009.03.010.
- [22] Toksoy, A.K. and M. Guden,(2010) *Partial Al foam filling of commercial 1050H14 Al crash boxes: The effect of box column thickness and foam relative density on energy absorption*. Thin-Walled Structures. 48(7): p. 482-494, doi:10.1016/j.tws.2010.02.002.
- [23] Ahmad, Z. and D.P. Thambiratnam,(2009) *Dynamic computer simulation and energy absorption of foam-filled conical tubes under axial impact loading*. Computers & Structures. 87(3-4): p. 186-197, doi:10.1016/j.compstruc.2008.10.003.
- [24] Zheng, G., T. Pang, G.Y. Sun, S.Z. Wu, and Q. Li,(2016) *Theoretical, numerical, and experimental study on laterally variable thickness (LVT) multi-cell tubes for crashworthiness*. International Journal of Mechanical Sciences. 118: p. 283-297, doi:10.1016/j.ijmecsci.2016.09.015.

EFFECT OF ENERGY INPUT ON WEAR PERFORMANCE OF BORON COATING MADE WITH PTA

Musa KILIÇ¹

It is inevitable that wear on the surfaces occur when especially metal surfaces contact each other. One of the most crucial problems among surface machining is wear problem. In this study, surface of 316 L stainless steel was coated with boron via plasma arc method and 160, 165 and 170 current values were utilized as welding parameters.

The effect of the energy input on microstructure and on the abrasion resistance of the hard structures formed in the coating region was investigated.

It was determined from optical microscope and SEM analysis that the coating area consisted of branched and leaf-shaped dendritics; and eutectic structures were formed between these dendritics. As a result of EDX taken from coated region, Fe, B and Cr elements were found. After wear test, low mass loss was determined in samples coated with Boron 2 and it is clear that coating os Boron on 316 L stainless steel substrate is increased wear resistance. While the highest weight loss was occurred in 316 L satinless steel with 45 mg and the lowest weight loss was obtained from Boron 2 sample with 27 mg.


Key Words: PTA, Boron, Abrasive resistance, Coating

1. Introduction

Wear is one of the problems which is not wanted in industry as a consequence of damages that it leads to in engineering processes in terms of cost, labor and time when the metals contact to each other.

According to their usage places, the tribology properties of metals can be improved by using surface coating methods in order to eliminate the damages such as fatigue, friction and wear occurring in metals [1-2].

As surface coating methods, hard filling processes such as plasm transferred arc welding (PTA) and gas tungsten arc welding (GTAW) were used with the help of thermal sparying methods such as high velocity oxy fuel (HVOF), atmospheric plasma spraying (APS) and flame sparying(FS) [3-7].

¹ Department of Machinery and Manufacturing Engineering, University of Batman, Batman, Turkey, (musa.kilic@batman.edu.tr)
 <https://orcid.org/0000-0002-5808-6917>

PTA coating method is a preferred method because it is cheap and feasible. In addition, PTA method has attracted the attention of researchers in recent years due to its high welding speed, well penetration depth and good arc stability, as well as its wear-corrosion resistance and improved fatigue strength [8-11]. In particular, in this method, besides the wide range of materials, the performance of the material surfaces can be greatly improved by low dilution and deterioration between the hard filler layer formed on the coated surfaces and the substrate material [12-16]. Plasma transferred arc (PTA) technique provides strong metallurgical bond formed between the coating and substrate, low porosity, high energy conversion efficiency, high precipitation rate, low heat input [17].

Since the materials are melted in PTA coatings, the melting temperature of the metal to be formed with the base material should be approximately the same or lower than the base metal. Otherwise, the plasma arc does not melt or partially melt the material to be coated while melting the base metal at high temperatures. In this case, since a good diffusion cannot be achieved, the coating layer cannot be formed completely [18].

Q.Y. Hou et al. [19] investigated the effects of molybdenum on the microstructure and wear resistance of nickel-based alloy coatings with PTA method and established that the wear resistance increased by 47.2%.

Y. F. Liu et al. [20] investigated the microstructure and non-lubricated shear wear properties of TIC reinforced composite coating performed by PTA method; and obtained the result of high surface hardness and non-lubricated wear resistance of the composite coating.

L. Bourithis et al. [21] applied boroning process to AISI 1018 steel with the help of PTA coating method and obtained coatings in thicknesses ranging from 1 to 1.5 mm and in hardness ranging from 400 to 1600 HV. In the examination, they observed that the wear was quite low.

R. Iakovu et al. [22] showed that hardness values were established between 1000-1300 HV as a result of coating, and that tool steels were successfully coated with boron by using PTA coating method. They determined that the boroned surface contained austenitic and martensitic mixtures together with the Fe₂B-type boride layer, and that some cracks were observed in the austenitic regions and these cracks did not have any critical effects on slip wear.

L. Bourithis and G. Papadimitrou [23] achieved successful coatings in boron and CrB₂ coating work of the plain carbon steel surface with PTA coating method. As a result of the study, they stated that the wear rates were low in both coatings, and they obtained hardness between 1000-1300 HV in boron coatings and 900 HV hardness in coating made with CrB₂ powder.

In this method, since the arc temperature rises to high temperatures, the surface of metal and metal alloys with high melting temperature is applied by using many coating powders and combinations of these powders. Thanks to its high coating thickness and high energy density, PTA hard fill coating is widely used in sectors such as defense industry, aircraft industry, machinery and manufacturing, medicine, automotive industry [24-26].

Boron and boron-derived products with different uses have also been widely used in the surface hardening process of steels in the industry [27].

Boron surface coating can be applied to tempered steels, tool steels, stainless steels, cast steels, cast irons, non-ferrous metals and alloys such as sintered metal powders, nickel, cobalt, molybdenum and titanium [28-29].

The high hardness of the boride layer and the low friction coefficient contribute to the increase of wear resistance [22, 29].

Boroning can increase the service life of the steels by increasing the wear resistance, corrosion-erosion resistance and microhardness [30-31]. The surface coating process with boroning method is a method that is used a lot in the industry, and it brings the surface of the applied material to very high hardness values. The hardness of the boron layer varies between 1800-2100 HV and can reach up to 2400 HV in high alloy steels [22, 32]. In addition, boron coating contributes to increase the breaking and flowing fatigue and corrosion fatigue resistance of metals [33-34].

In this study, surface of 316 L stainless steel was coated with boron element by plasma transfer arc method (PTA). Coating morphology was characterized by optical microscope and SEM-EDX. The effect of energy in put on the hard structures which formed after coating on substrate was examined by wear test and under the load of 5N, 10N and 20N for ASTM G99 standards with the help of a pin on disc method. The mass loss of the wear zone after the wear process was characterized by microstructure.

2. Materials and Method

In this study, surface coating was applied to the surface of AISI 316 L steel by using elemental boron powder with PTA. The chemical composition of boron powder and substrate materials are given in Table 1 and Table 2, respectively. The boron used in the coating process had a grain size of 1 μ m. Table 2 shows the chemical composition of boron powder and the properties of the powder.

Table 1: Boron chemical composition

	Purity (%)	Average particle size	Melting Temp. (°C)	Density (gr/cm ³)	Molecular weight (gr/mol)
Boron	96.21	<1.5 μ m	2076	2.34	10.81

Table 2: AISI 316L stainless steel chemical composition

Cr	C	S	Ni	Si	Mn	Mo	P
18.0	0,03	0,03	14.0	0,75	2.0	3.0	0.045

Before coating, the surface of AISI 316L stainless steel, which would be used as substrate material, was cleaned with a lathe to remove dirt and oxides. As shown in Figure 1a, 10mm width and 3mm deep grooves were opened on the surface of AISI 316 L stainless steel with the help of milling machine so that dust can be deposited on the substrate after surface cleaning process.



Figure 1: (a) AISI 304 stainless steel substrate, (b) Boron powder laid base

After the grooving process was completed, the samples were then cleaned by washing in acetone bath to remove dirt and debris.

Into the groove opened sample, the boron element was deposited in the substrate after soaked with polyvinyl alcohol in an atmosphere of argon gas Figure 1b. Samples were placed in the oven at 30°C and dried so that the wetting agent would be removed from coating zone before coating with PTA. The main purpose of wetting the powders with polyvinyl alcohol is prevent flying of boron powder from channel during arc blow.. For the welding parameters(160A, 170A and 180A), only the mechanical impacts provided by the different current values on the coating surface and the interface surface were examined.

After the samples were prepared, coating was performed with plasma arc welding using the parameters given in Table 3. The schematic picture of the plasma source used in the experimental phase and the coating sample produced after the process are given in Figures 2a and b.



Figure 2: (a)Schematic figure of PTA source and coating process [23] , (b) Sample processed with coating, (c) Wear device schematic picture

After successful coating process, samples were cut in a precision cutting machine in a perpendicular direction to the coating for wear and microstructure analysis. The samples, of which the cutting process was completed, were subjected to coarse polishing with optical microscope, SiC sandpaper with 240-1200 mesh size for SEM-EDX analysis. In the fine polishing process, the samples were polished with 1 micron diamond paste and broadcloth. In microstructure and SEM-EDX analysis, samples were etched with Nital solution before internal structure analysis. Microstructured analysis of the etched samples was carried out with Nikon optical microscope. JSM5600 Brand SEM-EDX device was used for detailed microstructure and elemental analysis.

Table 3: Boron coating process parameters

Sample No	Setback Adjustment (mm)	Nozzle Diameter (mm)	Current (A)	Protective Gas L/min	Plasma Gas L/min
Boron-1	0,8	2,4	160	25	0,5
Boron-2	0,8	2,4	165	25	0,5
Boron-3	0,8	2,4	170	25	0,5

Samples with coating process were subjected to abrasion using the ASTM G99 standard with the pin-on disk device of Turkeyus Podwt, the schematic picture of which is given in Figure 2c.

The wear parameters were chosen as applied load 10 N, the sliding speed 0.4 m / s and the sliding distances 250 m, 5000 m and 1000 m. staked grit sandpaper was used as abrasive. Mass Losses from the sample after wear were determined by weighing the residue on a balance with a sensitivity of 0.0001 mg.

3. Results and Discussion

3.1. Microstructure

The optical microscope, SEM pictures of the coating layers are shown in Figure 3 a, c, d and in Figure 3b, the EDS result table in the SEM image.

As seen in Figure 4, the XRD result containing the phase compounds obtained in the coating layer is given.

It was observed that the coating zone did not contain any adverse effects such as cracks and pores. The feed rate and energy inputs used in PTA surface coating process melted the substrate material together with the coating material, resulting in metallurgically bonded coatings [35]. However, with the increasing current value, the increase of energy input increased the melting of the substrate material.

It is estimated that the melting depth has increased in parallel with the increase in the current value and the increase in the melting rate [9].

In the coating process, the tungsten electrode in the plasma arc welding torch was used as heat source. The method allows the formation of a liquid bath with the coating layer and the substrate melting together with the start of the arc. It is based on the rapid solidification of the liquid bath with the advancement of the torch. **Fu Liu et al.** stated that with the advancement of the torch in the coating process with PTA, the melt at the bottom of the melting pool would result in solidification in the form of a fusion line. They also noted that with the formation of the fusion line, interdiffusion occurred between the coating layer and the substrate, and a high-quality metallurgical bond was formed [2]. Diffusion between the substrate and the coating layer appears to have been successful. As shown in the optical microscope picture, deep lines seen in the substrate region are thought to be traces of rolling. In the coating area, it was determined that dendritic structures were formed intensely together with the eutectic structure.

The diffusion occurring in the solid with the solidification of the liquid bath changes the distribution of the dissolved substrate and the elements of the coating layer. The dendrite formed after solidification causes a minimum soluble content in the arms [36]. Dendrites occurring in the form of primary and secondary arms in metal or alloy elements are the most frequently observed microstructure in solidified metals and other materials. While rapid cooling produces thin dendrites, slow cooling affects the properties of the materials by providing large and coarse dendrites [37-39].

Dendritic structures formed in the form of leafy, cellular and branched shapes at the same time, especially in the region close to the interface and in the coating area, are more clearly seen in SEM pictures given in Figure 3b. The dendritic arms formed showed a developed perpendicular to the coating layer.

This liquid bath was determined after XRD analysis that substrate elements and coating material formed hard phases such as FeB, Fe₂B and CrB after solidification.

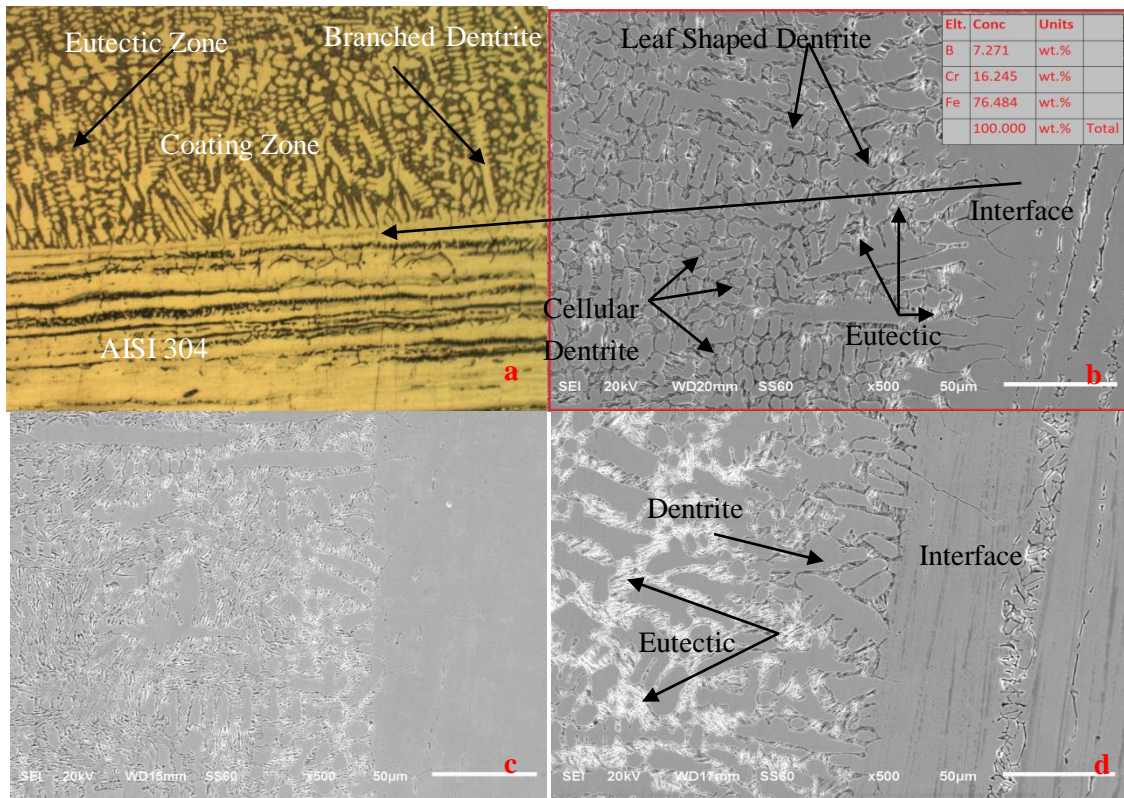


Figure 3: (a) Picture of Optical Microscope, (b) Boron1 coating zone SEM picture and EDS table, (c) Boron2 coating zone SEM picture, (d) Boron3 coating zone SEM picture

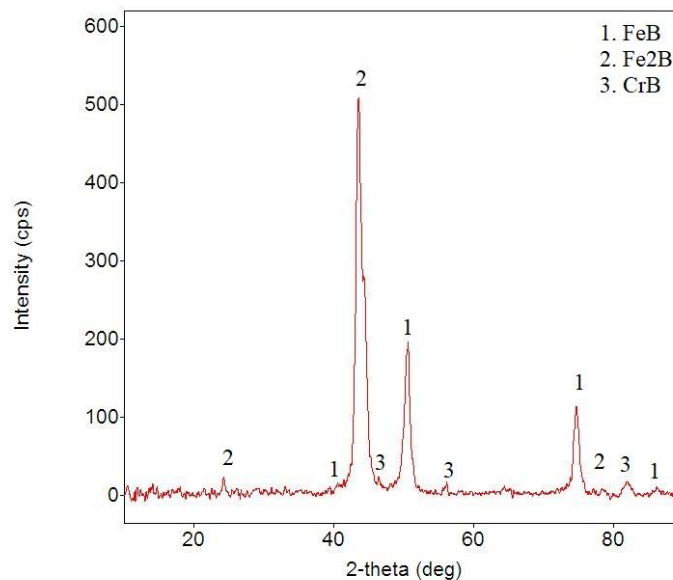


Figure 4: XRD result

In Figure 3b,c and d SEM picture of the coating zone and 3b SEM picture EDX result are given. The interface is evident in SEM pictures. The coating zone consists of dendrite and eutectic structures. Dendrite structures are observed to be mostly composed of cellular dendrites and leaf-shaped dendrites. As shown in Figure 3 SEM picture, with the high temperature occurring as a result

of plasma arc temperature, diffusion transitions have occurred from the coating layer to the base material and from the base material to the coating layer [35]. Figure 4 presents the XRD analysis result. It was determined that FeB, Fe₂B and CrB compound phases are formed.

As a result of EDS analysis, wt. 7,271% B, wt. 16,245% Cr and wt. 76,484% Fe elements were determined. According to these results, when Fe-B-Cr phase binary and ternary diagrams are examined in Figure 5 SEM-EDS, it is thought that FeB, Fe₂B and CrB compound phases are formed. Homolová et al. stated that chromium has solubility in iron borides and iron in chromium borides, as a result of which Cr₂B, Cr₅B₃, CrB, Cr₃B₄, CrB₂ and CrB₄, two iron borite Fe₂B and FeB phase compounds are formed in the isothermal section study of the B-Cr-Fe triple phase system, [40]. In the study Gür et al. conducted, they stated that FeCrC TIC, SIC and B₄C powders were melted as a result of PTA source energy after the solidification, as a result of EDS analysis in micro-structure EDS analysis, Fe,Cr,B,Si elements were formed, and in XRD results, FeB, Fe₂B, Fe₃(C, B), C₃B₆ phases applied for surface coating were formed [41]. As a result of this study, it is thought that there are probably the same phase compounds in their structures that have similar results with our EDS analysis.

As a result of the literature review, the authors match the phase compounds obtained after their analysis with the phase compounds obtained after XRD analysis in this study.

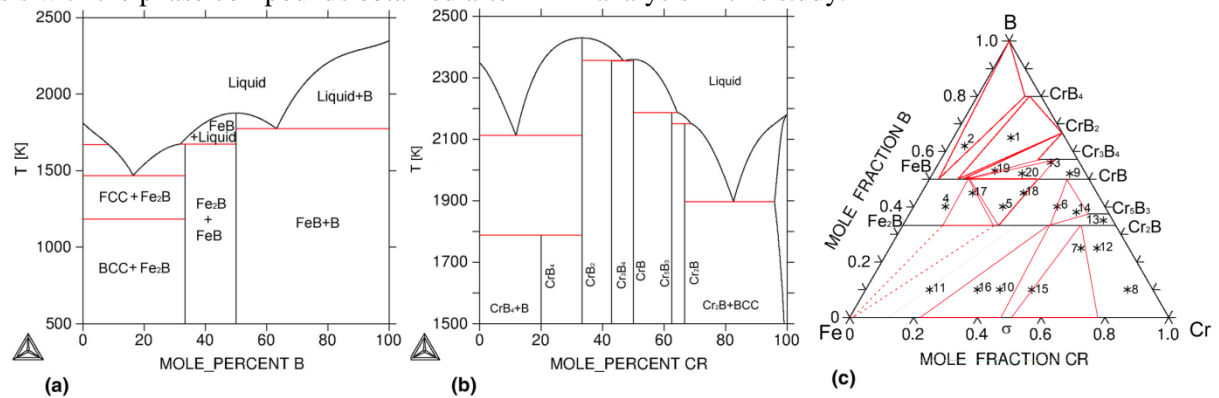


Figure 5: a) Fe-B binary, b) Fe-Cr binary c) Fe-B-Cr ternary phase diagram system [40].

3.2. Surface Wear

Other processes such as load, sliding distance, sliding time, lubrication status, material pair and coating methods applied in the wear of the materials are very important parameters. Some of these parameters are important when producing materials and some are important when making new processes such as coating on the produced material. The rest can be intervened in the wear test device. When these parameters are considered as a whole during the experiment, the important thing is the heat released during the friction, whether the tribo surface is formed, the friction coefficient value and the loss of mass or shape have changed [42]. According to the parameters specified in Table 1 on AISI 316 L stainless steel, the friction coefficients were measured during the wear tests of the materials coated with Boron. In Figure 6, the friction coefficient measured for 2250 s in abrasive wear experiments is given.

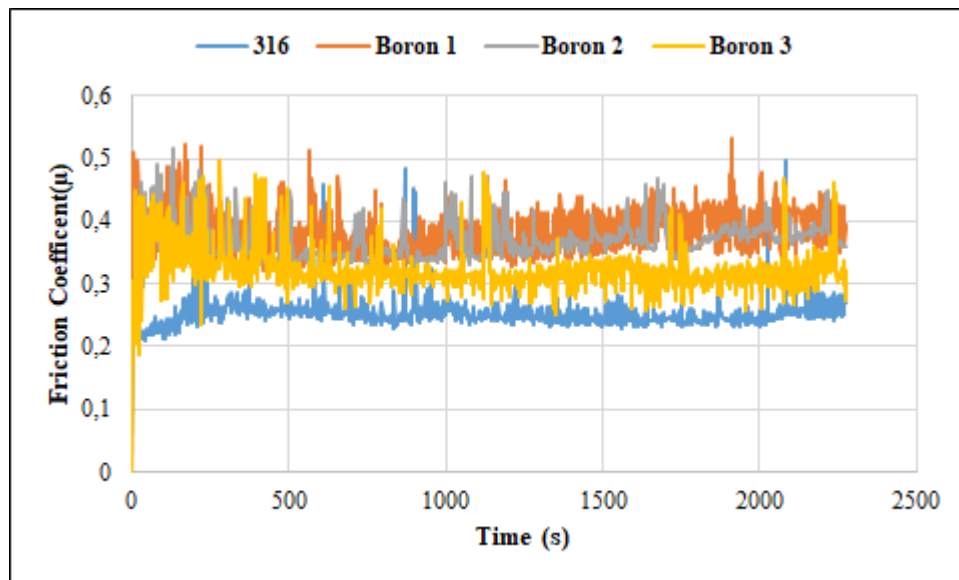


Figure 6: Graph of friction coefficient depending on time after wear

In abrasive wear experiments, it is seen that fluctuations occur while friction coefficient graph is obtained. In abrasive experiments, the fact that abrasive sanding has some certain pores and that it continuously ruptures materials from the surface of material has been the biggest factor in these fluctuations. When we look at the friction coefficient result of Boron 1 and Boron 2 samples, it is seen that it starts with 0,5 and continues in a stable direction with 0,4. Boron 3 sample, on the other hand, starts with 0,4, and draws a linear graphic with fixed 0,3 value. No difference is observed in values and graphics of friction coefficient obtained for different sliding distances. Accordingly, the average friction coefficients should be taken into account, especially when measuring the friction coefficient. Average friction coefficients of AISI 316 L material and materials coated with Boron1, Boron2 and Boron3 are obtained 0,276; 0.381; 0.368 and 0.324, respectively. According to the average friction coefficient results, it is seen that the friction coefficient of the coated layers is higher than the substrate. Studies have reported that there are opinions that the friction coefficient increases or decreases depending on the wear parameters, and the reason for this is related to the formation of the tribo surface [43]. The tribo surface formed between the wear part and the sliding surface reduces the friction coefficient. In other words, when the load increases, the nominal contact area between the pin and the opposite surface increases, so the increase in the contact temperature leads to softening of the surface, thereby resulting in more sliding movement between the contact surfaces, thus reducing the coefficient of friction [44]. In Figure 7, mass losses due to shear distance are given in abrasive wear tests.

The mass loss graph obtained as a result of the wear analysis is given in Figure 7. As seen in the results, the highest mass loss was obtained from the AISI 316L stainless steel uncoated sample. It is seen that losses of approximately the same value occurred in the coated samples. Wear losses increased due to the sliding distance and this is an expected case. As shown in the graph in Figure 7, the lowest weight loss value at 250 m distance was obtained in Boron2 sample with approximately 5 mg, while the highest value was obtained from uncoated AISI 316L sample with a value of 13 mg.

While the distance was about 1000m, the lowest weight loss value was obtained with Boron2 sample with approximately 25 mg, while it was found that there was a loss of approximately 45 mg in the uncoated AISI 316 L sample.

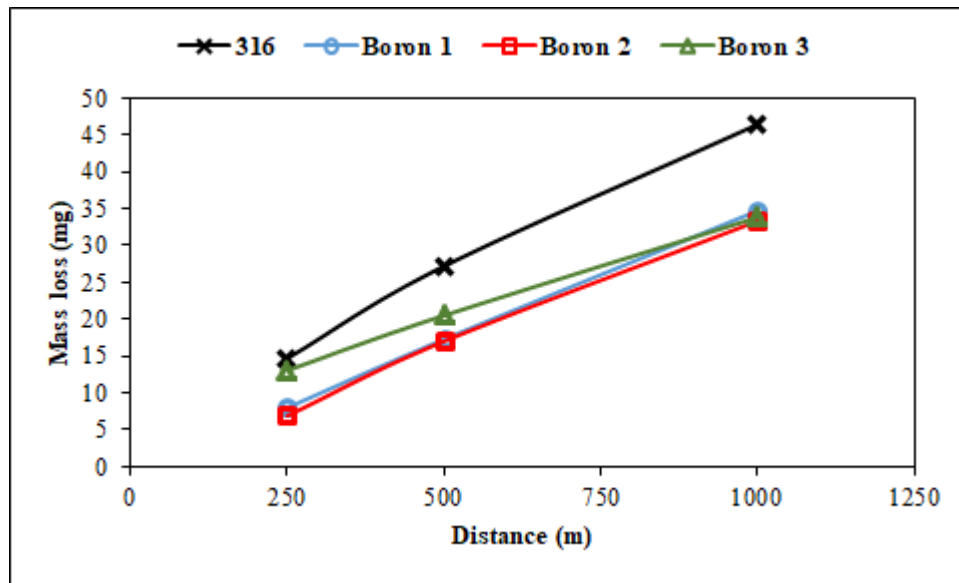


Figure 7: Mass loss graphic based on post-wear distance

According to these results, it is thought that hard boride structures formed as a result of coating with boron reduce the wear losses. An inverse proportion was found between mass loss and friction coefficient. The main reason for this inverse ratio is thought to be caused by hard boride layers formed on the surface. Kainz et al. stated that the addition of B, C or a combination of these during their surface treatment resulted in an increase in mechanical properties [45]. Çelik and Kilickap stated that hard particles also improved their tribological properties as they increased the hardness of the material [46]. With the results obtained, the surface losses of boron-coated samples were less than that of the uncoated sample. According to the results, it was determined that the coated samples had better abrasion resistance.

4. Conclusions

In this study, BORON coatability on AISI 316L steel surface was investigated by Plasma Arc Welding method. For this purpose, the following results have been achieved depending on the factors affecting the coating process, microstructure and abrasion results at different current values.

1. It has been determined that less mass loss has occurred in the coated samples compared to the uncoated sample as can be seen in the graph obtained.
2. 316 LL stainless steel with low hardness and weak abrasion resistance is thought to give more efficient results as a result of coating process with these materials.
3. From the microstructure analysis after coating, it is seen from the microstructure pictures that a good bond has been formed as a result of successful diffusion between coating layer in the materials coated with boron.

4. It has been determined that dense dendritic arms and eutectic structures have been formed between the coating samples, especially in the coating area, and the formed dendritic structures have been perpendicular to the coating layer.
5. As a result of XRD analysis, it was determined that the microstructure consists of CrB, F2B and FeB phase compounds.

References

- [1] L. Bourithis L., G.D. Papadimitriou D.G.(2009). The effect of microstructure and wear conditions on the wear resistance of steel metal matrix composites fabricated with PTA alloying technique. *Wear* 266,1155–1164, doi:10.1016/j.wear.2009.03.032
- [2] Yuan-Fu Liu, Zhi-Cheng Feng, Fei Pu, Zhi-Ying Xia, Guang-Bao Sun, Long-Hua Zhang, Chen-Xiao Shi, Zheng Zhang. (2018). Microstructure and dry-sliding wear properties of TiC/CaF₂/γ-Ni selflubricating wear-resistant composite coating produced by co-axial powder feeding plasma transferred arc (PTA) cladding process. *Surface & Coatings Technology* 345, 61–69, <https://doi.org/10.1016/j.surfcoat.2018.04.003>
- [3] Fernandes F., Cavaleiro A., Loureiro A. (2012). Oxidation behavior of Ni-based coatings deposited by PTA on gray cast iron, *Surface & Coatings Technology* 207, 196–203, doi:10.1016/j.surfcoat.2012.06.070
- [4] Gür K.A., Kaya S. (2017) "PTA Kaplamalarda Abrasive Aşınma Davranışının Değerlendirilmesinde; Bir Taguchi Yaklaşımı" *F.Ü. Mühendislik Bilimleri Dergisi* 29(2) 195-202
- [5] Buytoz, S., Yildirim, M. M., & Eren, H. (2005). Microstructural and microhardness characteristics of gas tungsten arc synthesized Fe–Cr–C coating on AISI 4340. *Materials Letters*, 59(6), 607-614.
- [6] Islak, S., Kir, D., Buytoz, S., Özorak, C., Akkaş, M., Çaligülü, U., Yildirim, M. M. (2015). Yüksek Hızlı Oksi Yakıt İle Üretilen Wcco-Mo Esaslı Kaplamaların Mikroyapı Karakterizasyonu. *Pamukkale University Journal of Engineering Sciences*, 21(8).
- [7] Lisowski, W., Hemmes, H., Jäger, D., Stöver, D., & van Silfhout, A. (1992). Interaction between plasma sprayed YBaCuO and nimonic substrates. *Applied surface science*, 62(1-2), 13-20
- [8] Apay S., Gülenç B. (2013). Kobalt Bazlı Tozların PTA Yöntemiyle Düşük Karbonlu Çelik Üzerine Kaplanması ve Kaplama Bölgesinin İncelenmesi, *Düzce Üniversitesi Bilim ve Teknoloji Dergisi* 1.1: 77-87.
- [9] Buytoz S., Orhan A., Gür K.A. and Caligulu U., (2013), Microstructural Properties of Fe-Cr-C and B₄C Powder Alloy Coating on Stainless Steel by Plasma Transferred Arc Weld Surfacing, *Arabian Jou. for Sci. and Eng.(ASJE)*, 38(8), 2197-2204 DOI:10.1007/s13369-013-0599-9

- [10] Hou, Q. Y., J. S. Gao, F. Zhou (2005). Microstructure and wear characteristics of cobalt-based alloy deposited by plasma transferred arc weld surfacing. *Surface and Coatings Technology* 194.2: 238-243.
- [11] Bourithis, E., A. Tazedakis A., Papadimitriou G. (2002). A study on the surface treatment of "Calmax" tool steel by a plasma transferred arc (PTA) process. *Journal of Materials Processing Technology* 128.1: 169-177.
- [12] Deuis, R. L., J. M. Yellup J.M., C. Subramanian C. (1998). Metal-matrix composite coatings by PTA surfacing. *Composites science and technology* 58.2: 299-309.
- [13] Kucita P., Wang S.C., Li W.S., Cook R.B., Starink M.J. (2019). The effects of substrate dilution on the microstructure and wear resistance of PTA Cu-Al-Fe aluminium bronze coatings, *Wear* 440-441, 203102, <https://doi.org/10.1016/j.wear.2019.203102>
- [14] Deng X., Zhang G., Wang T., Ren S., Shi Y., Bai Z., Cao Q. (2019). Microstructure and oxidation resistance of a multiphase Mo-Si-B ceramic coating on Mo substrates deposited by a plasma transferred arc process, *Ceramics International* 45, 415–423, <https://doi.org/10.1016/j.ceramint.2018.09.182>
- [15] Dai W., Miao Y., Li J., Zheng Z., Zeng D., Huang Q. (2016). Investigation on morphology and micro-hardness characteristic of composite coatings reinforced by PTA copper alloying on nodular cast iron, *Journal of Alloys and Compounds* 689, 680-692, <http://dx.doi.org/10.1016/j.jallcom.2016.08.007>
- [16] Deng X., Zhang G., Wang T., Ren S., Li Z., Song P., Shi Y. (2019). Characterization and oxidation resistance of B-modified Mo₃Si coating on Mo substrate, *Journal of Alloys and Compounds* 807, 151693, <https://doi.org/10.1016/j.jallcom.2019.151693>
- [17] A. K. Gur, C. Ozay, A. Orhan, S. Buytoz, U. Caligulu, and N. Yigitturk (2014) "Wear Properties of Fe-Cr-C and B₄C Powder Coating on AISI 316 Stainless Steel Analyzed by the Taguchi Method, *Materials Testing*, 56(5), 393-398
- [18] Gür K.A., (2013) "Investigating Wear Behavior By Using Taguchi Method FeCrCB₄C Powder Alloys Coating By Plasma Transferred Arc Weld Surfacing", *Materials Testing*, 55(6): 462-467
- [19] Hou Q.Y., He Y.Z., Zhang Q.A., Gao J.S. (2007). Influence of molybdenum on the microstructure and wear resistance of nickel-based alloy coating obtained by plasma transferred arc process." *Materials and Design* 28, 1982–1987
- [20] Liu Y. F., Mu J. S., Xu X. Y., Yang S. Z. (2007). Microstructure and dry-sliding wear properties of TiC-reinforced composite coating prepared by plasma-transferred arc weld-surfacing process. *Materials Science and Engineering: A*, 458(1), 366-370.
- [21] Bourithis L., Papaefthymiou S., Papadimitriou G.D. (2002). Plasma transferred arc boriding of a low carbon steel: microstructure and wear properties. *Applied Surface Science* 200.1: 203-218.

- [22] Iakovou R., Bourithis L., Papadimitriou G.(2002). Synthesis of boride coatings on steel using plasma transferred arc (PTA) process and its wear performance. *Wear* 252.11: 1007-1015.
- [23] Buytoz S., Ulutan M., Kurt B. Islak S., Somunkıran İ. (2010). Plazma Transferli Ark Kaynak Yüzey İşlemiyle AISI 304 Paslanmaz Çelik Yüzeyine WC-Ni-B4C Kompozit Kaplamasının Mikroyapısal Karakteristiği. *e-Journal of New World Sciences Academy*, Volume: 5, Number: 1, Article Number: 1A0063
- [24] Tosun, G. (2011). 1010 Çeliğinin Ni-WC Tozları ile PTA Yöntemi Kullanılarak Kaplanması." 6 th International Advanced Technologies Symposium (IATS'11), 16-18 May 2011, Elazığ, Turkey 126-131
- [25] Acevedo-D_avila J.L., Mu~noz-Arroyo R., Hdz-García H.M., Martinez-Enriquez A.I., Alvarez-Vera M., Hern_andez-García F.A. (2017) Cobalt-based PTA coatings, effects of addition of TiC nanoparticles, *Vacuum* 143, 14-22, <http://dx.doi.org/10.1016/j.vacuum.2017.05.033>
- [26] Mehmet AY M.G., Çelik N.O. (2019) Inspection of nickel-based boron carbide PTA coatings on AISI 4140 steel, *Industrial Lubrication and Tribology*, 71/4, 548–556, DOI 10.1108/ILT-06-2018-0224.
- [27] Er Ü., Bilal Par B. (2004). Bor Yayınımla Yüzeyi Sertleştirilmiş AISI 1030 ve AISI1050 Çeliklerinin Abrazif Aşınma Dayanımlarının İncelenmesi. *Osmangazi Üniversitesi Müh.Mim.Fak.Dergisi C.XVII, S.1.*
- [28] Uluköy A., Can Ç.A.. (2006). Çeliklerin Borlanması. *Pamukkale Üniversitesi Mühendislik Bilimleri Dergisi*, 12.2: 189-198.
- [29] Ozbek I. (1999). Borlama Yöntemiyle AISI M50, AISI M52 Yüksek Hız Çeliklerinin ve AISI W1 Çeliğinin Yüzey Performansının Geliştirilmesi, *Doktora Tezi, Sakarya Üniversitesi, Sakarya.*
- [30] Uluköy, A., Can Ç.A. (2006). Çeliklerin Borlanması. *Pamukkale Üniversitesi, Mühendislik Bilimleri Dergisi*, 12 (2) 189-198.
- [31] S. Anil Kumar Sinha. (1991). "Boriding(Boronizing)." *ASM International, ASM Handbook.4: 437-447.*
- [32] Diktaşlı E. (2014). Bazı Alaşımli Çeliklerin Yüksek Sıcaklık Aşınma Davranışına Borlama İşleminin Etkisi. *Yüksek Lisans Tezi, İstanbul Teknik Üniversitesi Fen Bilimleri Enstitüsü.*
- [33] Ünüvar F. (2013). Saf Kobaltın Borlama Özelliklerinin İncelenmesi, *Yüksek Lisans Tezi, Süleyman Demirel Üniversitesi, Isparta.*
- [34] Çalık, A. (2005). Termokimyasal Borlama Yöntemleri ve Önemi. *4th International Advanced Technologies Symposium, 839-844, Konya.*

- [35] Yildiz T., Gür K.A., (2011) Microstructural Characteristic Of N₂ Shielding Gas in Coating FeCrC Composite to The Surface of AISI 1030 Steel with PTA Method, Archives of Metallurgy and Materials, 56, 723-729
- [36] Bower F.T., Brody D. H., M. Flemings C.M. (1966). Measurements of Solute Redistribution in Dendritic Solidification. Transactions of the metallurgical society of aime, 624-volume 236.
- [37] Choudhury A., Reuther K., Wesner E., August A., Nestler B., Rettenmayr M.. (2012). Comparison of phase-field and cellular automaton models for dendritic solidification in Al–Cu alloy. Computational Materials Science 55, 263–268, doi:10.1016/j.commatsci.2011.12.019.
- [38] Jabbari Behnam M.M., Davami P., Varahram N. (2010). Effect of cooling rate on microstructure and mechanical properties of gray cast iron. Materials Science and Engineering A 528 (2010) 583–588, doi:10.1016/j.msea.2010.09.087.
- [39] Karagöz Ş., Rıdvan Ymanoğlu R., Atapek H. Ş. (2009). Atomize Tozlarda Katılma ve Mikroyapısal Karakterizasyon, Pamukkale Üniversitesi Mühendislik Bilimleri Dergisi, Cilt 15, Sayı 3, Sayfa 309-316.
- [40] Homolová V., Hiripová L. (2017). Experimental Investigation of Isothermal Section of the B-Cr-Fe Phase Diagram at 1353K, Hindawi Advances in Materials Science and Engineering Volume 2017, Article ID 2703986, 7 pages <https://doi.org/10.1155/2017/2703986>
- [41] Gür K.A., Cengiz H.M., Taşkaya S.(2019). Mikroalaşımli Hardox 400 Çelik Malzemenin plazma Transferli Ark Kaynak Yöntemiyle Alaşımlandırılması ve İncelenmesi. DÜMF Mühendislik Dergisi 10:3 (2019) : 969-979 , doi: 10.24012/dumf.529451.
- [42] Demir E.M., Çelik H.Y. , Erol K. (2019). Effect of matrix material and orientation angle on tensile and tribological behavior of jute reinforced composites. Materials Testing, 61(8), 806-812.
- [43] Çelik H.Y., Demir E.M., Erol K., Kalkanlı A. (2020). Investigation of wear behavior of aged and non-aged SiC-reinforced AlSi7Mg2 metal matrix composites in dry sliding conditions. Journal of the Brazilian Society of Mechanical Sciences and Engineering, 42(1), Article Number 8, 1-9.
- [44] Çelik H.Y, Seçilmiş K. (2017). Investigation of wear behaviours of Al matrix composites reinforced with different B₄C rate produced by powder metallurgy method. Advanced Powder Technology, 28(9), 2218-2224, Doi: 10.1016/j.apt.2017.06.002.
- [45] Christina Kainz, Nina Schalk, Michael Tkadletz, Christian Mitterer, Christoph Czettel (2019). The effect of B and C addition on microstructure and mechanical properties of TiN hard coatings grown by chemical vapor deposition. Thin Solid Films, 688, 137283, <https://doi.org/10.1016/j.tsf.2019.05.002>
- [46] Çelik H.Y. , Erol K (2019). Hardness and wear behaviours of Al matrix composites and hybrid composites reinforced with B₄C and SiC. Powder Metallurgy and Metal Ceramics, 57(9-10), 613-622.

PERFORMANCE ANALYSIS OF COOLING SYSTEM WITH HORIZONTAL TYPE GROUND SOURCE HEAT PUMP FOR DIYARBAKIR CONDITIONS


Fatih KOÇYİĞİT^{1*}

In this study, the performance of the horizontal type ground source heat pump cooling system in the summer was analyzed for cooling the testing area with a size of 9x8x2.8m in Diyarbakır province with a warm climate. Energy and exergy analysis was applied to the system and system units by examining the results obtained in the summer in the evaluated system. The monthly and seasonal mean values of the data in the summer (01.06.2018 / 30.08.2018) were taken for 11 node points determined in the installed system. In the energy analysis performed with the results obtained, it was calculated that the energy loss in the system was 2.499kW and the energy efficiency 76.86%. For the system units, the unit operating with the lowest energy efficiency was determined as the compressor. According to exergy analysis applied to the system, it was calculated that the exergy loss of the system was 2.150 kW and the second law efficiency was 20.70%. The compressor was also determined as the unit with the highest exergy loss in the system. Compressor should be prioritized for improvement studies to be planned according to both energy and exergy analysis results. The COP value of the system was found to be 4.05, and it was determined that the system, the use of which was examined in the summer, could be used for Diyarbakır province.

Key words: *Groud Source Heat Pump, Horizontal Type Ground Source Heat Pump, Energy Analysis, Exergy Analysis,*

1. Introduction

Due to gradual reduction of energy resources and the rapid increase in energy prices nowadays, efficient use of energy has become a necessity. The increase in harmful effects of fossil fuel-powered systems on the environment along with the increasing energy needs in parallel with the growing population has caused users to search for different solutions with the developing technology [1]. In this context, ensuring energy efficiency has become very important for the efficient use of energy and the energy economy. Most of the energy produced is consumed in the heating and cooling of the houses. Many studies are carried out to use energy more efficiently in the world and alternative solutions are sought for conventional air conditioning systems. Heat pumps are preferred in many applications and are increasingly used due to their high usage efficiency and environmentally friendly technologies in compared to commonly used conventional air conditioning systems. Ground source heat pump systems are mainly preferred for the air conditioning of the houses. In previous studies, it was indicated that the

¹ Department of Airframe and Powerplant, School of Civil Aviation, University of Dicle, Turkey, TR (fatih.kocyigit@ule.edu.tr) 
<https://orcid.org/0000-0001-6383-3163>

energy consumed in the air conditioning of the houses could be reduced with the help of heat pumps, and thus, energy could be used more efficiently. In the literature, many studies were carried out on the use and evaluation of heat pumps for air conditioning. Kıncaç and Temir [2] carried out a study on the dimensioning of vertical type ground source heat pump system for a villa. Akbulut et al. [3] performed the energy and exergy analysis of the integrated wall cooling system with vertical type ground source heat pump in the Renewable Energy House at Yıldız Technical University. Furthermore, Akbulut et al. [4] performed the exergoeconomic and environmental analyses of the integrated wall cooling system with vertical type ground source heat pump used in the cooling season. Nevertheless, Akbulut et al. [5] performed the exergy, exergoeconomic and environmental analysis of the integrated wall heating system with a vertical ground source heat pump in the winter for the specified testing area. In their study, they indicated that the vertical type ground source heat pump system could be used for Istanbul province. Ünal et al. [6] performed the energy, exergy and exergoeconomic analysis of the solar powered vertical type ground source heat pump system for the heating season in Midyat district of Mardin province. In their study, they reported that it was appropriate to use the solar powered vertical type ground source heat pump system in Mardin province. Ünal and Temir [7] performed the exergoeconomic analysis of the cooling system with a ground source heat pump for the testing area they determined in Mardin province. Hepbaşlı et al. [8] conducted experimental studies to examine the performance of a vertical type ground source heat pump with a depth of 50 m in order to meet the air conditioning needs of a 65 m² room in İzmir province. Nagano et al. [9] conducted studies to improve the design of the ground source heat pump in Sapporo. In their study, they also compared CO₂ emission data and determined the payback period for the specified region of the system they designed as 9-14 years. Niğdelioğlu [10] evaluated the system performance with parameters affecting a ground source heat pump system used for cooling in the summer in Kütahya province. As a result of the experimental analyses, they determined that the mean COP value of the ground source heat pump system used was 3.41, and they indicated that the system could be used for Kütahya province. Özgener and Hepbaşlı [11] conducted studies on performance evaluation by modeling the ground source heat pump system. In their studies, they performed the performance analysis of the vertical type and horizontal type ground source heat pump systems that they modelled, and they compared the systems with the results obtained. Karabacak et al. [12] conducted an experimental investigation to determine the performance of the vertical type ground source heat pump system in the summer in Denizli. In their study, the COP values were obtained as 3.1–4.8 for the system investigated. Zhai and Yang [13] experimentally analyzed the ground source heat pump system with a cooling capacity of 500 kW in Shanghai. According to the results of the analyses, they determined that the system to be installed would have a two-year payback period. In his study, Kılıç [14] designed a ground source heat pump system by using two different methods to meet both the heating and cooling needs of a two-storey villa in Adana. He analyzed the designed system for both summer and winter seasons. Ünal and Akan [15] performed the energy and exergy analysis of the solar powered vertical type ground source heat pump in Mardin province depending on the experimental data obtained. In their analysis, they indicated that the system unit with the highest exergy loss rate was the compressor. Esen [16] designed a vertical type ground source heat pump system with drilling wells of different depths, 30 m, 60 m and 90 m, to be used in the garden of a house in the summer and winter seasons in Elazığ. He compared the performance of three systems by using different artificial neural network methods. With the results obtained in the summer and winter seasons, he indicated that the ground source heat pump system with a depth of 90 m had the highest system performance. Isık et al. [17] an analysis was made according to the second law of thermodynamics, to an existing thermal power

plant that uses lignite fuel. In their studies, useful power, reversible power and irreversibility amounts were determined for the turbine from the power plant components forming the system and the overall efficiency of the system was calculated

In this study, unlike the studies in the literature, a horizontal type ground source heat pump cooling system was built Diyarbakır province Bismil county, which has a warm climate and provides its needs for air conditioning mainly with fossil-based fuels. Depending on the results of the experimental studies conducted during the summer in the system built, energy and exergy analysis was applied to the system and its units and the usability of the system analyzed in this county was evaluated.

2. Material And Method

In this study, a horizontal type ground source heat pump was used for testing in order to meet the cooling needs of a 9x8x2.8 m ground floor of a workplace in Diyarbakır, Bismil county, and a thermodynamic analysis of the system was made for the summer season. The test facility has nine units consisting of compressor, condenser, evaporator, throttle valve, two circulation pumps, horizontal type underground heat exchanger, accumulation tank and fan coil panel and 11 node points where measurements are taken. The test facility is used to meet the cooling need of the location. In addition, temperature measurements were made with PT-100 type thermocouples (sensitivity $\pm 1^\circ\text{C}$) placed in 11 node points determined in the system and the flow rates of the fluid were measured with GT-TD-20 type $\frac{3}{4}$ " PVC turbine flowmeters (sensitivity 1%) placed after the pumps and the refrigerant fluid flow was measured from the controller of the heat pump. Pressure measurements in the system were made with the help of manometers on the heat pump. The data obtained by the measurements were recorded instantaneously with the help of 24 channel datalogger. The electricity meter connected to the network is used for the measurements of the electricity consumption of the compressor, pumps and fan coil panel. The data obtained were averaged over a 3-month period determined for the summer season, and evaluation was performed for the system and its units. The general scheme of the system used for cooling is presented in Figure 1. During the theoretical operation of the system, the fan coil panel transfers the heat it extracts from the space (\dot{E}_{FCP}) to the evaporator. Then, heat transfer fluid is converted into gas with the heat extracted with evaporator (\dot{E}_L). When the heat transfer fluid is in gaseous state, its temperature and pressure are increased by the compression process performed in the compressor and transported to the condenser. The heat generated during the condensation process in the condenser (\dot{E}_H) is transferred to the underground circuit (\dot{E}_G). Then the refrigerant passes through the throttle valve and the cycle continues in this way.

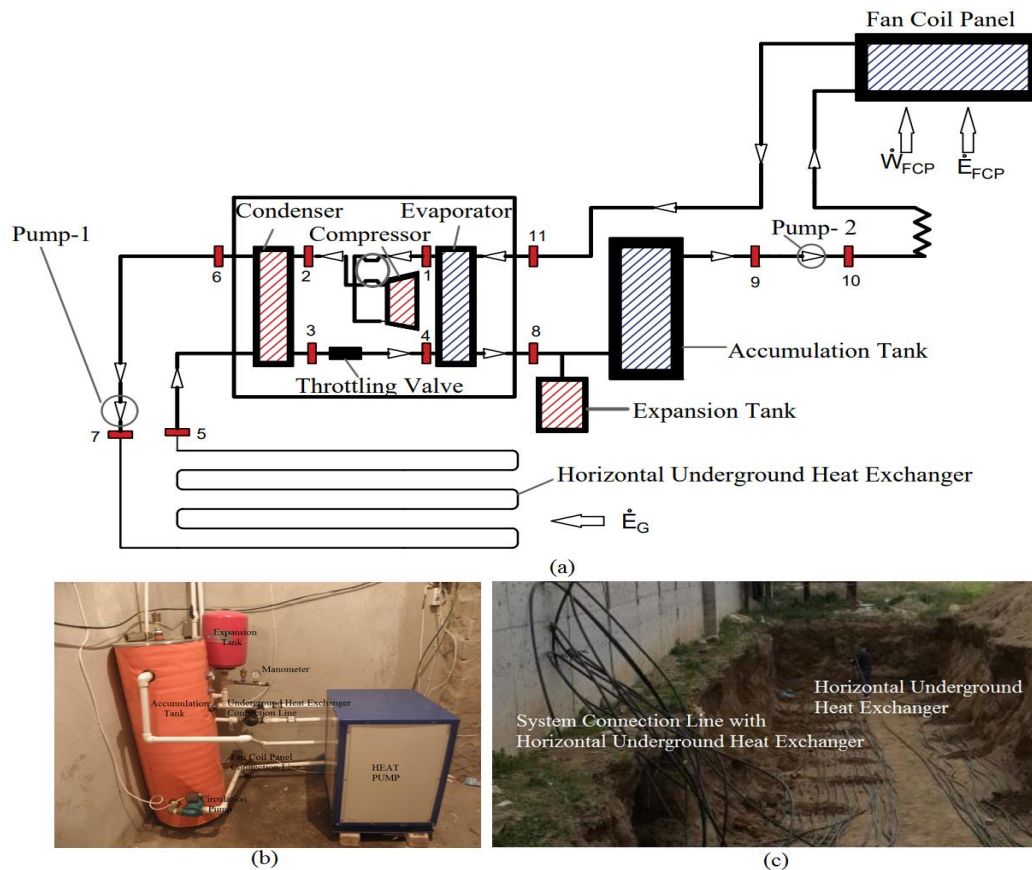


Figure 1. a) Flow chart of the system in the summer season b) Heat pump room c) Horizontal underground heat exchanger

The information about the features and assumptions of the system used in the experimental study are presented below:

- The system analyzed is a system that complies with the continuous-flow open system model. The cooling capacity of the horizontal type ground source Restherma brand heat pump used in the system to meet the cooling needs of the test site is given as 9 kW in the catalog data.
- For the horizontal type underground heat exchanger, 15 m long and 10 m wide, 150 m² area was laid horizontally to a depth of 2 m. A total of 730 m long PE 80 type pipe was used for the horizontal type underground heat exchanger. Since the underground heat exchanger was completely surrounded by soil, heat losses in this unit were neglected.
- The heat exchanger I functions as an evaporator. The heat exchanger II functions as a condenser. Scroll type Copeland brand compressor was used in the system. There was no enthalpy loss in the throttle valve ($h_3 = h_4$). The accumulation tank used has a capacity of 200 liters. Heat loss occurred although the accumulation tank had insulation. Accumulation tank was used as a balance tank functioning for cold water storage in the system. In the system, cassette floor type 2 pipe AE 400 model fan coil panel is used.
- Underground heat exchanger in the system, water in the fan coil panel, and refrigerant R407C in the heat pump were used as the heat carrier fluid. While the properties of the water were determined by the EES package program, the properties of the R407C were determined with the help of the Refprop package program.
- In the exergy analysis, reference environmental values were used as $T_0 = 0.01^\circ\text{C}$ and $P_0 = 1$ bar.

2. 1. Analyses

While the first law of thermodynamics is taken as a basis in energy analyses, both the first and second laws of thermodynamics are used together in exergy analyses. The energy balance for the examined system, which fits a continuous-flow open system, is expressed by Equation 1.

$$\dot{E} = H + KE + PE = \dot{m} \left[h + \frac{v^2}{2} + g \cdot z \right] \quad (1)$$

In the system analyzed, the height change was zero, and thus, potential energy was considered zero. Kinetic energy was considered zero since the energy change due to the velocity change of the fluid was very small compared to the internal energy. When potential energy and kinetic energy are neglected, the energy balance is presented by Equation 2.

$$\dot{E} = \dot{m} \cdot h \quad (2)$$

In this study, the expression of energy loss is given by Equation 3.

$$\dot{E}_{\text{loss}} = \dot{E}_{\text{in}} - \dot{E}_{\text{out}} \quad (3)$$

The efficiency of the system or system element (COP: Coefficient of Performance) was found by dividing the value desired to be obtained by the value required to be spent for this purpose.

$$\eta = \frac{\text{value desired to be obtained}}{\text{value required to be spent}} \quad (4)$$

The most useful work that a system can do in a given state is defined as exergy (availability). The term exergy is a feature related to the states of the system and the environment. In this study, only physical exergy equations were used. Physical exergy is given by Equation 5.

$$\dot{E}x = \dot{m} \cdot \Psi = \dot{m} [(h - h_0) - T_0(s - s_0)] \quad (5)$$

Furthermore, the exergy of the work transferred at the system boundaries is equal to its own value. In this context, the exergy expression of the work is presented by Equation 6. The exergy value of the transferred heat is calculated by multiplying its value by the Carnot Efficiency calculated by evaluating the temperature at the system boundary and the ambient temperature. The exergy expression of the transferred heat is presented by Equation 7.

$$\dot{E}x_W = W \quad (6)$$

$$\dot{E}x_Q = Q \left(1 - \frac{T_0}{T} \right) \quad (7)$$

In this study, exergy loss, in other words, exergy destruction is given by Equation 8.

$$\dot{E}x_{\text{loss}} = \dot{E}x_{\text{in}} - \dot{E}x_{\text{out}} = \dot{E}x_{\text{destruction}} \quad (8)$$

In this study, after the exergy loss in each unit of a system was determined, the exergy loss rate was achieved by proportioning the exergy loss of the relevant unit to the exergy loss in the whole system. The exergy loss rate is presented by Equation 9

$$d_k = \frac{\dot{E}x_{\text{loss,unit}}}{\dot{E}x_{\text{loss,system}}} \quad (9)$$

The second law efficiency was defined as expressed in Equation 10 according to the fuel-product principle.

$$\eta_{II} = \frac{\dot{E}x_{\text{product}}}{\dot{E}x_{\text{fuel}}} \quad (10)$$

The equations used in the energy and exergy analysis performed in the study are presented in Table 1.

Table 1. Equations Used in Thermodynamic Analysis

Unit	Energy Balances	Exergy Balances
System	$\dot{E}_{\text{loss}} = \dot{m}_{\text{FCP}}h_{\text{FCP}} + \dot{W}_{\text{in}} - \dot{m}_G h_G$ $\dot{W}_{\text{system}} = \dot{W}_{\text{in}} = \dot{W}_{\text{p1}} + \dot{W}_{\text{comp}} + \dot{W}_{\text{p2}} + \dot{W}_{\text{FCP}}$ $\text{COP}_{\text{system}} = \frac{\dot{E}_G}{\dot{W}_{\text{system}}}$	$\dot{E}x_{\text{loss}} = \dot{m}_{\text{FCP}}\Psi_{\text{FCP}} + \dot{W}_{\text{in}} - \dot{m}_G\Psi_G$ $\dot{W}_{\text{system}} = \dot{W}_{\text{in}} = \dot{W}_{\text{p1}} + \dot{W}_{\text{comp}} + \dot{W}_{\text{p2}} + \dot{W}_{\text{FCP}}$ $\eta_{II} = \frac{\dot{E}x_{\text{product}}}{\dot{E}x_{\text{fuel}}}$
Compressor	$\dot{E}_{\text{loss}} = \dot{m}_1 h_1 + \dot{W}_{\text{comp}} - \dot{m}_2 h_2$	$\dot{E}x_{\text{loss}} = \dot{m}_1 \Psi_1 + \dot{W}_{\text{comp}} - \dot{m}_2 \Psi_2$
Condenser	$\dot{E}_{\text{loss}} = \dot{m}_2 h_2 + \dot{m}_5 h_5 - \dot{m}_3 h_3 - \dot{m}_6 h_6$	$\dot{E}x_{\text{loss}} = \dot{m}_2 \Psi_2 + \dot{m}_5 \Psi_5 - \dot{m}_3 \Psi_3 - \dot{m}_6 \Psi_6$
Evaporator	$\dot{E}_{\text{loss}} = \dot{m}_4 h_4 + \dot{m}_{11} h_{11} - \dot{m}_8 h_8 - \dot{m}_1 h_1$	$\dot{E}x_{\text{loss}} = \dot{m}_4 \Psi_4 + \dot{m}_{11} \Psi_{11} - \dot{m}_1 \Psi_1 - \dot{m}_8 \Psi_8$
Throttling Valve	$\dot{E}_{\text{loss}} = \dot{m}_3 h_3 - \dot{m}_4 h_4$	$\dot{E}x_{\text{loss}} = \dot{m}_3 \Psi_3 - \dot{m}_4 \Psi_4$
Pump 1	$\dot{E}_{\text{loss}} = \dot{m}_6 h_6 + \dot{W}_{\text{p1}} - \dot{m}_7 h_7$	$\dot{E}x_{\text{loss}} = \dot{m}_6 \Psi_6 + \dot{W}_{\text{p1}} - \dot{m}_7 \Psi_7$
Underground Heat Exchanger	$\dot{E}_{\text{loss}} = \dot{m}_7 h_7 - \dot{E}_G - \dot{m}_5 h_5$	$\dot{E}x_{\text{loss}} = \dot{m}_7 \Psi_7 - \dot{E}x_G - \dot{m}_5 \Psi_5$
Pump 2	$\dot{E}_{\text{loss}} = \dot{m}_9 h_9 + \dot{W}_{\text{p2}} - \dot{m}_{10} h_{10}$	$\dot{E}x_{\text{loss}} = \dot{m}_9 \Psi_9 + \dot{W}_{\text{p2}} - \dot{m}_{10} \Psi_{10}$
Acc. Tank	$\dot{E}_{\text{loss}} = \dot{m}_8 h_8 - \dot{m}_9 h_9$	$\dot{E}x_{\text{loss}} = \dot{m}_8 \Psi_8 - \dot{m}_9 \Psi_9$
Fan Coil Panel	$\dot{E}_{\text{loss}} = \dot{m}_{10} h_{10} + \dot{E}_{\text{FCP}} + \dot{W}_{\text{FCP}} - \dot{m}_{11} h_{11}$	$\dot{E}x_{\text{loss}} = \dot{m}_{10} \Psi_{10} + \dot{E}x_{\text{FCP}} + \dot{W}_{\text{FCP}} - \dot{m}_{11} \Psi_{11}$

The mean flow, temperature and pressure values measured at the node points determined in the summer, the enthalpy and entropy values, and the energy and exergy values obtained with the help of determined equations are presented in Table 2.

Table 2. Values Obtained for the Node Points in the Summer

Node Number	1	2	3	4	5	6	7	8	9	10	11
Mass Flow (kg/s)	0.041	0.041	0.041	0.041	0.330	0.330	0.330	0.210	0.210	0.210	0.210
Pressure (bar)	4.90	11.80	11.80	4.90	1.65	1.65	1.65	1.53	1.53	1.53	1.53
Temperature (°C)	8.09	50.48	22.63	2.26	20.48	26.32	26.34	13.75	14.28	14.31	25.12
Enthalpy (kJ/kg)	422.38	444.42	227.61	227.61	85.682	110.71	110.84	59.982	60.169	60.312	105.58
Entropy (kJ/kgK)	17.985	18.149	11.095	11.096	0.303	0.386	0.386	0.206	0.208	0.209	0.366
Energy Rate (kW)	17.318	18.221	9.332	9.332	28.275	36.534	36.577	12.596	12.635	12.666	22.172
Exergy Rate (kW)	6.755	7.475	6.486	6.485	0.976	1.754	1.797	0.788	0.713	0.685	1.186

In addition to the values given in Table 2, the power consumed by the compressor in the winter season is 1.705 kW, the power consumed by each of the circulation pumps is 0.048 kW and the power consumed by the fan coil panel is 0.250 kW. In addition, the heat transferred to the soil is determined to be 8.302 kW and the exergy value is 0.561 kW, the heat drawn from the experimental area with the fan coil panel is 8.750 kW and the exergy value is 0.660 kW. ($\dot{W}_{komp} = 1.705$ kW, $\dot{W}_{P1} = 0.048$ kW, $\dot{W}_{P2} = 0.048$ kW, $\dot{W}_{FCP} = 0.250$ kW, $\dot{E}_G = 8.302$ kW, $\dot{E}_{FCP} = 8.750$ kW, $\dot{E}_{XG} = 0.561$ kW, $\dot{E}_{XFCP} = 0.660$ kW)

For the summer season, the energy analysis of the system units was performed by using the equations presented in Table 1 depending on the values in Table 2. The results of the energy analysis performed for the system and its units are presented in Table 3.

Table 3. Energy analysis results for the system and its units in the summer.

Unit	System	Comp.	Cond.	Evap.	Throtling Valve	Pump-1	UHE	Pump-2	Acc. Tank	Fan Coil Panel
\dot{E}_{in} (kW)	10.801	19.023	46.496	31.504	9.332	36.582	36.577	12.683	12.596	21.666
\dot{E}_{out} (kW)	8.302	18.221	45.866	29.914	9.332	36.577	36.577	12.666	12.635	22.172
\dot{E}_{loss} (kW)	2.499	0.801	0.630	1.590	0.000	0.005	0.000	0.018	-0.039	-0.506
\dot{E}_{fuel} (kW)	10.801	1.705	8.889	9.576	9.332	0.048	8.302	0.048	12.635	9.756
$\dot{E}_{product}$ (kW)	8.302	0.904	8.259	7.986	9.332	0.043	8.302	0.030	12.596	8.750
η (%)	76.86	53.00	92.91	83.40	100.00	89.38	100.00	62.56	99.69	89.69

The values of energy loss amounts along with the energy input and output energy for the system and its units are presented in Table 3. Furthermore, fuel energy amount and product energy amount values of the system and its units and the energy efficiency of the system and system units obtained from these values are also presented. As a result of the analysis, the amount of energy loss in the whole system was determined to be 2.499 kW. The energy efficiency of the system was achieved as 76.86%. According to the results presented in Table 3, the energy efficiency value of the compressor was determined as the unit with the lowest efficiency of the system by 53.00%. Energy loss of system units in the summer is given in Figure 2. The monthly distribution of the amount of energy loss observed in the system for the summer season is presented in Figure 3.

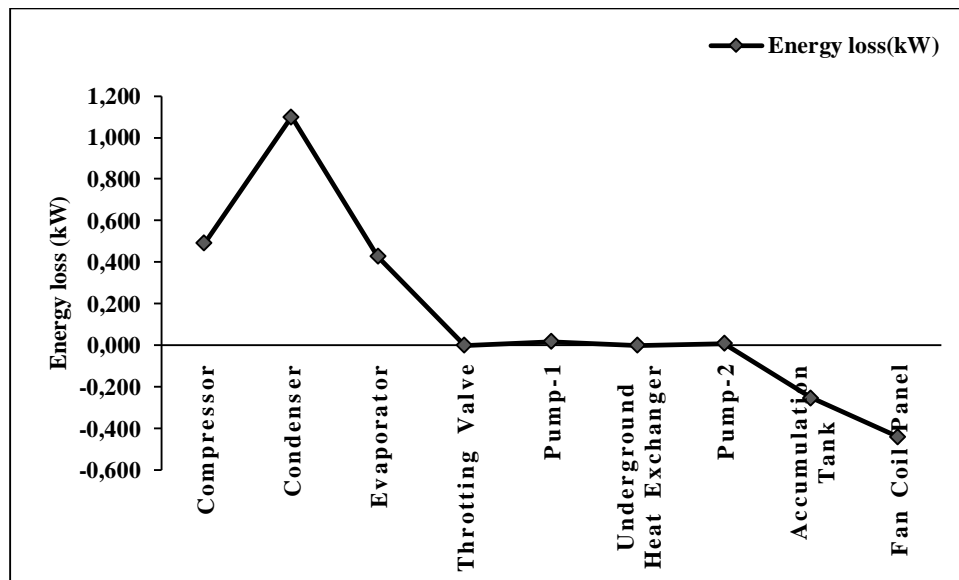


Figure 2. Distribution of energy loss in the system to the system units in the summer.

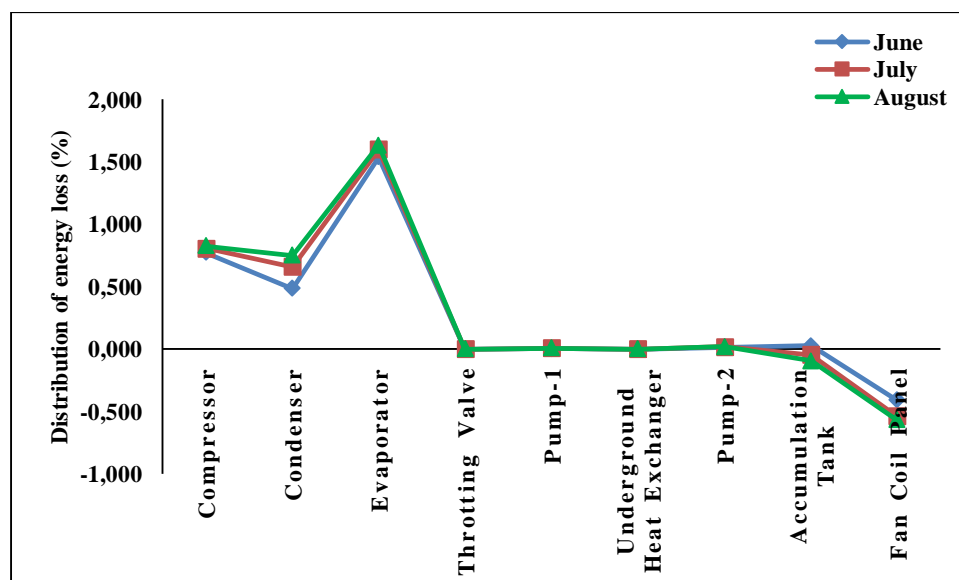


Figure 3. Monthly distribution of the energy loss in the system to the system units in the summer season.

In the assumptions and calculations made for system units in Figure 3, evaporator, compressor, condenser and fan coil panel energy, respectively, were determined as the units with high saving potential. The maximum energy loss for the summer season in the system was determined in the evaporator and compressor by 1.590 kW and 0.801 kW, respectively. In the energy analyses, no energy loss was observed in the underground heat exchanger and throttle valve. Because it was accepted that there was no heat loss in these units. In the summer, there was an average of 0.506 kW energy gain for the Fan Coil Panel and 0.039 kW energy gain for the accumulation tank. The energy analysis results obtained for the summer season of the horizontal type ground source cooling system are presented in Table 4.

Table 4. Monthly energy analysis results for the summer season.

Months worked	June	July	August	Average
$\dot{W}_{comp.}$ (kW)	1.63	1.73	1.76	1.70
\dot{W}_{system} (kW)	1.98	2.08	2.11	2.05
COP_{system}	4.16	4.04	3.95	4.05
$COP_{heat\ pump}$	5.05	4.76	4.71	4.84

According to the results presented in Table 4, it was determined that the average amount of energy consumed by the horizontal type ground source heat pump supported evaporative cooling system in the summer was 2.05 kW, the average amount of energy consumed by the compressor was 1.70 kW and the mean COP value of the heat pump was 4.84.

For the summer season, the exergy analysis of the system units was performed by means of the equations in Table 1 with the values presented in Table 2. The exergy analysis results for the system and its units are presented in Table 5.

Table 5. Exergy analysis results of the system units in the summer.

Unit	System	Comp.	Cond.	Evap.	Throttling Valve	Pump-1	UHE	Pump-2	Acc. Tank	Fan Coil Panel
$\dot{E}_{x_{in}}$ (kW)	2.711	8.460	8.451	7.671	6.486	1.802	1.797	0.761	0.788	1.345
$\dot{E}_{x_{out}}$ (kW)	0.561	7.475	8.239	7.543	6.485	1.797	1.537	0.685	0.713	1.186
$\dot{E}_{x_{loss}}$ (kW)	2.150	0.985	0.212	0.127	0.001	0.005	0.259	0.075	0.075	0.159
$\dot{E}_{x_{fuel}}$ (kW)	2.711	1.705	0.989	0.398	6.486	0.048	0.821	0.048	0.788	0.660
$\dot{E}_{x_{product}}$ (kW)	0.561	0.720	0.778	0.270	6.485	0.043	0.561	0.027	0.713	0.501
η_{II} (%)	20.70	42.228	78.60	68.00	99.98	89.38	68.38	56.94	90.43	75.86

Exergy values of the system units in the summer season are given in Figure 4. The monthly exergy loss distribution of the system units for the summer season is presented in Figure 5. When this table is evaluated, system units can be compared.

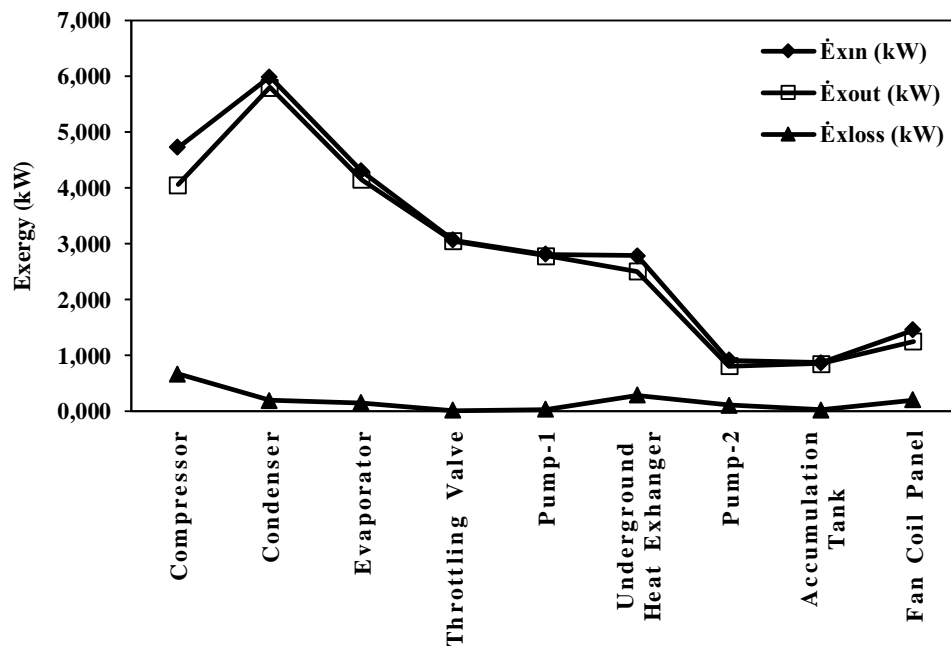


Figure 4. Exergy values of system units in the summer season.

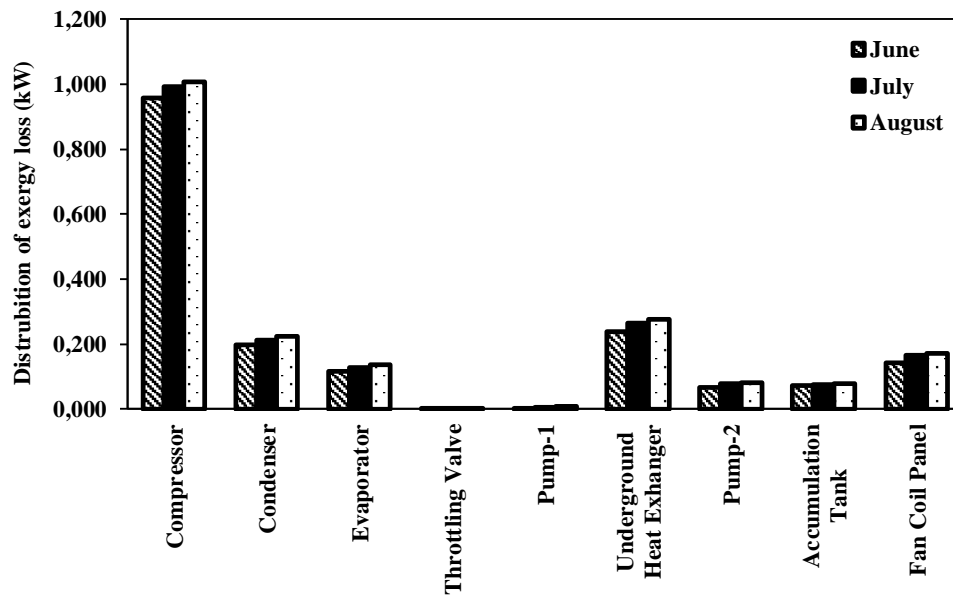


Figure 5. Monthly exergy loss of the system units in the summer.

When Figure 5 was examined, it was observed that the monthly exergy loss amounts of the system units increased in direct proportion to the external air temperature. Maximum amount of exergy loss occurred in the compressor by 0.985 kW. The exergy loss rate values obtained by dividing the exergy loss amount in a unit of the horizontal type ground source heat pump cooling system in the summer by the amount of exergy loss in the whole system are presented in Figure 6.

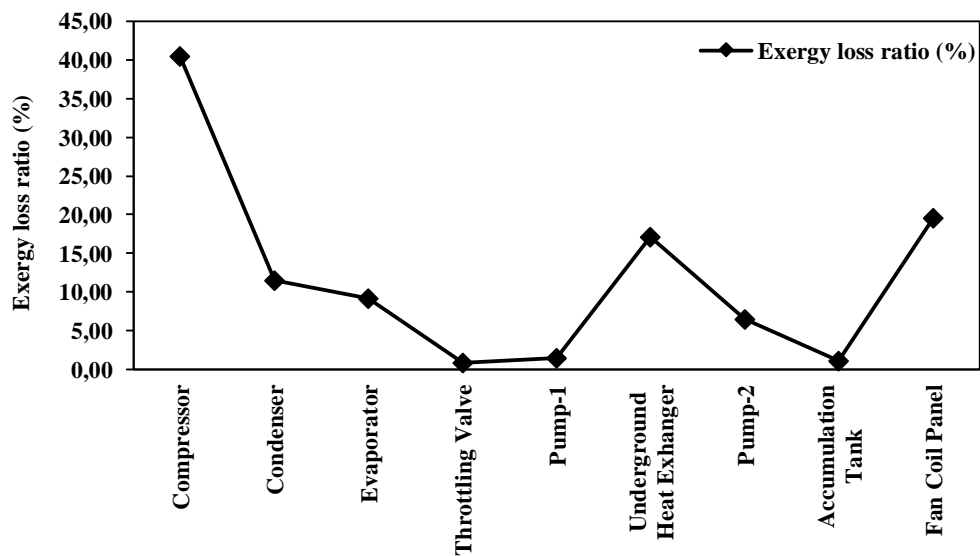


Figure 6. Exergy loss rates of the system units in the summer.

According to the assumptions and thermodynamic calculations made for the summer season in Figure 6, the compressor in the system was the unit with the highest exergy loss rate by 40.51%. In this context, exergy loss rates are among the parameters to be considered first in the improvements considered to be made in the horizontal type ground source heat pump cooling system. The improvements to be made in the unit with high exergy loss will decrease the exergy loss of the unit and also increase the exergy efficiency of the system.

3. Conclusions

In the summer (01 June 2018 - 31 August 2018), the electricity consumption of the scroll type compressor used in the horizontal type ground source heat pump cooling system was affected in direct proportion to external air temperature, therefore, it was determined that scroll type compressor started to operate more at high air temperatures. In the analyses performed in this context, it was determined that system COP values were also affected in direct proportion to external air temperatures. During the summer season analyzed, the outside air temperature was measured as 26.5°C and 31.4°C on average, respectively, in June and August, that are the coldest and hottest months. The soil temperature at the depth of the well excavated as 2 m was measured as an average of 18.6 °C in August, an average of 17.1°C in June and an average of 17.7°C in the summer. It was observed that the amount of energy transferred from the system to the soil varied between 8.04-8.45 kW in direct proportion to outside air temperature. The average amount of energy transferred from the system to the soil during the summer season was calculated as 8.30 kW. Water was prepared at 12.50–14.25°C in the accumulation tank in order to meet the heat gain in the testing room during the summer season analyzed. In this process, the total amount of electricity consumed by the system from the meter (compressor, fan coil panel and circulation pumps) was measured as an average of 2.05 kW. The energy drawn by the horizontal type ground source heat pump cooling system from the determined testing room varied between 9.23-9.66 kW and was affected in direct proportion to the change of the outside air temperature. Nevertheless, the COP value of the whole system was determined between 3.95-4.16.

When the exergy analysis results related to the units of the system examined during the summer season were evaluated, it was determined that the units with the highest exergy loss were compressor and evaporator, respectively. The units with the highest exergy loss rate in the system were compressor and fan coil panel. Although at first glance it appears that the energy loss in the evaporator was higher compared to the compressor, the exergy loss was much lower when compared to the compressor. Furthermore, when the energy efficiency and exergy efficiency were evaluated together as a result of the analyses performed in the system, the compressor stood out as the most inefficient unit. Therefore, the compressor should be considered first for the improvements to be planned. Considering these improvements, the first priority should be to evaluate the conditions that will allow the scroll type compressor to operate less often during system operation. For this purpose, the specified operating temperature ranges of the heat pump can be increased in the software of the system. Thus, the efficiency of the compressor of the horizontal type ground source heat pump, which is known to provide high thermal comfort in lower temperature regimes, will be increased. Thus, the system will be able to operate in lower temperature regimes for a longer period and the efficiency of the scroll type compressor will be increased. Along with the operation of the system in this way, both the exergy loss will be reduced and the electricity consumption will be further reduced. The improvements planned to be made in other system units should be as low-cost as possible and measures to reduce energy loss.

In conclusion, the system was observed to be very successful when it was considered in terms of reducing the energy consumption of the horizontal type ground source heat pump cooling system used for cooling, and more efficient use of energy in Diyarbakır province Bismil county, which usually meets its needs for air conditioning with primary energy sources. Nevertheless, energy is used more efficiently with the preference of such systems that can be alternative, and their usage is considered to be beneficial both in terms of economy and environmental protection.

References

- [1] Akan, A. E. ve Ünal, F.(2019). 4E Analysis of Thermal Power Plants, Theoretical Investigations and Applied Studies in Engineering, Chapter 17, 1st Edition, Ekin Publishing House, Turkey.
- [2] Kıncay, O. ve Temir, G., (2002). “Economic Analysis of Soil and Air Source, Heat Pump Systems”, Journal of Plumbing Engineering, 68: 31-37.
- [3] Akbulut, U., Kıncay, O., Utlü, Z.,(2016).” Analysis of a wall cooling system using a heat pump”, Renewable Energy, 85: 540-553
- [4] Akbulut, U., Utlü, Z., Kıncay, O., (2016).” Exergoenvironmental and exergoeconomic analyses of a vertical type ground source heat pump integrated wall cooling system” Applied Thermal Engineering, 102: 904–921
- [5] Akbulut, U., Utlü, Z., Kıncay, O., (2016).” Exergy, exergoenvironmental and exergoeconomic evaluation of a heat pump-integrated wall heating system, Energy, 107: 502-522
- [6] Ünal, F., Temir, G., Köten, H., (2018). “Energy, exergy and exergoeconomic analysis of solar-assisted vertical ground source heat pump system for heating season, Journal of Mechanical Science and Technology, 32(8): 3929-3942
- [7] Ünal, F., Temir, G., (2014). “Exergoeconomic Analysis Of The Ground Source Heat Pump For Cooling Season In The Mardin Province”, Sigma Journal of Engineering and Natural Sciences, 32: 477-488
- [8] Hepbaşlı, A., Akdemir, O. ve Hancıoğlu, E.,(2003). “Experimental Study of a Closed Loop Vertical Ground Source Heat Pump System”, Energy Conversion and Management, 44: 527-548.
- [9] Nagano, K., Katsura, T. ve Takeda, S., (2006). “Development of a Design and Performance Prediction Tool for the Ground Source Heat Pump System”, Applied Thermal Engineering, 26: 1578-1592.
- [10] Niğdelioğlu, O., (2006). Design of Earth Source Heat Pump and Techno-Economic Performance Analysis, Master Thesis, Dumlupınar University FBE, Kütahya.
- [11] Özgener, Ö. ve Hepbaşlı, A., (2007). “Modeling and Performance Evaluation of Ground Source (Geothermal) Heat Pump Systems”, Energy and Buildings, 39: 66-75.
- [12] Karabacak, R., Acar, Ş., G., Kumsar, H., Gökgöz, A., Kaya, M. ve Tülek, Y., (2011). “Experimental investigation of the Cooling Performance of a Ground Source Heat Pump System in Denizli, Turkey”, International Journal of Refrigeration, 34: 454-465.
- [13] Zhai, X., Q. Ve Yang, Y., (2011). “Experience on the Application of a Ground Source Heat Pump System in Archives Building”, Energy and Buildings, 43: 3263-3270.
- [14] Kılıç, İ., (2007). “Evaluation of Different Design Methods in Ground Source Heat Pumps”, Journal of Ç.Ü. Engineering and Architecture Faculty,22(1):279-289.
- [15] Ünal, F., Akan, A. E., (2017). “Thermodynamic Analysis of Heating with Solar Assisted Vertical Type Ground Source Heat Pump: Mardin Case Study”, International Journal of Scientific and Technological Research, 3(2):1-8.
- [16] Esen, H., (2007). Investigation of Seasonal Behavior of Vertical Pipe Soil Source Heat Pump in Residential Air Conditioning Systems, PHD Thesis, Fırat University FBE, Elazığ.
- [17] Isık, E., Bernt, H.K., Gök, M., (2017). “Second Law Analysis of A Gas Turbine of A Lignite-Fired Power Station” Science and Eng. J of Fırat Univ., 29(2), 23-30.

OPTIMIZATION OF PROCESS CONDITIONS FOR ADSORPTION OF METHYLENE BLUE ON FORMALDEHYDE-MODIFIED PEANUT SHELLS USING BOX-BEHNKEN EXPERIMENTAL DESIGN AND RESPONSE SURFACE METHODOLOGY


Sinan KUTLUAY^{1}, Orhan BAYTAR², Ömer ŞAHİN³, Ali ARRAN⁴*


This paper presents the use of formaldehyde-modified peanut shells as bioadsorbent for the adsorption of methylene blue for the first time. Firstly, the effect of medium pH, which is one of the important parameters for the adsorption process, was determined. Then, the adsorption process conditions such as adsorption time (30-150 min), initial concentration (50-200 ppm) and ambient temperature (25-40°C) were optimized by using response surface methodology (RSM) based on Box-Behnken experimental design. The pseudo-first-order and pseudo-second-order kinetic models were used to evaluate the adsorption kinetic in this study under optimized process conditions. The maximum adsorption capacity was found under optimum process conditions; 92.25 min adsorption time, 191.87 ppm initial concentration, 39.70°C adsorption temperature. The maximum adsorption capacity for methylene blue was determined to be 43.84 mg/g using RSM based on Box-Behnken experimental design. Adsorption kinetic results showed that the plots of the pseudo-second-order kinetic model were fit the experimental data better when compared to the pseudo-first-order model. Besides, results indicated that formaldehyde-modified peanut shells could be used as low-cost and effective bioadsorbent for the adsorption of methylene blue, which is one of the important dyes. Furthermore, it was concluded that the RSM based on Box-Behnken experimental design can be applied successfully for the methylene adsorption process.


Keywords: *Response surface methodology; Box-Behnken experimental design; Bioadsorbent; Methylene blue adsorption*


1. Introduction

Increasing environmental pollution in the world is of great concern and has caused irreversible damages to all creatures. Industrial and domestic wastes are the main sources of organic, inorganic and biological pollutants in terrestrial ecosystems and waters. Wastes from the textile, paint, pesticide,

¹Department of Chemical Engineering, University of Siirt, Siirt, Turkey, (sinankutluay@siirt.edu.tr, 04842121111) 
<https://orcid.org/0000-0001-9493-918X>

²Department of Chemical Engineering, University of Siirt, Siirt, Turkey, (baytarorhan@gmail.com, 04842121111) 
<https://orcid.org/0000-0002-2915-202X>

³Department of Chemical Engineering, University of Siirt, Siirt, Turkey, (sahinomer2002@yahoo.com, 04842121111) 
<https://orcid.org/0000-0003-4575-3762>

⁴Department of Chemical Engineering, University of Siirt, Siirt, Turkey, (ali.alaran2@gmail.com, 04842121111) 
<https://orcid.org/0000-0005-8659-215X>

fertilizer, pharmaceutical, refinery, leather and paper industries contain toxic and hazardous chemicals that pose a potential health hazard to life [1-3]. Dyes are widely used in many industries such as the textile, food and photoelectrochemical industries. Most dyes are dangerous and toxic, prevent water from penetrating sunlight and produce carcinogenic, teratogenic and mutagenic effects [4, 5]. The intensive use of organic dyes causes them to be present in a high proportion of wastes and therefore solutions are recommended for their removal and disposal. Numerous studies have been conducted to remove micro-pollutants and water-soluble dyes from wastewater, including ultrafiltration, reverse osmosis, centrifugation, coagulation, oxidation, electrochemical methods, bio-healing, photocatalytic degradation and adsorption [6-10]. Among these methods, adsorption has been an economically viable approach that can remove multiple contaminants at the same time using a wide variety of adsorbents. Besides, adsorption technology has been recognized as an effective and economic control strategy as it has the potential to recover and reuse both adsorbent and adsorbent [11, 12]. Another approach to the problem of dyes adsorption is based on the use of materials in the natural environment known as bioadsorbents [13]. The reason for the use of activated carbon as an adsorbent in adsorption processes is due to its excellent properties [14, 15]. However, since activated carbon is highly costly, it has encouraged researchers to synthesize other low-cost adsorbents to remove dyes. Therefore, yellow passionflower fruit waste [16], sugar cane [17], neem leaf powder (*Azadirachta indica*) [18], *Posidonia Oceanica* (L.) fibers [19], rice husk [20], wheat husk [21], garlic husk [22], coffee husks [23], papaya seeds [24], Brazilian pine-fruit shell [25], *Elaeagnus Angustifolia* seeds [26], onion skins [27] and acorn shell [28] to be included some biomasses were converted to cheap biosorbents.

The experimental design is applied for statistical modeling and systematic analysis of a problem in which the desired responses or output criteria are optimized by input variables or factors. One of the numerous experimental designs for empirical modeling is the response surface methodology (RSM), which can be considered a decisive sequential technique for developing leading processes, improving the design and formulation of new products and improving their performance. The greatest advantage of RSM over the traditional time-domain approach of a variable in each trial is the reduction in the number of experimental studies required for faster and more systematic investigation of process variables for selected-response parameters, including simultaneous and interaction of variables. One of the major advantages of RSM is that it allows the optimization of multiple experimental parameters that have an impact on the process response by performing a small number of experimental studies. The Box-Behnken design is the most commonly used combination design of the RSM model, which is adopted as an experimental design model to investigate the effect of the interaction of various parameter combinations [29-33]. The experimental design of Box-Behnken is an ideal method for performing a series of evaluations through rationalized design points along with a reliable curvature prediction [34].

In this study, RSM based on Box-Behnken experimental design was applied to optimize the process parameters that effective in adsorption of methylene blue, one of the most important dyes. This study aimed to investigate the use of formaldehyde-modified peanut shells as a low-cost bioadsorbent and to determine optimum process parameters for methylene blue adsorption. Also, it was aimed to develop an approach that provides a better understanding of the effects of conditions such as adsorption time, methylene blue initial concentration and adsorption temperature on the adsorption capacity and to determine the maximum adsorption capacity under optimum conditions.

2. Materials and methods

2.1. Preparation of bioadsorbent

In this study, the adsorption of methylene blue used in the paint and pharmaceutical industry using peanut shells was investigated. At the beginning of the study, peanut shells were ground (Retsch SR300) and classified according to particle size (Retsch AS200). Peanut shells were treated for 24 hours with 1% formaldehyde solution in 1/5 ratio (peanut shells: formaldehyde; w/v) for color immobilization and removal of water-soluble substances. The peanut shells were then removed by filtration and washed with hot deionized water to remove formaldehyde. The washed peanut shells were dried at 80°C for 24 hours and stored in closed containers for use in adsorption experiments.

2.2. Adsorption experiments

In adsorption experiments, the effects of parameters such as solution pH (2, 4, 6, 8 and 10), adsorption time (30-150 min), methylene blue initial concentration (50-200 ppm) and ambient temperature (25-40°C) were determined separately. The studies were started by examining the effect of solution pH and pH adjustments were performed using 0.1 M NaOH and 0.1 M HCl. At the end of the process, solution concentrations were determined by a UV-Vis spectrophotometer (Hitachi U-0080D) at a wavenumber of 616 nm.

The adsorption capacity of methylene blue on the formaldehyde-modified peanut shells was calculated with equation 1.

$$q = \frac{C_0 - C_e}{m} \times V \quad (1)$$

Where q (mg/g) is the adsorption capacity, V (L) is the solution volume, m (g) is the amount of adsorbent and C₀ (ppm) and C_e (ppm) are the initial and equilibrium concentrations of methylene blue.

2.3. Design of experiments

In the experimental design, the relationship between adsorption time (X₁), initial concentration (X₂) and temperature (X₃) independent variables and adsorption capacity (Y) response was modeled by using Box-Behnken approach and RSM. The values of the independent variables for design points are presented in Table 1. The relationship of the response variable with the independent variables was represented by the second-order polynomial equation given below. The statistical significance level of the model was measured with the F-value (p < 0.05) at 95% confidence interval. Adeq precision, regression coefficient (R²), adjusted regression coefficient (Adj. R²) and predicted regression coefficient (Pred. R²) parameters were used in the evaluation of the model.

Table 1. Independent variables and levels of the process for Box-Behnken experimental design

Independent variables	Symbol	Levels of independent variables		
		-1	0	+1
Adsorption time (min)	X ₁	30	90	150
Initial concentration (ppm)	X ₂	50	125	200
Temperature (°C)	X ₃	25	32.5	40

In the optimization process, the response can be correlated with variables selected by linear or quadratic models. A quadratic model was given in the following equation.

$$Y = b_0 + b_1X_1 + b_2X_2 + b_3X_3 + b_{12}X_1X_2 + b_{13}X_1X_3 + b_{23}X_2X_3 + b_{11}X_1^2 + b_{22}X_2^2 + b_{33}X_3^2 \quad (2)$$

Where Y is the response variable (q), b_0 is constant, b_i is linear coefficient, b_{ii} is quadratic coefficient, b_{ij} is interaction coefficient, X_i is the coded variable level and i or j are the number of independent variables.

2.4. Analysis of variance (ANOVA)

The results obtained by Box-Behnken experimental design studies are given in the statistical analysis program. The results of the studies using the experimental data are evaluated according to statistical data such as p-value calculated by the program, adequate precision, adjusted and predicted regression coefficients (Adj. R^2 , Pred. R^2). From the data obtained statistically, it was paid attention that the p-value is less than 0.05. Because the p-value is less than 0.05, the effect of the variable on the response is statistically significant, if it is greater than 0.100 indicates that the effect of the variables on the response is statistically insignificant. Besides, a sufficient sensitivity value greater than 4 indicates that the model used can be included in the design area. The difference between the adjusted regression coefficient and predicted regression coefficient values is less than 0.2 is another criterion showing the suitability of the model.

3. Results and discussion

3.1. pH effect on the adsorption process

Studies examining the effect of solution pH on methylene blue adsorption capacity were performed for 100 ppm initial concentration and 30°C process temperature, 24 hours impregnation time and 75 rpm stirring speed. The results were given in Figure 1.

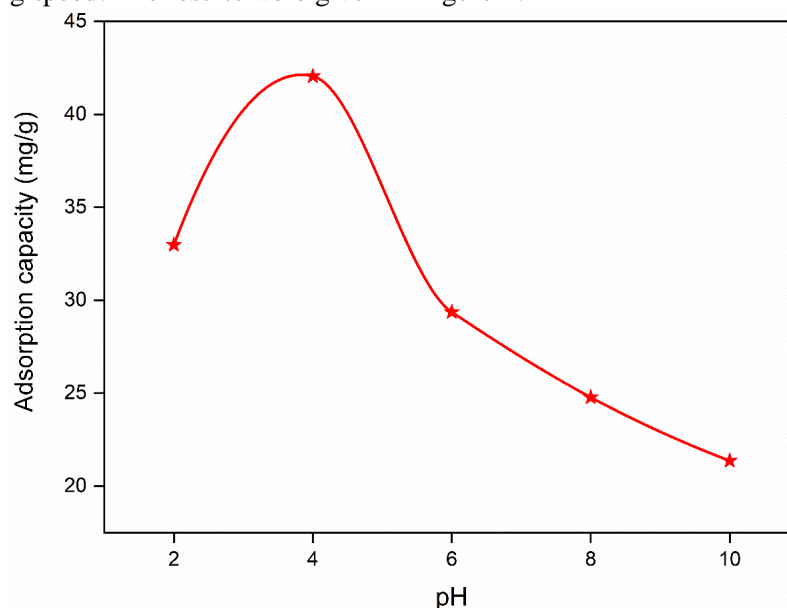


Figure 1. pH effect on the adsorption capacity of methylene blue.

As can be seen from the figure, especially after pH=4, the adsorption capacity decreased with increasing solution pH. This is probably due to the excess OH^- ion in the medium and the cationic structure of the dye. At basic pHs, it is thought that excess OH^- ion in the environment forms complex with cationic dye and reduces adsorption. It was also seen that adsorption capacity decreased because the pH is less than 4. The possible reason for this is thought to be the repulsion of the cationic dyes as a

result of the decrease in the negative charge regions of the adsorbent when the pH decreases and the increase in the positive charge regions on the surface.

3.2. Statistical analysis and modeling by RSM

The adsorption capacity response variable value obtained from the experiments carried out according to the experimental design created with Box-Behnken approach-based RSM are presented in Table 2.

Table 2. Experimental design and results of the Box-Behnken experimental design.

Run	Factor 1		Factor 1	Response
	X ₁ : Time (min)	X ₂ : Concentration (ppm)	X ₃ : Temperature (°C)	Adsorption capacity (mg/g)
1	150	125	40	42.93
2	150	125	25	25.20
3	90	125	32.5	33.40
4	90	125	32.5	35.87
5	90	50	25	12.08
6	90	125	32.5	36.36
7	150	50	32.5	25.39
8	30	125	25	14.89
9	90	50	40	21.32
10	30	125	40	33.58
11	150	200	32.5	39.92
12	30	50	32.5	12.38
13	30	200	32.5	26.21
14	90	200	40	42.79
15	90	200	25	23.27

Table 3. Model summary statistics for methylene blue adsorption response.

Source	R ²	Adjusted R ²	Predicted R ²	F-value	p-value	
Linear	0.8282	0.7813	0.7265	17.68	0.0002	
2FI	0.8457	0.7300	0.5753	0.3026	0.8229	
Quadratic	0.9863	0.9616	0.8259	17.11	0.0046	Suggested
Cubic	0.9967	0.9770		2.12	0.3367	

Some statistical results were evaluated, such as ANOVA to check the accuracy of the model for methylene blue adsorption. It was suggested that adsorption capacity was a model that fitted the quadratic equation according to ANOVA results (Table 3). According to ANOVA results, the quadratic equation obtained for methylene blue adsorption was given below.

$$q = 40.15 + 2.22X_1 + 7.16X_2 + 8.34X_3 + 3.63X_1 + 1.67X_1X_3 + 2.20X_2X_3 - 4.63X_1^2 - 0.98X_2^2 - 3.36X_3^2 \quad (2)$$

In the equation, q was represented the adsorption capacity of methylene blue, and X_1 , X_2 , and X_3 were independent variables, as previously mentioned. To demonstrate the validity of this model, q_{exp} and q_{mod} (mg/g) were compared to the adsorption capacities determined by experimental and model (Figure 2). As can be seen from Figure 2, the estimated results with the quadratic regression model and the actual experimental results were found to be quite close to each other. In addition, the magnitude of the independent variable (X_1 , X_2 , and X_3) coefficients in the model equations confirmed the ANOVA results according to the most effective parameter evaluation.

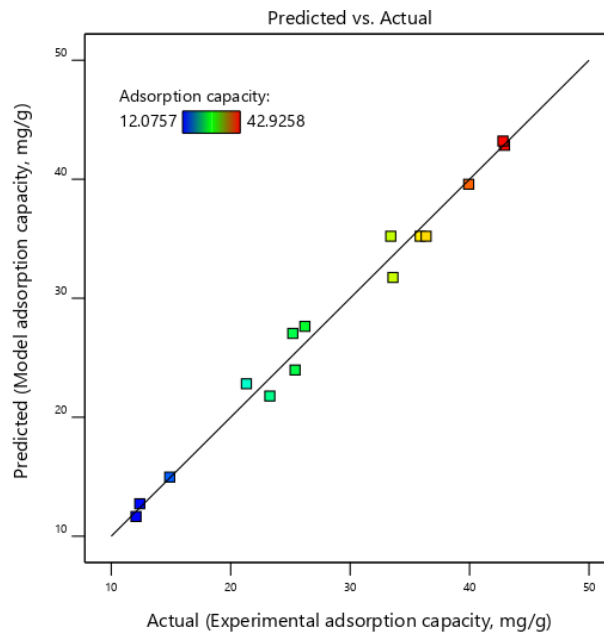


Figure 2. Comparison of experimental and model adsorption capacities of methylene blue.

Table 4. ANOVA for the quadratic model.

Source	Sum of Squares	Degree of Freedom	Mean Square	F-value	p-value	
Model	1506.98	9	167.44	40.00	0.0004	significant
X ₁ -Time	268.69	1	268.69	64.18	0.0005	
X ₂ -Concentration	465.72	1	465.72	111.25	0.0001	
X ₃ -Temperature	531.01	1	531.01	126.84	< 0.0001	
X ₁ X ₂	0.1268	1	0.1268	0.0303	0.8686	
X ₁ X ₃	0.2348	1	0.2348	0.0561	0.8222	
X ₂ X ₃	26.39	1	26.39	6.30	0.0538	
X ₁ ²	22.58	1	22.58	5.39	0.0678	
X ₂ ²	168.67	1	168.67	40.29	0.0014	
X ₃ ²	47.49	1	47.49	11.34	0.0199	
Residual	20.93	5	4.19			
Lack of Fit	15.92	3	5.31			
Pure Error	5.01	2	2.51			
Cor Total	1527.92	14				

ANOVA results of the quadratic polynomial function proposed by Box-Behnken approach for the relationship between the response variable and independent variables are given in Table 4. Accordingly, the F-value of the model determined by the adsorption capacity ANOVA results of methylene blue was found to be significant at 40.00. Adeq precision value measures the signal to noise ratio. This ratio is requested to be greater than 4.00 in respect of the model's estimation suitability. Accordingly, as shown in Table 4, the adeq precision of the model for methylene blue was determined to be 18.89, which means that the model is suitable for these studies. Besides, the p-value of the model is less than 0.05, meaning that the terms of the model are meaningful and that it is more than 0.100 means that it is meaningless. According to the model obtained from the methylene blue study, p-values less than 0.05 showed that the model terms were significant. Adj. R² and Pred. R² are expected to be close to each other and the difference between them is expected to be less than 0.2 [35, 36]. The Pred. R² of 0.8259 is in reasonable agreement with the Adj. R² of 0.9616; i.e. the difference is less than 0.2 for the methylene blue adsorption capacity response. This result showed that the model has high precision and reliability.

3.3. The effect of adsorption time and initial concentration on the adsorption capacity

The results obtained for the studies in which the effect of adsorption time and initial solution concentration on the methylene blue adsorption capacity are examined are given in Figure 2. As can be seen from the figure, the adsorption capacity increased with increasing adsorption time and initial concentration. This result showed that the adsorption of methylene blue depends on time and initial concentration. When this result and ANOVA results (F-value and p-value) were evaluated together, it was concluded that initial concentration was more effective than adsorption time.

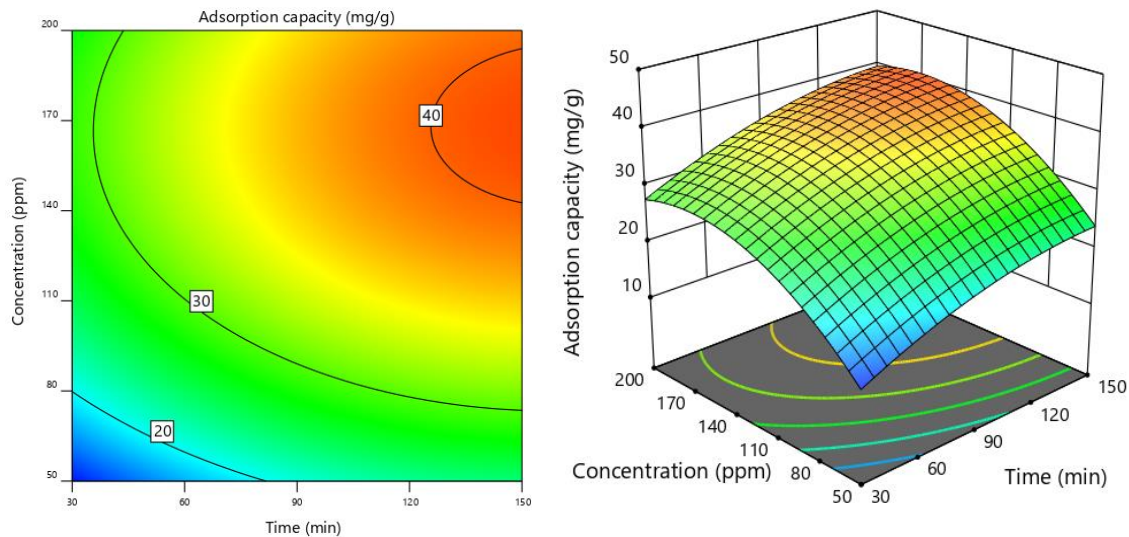


Figure 3. Contour and 3D response surface graphs showing the effect of time and methylene blue initial concentration on the adsorption capacity (Process conditions: pH = 4, temperature = 32.5°C, amount of adsorbent= 0.1 g, stirring speed = 75 rpm).

3.4. The effect of adsorption time and temperature on the adsorption capacity

The results obtained for the studies in which the effect of adsorption time and solution temperature on methylene blue adsorption capacity are examined are given in Figure 3. As can be seen from the figure, the amount of methylene blue adsorbed generally tends to increase with increasing adsorption time and temperature. This result showed that the adsorption capacity of methylene blue depends on both time and temperature. Based on ANOVA results (F-value and p-value), it was found that this result was significant and the effect of temperature parameter on the adsorption process was higher.

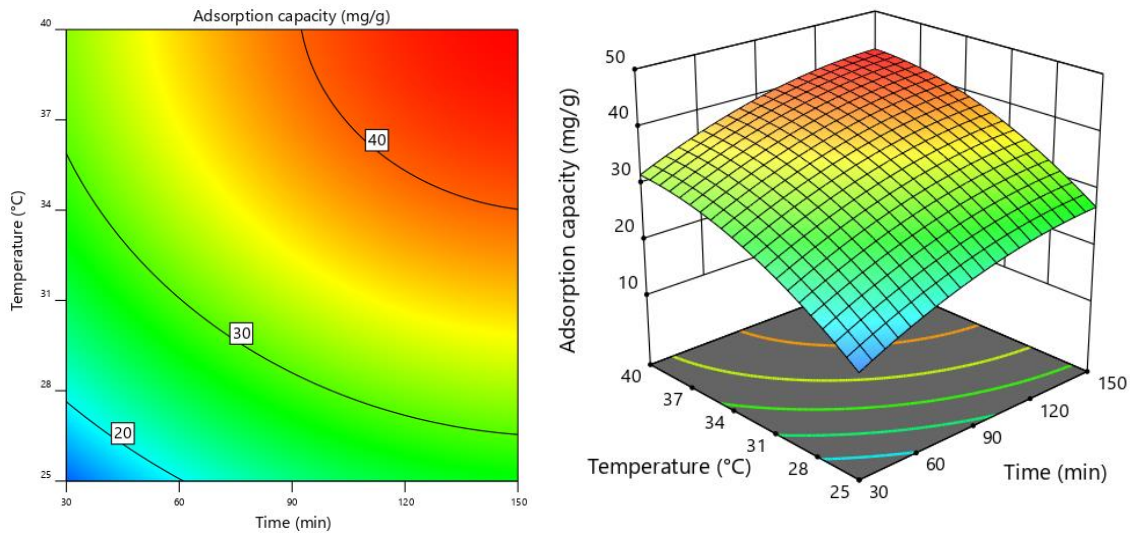


Figure 4. Contour and 3D response surface graphs showing the effect of time and temperature on the adsorption capacity (Process conditions: pH = 4, initial concentration = 125 ppm, amount of adsorbent= 0.1 g/100 mL, stirring speed = 75 rpm).

3.5. The effect of initial concentration and temperature on the adsorption capacity

The results obtained for the studies examining the effect of solution initial concentration and temperature on methylene blue adsorption capacity are given in Figure 4. As can be seen from the figure, the adsorption capacity generally tends to increase with increasing temperature and initial concentration. This result showed that adsorption capacity was dependent on both initial concentration and temperature. It can be said that the temperature is more effective on the methylene blue adsorption capacity according to the evaluation made based on ANOVA results (F-value and p-value) in which binary parameter effects are determined.

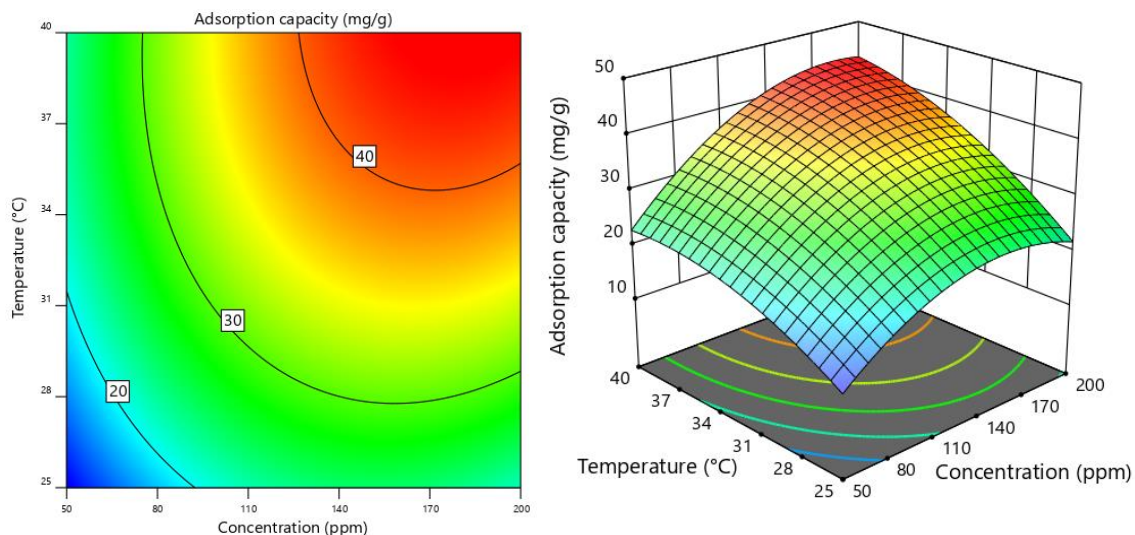


Figure 5. Contour and 3D response surface graphs showing the effect of initial concentration and temperature on the adsorption capacity (Process conditions: pH = 4, adsorption time = 90 min, amount of adsorbent= 0.1 g/ 100 mL, stirring speed = 75 rpm).

3.6. Optimization of process parameters for methylene blue adsorption

The main objective of this study was to find a combination of experimental variable levels that provide the maximum adsorption capacity value for the methylene blue response variable. Adsorption time (A: X_1), initial concentration (B: X_2) and (C: X_3) temperature variables were optimized to determine the maximum adsorption capacity in the studied range. In this context, in the adsorption study using modified peanut shells, the optimum numerical values of experimental parameters were determined by applying the Box-Behnken experimental design method as an effective tool to find the maximum adsorption capacity of methylene blue (Figure 6). Under the determined optimum conditions, the maximum adsorption capacity of methylene blue was found as 43.84 mg/g. The desirability [37] of these parameters, which completely represents the desired or ideal response values, was found to be 0.999 for methylene blue adsorption. For optimum point evaluation, validation experiments were performed for optimum process conditions corresponding to 10 different desirability levels among different desirability levels recommended by the package program and under these conditions, the maximum adsorption capacity for methylene blue was obtained as 42.95 mg/g. According to the results of the validation tests, the absolute error values between the test results obtained for the methylene blue response and the proposition values are below 3% and are acceptable. Based on all these evaluations, it can be concluded that the proposed model outputs are fully consistent with the experimental results.

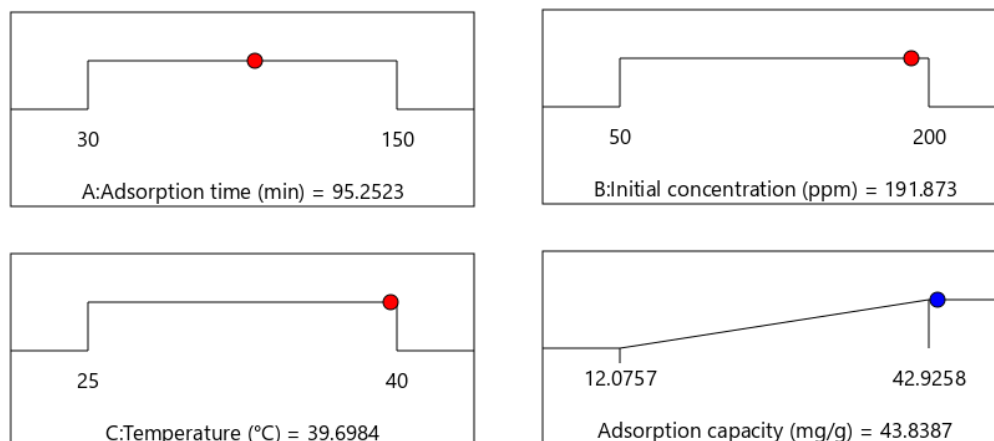


Figure 6. Desirability ramp for numerical optimization of adsorption conditions.

3.7. Adsorption kinetic studies

Adsorption kinetics is an important characteristic that must be examined to understand the adsorption dynamics between adsorbate and adsorbent and to determine the kinetic parameters [38]. The pseudo-first-order and pseudo-second-order kinetic models were used to evaluate the adsorption kinetic in this study under optimized process conditions. The validity of kinetic models was assessed by R^2 , regression coefficient, and Δq (%). The non-linear forms and parameters of the kinetic models studied are given in Table 5. Adsorption kinetic models were fitted to experimental data using non-linear regression analysis. The estimated kinetic parameters were listed in Table 6. The non-linear plots of the pseudo-first-order and pseudo-second-order kinetic models are shown in Figure 7. As can be seen from this Figure, it is clear that the plots of the pseudo-second-order kinetic model were fit the experimental data better when compared to the pseudo-first-order model.

Table 5. Non-linear forms and parameters of the adsorption kinetic models

Kinetic models/Standard deviation	Equation	Reference
Pseudo-first-order model	$q_t = q_e [1 - e^{(-k_1 t)}]$ ¹	[39]
Pseudo-second-order model	$q_t = \frac{k_2 q_e^2 t}{1 + k_2 q_e t}$ ²	[40]
Normalized standard deviation	$\Delta q(\%) = 100 \sqrt{\frac{\sum[(q_{exp} - q_{mod})/q_{exp}]^2}{N-1}}$ ³	[41]

¹ q_e and q_t (mg/g) = the adsorption capacities at equilibrium and at time t (min), respectively, k_1 = the adsorption rate constant of the pseudo-first-order kinetic model (1/min).

² k_2 = the adsorption rate constant of the pseudo-second-order kinetic model (g/mg/min).

³ q_{exp} and q_{mod} (mg/g) = the adsorption capacities of kinetic experiments and models, respectively, N = the number of adsorption kinetics data points, Δq = the normalized standard deviation.

Table 6. Kinetic models parameters for the adsorption of methylene blue on formaldehyde-modified peanut shells

Kinetic models	Parameters	Results
Pseudo-first-order	q_e (mg/g)	23.60
	k_1 (1/min)	0.029
	R^2	0.971
	Δq (%)	9.65
Pseudo-second-order	q_e (mg/g)	27.07
	k_2 (g/mg/min)	0.00096
	R^2	0.997
	Δq (%)	1.85

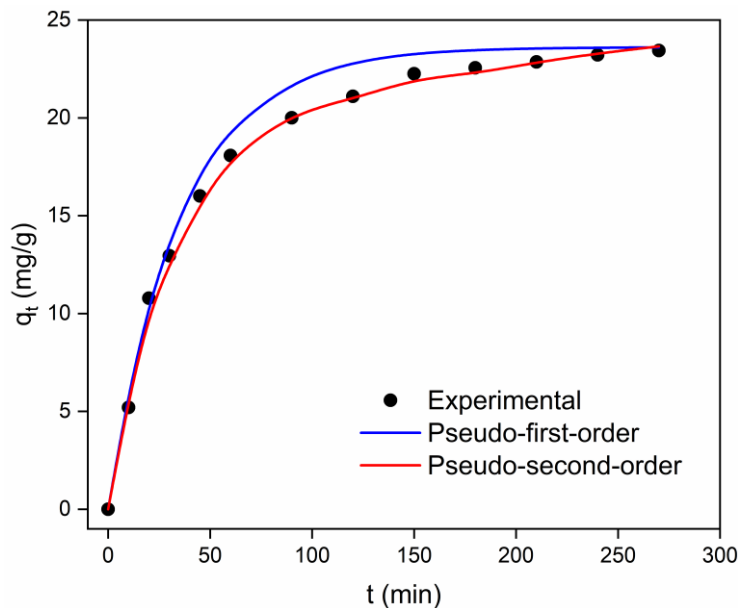


Figure 7. Adsorption kinetics model fitting results and experimental kinetics of methylene blue on the formaldehyde-modified peanut shells.

4. Conclusions

In this study, the first use of formaldehyde-modified peanut shells as bioadsorbent to remove methylene blue from aqueous solutions was investigated. Firstly, the effect of solution pH, which is one of the important parameters for the adsorption process, was determined. Then, conditions such as adsorption time, initial concentration and ambient temperature, which play a key role in the adsorption process, were optimized using the RSM based on Box-Behnken experimental design. The pseudo-first-order and pseudo-second-order kinetic models were used to evaluate the adsorption kinetic in this study

under optimized process conditions. Adsorption kinetic results showed that the plots of the pseudo-second-order kinetic model were fit the experimental data better when compared to the pseudo-first-order model. Besides, the maximum adsorption capacity was found under optimum process conditions; 95.25 min adsorption time, 191.87 ppm initial concentration, 39.70°C adsorption temperature. The maximum adsorption capacity for methylene blue was determined to be 43.84 mg/g using RSM based on Box-Behnken experimental design. Also, results indicated that formaldehyde-modified peanut shells could be used as low cost and effective bioadsorbent for the adsorption of methylene blue, which is one of the important dyes. Furthermore, it was concluded that the RSM based on Box-Behnken experimental design can be applied successfully for the methylene adsorption process.

5. References

- [1] Richardson, S.D., Kimura, S.Y., Water Analysis: Emerging Contaminants and Current Issues, *Analytical Chemistry*, 88 (2016), pp.546-582.
- [2] Schwarzenbach, R.P., Escher, B.I., Fenner, K., Hofstetter, T.B., Johnson, C.A., Von Gunten, U., Wehrli, B., The Challenge of Micropollutants in Aquatic Systems, *Science*, 313 (2006), pp.1072-1077.
- [3] Shannon, M.A., Bohn, P.W., Elimelech, M., Georgiadis, J.G., Marinas, B.J., Mayes, A.M., Science and Technology for Water Purification in the Coming Decades, *Nature*, 452 (2008), pp.301-310.
- [4] Birhanli, A., Ozmen, M., Evaluation of the Toxicity and Teratogenicity of Six Commercial Textile Dyes using the Frog Embryo Teratogenesis Assay–Xenopus, *Drug and Chemical Toxicology*, 28 (2005) 51-65.
- [5] Jadhav, J., Kalyani, D., Telke, A., Phugare, S., Govindwar, S.P., Evaluation of the Efficacy of a Bacterial Consortium for the Removal of Color, Reduction of Heavy Metals, and Toxicity from Textile Dye Effluent, *Bioresource Technology*, 101 (2010), pp.165-173.
- [6] Ali, I., New Generation Adsorbents for Water Treatment, *Chemical Reviews*, 112 (2012), pp.5073-5091.
- [7] Brillas, E., Martínez-Huitle, C.A., Decontamination of Wastewaters Containing Synthetic Organic Dyes by Electrochemical Methods, an Updated Review, *Applied Catalysis B: Environmental*, 166 (2015), pp.603-643.
- [8] Chong, M.N., Jin, B., Chow, C.W., Saint, C., Recent Developments in Photocatalytic Water Treatment Technology: A Review, *Water research*, 44 (2010), pp.2997-3027.
- [9] Kumar, S.S., Shantkriti, S., Muruganandham, T., Muruges, E., Rane, N., Govindwar, S.P., Bioinformatics Aided Microbial Approach for Bioremediation of Wastewater Containing Textile Dyes, *Ecological Informatics*, 31 (2016), pp.112-121.
- [10] Li, J., Wang, X., Zhao, G., Chen, C., Chai, Z., Alsaedi, A., Hayat, T., Wang, X., Metal–Organic Framework-Based Materials: Superior Adsorbents for the Capture of Toxic and Radioactive Metal Ions, *Chemical Society Reviews*, 47 (2018), pp.2322-2356.
- [11] Kutluay, S., Baytar, O., Şahin Ö., Equilibrium, Kinetic and Thermodynamic Studies for Dynamic Adsorption of Benzene in Gas Phase onto Activated Carbon Produced from Elaeagnus Angustifolia Seeds, *Journal of Environmental Chemical Engineering*, 7 (2019), pp.102947.
- [12] Kutluay, S., Baytar, O., Şahin Ö., Adsorption Kinetics, Equilibrium and Thermodynamics of Gas-Phase Toluene onto Char Produced from Almond Shells, *Research on Engineering Structures and Materials*, 5 (2019), pp.279-298.
- [13] Khorramfar, S., Mahmoodi, N.M., Arami, M., Gharanjig, K., Equilibrium and Kinetic Studies of the Cationic Dye Removal Capability of a Novel Biosorbent Tamarindus Indica from Textile Wastewater, *Coloration Technology*, 126 (2010), pp.261-268.
- [14] Baytar, O., Şahin, Ö., Saka, C., Sequential Application of Microwave and Conventional Heating Methods for Preparation of Activated Carbon from Biomass and Its Methylene Blue Adsorption, *Applied Thermal Engineering*, 138 (2018), pp.542-551.
- [15] Özhan, A., Şahin, Ö., Küçük, M.M., Saka, C., Preparation and Characterization of Activated Carbon from Pine Cone by Microwave-Induced ZnCl₂ Activation and Its Effects on the Adsorption of Methylene Blue, *Cellulose*, 21 (2014), pp.2457-2467.
- [16] Pavan, F.A., Lima, E.C., Dias, S.L., Mazzocato, A.C., Methylene Blue Biosorption from Aqueous Solutions by Yellow Passion Fruit Waste, *Journal of Hazardous Materials*, 150 (2008), pp.703-712.
- [17] Low, L.W., Teng, T.T., Rafatullah, M., Morad, N., Azahari, B., Adsorption Studies of Methylene Blue and Malachite Green from Aqueous Solutions by Pretreated Lignocellulosic Materials, *Separation Science and Technology*, 48 (2013), pp.1688-1698.
- [18] Bhattacharyya, K.G., Sharma, A., Kinetics and Thermodynamics of Methylene Blue Adsorption on Neem (Azadirachta Indica) Leaf Powder, *Dyes and Pigments*, 65 (2005), pp.51-59.
- [19] Ncibi, M.C., Mahjoub, B., Seffen, M., Kinetic and Equilibrium Studies of Methylene Blue Biosorption by Posidonia Oceanica (L.) Fibres, *Journal of Hazardous Materials*, 139 (2007), pp.280-285.

- [20] Vadivelan, V., Kumar, K.V., Equilibrium, Kinetics, Mechanism, and Process Design for the Sorption of Methylene Blue onto Rice Husk, *Journal of Colloid and Interface Science*, 286 (2005), pp.90-100.
- [21] Bulut, Y., Aydın, H., A Kinetics and Thermodynamics Study of Methylene Blue Adsorption on Wheat Shells, *Desalination*, 194 (2006), pp.259-267.
- [22] Hameed, B., Ahmad, A., Batch Adsorption of Methylene Blue from Aqueous Solution by Garlic Peel, an Agricultural Waste Biomass, *Journal of Hazardous Materials*, 164 (2009), pp.870-875.
- [23] Oliveira, L.S., Franca, A.S., Alves, T.M., Rocha, S.D., Evaluation of Untreated Coffee Husks as Potential Biosorbents for Treatment of Dye Contaminated Waters, *Journal of Hazardous Materials*, 155 (2008), pp.507-512.
- [24] Hameed, B., Evaluation of Papaya Seeds as a Novel Non-Conventional Low-Cost Adsorbent for Removal of Methylene Blue, *Journal of Hazardous Materials*, 162 (2009), pp.939-944.
- [25] Royer, B., Cardoso, N.F., Lima, E.C., Vaghetti, J.C., Simon, N.M., Calvete, T., Veses, R.C., Applications of Brazilian Pine-Fruit Shell in Natural and Carbonized Forms as Adsorbents to Removal of Methylene Blue from Aqueous Solutions-Kinetic And Equilibrium Study, *Journal Of Hazardous Materials*, 164 (2009), pp.1213-1222.
- [26] Ceyhan, A.A., Baytar, O., Güngör, A., Saygınlı, E., Söylemez, C., Removal of Malachite Green from Aqueous Solutions using Formaldehyde Treated *Elaeagnus Angustifolia* Seeds, *Selcuk University Journal of Engineering, Science and Technology*, (2013).
- [27] Saka, C., Sahin, Ö., Removal of Methylene Blue from Aqueous Solutions by using Cold Plasma- and Formaldehyde- Treated Onion Skins, *Coloration Technology*, 127 (2011), pp.246-255.
- [28] Saka, C., Şahin, Ö., Adsoy, H., Akyel, Ş.M., Removal of Methylene Blue from Aqueous Solutions by Using Cold Plasma, Microwave Radiation and Formaldehyde Treated Acorn Shell, *Separation Science and Technology*, 47 (2012), pp.1542-1551.
- [29] Amini, M., Abbaspour, K.C., Johnson, C.A., A Comparison of Different Rule-Based Statistical Models for Modeling Geogenic Groundwater Contamination, *Environmental Modelling & Software*, 25 (2010), pp.1650-1657.
- [30] Bashir, M.J., Aziz, H.A., Yusoff, M.S., Adlan, M.N., Application of Response Surface Methodology (RSM) for Optimization of Ammoniacal Nitrogen Removal From Semi-Aerobic Landfill Leachate Using Ion Exchange Resin, *Desalination*, 254 (2010), pp.154-161.
- [31] Geyikçi, F., Kılıç, E., Çoruh, S., Elevli, S., Modelling of Lead Adsorption from Industrial Sludge Leachate on Red Mud by Using RSM And ANN, *Chemical Engineering Journal*, 183 (2012), pp.53-59.
- [32] Hamzaoui, A.H., Jamoussi, B., M'nif, A., Lithium Recovery from Highly Concentrated Solutions: Response Surface Methodology (RSM) Process Parameters Optimization, *Hydrometallurgy*, 90 (2008), pp.1-7.
- [33] Kalavathy, H., Regupathi, I., Pillai, M.G., Miranda, L.R., Modelling, Analysis and Optimization of Adsorption Parameters for H₃PO₄ Activated Rubber Wood Sawdust Using Response Surface Methodology (RSM), *Colloids and Surfaces B: Biointerfaces*, 70 (2009), pp.35-45.
- [34] Ghelich, R., Jahannama, M.R., Abdizadeh, H., Torknik, F.S., Vaezi, M.R., Central Composite Design (CCD)-Response Surface Methodology (RSM) of Effective Electrospinning Parameters on PVP-B-Hf Hybrid Nanofibrous Composites for Synthesis of Hf₂-Based Composite Nanofibers, *Composites Part B: Engineering*, 166 (2019), pp.527-541.
- [35] Erbay, Z., Icier, F., Optimization of Hot Air Drying of Olive Leaves Using Response Surface Methodology, *Journal of Food Engineering*, 91 (2009), pp.533-541.
- [36] Rai, A., Mohanty, B., Bhargava, R., Supercritical Extraction of Sunflower Oil: A Central Composite Design for Extraction Variables, *Food Chemistry*, 192 (2016), pp.647-659.
- [37] Pimenta, C.D., Silva, M.B., de Moraes Campos, R.L., de Campos Junior, W.R., Desirability and Design of Experiments Applied to the Optimization of the Reduction of Decarburization of the Process Heat Treatment for Steel Wire SAE 51B35, *American Journal of Theoretical and Applied Statistics*, 7 (2018), pp.35-44.
- [38] Vargas, A.M.M., Cazetta, A.L., Kunita, M., Silva, T.L., Almeida, V., Adsorption of Methylene Blue on Activated Carbon Produced from Flamboyant Pods (*Delonix Regia*): Study of Adsorption Isotherms and Kinetic Models, *Chemical Engineering Journal*, 168 (2011), pp.722-730.
- [39] Sari, A., Tuzen, M., Citak, D., Soylak, M., Equilibrium, Kinetic and Thermodynamic Studies of Adsorption of Pb(II) from Aqueous Solution onto Turkish Kaolinite Clay, *Journal of Hazardous Materials*, 149 (2007), pp.283-291.
- [40] Dursun, A.Y., Kalayci, Ç.S., Equilibrium, Kinetic and Thermodynamic Studies on the Adsorption of Phenol onto Chitin, *Journal of Hazardous Materials*, 123 (2005), pp.151-157.
- [41] KUTLUAY, S., Benzen Uçucu Organik Bileşiminin Badem Kabuğundan Üretilen Char Üzerine Gaz Fazı Adsorpsiyonu: Kinetik, Denge ve Termodinamik, *Bitlis Eren Üniversitesi Fen Bilimleri Dergisi*, 8 (2019), pp.1432-1445.

THE ROLE OF STATIC VAR COMPENSATOR AT REACTIVE POWER COMPENSATION

Behçet KOCAMAN^{1*}, *Nurettin ABUT*²

As the need for electricity has increased and the cost of energy generation has arised. For this reason, it is important to use the generated energy in good quality, safely and efficiently. Reactive power compensation is one of the most effective application to reduce transmission losses, prevent voltage drops, prevent consumers from paying for reactive energy, facilitate operating, increase efficiency and save energy in energy systems. However, due to improvements in semiconductor technology, reactive power compensation systems have gained a new dimension. The power compensation made by the use of semiconductor power elements is called Static VAR Compensation. This compensation is used for the compensation of loads such as arc furnaces, elevators, automotive; paper packaging, food and textile, point welding machines, port cranes, flat welds. Transient events are minimized, losses are reduced, back uped possibility,controled flexibility and reliability are ensured by using Static VAR Compensation systems in power network. In this study, thyristor triggering angles and power factor values of a system, that contains reactive loads and controlled by Static VAR Compensation, were obtained by using the computer software developed by Microsoft C Sharp (C#) programming language. The results were discussed in terms of importance of using such controlling structures in power networks.


Key words: *Energy efficiency, Reactive power, Static VAR compensation*

1. Introduction

Due to the fact that operating costs are high in energy generating units, the efficiency of renewable energy sources is in the development process, the leakage losses in the transmission and distribution system are large, the state does not have enough resources to reduce losses and the demand for electricity increases day by day, need of more quality and reliable energy has appeared[1].

For this reason, reactive reactive power compensation has become compulsory and the prospect has begun to increase day by day to use the produced energy better and more efficiently, to reduce transmission losses, to prevent voltage drops, and to pay the price of reactive energy that causes financial burden on consumers[2]. Because reactive power compensation is one of the most effective measurements to facilitate operation in power systems, it increase efficiency and ensure energy saving.

¹ Department of Electrical&Electronics Engineering, University of Bitlis Eren, Bitlis, Turkey, (bkocaman@beu.edu.tr)  <https://orcid.org/0000-0002-1432-0959>

² Department of Electrical Engineering, University of Kocaeli, Kocaeli, Turkey, (abut@kocaeli.edu.tr)  <https://orcid.org/0000-0001-6732-7575>

According to the "Procedures and Principles Regarding Tariff Applications of Distribution Licensee Legal Entities and Supply Companies" accepted by the Energy Market Regulatory Authority at its meeting dated 30.12.2015, For customers with a power of less than 50 kVA, the inductive reactive power consumption exceeds 33% of the active power, the capacitive reactive energy to the system exceeds 20%; Inductive reactive power consumption exceeding 50 kVA and over 20% of active power users are obliged to pay reactive power rating in case of capacitive reactive energy supply to the system exceeding 15%. For this reason, when the reactive power limits are exceeded, reactive power consumption fee is applied. While different methods are being developed for the production of electricity every day, various techniques and methods are being investigated in order to use the produced energy in the most efficient way.

Reactive power can be controlled by switching shunt capacitors and reactors. If thyristors are used as a switch, these use for the current control within capacitors and /or shunt reactors. These can provide fast and stepless control of reactive power. In recent years, with the developing technology, power electronics components can be manufactured with greater power. In addition, the performance of the control elements has also been improved[3]. The Flexible AC Transmission System (FACTS) implementation is predominantly for dynamic issues, this design proves the point that there are mainly three main variables whose direct control in the power system might have an impact on performance. They are voltage, angle, impedance. FACTS Controllers use for Power Systems' Controllability[4].

In general terms FACTS devices, especially SVCs have become fundamental components in planning, operation and control stages of power systems[5].

There are different types FACTS Controllers. These are; Thyristor Controlled Series Compensation (TCSC), Static Synchronous Series Controller (SSSC), Thyristor-switched series capacitor (TSSC), Static Synchronous Compensator (STATCOM), Static VAR Compensator (SVC) and Unified Power Flow Controller (UPFC). Research focuses on the impact of compensation of the SVC and STATCOM controllers, especially on the steady-state analysis and for first-swing stability enhancement [6-8]. Comparison for different FACTS Controllers given by Table 1.

Table 1. Comparison for different FACTS Controllers [9]

Control Attributes	FACTS Controllers					
	TCSC	SSSC	TSSC	STATCOM	SVC	UPFC
Power flow control	x	x	x			x
Voltage profile improvement				x	x	x
Line commutated	x		x		x	
Forced commutated		x		x		x
Voltage source converter		x		x		x
Current source converter	x	x	x	x	x	
Transient and dynamic converter	x	x	x		x	x
Damping oscillation	x	x	x	x	x	x
Fault current limiting	x		x			x
Voltage stability	x	x	x	x	x	x

2. Classification of Reactive Power Compensation

In practice, compensation is provided by controlling reactive power by using contactor and semiconductor power elements. The compensation made using the contactor is called conventional compensation and the compensation made using semiconductor power elements is called Static VAR Compensation.

2.1. Conventional compensation

Most of the electrical loads used in the industry are inductive reactive power from the electric grid. In order to compensate this inductive reactive power, capacitors groups with different capacity values are used after the meters in the plant.

Devices called reactive power control relays determine the reactive power needed by the system and either activate or deactivate groups of capacitors that will provide the capacity value to compensate for this power[10].

When reactive power compensation is required, the capacitor groups are only activated within 5 to 10 seconds in the conventional compensation systems. Such a long time causes overloads and major losses in the electric grid. The total loss that occurs when losses are taken into account by thousands of end-users is reaching levels of reparability for power distribution companies.

In addition, these systems cause transient voltages, arcs, sudden voltage increases and electrical noise during switching because the power factor correction process takes the capacitor blocks out of contact by means of contactors[11]. Along with that, this system tries to supply capacitive reactive energy to the system through reactive power control relay and contactor.

However, it can not respond to loads that powerful and quickly enter and exit the circuit. To be able to perform a complete compensation, a large number of single-phase grades must be used. In addition, entering and leaving a large number of circuits in a short time has an adverse effect on the capacitor and arcing occurs in the contacts of the contactors[12].

The In order to compensate the reactive power when the loads are switched on and off fast, a instantaneous start current as shown in Figure 1. on capacitors when capacitors switched on contactors.

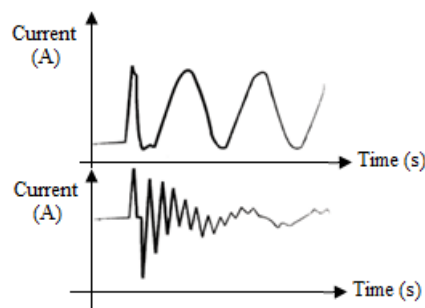


Figure 1. Instantaneous start current change

As the loading and unloading operations of the loads become more frequent, instantaneous start current and arc effect cause deformation of the contactor contacts and after a while the contacts stick.

In many cases, this situation, which occurs in contactors, can cause the contactors to burn. This also causes shortening of life due to continuous current draw of the capacitors. The disadvantages of conventional compensation systems and the development of semiconductor technology have brought reactive power compensation systems to a new dimension.

It is not possible to respond to fast variable loads by switching with mechanical contactors in conventional systems. Such workings can only be answered by switching with a thyristor. In thyristor systems, since capacitors are activated at zero crossings, the obligation to wait for discharge times is eliminated. In addition, when the capacitors are switched on for the first time, it is possible to switch them on and off at a high speed since the current drawn is minimum. Thus, the life and power quality of capacitors and switching elements are also positively affected. In addition, panel maintenance costs are minimized. For this reason, using static VAR compensator at reactive power compensation is important.

2.2. Static VAR Compensation

The static VAR compensators (SVCs) are traditionally used to dynamically compensate reactive power[13]. SVC systems, which are implemented as thyristor-switched compensation systems, are one of the most effective methods of ensuring energy efficiency. The basic types of reactive power control elements that bring the whole or a part of a SVC system into play are; thyristor controlled reactor (TCR), thyristor switched reactor (TSR) ve thyristor switched capacitor (TSC)[14- 15]. SVCs increases the quality of power in many respects. There are many functional benefits of the SVC. Such as flicker reduction, Voltage stabilisation, reactive power compensation, reduction of harmonics, energy savings, increase in productivity. It has the ability to provide maximum capacitive and inductive power limits and every value between these limits. In general, the SVC circuit diagram is given in Figure 2.

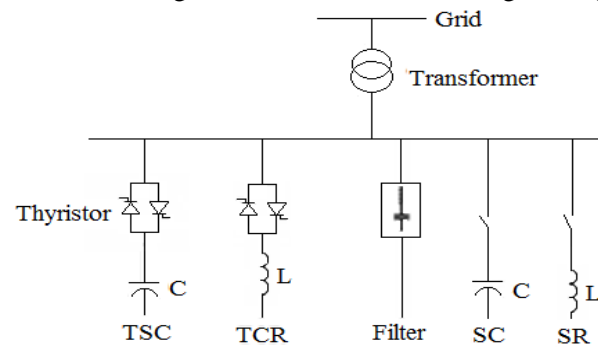


Figure 2. SVC circuit diagram

It is provided the capacitors to be switched on in less than 10 ms by using thyristor modules. In addition, a high instantaneous starting current generated during the switching of the capacitors is prevented and only the normal capacitor current flows, as shown in Figure 3. In this way, rapidly varying loads can be easily compensated, the compensation response time can be adjusted between 20 and 500 ms.

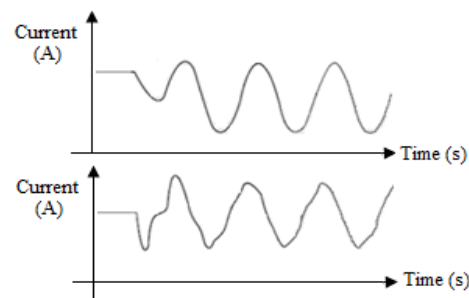


Figure 3. The capacitor's own nominal current change

Static VAR compensation systems have advantages such as minimizing transient events, reducing losses, providing redundancy, control flexibility and high reliability. However, it is an important question that causes harmonics that affect energy quality. This compensation is used compensation of loads such as especially in the fields of arc furnaces, elevators, automotive, paper, packaging, food, textile, glass, cement sectors, point welding machine, harbor cranes, flat welds, where power factor coming in and out very frequently and in short period shows frequent and big changes. The implementation diagram for a three-phase Static VAR Compensation implemented as a thyristor-switched compensation system shown in Figure 4.

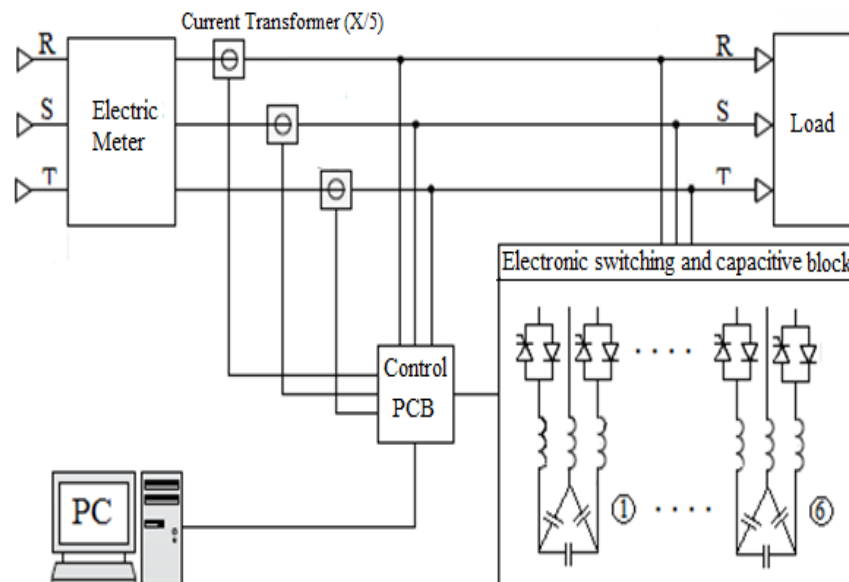


Figure 4. Three-phase SVC application scheme[4]

3. Static VAR Compensation Application

In a fixed-capacitor thyristor controlled reactor (FC-TCR), the fixed capacitors generate reactive power while the TCR will consume power. Since the reactive power generation of the capacitor group is fixed at a certain voltage level, the reactive power generation of the system provided by the reactor is determined by changing the triggering angle of the thyristors.

Changing the triggering angle of the thyristor will control the main component of the reactor current, thus controlling the magnitude of the reactive power[16].

An facility has been selected for such a static VAR compensation system application. The maximum power of the selected facility is 292 kW and the maximum current drawn from the network is 738 A. When all loads in the system are activated, the power factor $\cos \varphi = 0.6$, ie the largest phase difference is 53° . In this facility, FC-TCR compensation method is used to raise the power factor to nearly 1. The fixed capacitor value used in the system has been selected to be $8,817 \mu\text{F}$, the power 400 kVAr and the reactor value $X_L = 1.1 \text{ mH}$. The principle connection diagram of the compensation system is given in Figure 5[11].

System includes a control and measurement unit as shown in Fig.5. This structure is the most important component of overall system. Because triggering angles are being adjusted by this unit. This adjustment can be summarized as given below;

- . Measure grid current and terminal voltage

- . Measure phase angle
- . Calculate active power
- . Calculate reactive power
- . Obtain difference of fixed capacitor power value and calculated reactive power
- . Calculate triggering angle by using from Equation 1 to Equation 8
- . Output calculated triggering angle value

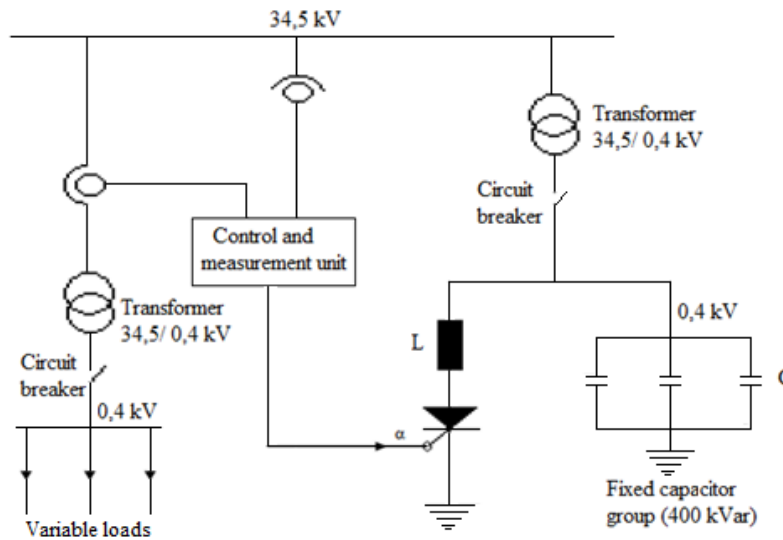


Figure 5. Principle connection diagram of the compensation system

The power factor is reduced when dissimilar loads in the system enter the operation at different times. The fixed capacitor group will remain active after compensating the reactive load to bring the power factor closer to 1.

For this power compensation, this increased capacitive reactive power will be compensated by producing an inductive reactive power, depending on the α angle of trigger of the thyristor [17].

In order to find the reactive power generated on the reactor depending on the angle of trigger of α thyristor, it is necessary to calculate the effective values of the current and the voltage depending on the trigger angle of the Equation 1.

$$QB(\alpha) = V_{\text{eff}}(\alpha) \cdot I_{\text{eff}}(\alpha) \tag{1}$$

The time-dependent variation of the current and voltage at the α triggering angle of the thyristor-connected reactor circuit is given in Figure 6.

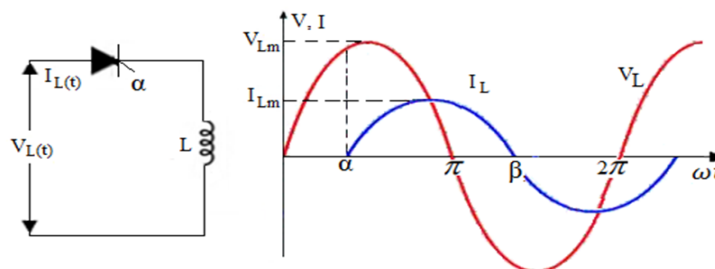


Figure 6. Time-dependent change of current and voltage

$$I_{L(t)} = \frac{1}{L} \cdot \int VL(t)dt + I_0 \tag{2}$$

$$I_{L(t)} = \frac{Vm}{\omega L} \text{Sin}(\omega t - 90^\circ) + I_0 \tag{3}$$

$$I_0 = -\frac{Vm}{\omega L} \text{Sin}(\alpha - 90^\circ) \tag{4}$$

If Equation (4) is written in place of Equation (3), Equation (5) is obtained.

$$I_{L(t)} = \frac{Vm}{\omega L} \text{Sin}(\omega t - 90^\circ) + (-\frac{Vm}{\omega L}) \text{Sin}(\alpha - 90^\circ) \tag{5}$$

As shown in Figure 6., in the cases of $\omega t = \alpha$ and $\omega t = \beta$, $I_L(t) = 0$ and $\beta = 2\pi - \alpha$.

$$I_{eff}(\alpha) = \frac{1}{2\pi} \int_{\alpha}^{\beta=2\pi-\alpha} I^2(t) dt \tag{6}$$

The effective value of the current passing through the reactor after integration in Equation (6) depends on the α trigger angle is calculated by Equation (7).

$$I_{eff}(\alpha) = \frac{Vm}{\omega L} \sqrt{\frac{(\pi-2\alpha)(1-0.5\text{Cos}2\alpha)-1.5\text{Sin}2\alpha}{\pi}} \tag{7}$$

Similarly, the effective value of the voltage, depending on the α trigger angle, is calculated from Equation (8).

$$V_{eff}(\alpha) = \frac{Vm}{\sqrt{2}} \sqrt{\frac{\pi-2\alpha-\text{Sin}\alpha}{\pi}} \tag{8}$$

According to the information described above, the flow chart of the overall system includes thyristors and other components is given in Figure 7.

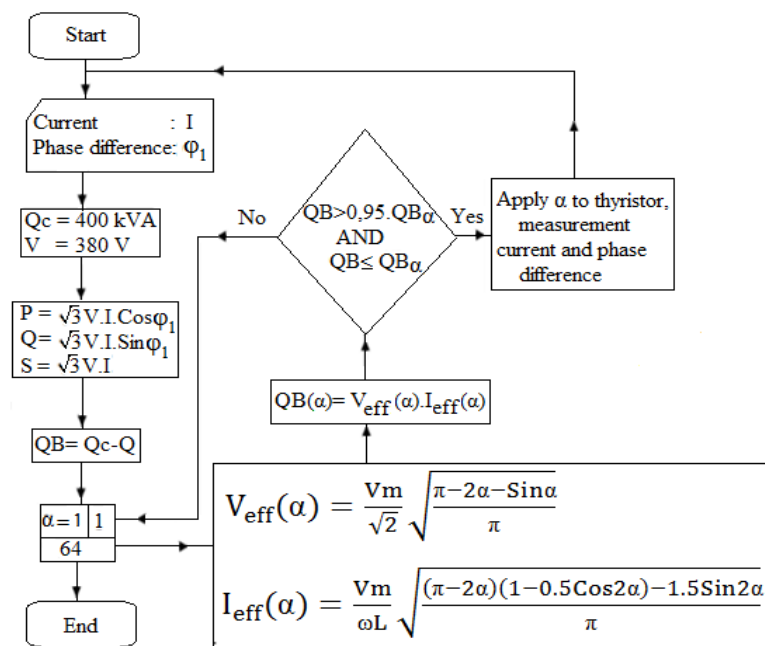


Figure 7. Flow chart of the SVC system

As shown in Figure 7, the current and phase difference obtained from the network is measured. Grid voltage and fixed capacitor power are known. Active, reactive and apparent powers are calculated from these values. A loop was created to see which of the triggering angles of the thyristor of the inductive reactive power compensating capacitive reactive power remaining from the reactive power difference with the fixed capacitor power.

The inductive reactive power generated on the reactor due to the α triggering angle of the thyristor is calculated according to Equations. (1), (7) and (8). These calculate has been provided by the computer software developed by Microsoft C Sharp (C#) programming language. If the power factor is close to 1 or 1, the program will start to measure new values for the load changes after having found the α trigger angle of the thyristor. The state of the computer program that computes the angle of trigger α and the after compensation power factor according to the different load cases in facility with the program are given by Table 2-5.

Table 2. Algorithm result for case 1

Case 1	Value
Power factor before compensation	0,65
Measured current value	654 A
Measured phase angle	49°
Active power	282073 W
Fixed capacitor power	400 kVAr
Residual capacitive power after compensating reactive power in the system	75,53 kVAr
Thyristor controlled reactive power	78,8 kVAr
Angle of thyristor trigger	37°
Power factor after compensation	1

Table 3. Algorithm result for case 2

Case 2	Value
Power factor before compensation	0,70
Measured current value	595 A
Measured phase angle	45°
Active power	276593 W
Fixed capacitor power	400 kVAr
Residual capacitive power after compensating reactive power in the system	123,419 kVAr
Thyristor controlled reactive power	125,178 kVAr
Angle of thyristor trigger	29°
Power factor after compensation	1

Table 4. Algorithm result for case 3

Case 3	Value
Power factor before compensation	0,84
Measured current value	345 A
Measured phase angle	32°
Active power	192341 W
Fixed capacitor power	400 kVAr
Residual capacitive power after compensating reactive power in the system	279,8 kVAr
Thyristor controlled reactive power	287 kVAr
Angle of thyristor trigger	10°
Power factor after compensation	0,99

Table 5. Algorithm result for case 4

Case 4	Value
Power factor before compensation	0,94
Measured current value	312 A
Measured phase angle	19°
Active power	193934 W
Fixed capacitor power	400 kVAr
Residual capacitive power after compensating reactive power in the system	333,2 kVAr
Thyristor controlled reactive power	341,5 kVAr
Angle of thyristor trigger	5°
Power factor after compensation	0,99

5. Conclusion

The energy used in industrial facilities must be uninterrupted and of good quality. Therefore, the important of the continuity and quality of the electric energy transmitted is increasing day by day. It has become imperative to reduce energy quality deficiencies resulting from reactive power change and voltage fluctuations. Conventional compensation systems cause disruptive effects in the network and cause overcurrents and voltages. SVC systems eliminate such negative effects.

SVC application is the most suitable solution for medium voltage installations where disturbing effects are present in the grid. Voltage stability is ensured with reactive power compensation by this application, harmonic and flicker levels are reduced to the values according to the standards. Thus, in addition to saving energy, production time is also shortened. SVC systems; it is the ideal solution for the compaction of loadings coming and going fast in the circuit. These systems, requirements provide a great advantage over conventional reactive power compensation systems because they provide precise and complete compensation against unbalanced loads.

For this reason, SVC systems are provide a lot of benefits to facilities as an alternative to conventional compensation systems. With the development of technology, the prices of power electronic components will be reduced and SVC systems will be an economical solution within small businesses.

In this respect, the role of SVC in reactive power compensation at power plants is large. With the computer program developed, the α trigger angle of the thyristor is calculated according to the different load conditions in operation and the states on the application are given. As the loads change, the reactive power is compensated by changing the α trigger angle of the thyristor with programme.

References

- [1] Vardar, T., Çam, E., Yalçın, E. (2010). Reaktif Güç Kompanzasyonu ile Enerji Verimliliği ve Kamu Kurumlarında Reaktif Güç Kompanzasyonu. *International Journal of Engineering Research and Development*, 2 (2), 20-24.
- [2] Gelen A. A., Yalçınöz T. (2009). Tristör Anahtarlama Kapasitör (TSC) ve Tristör Anahtarlama Reaktör-Tabanlı Statik VAR Kompanzator'un (TSR-Tabanlı SVC) PI ile Kontrolü. *Gazi Üniv. Müh. Mim. Fak. Dergisi*, 24 (2), 237-244.

- [3] Idoniboyeobu, D.C., Wokoma, B.A., Evoh, S. (2018). Reactive Power Compensation Improvement Technique for Injection Substations in Nigeria. *International Journal of Scientific & Engineering Research*, 9 (4), 1183-1189.
- [4] Pallavi, T., Smita, S. (2014). Benefits of Facts Controllers Over AC Transmission Systems. *International Journal of Electronics, Communication & Instrumentation Engineering Research and Development (IJECIERD)* 4 (4), 13-26.
- [5] Efe, S.B. (2018). UPFC Based Real-Time Optimization of Power Systems for Dynamic Voltage Regulation. *Computer Modeling in Engineering & Sciences*, 116 (3), 391-406.
- [6] Mehta, S., Prakash, S. (2018). Performance Evaluation of FACTS Controllers for Short Transmission Line. *International Journal of Applied Engineering Research*, 13(7), 5140-5153.
- [7] Kamarposhti, M. A., Lesani, H. (2010). Comparison between parallels and series FACTS devices on static voltage stability using MLP index. In International symposium on power electronics electrical drives automation and motion, SPEEDAM, 257–262.
- [8] Moazzami, M., Hooshmand, R.A., Khodabakhshian, A., Yazdanpanah, M. (2013). Blackout prevention in power system using flexible AC transmission system devices and combined corrective actions. *Electric Power Components and Systems*, 41(15), 1433–1455.
- [9] Vandana, Dr. Verma, S.N. (2014). Comparative Study of Different Facts Devices. *International Journal of Engineering Research & Technology (IJERT)*, 3 (6), 1819-1822.
- [10] Gayatri, M.T.L., Alivelu, M. P., Pavan K.A.V. (2018). A review of reactive power compensation techniques in microgrids. *Renewable and Sustainable Energy Reviews*, 81 (1), 1030-1036.
- [11] <http://idilpr.com.tr/wp-content/uploads/2014/06/PMI-GESS-Tristorlu-Kompanzasyon-Sistemleri-TR.pdf> (Access Date: 15 November 2019)
- [12] Vardar, T., Yıldırım F., Çam E. (2011). Yeni Nesil Kompanzasyon Sistemi SVC. TMMOB EMO Ankara Şubesi Haber Bülteni, 2011(4), 14-17.
- [13] Wang, L., Lam, C. S., Wong, M. C. (2017). Design of a thyristor controlled LC compensator for dynamic reactive power compensation in smart grid. *IEEE Transactions on Smart Grid*, 8(1), 409–417.
- [14] Aguila T. A., Lopez, G., Isaac, I., Gonzalez, J. W. (2018). Optimal reactive power compensation in electrical distribution systems with distributed resources. Review. *Heliyon*, 4 (8), 1-30.
- [15] Pavlos S.G., Peter, G.V. (2011). Flexible AC Transmission System Controllers: An Evaluation, *Materials Science Forum*, 670, 399-406.
- [16] Bostancı, A. (2008). Static Compensation System Design And Application. MSc thesis, Yildiz Technical University, İstanbul, Turkey.
- [17] Kocaman, B. (1997). Static Compensation and Its Application. MSc thesis, Kocaeli University, Kocaeli, Turkey.

IDENTIFICATION OF PARKINSON'S DISEASE BY AR MODELLING OF GAIT SIGNALS

Omer AKGUN^{1*}, Aydin AKAN²

Parkinson's is a neurodegenerative disease that, as in the case of other neurodegenerative diseases, has disruptive effects on human mobility. In this study, gait markers were obtained by using sensors under the foot, giving an output proportional to the force. Normal gait markers were compared with those of Parkinson's patients. Thus, individuals with Parkinson's were identified by comparing the impulse model of gait markers obtained from normal individuals with those of Parkinson's patients.

Key words: *Parkinson, gait markers, impulse model*

1. Introduction


Disease was identified using the differences between the impulse models of these processes. One of the fundamental objectives of current clinical research into neurodegenerative diseases is the development of early detection methods and presymptomatic diagnosis of neuronal dysfunction [1]. Several different approaches are being undertaken to identify bioindicators, involving the use of imaging, neurophysiological and cognitive tests, in addition to the latest technologies such as biochemical, proteomic, metabonomic and gene-array profiling of tissue and biofluids taken from patients. Key recent findings in each of these areas are discussed, including the walking function [2].


In order to be able to walk for long periods of time without tiring, the muscle-skeleton and nervous systems need to be healthy. Brain, spinal cord, peripheral nerves, muscles, bone and joints should work together; joint movements, timing and force of the contractions muscular contractions should be adequate.

In order to move the body forwards, a repetitive series of movements occur in the legs. This movement cycle, which is repeated in a defined sequence, is called the walking cycle.

Gait analysis is the examination of a person's walk, both kinetically (in terms of factors which cause joint movements such as force, pressure, momentum, torque and factors which determine kinematical sizes) and kinematically (in terms of translocation, linear speed, acceleration, and corresponding angular sizes) [3].

Scientific evaluation of human movement goes back to the time of Aristo. In 350 B.C., Aristo found that the joint movements were caused by muscle contraction. A few centuries later, Galen (A.D. 131-201) asserted that nerves governed muscle contraction. During the Renaissance period, Galileo's student Borelli, and Marey, in the 19th century, conducted dynamic studies relating to the human walk. In the late nineteenth century, the photographer Eadweard Muybridge made significant

¹ Department of Computer Engineering University of Marmara, Istanbul, Turkey (e-mail: oakgun@marmara.edu.tr)
 <https://orcid.org/0000-0003-3486-2197>

² Department of Biomedical Engineering University of Izmir Katip Celebi, Istanbul, Turkey (e-mail: aydin.akan@ikcu.edu.tr)
 <https://orcid.org/0000-0001-8894-5794>

contributions to gait analysis. Braune and Fischer subsequently converted photographic images to numeric variables in 1895. In the 1930s, Eberhart and Inman repeated these experiments in detail by using a rotating perforated disk in front of the camera lens. Verne Inman and Jacquelin Perry introduced scientific gait analysis as we know it today into clinical practice, with their studies beginning in the 1950s. Since the rapid development of personal computers in the 1980s, walking analysis systems have been developed for clinical practice and are widely used throughout the world [4].

Gait analysis is the numeric evaluation, definition and interpretation of walking. Although many walking problems can be detected with visual examinations conducted by experienced doctors, walking analysis technology is required in order to interpret the problem numerically, to record and subsequently re-evaluate it, and to objectively evaluate the effectiveness of the treatment [5]. In modern walking analysis laboratories, the patient's walk is first evaluated visually and with video recordings. Movement data is then transferred to the computer via transmitter or reflectors attached to appropriate points on the patient's body; additionally, variations in floor reaction force measured when standing on a floor-mounted force platform are also uploaded to the computer. It is also possible to measure dynamic electromyography and energy consumption [6]. Diagnosis is made, based on evaluation of the data and the clinical status of the patient. Previous studies, which come within the scope of this paper on the numerical evaluation of neurodegenerative diseases and gait dynamics, were conducted by Hausdorff et al. [6,7]. Those studies were generally based on analysis relating to gait rhythm [7].

The present study is based on the modeling of gait markers, obtained by using sensors sensitive to the force beneath the foot, using the AR process. Parkinson Disease was identified using the differences between the impulse models of these processes.

2. Parkinson Disease

Parkinson Disease (PD) is the second most prevalent neurodegenerative disease worldwide, and is the primary movement disorder in terms of frequency.

Parkinson's is a slow onset clinical outlook, which generally emerges in those over the age of 50, and which rarely appears under the age of 40. One of the most distinct symptoms in Parkinson's is the tremor observed in the resting state, which is mostly observed in the hands. This tremor generally has 3-7 beats per second and disappears during purposeful movement and sleep, for example when reaching to pick up an object. This type of tremor observed in Parkinson's patients is one of the most important clinical symptoms in which the electroencephalography (EEG), electromyogram (EMG) interaction is clearly observed [8].

Another important symptom of Parkinson's is the increase in muscle tone. Consequently, there is stiffening in the patient, when the patient attempts a passive movement, a resistance is encountered. For example, when one attempt to open the patient's bent arm opening the elbow joint, the movement becomes more difficult due to the resistance encountered.

Another important symptom is the general slowing of movements. In Parkinson Disease and Parkinsonism, which are the most important diseases of the extrapyramidal system, walking is pathognomonic. Patients walk with a flexed posture, with small and gradually more rapid steps. Patients have difficulty in commencing walking, changing direction and stopping whilst walking; The number of steps per minute does not vary significantly; The step width increases; Hip, knee and foot joint movements are reduced; Arm swing reduces; Opposite direction pelvis and body rotation is

observed; In the initial contact phase, stepping with the entire foot sole instead of the heel is observed, and turning in the heel deteriorates.

In addition to the above symptoms, patients may display reduction in mimics, talking with a monotonous and low voice and difficulty in sitting down or getting up [9].

In Parkinson Disease, the nerve cells in the substantia nigra, the structure of the brain which produces dopamine, are damaged and reduced. The reason for the damage caused to these cells is still unknown at present. It is evident that this is not a random situation and that it is not due to atherosclerosis, weak blood circulation, or inflammatory or changes of microbial origin. It has been suggested that a deficiency in certain undefined substances, or an unknown toxin may be responsible for this cell damage.

The extensions of these cells are in areas called “striatum” (stripy object). The excreted dopamine adheres to the receptive structures (receptors) found here and transmits information from one nerve cell to another. As sufficient dopamine is not produced in the brain, symptoms of Parkinson Disease emerge which manifest themselves in the form limb tremors in the resting state, muscle rigidity, slowness of movement and posture deformity. Before the symptoms emerge, approximately 60% of the dopaminergic neurons in substantia nigra and 80% of the dopamine in the striatum are lost [10].

3. Application

This study is based on the kinetically analysis of gait dynamics. Kinetically analysis is the examination of the forces which create movement (floor reaction forces, joint moments, and joint strengths). The only measurable data in kinetically analysis is the floor reaction force vector (FRFV) [11]. FRFV is measured with pressure-sensitive plates, called a force platform, which measure the total force applied on the floor by the foot. Transducers placed on both sides, front, back and inside of the platform measure the components in all three planes of the load placed on the surface of the platform and transfer this data to the computer [12]. Another option, used in the present study, is to record gait markers by placing force sensitive piezoelectric sensors under the foot (Figure 1).

In this way, 60 second long gait markers were recorded. These were converted to 18,000 series at 300 Hz frequency using an analog-digital converter and transferred to the computer. Gait markers were taken from the left feet of 11 normal individuals and 12 Parkinson patients.

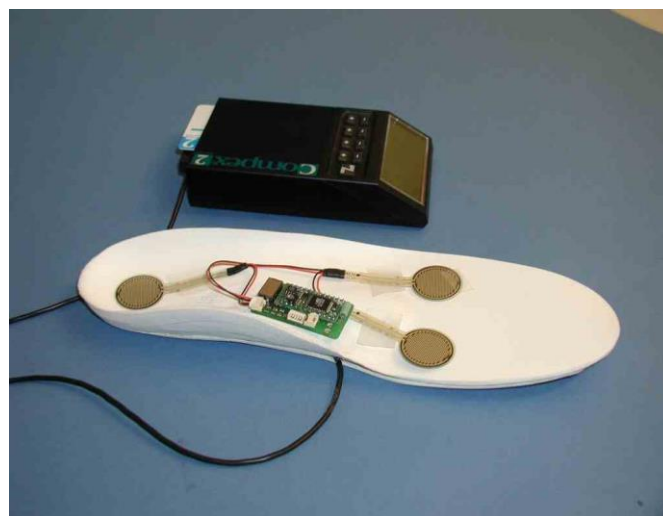


Figure 1. Piezoelectric sensors under the foot.

4. AR Modelling of Gait Signals

Model-based (parametric) methods are based on modeling of the $y(n)$ data series as the output of a linear system characterized by a rational system [13].

A dynamic linear system (Figure 2a)) is defined by unit impulse response [14]. With $x(n)$ as input, $y(n)$ as output and $v(n)$ as noise markers, the system is modeled with h_n unit impulse response. Output expression gives the formula:

$$y(n) = \sum_{k=1}^{\infty} h(n).x(n - k) + v(n) \tag{1}$$

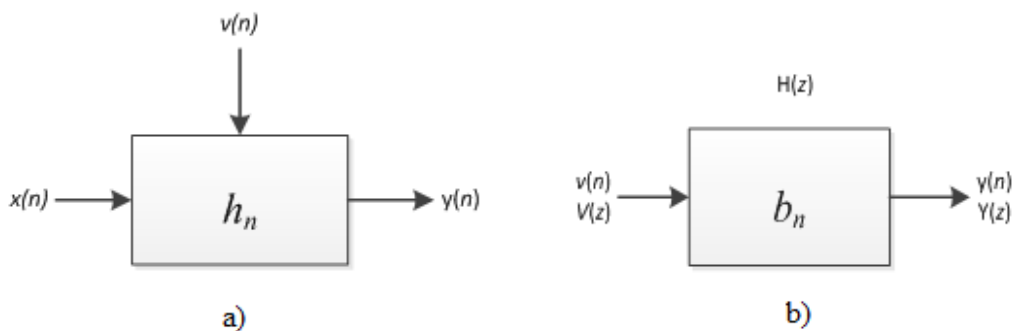


Figure 2. A dynamic linear system.

AR models are used in discrete time systems encountered in practical applications, and in situations when it is necessary to model the system using only the output values as data. In the AR model, the $y(n)$ gait marker’s current value and previous values are equal to the total of $y(n-1), y(n-2), \dots, y(n-M)$ finite linear combination and the error term $v(n)$. Therefore, if a $y(n)$ time series provides the difference equation

$$y(n) = b_1.y(n - 1) + b_2.y(n - 2) + \dots + b_M.Y(n - M) + v(n) \tag{2}$$

This is an AR process of the M . degree. The b_1, b_2, \dots, b_M constants are AR parameters, whilst $v(n)$ is a white noise process [15,16,17].

In Figure 3, the system, which is only $y(n)$ output expression, is expressed with the formula:

$$y(n) = \sum_{k=0}^M b_k .v(n - k) + v(n) \quad b_0=1 \tag{3}$$

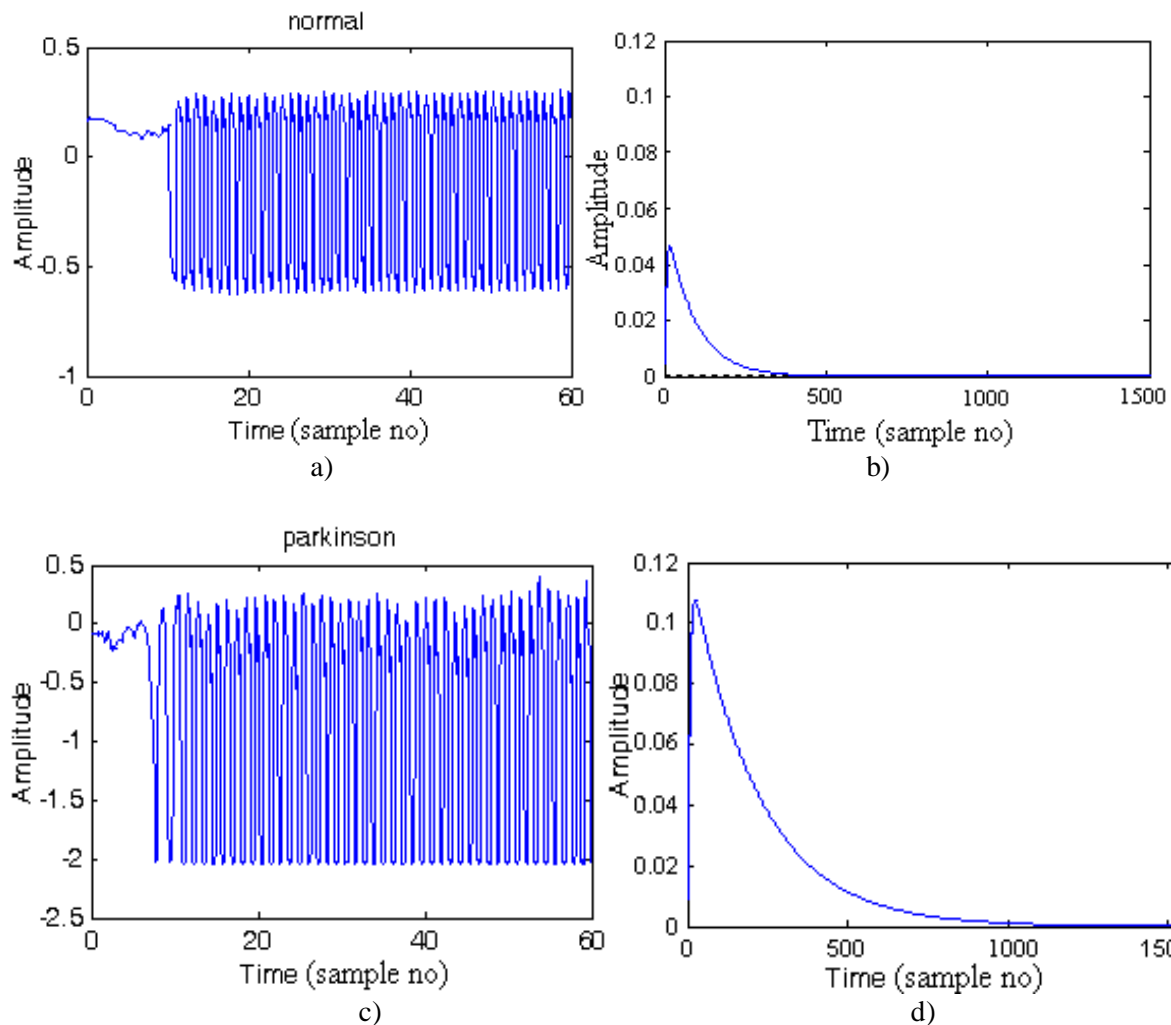
The transfer function of the AR model using Z transformation will be:

$$H(z) = \frac{Y(z)}{V(z)} = \frac{1}{\sum_{n=0}^M b_n .z^{-n}} \tag{4}$$

The impulse models of normal and Parkinson gait markers modelled with a 4th degree AR process as in Figure 2b) are shown in Figure 3.a),b),c),d).

Table 1. Peak values of impulse models of gait markers.

Patient No	Normal	Parkinson
1	0.0464	0.107
2	0.047	0.116
3	0.0473	0.119
4	0.0405	0.112
5	0.149	0.137
6	0.0421	0.118
7	0.131	0.106
8	0.158	0.127
9	0.151	0.104
10	0.0373	0.126
11	0.0441	0.128
12		0.112



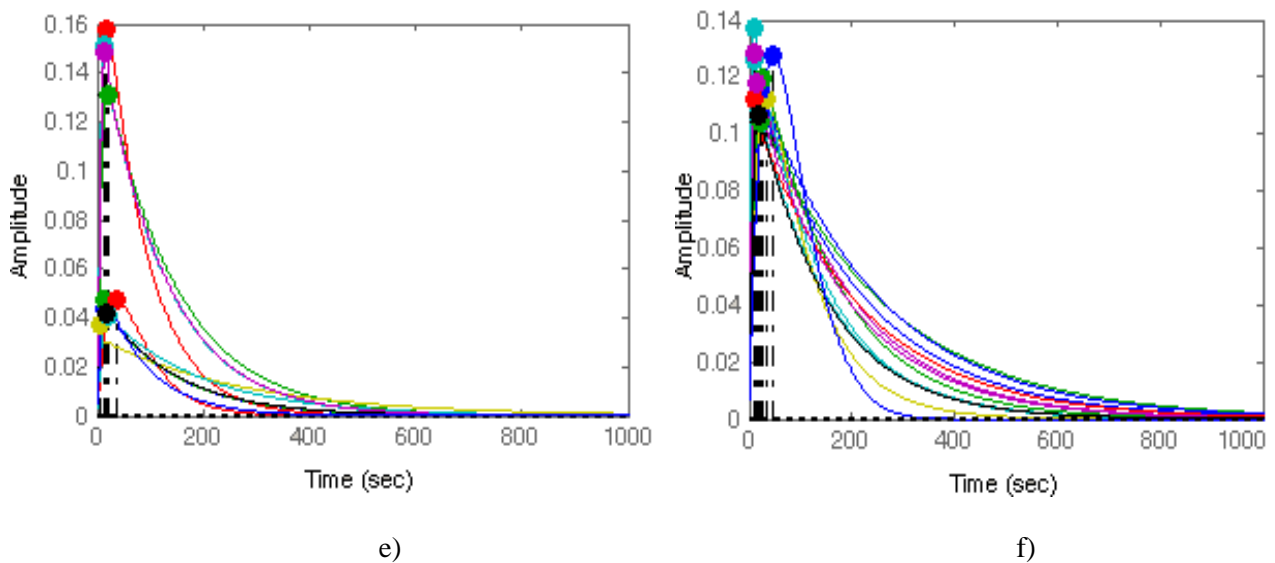


Figure 3. a) Gait markers taken from normal individual
 b) impulse model
 c) Gait markers taken from Parkinson's patient
 d) Parkinson's patient impulse model
 e) Impulse responses of gait markers of 11 normal
 f) Impulse responses of gait markers of 12 Parkinson's patients

5. Conclusions

The peak values of the impulse models of normal gait markers are collected in two groups. Whilst the first group typically has values in the region of 0.04, the second group takes values in the region of 0.13, 0.14 and 0.15.

The peak values of impulse models of Parkinson patients' gait markers are differentiated from normal markers, with values in the region of 0.11 and 0.12 (Figure 3 e),f) and Table 1).

References

- [1] Beal, M.F., Lang, A.E., Ludolph, A.C., *Neurodegenerative Diseases: Neurobiology, Pathogenesis and Therapeutics*, Cambridge University Press, London, UK, 2005.
- [2] Galimberti, D., Scarpini, E., *Neurodegenerative Diseases: Clinical Aspects, Molecular Genetics and Biomarkers*, Springer London, 2014.
- [3] Yalcın S., Ozaras N., *Gait Analysis*, Avrupa Publications, Istanbul, 2001 (in Turkish).
- [4] Whittle, M.W., *Gait Analysis: An Introduction*, Butterworth-Heinemann, Waltham, 2007.
- [5] Gabel, M., Gilad-Bachrach, R., Renshaw, E., Schuster, A. (2012), Full Body Gait Analysis with Kinect, Engineering in Medicine and Biology Society (EMBC), *Annual International Conference of the IEEE*, San Diego, CA
- [6] Hausdorff, J.M., Mitchell, S.L., Firtion, R., Peng, C.K., Cudkovicz, M.E., Wei, J.Y., Goldberger, A.L. (1997). Altered fractal dynamics of gait: reduced stride-interval correlations with aging and Huntington's disease. *J. Applied Physiology*, 82, 262-269.

- [7] Hausdorff, J.M., Lertratanakul, A., Cudkowicz, M.E., Peterson, A.L., Kaliton, D., Goldberger, A.L. (2000). Dynamic markers of altered gait rhythm in amyotrophic lateral sclerosis. *J. Applied Physiology*, 88, 2045-2053.
- [8] Budzianowska, A, Honczarenko, K. (2008). Assessment of rest tremor in Parkinson's disease, *Polish J. Neurol. Neurosurg.*, 42, 12 -21 .
- [9] Weiner, W.J., Shulman, L.M., Lang, A.E., *Parkinson's Disease: A Complete Guide for Patients and Families*, The Johns Hopkins University Pres, Baltimore, 2006.
- [10] Pahwa, R., Lyons, K., *Treatment Decisions in Parkinson's Disease*, Oxford University Pres, Northants, 2010.
- [11] Watanabe, K., Hokari, M. (2006). Kinematical analysis and measurement of sports form, *IEEE Trans. Syst. Man Cybern. Part A*, 36, 549–557.
- [12] Kimmeskamp, S., Hennig, E.M. (2001). Heel to toe motion characteristics in Parkinson patients during free walking. *Clin. Biomech.* ;16, 806–812.
- [13] Walter, E., Pronzato, E., *Identijication of Parametric Models from experimental data*, Springer, Londra, 1997.
- [14] Tsuruoka, M., Tsuruoka, Y., Shibasaki, R., Yasuoka, Y., Murai, S. (2004). Analysis of impulse response on walking stability using accelerometers, *Engineering in Medicine and Biology Society*, 2, 4924 – 4927 .
- [15] Akgun, O., Demir, H., Akan, A, (2008). Detection of ALS Disease Using AR Models of Gait Dynamics, *Electrical, Electronic and Computer Engineering Symposium (ELECO)*, Bursa Turkey.
- [16] Tsuruoka, M., Tsuruoka, Y., Shibasaki, R., Yasuoka, Y., Murai, S, (2001). Analysis of impulse response on walking stability by a synchronized system of two accelerometers. *Computer-Based Medical Systems.*, 348 – 353.
- [17] Tsuruoka, M., Tsuruoka, Y., Shibasaki, R., Yasuoka, Y., Murai, S. (1999). Spectral analysis of human movement stability using time series data in medicine. *Computer-Based Medical Systems*, 190 – 195.

INVESTIGATION OF ROUTE TRACKING PERFORMANCE WITH ADAPTIVE PID CONTROLLER IN QUADROTOR


Ayşegül SUNAY¹, Aytaç ALTAN², Egemen BELGE³, Rifat HACIOĞLU^{4}*


Depending on the intended use, the Unmanned Aerial Vehicle (UAV) must either be able to calculate the route itself to follow or be loyal to the predetermined route. In addition, in some cases, it is of paramount importance to follow the route, reduce the cost and follow the route in the most accurate way, especially under difficult conditions. The aim of this study is to investigate the system modeling of quadrotor to design the position and route following control algorithms of the system which is based on this modeling and to simulate the mentioned algorithms with adaptive proportional-integral-derivative (PID) controller. Firstly, system modeling and mathematical equations has been developed. Secondly, the simulation environment has been created through the MATLAB program. Route tracking in this simulation environment has been performed on three different geometries, rectangle, lemniscate, spiral route tracking and the rate of the quadrotor on these routes and the amount of error has been determined. The comparison of these geometric shapes revealed the necessity of adaptive PID approaches in cases of sudden maneuvers.


Key words: *Quadrotor, UAV modeling, route tracking, adaptive PID controller.*


1. Introduction

Unmanned aerial vehicles (UAVs) in the national intelligence and defense industry, search and rescue activities, the security of places where geographical structure is inaccessible and difficult, and in civilian projects in daily life (monitoring of sports in challenging tracks, detecting illegal flow, etc.) is frequently used. For the last 10 years, UAVs have been preferred in military and civilian applications due to their ability to move autonomously or manually, to leave the beneficial loads on the specified targets and to perform autonomous descent and takeoff [1]. UAVs are produced in different sizes and structures according to the tasks they will perform. Aerodynamic structures play an important role in performing the assigned tasks [2].

¹ Department of Electrical Electronics Engineering, Zonguldak Bülent Ecevit University, Zonguldak, Turkey, (aysegulsunay90@gmail.com)  <https://orcid.org/0000-0001-5494-7820>

² Department of Electrical Electronics Engineering, Zonguldak Bülent Ecevit University, Zonguldak, Turkey, (aytacaltan@beun.edu.tr)  <https://orcid.org/0000-0001-7923-4528>

³ Department of Electrical Electronics Engineering, Zonguldak Bülent Ecevit University, Zonguldak, Turkey, (egemenbelge@beun.edu.tr)  <https://orcid.org/0000-0001-5852-1085>

⁴ Department of Electrical Electronics Engineering, Zonguldak Bülent Ecevit University, Zonguldak, Turkey, (hacirif@beun.edu.tr)  <https://orcid.org/0000-0002-2480-0729>

UAVs, like many other vehicles, can be produced in various geometries depending on the location and area where the activity will take place. One of the most commonly used and preferred UAVs is the four propeller UAVs called quadrotor. The four-propeller UAVs, in its most basic structure, include a microcontroller, sensor, brushless DC motor, speed controller and power supply [3].

The planning of the trajectories that the UAVs will follow to fulfill the assigned tasks and the completion of the task by the UAV following this trajectory is vital for the UAV activities in strategic regions. In this study, the performance of trailing trajectories with different geometries of quadrotor with adaptive PID controller is examined under external disturbance.

In this paper, system modeling of the UAV are defined in order to get dynamic response as well as route tracking problem. In the third section, PID and adaptive PID properties are explained including advantages of adaptive PID and its use in UAVs. The applications of PID and adaptive PID methods on different geometries are examined in the fourth section. As a result, the performance of the UAV tracing trajectories with different geometries is examined with PID and adaptive PID controllers and the necessity of adaptive PID controllers is demonstrated in case of sudden maneuvers. The nomenclature of variables and abbreviations used in this article are shown in Tab. 1.

Table 1. Nomenclature of variables and abbreviations used in the article

Variables	Descriptions
$\{g\}$	Body frame
$\{G\}$	Coordinate frame
X, Y, Z	North, east, down positions of quadrotor, respectively.
x, y, z	North, right, down positions of quadrotor, respectively.
ϕ, θ, ψ	Roll, pitch and yaw angles, respectively.
p, q, r	Yaw, pitch and yaw rates, respectively.
$c(\cdot), s(\cdot), t(\cdot)$	$\cos(\cdot), \sin(\cdot), \tan(\cdot)$, respectively.
u_1, u_2, u_3, u_4	Total thrusts, roll angle input, pitch angle input, yaw angle input, respectively.
ω_i, K_d, K_T, ℓ	Motor angular speed, drag torque ratio constant, thrust constant, arm length, respectively.
I_x, I_y, I_z	The moment of inertia around each axis
m, J_{TP}	Mass of quadrotor, moment of inertia, respectively.
X_d, Y_d, Z_d	Desired positions in each axis
K_P, K_I, K_D	Proportional, integral, derivative control gain, respectively.
$K_{\chi_1}, K_{\chi_2}, K_{\phi_1}, K_{\phi_2}$	Gain coefficient matrices
u_1, ϕ_d, θ_d	Control signal, rolling and pitching desired signals, respectively.

2. System Model of Quadrotor

A quadrotor is defined as a multicopter that can fly through four rotors and provide movement maneuver. Compared to conventional helicopters using a main rotor and tail rotor, quadrotor using four rotors are preferred because they are easy to install and complex to control. In classical helicopters, complex mechanical systems consisting of many moving parts are controlled by commands transmitted to the rotors. On the other hand, quadrotors are generally advantageous in terms of ease of system

control. Quadrotor motors are fixed pitch, the use of chassis without simple and moving parts, and forward maneuverability due to high propulsion are the prominent features of the quadrotors. UAVs provide this movement with various torque and thrust forces. Each rotor contains a brushless DC motor. The rotors of the quadrotors are symmetrical and mutually arranged. The rotational directions and speeds of the rotors are changed and the movement of the quadrotors in three-dimensional space (on the x, y and z plane) is provided [4].

The rotation directions of the motors on the quadrotor, which are placed symmetrically about the horizontal and vertical axis, are shown in Fig. 1. Motors 1 and 3 rotate counterclockwise, motors 2 and 4 rotate clockwise. This applies to all multicopters. The aim is to prevent the UAV from moving uncontrolled about its own axes. By moving the propellers in different directions, the torque (rotating force) is balanced and the movement of the UAV is provided depending on the speed and direction of the propellers [5]. When the rotors move at the same speed, the aircraft takes off if gyroscopic effects are neglected. The thrust force generated by each motor must be the same to ensure stable aeration. A slight change in the propulsion of any of the engines (external disturbances such as wind, rain) can lead to an increase in the amount of error in aircraft control. By changing the speed of a single motor, the bearing force can be changed; horizontal and vertical axis movements can be achieved in this way [6]. In Fig. 1, quadrotor; Euler roll, pitch and yaw angles are indicated by body frame $\{g\}$ and the overall coordinate frame $\{G\}$. Hence the state variables is defined as in [6]; X, Y, Z , general (north, east, down) position; x, y, z , body (north, right, down) position, ϕ, θ, ψ roll, pitch and yaw angles; p, q, r , roll, pitch and yaw rates of the four propeller, respectively

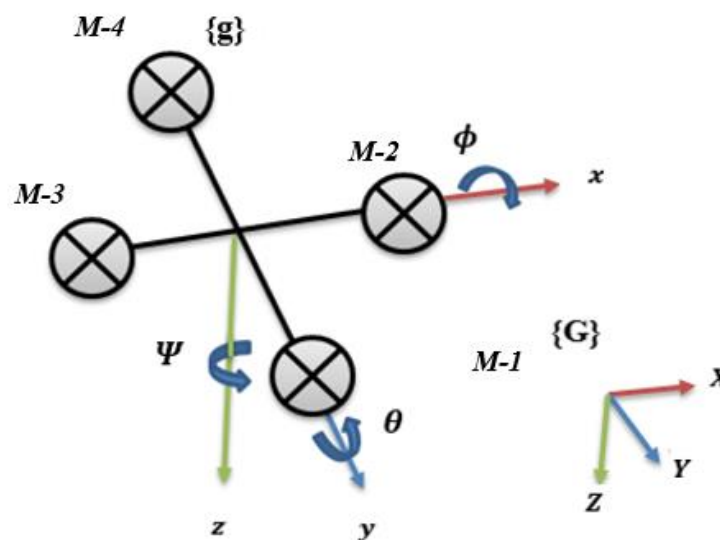


Figure 1. Rotational motion of the four-propeller UAV motors.

The quadrotor moves in six degrees of freedom, three cycles and three rotations. These movements are achieved by changing the direction of rotation and speed of the motors. The movement of the quadrotor motors according to the direction of rotation is shown in Fig. 2. Thick arrows indicate fast, thin arrows indicate slow rotation. According to this; (a) forward motion, (b) backwards motion, (c) movement left, (d) movement right, (e) increase altitude, (f) decrease altitude, (g) leftwards rotation, (h) rightwards rotation [7]. Control of rolling, pitching and yawing rates, p, q, r , together with position variables is important when evaluating duty time in route tracking.

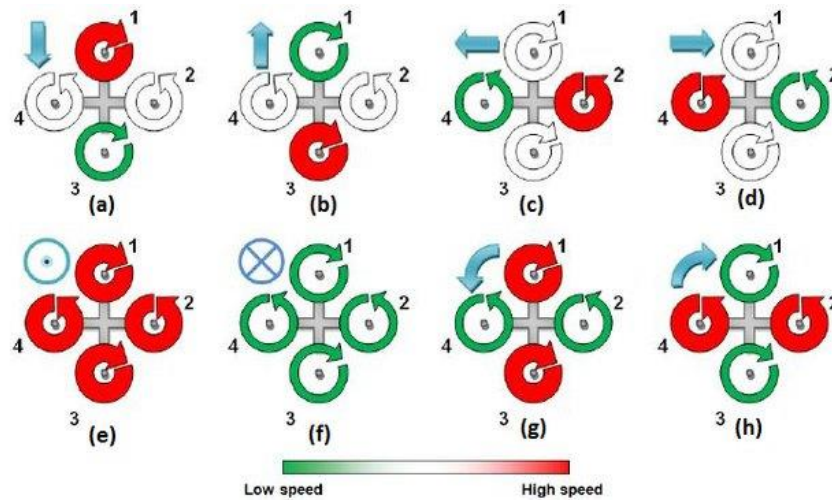


Figure 2. Quadrotor motions.

2.1. Modeling of Four-Propeller

The state variables for the speed of the UAV are generated via the coordinate frame $\{g\}$ on the body; however, the state variables specified for the position are on the global coordinate $\{G\}$ frame. Therefore, a transformation matrix must be created to transform the variables on the coordinate frame. The transformation on the general coordinate $\{G\}$ frame and the body coordinate frame $\{g\}$ is given as

$$x = R_G^b X, \quad y = R_G^b X, \quad z = R_G^b Z \quad (1)$$

$$R_G^b = R(\phi)R(\theta)R(\psi) = \begin{bmatrix} 1 & 0 & 0 \\ 0 & c(\phi) & s(\phi) \\ 0 & -s(\phi) & c(\phi) \end{bmatrix} \begin{bmatrix} c(\theta) & 0 & -s(\theta) \\ 0 & 1 & 0 \\ s(\theta) & 0 & c(\theta) \end{bmatrix} \begin{bmatrix} c(\psi) & s(\psi) & 0 \\ -s(\psi) & c(\psi) & 0 \\ 0 & 0 & 1 \end{bmatrix} \quad (2)$$

In this paper, $c(\cdot) = \cos(\cdot)$, $s(\cdot) = \sin(\cdot)$, $t(\cdot) = \tan(\cdot)$, has been represented for simplicity. Since angular velocities are defined in the body coordinate frame $\{g\}$ and Euler angles in intermediate coordinate frames, the transformation matrix is used to determine the relationship between the angular velocities and time derivatives of the Euler angles such as

$$\begin{bmatrix} p \\ q \\ r \end{bmatrix} = R(\phi)R(\theta) \begin{bmatrix} 0 \\ 0 \\ \dot{\psi} \end{bmatrix} + R(\phi) \begin{bmatrix} 0 \\ \dot{\theta} \\ 0 \end{bmatrix} + \begin{bmatrix} \dot{\phi} \\ 0 \\ 0 \end{bmatrix} \quad (3)$$

$$\begin{bmatrix} \dot{\phi} \\ \dot{\theta} \\ \dot{\psi} \end{bmatrix} = \begin{bmatrix} 1 & s(\phi)t(\theta) & c(\phi)t(\theta) \\ 0 & c(\phi) & -s(\phi) \\ 0 & \frac{s(\phi)}{c(\theta)} & \frac{s(\phi)}{c(\theta)} \end{bmatrix} \begin{bmatrix} p \\ q \\ r \end{bmatrix} \quad (4)$$

Brushless motor types are often used to produce the required thrusts and torques in UAVs. Each motor is energized by the electric battery and the electronic speed controller (ESC) receives the desired motor speeds output and sends these commands to each motor. The thrusts and moment equations are used to define as

$$\begin{bmatrix} u_1 \\ u_2 \\ u_3 \\ u_4 \end{bmatrix} = \begin{bmatrix} K_T & K_T & K_T & K_T \\ 0 & -\ell K_T & 0 & \ell K_T \\ \ell K_T & 0 & -\ell K_T & 0 \\ K_d & -K_d & K_d & -K_d \end{bmatrix} \begin{bmatrix} \omega_1^2 \\ \omega_2^2 \\ \omega_3^2 \\ \omega_4^2 \end{bmatrix} \quad (5)$$

for control inputs of the UAV where u_1 : total thrusts, $u_1^{min} \leq u_1 \leq u_1^{maks}$, u_2 : roll angle input, $u_2^{min} \leq u_2 \leq u_2^{maks}$, u_3 : pitch angle input, $u_3^{min} \leq u_3 \leq u_3^{maks}$, u_4 : yaw angle input, $u_4^{min} \leq u_4 \leq u_4^{maks}$, ω_i : i.th motor angular speed (rad/s), $\omega_i^{min} \leq \omega_i \leq \omega_i^{maks}$ $i = 1 \dots 4$, K_d : drag torque ratio constant, K_T : thrust constant, ℓ : arm length. It is important to limit the control inputs that can be calculated by the control system which are transferred to ESCs and converted to motor speeds.

Equations of motion used in the control of UAV, including (3)-(4) can be defined as

$$\begin{bmatrix} \ddot{X} \\ \ddot{Y} \\ \ddot{Z} \end{bmatrix} = \frac{-1}{m} \begin{bmatrix} K_{dx} & 0 & 0 \\ 0 & K_{dy} & 0 \\ 0 & 0 & K_{dz} \end{bmatrix} \begin{bmatrix} \dot{X} \\ \dot{Y} \\ \dot{Z} \end{bmatrix} - \frac{1}{m} \begin{bmatrix} c(\phi)s(\theta)c(\psi) + s(\phi)s(\psi) \\ c(\phi)s(\theta)s(\psi) - s(\phi)c(\psi) \\ c(\phi)c(\theta) \end{bmatrix} u_1 + \begin{bmatrix} 0 \\ 0 \\ g \end{bmatrix} \quad (6)$$

$$\begin{bmatrix} \dot{p} \\ \dot{q} \\ \dot{r} \end{bmatrix} = \begin{bmatrix} \frac{(I_z - I_y)}{I_x} qr \\ \frac{(I_x - I_z)}{I_y} rp \\ \frac{(I_y - I_x)}{I_z} pq \end{bmatrix} + \begin{bmatrix} -J_{TP} q \\ J_{TP} p \\ 0 \end{bmatrix} \Omega + \begin{bmatrix} \frac{l}{I_x} & 0 & 0 \\ 0 & \frac{l}{I_y} & 0 \\ 0 & 0 & \frac{1}{I_z} \end{bmatrix} \begin{bmatrix} u_2 \\ u_3 \\ u_4 \end{bmatrix} \quad (7)$$

where I_x , I_y and I_z represent the moment of inertia around each axis; m refers to the mass of quadrotor; J_{TP} refers to the moment of inertia caused by the rotation of the motor; $\Omega = \omega_1 + \omega_2 - \omega_3 + \omega_4$ and p, q, r refer to rolling, pitching and yawing rates respectively as in [8].

2.2. Route Tracking

In order to ensure that the UAVs move unmanned, to move to the desired route as soon as possible and to use minimal energy, it is essential that they follow course and ensure movement on the desired route. In order to follow the route, either the UAV has to advance along the predetermined route, or it has to establish its own route with specific algorithms and methods. There are many studies in the literature regarding the follow-up of the UAV [5-6, 9]. Accordingly, the route that the UAV will take first must be determined first. Reference points are determined on desired route. The trajectory optimization is performed over the determined points and the X, Y, Z position is determined for tracking the trajectory and converted to the x, y, z position via the body coordinate. This creates the rolling, pitching, deflection angles and provides motor control where the height, position, offset and speed values are adjusted and acceleration is provided in the horizontal-vertical plane.

Reference points are determined in all route tracking systems and the UAV's follow-up rate is examined. Accordingly, if X_d, Y_d, Z_d will determine the reference route in route tracking, X, Y, Z indicate the route of the UAV. Hence the error can be calculated as

$$e = \sqrt{(X_d - X)^2 + (Y_d - Y)^2 + (Z_d - Z)^2} \quad (8)$$

where UAV speed and task completion duration are important.

3. Controller Design for UAV

In this section, PID control and adaptive PID control are outlined and adaptive PID estimation method is mentioned. The most common type of control system is the Proportional-Integral-Derivative (PID) control system [10]. The PID controller is known as a closed loop feedback system. The control system calculates the difference between the actual and desired state and generates an error value. The measured values output from the sensor on the UAV are fed back to calculate this error signal and provide the balance between the desired value and the measured value [11]. The output of the PID control system is a control value that will bring the system closer to the desired state. Adaptive PID control, on the other hand, is a control method for changing system behavior to adapt to new situations. Adaptive PID control is inherently non-linear as it will adapt to new situations.

By using a PID controller, it is possible to move the UAV in the air, glide and move in the desired direction [12]. The PID controller is advantageous in terms of easy adjustment, design and strength of parameter gains; however, in non-linear and definite situations associated with the mathematical model, the quadrotor models limit the movement and performance of the UAV. The UAV controlled by the PID controller has control inputs $u(t)$,

$$u(t) = K_P e(t) + K_I \int_0^t e(\tau) d\tau + K_D \dot{e}(t) \quad (9)$$

where K_P , proportional control gain, K_I , integral control gain, K_D , derivative control gain and t , time variable is expressed. In this paper, PID parameters are obtained by taking the system stability into consideration in order to ensure the follow-up of the reference route. The PID parameters are embedded in the motor drive circuits of the UAV.

The adaptive PID control is intended for changes in parameters K_P , K_I , and K_D . The performance in determining the gain parameters directly affects the performance of the PID controller. Therefore, in the study, the gain parameters of the PID controller are determined by the Ziegler-Nichols method. The adaptive PID controller block diagram of the UAV is shown in Fig. 3. It is aimed to determine the orientation and deflection performance and speed of the UAV based on the system model by regulating the controller coefficients. Adaptive PID control generally includes three basic steps that are system modeling, controller design and adaptation of the controller [12-15]. The system modeling part is created by adapting the mathematical modeling of the UAV into the system. Then, the system is observed and their behavior is examined. A model is obtained from the input and output signal parameters of the observed system. This process is called parameter estimation [11].

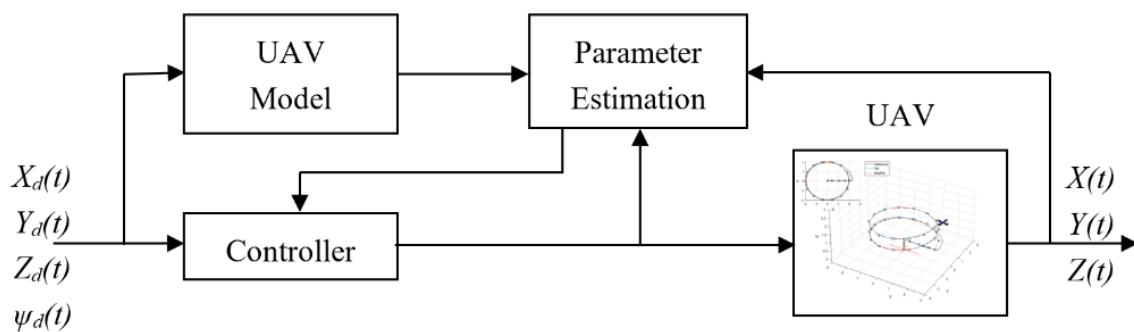


Figure 3. UAV adaptive PID controller block diagram.

Here, the UAV is examined and propeller speeds are controlled by obtaining the required thrust control signals. In the event that the frictional forces and gravity effects mentioned in Eqs. (3, 4) and (6, 7) are neglected, the dynamic model of UAV is obtained as

$$\ddot{\mathcal{X}} = \begin{bmatrix} \ddot{X} \\ \ddot{Y} \\ \ddot{Z} \end{bmatrix} = -\frac{1}{m} \begin{bmatrix} c(\phi)s(\theta)c(\psi) + s(\phi)s(\psi) \\ c(\phi)s(\theta)s(\psi) - s(\phi)c(\psi) \\ c(\phi)c(\theta) \end{bmatrix} u_1 + \begin{bmatrix} 0 \\ 0 \\ g \end{bmatrix} \quad (10)$$

$$\dot{\Phi} = \begin{bmatrix} \ddot{\phi} \\ \ddot{\theta} \\ \ddot{\psi} \end{bmatrix} = \begin{bmatrix} \frac{1}{J_x} & 0 & 0 \\ 0 & \frac{1}{J_y} & 0 \\ 0 & 0 & \frac{1}{J_z} \end{bmatrix} \begin{bmatrix} u_2 \\ u_3 \\ u_4 \end{bmatrix} \quad (11)$$

where the $\mathcal{X} = [x \ y \ z]^T$ position vector is the attitude vector containing the roll, pitch, and yaw angles $\Phi = [\phi \ \theta \ \psi]^T$ of UAV. If the slow change of Euler angles is linearized with Eqs. (6) and (7), the resulting reference model is \mathcal{X}_m, Φ_m state variables, \mathcal{X}_d, Φ_d target variables,

$$\dot{\mathcal{X}}_m = \dot{\mathcal{X}}_d + K_{\mathcal{X}_2}(\mathcal{X}_d - \mathcal{X}_m) + K_{\mathcal{X}_1}(\mathcal{X}_d - \mathcal{X}_m) \quad (12)$$

$$\dot{\Phi}_m = \dot{\Phi}_d + K_{\Phi_2}(\Phi_d - \Phi_m) + K_{\Phi_1}(\Phi_d - \Phi_m) \quad (13)$$

where $K_{\mathcal{X}_1}, K_{\mathcal{X}_2}, K_{\Phi_1}$, and K_{Φ_2} are gain coefficient matrices. Accordingly, position error and attitude error vectors are defined as

$$e_{\mathcal{X}} = \mathcal{X} - \mathcal{X}_m \quad \text{and} \quad e_{\Phi} = \Phi - \Phi_m \quad (14)$$

Adaptation rules to obtain Lyapunov-based stable control signals can be defined as

$$\dot{\Upsilon}_{\mathcal{X}} = K_{\mathcal{X}}(\dot{e}_{\mathcal{X}} + K_{\mathcal{X}_1}e_{\mathcal{X}}) \quad (15)$$

$$\dot{\Upsilon}_{\Phi} = K_{\Phi}(\dot{e}_{\Phi} + K_{\Phi_1}e_{\Phi}) \quad (16)$$

so that the control inputs

$$\vartheta = -[e_{\mathcal{X}} + \varphi_{\mathcal{X}}^T \Upsilon_{\mathcal{X}} + K_{\Phi_2} + K_{\mathcal{X}_2}(\dot{e}_{\mathcal{X}} + K_{\mathcal{X}_1}e_{\mathcal{X}})] \quad (17)$$

$$u = -[e_{\Phi} + \varphi_{\Phi}^T \Upsilon_{\Phi} + K_{\Phi_2}(\dot{e}_{\Phi} + K_{\Phi_1}e_{\Phi})] \quad (18)$$

are obtained. Here, ϑ control signal provides u_1, ϕ_d, θ_d rolling and pitching desired signals, while u control signal gives u_2, u_3, u_4 signals [16]. Also the gain matrices can be defined as

$$K_{\mathcal{X}} = \alpha_{\mathcal{X}} \varphi_{\mathcal{X}} \quad \text{and} \quad K_{\Phi} = \alpha_{\Phi} \varphi_{\Phi} \quad (19)$$

where $\alpha_{\mathcal{X}}, \varphi_{\Phi}$ positively defined matrices that determine the adaptation rate and

$$\varphi_x = \begin{bmatrix} K_{x_1} \dot{e}_x - \ddot{X}_m & | & 0 \\ 1 & & 1 \end{bmatrix}^T \quad (20)$$

$$\varphi_\phi = \text{diag}(K_{\phi_1} \dot{e}_\phi - \ddot{\Phi}_m) \quad (21)$$

control signals in Eqs. (17) and (18) include adaptive PID coefficients.

4. Route Tracking Results

In this section, the route tracking simulation is performed via the MATLAB program of UAV. While performing this simulation, two different control approaches, PID and adaptive PID, are applied and their performance is compared with each other. In this simulation, regulated control systems and route tracking modeling have been developed. UAV flight time is 60 sec where sampling time is 0.01 sec. The motion of the UAV with the PID and adaptive control algorithms on the x , y and z coordinates has been examined on a circle, rectangle, lemniscate ∞ and spiral trajectory. The trajectory tracking performances are examined on 3 different scenarios (a), (b), and (c) respectively, as shown in Fig. 4. The reason for examining follow-up performance trajectories is; the aim of the present study is to investigate the follow-up rate of hard turns for scenario 1, reverse turns for scenario 2 and soft turn - ramp up for scenario 3, and to determine the amount of error. The amount of error indicates the relationship between the specified route and the performance of the UAV to follow the route. If $X_d(t)$, $Y_d(t)$, $Z_d(t)$ are to determine the reference route in the course of the follow-up, $X(t)$, $Y(t)$, $Z(t)$ then total error according to the position of the UAV is

$$e_T = \sum_{t=1}^N \sqrt{(X_d(t) - X(t))^2 + (Y_d(t) - Y(t))^2 + (Z_d(t) - Z(t))^2} \quad (22)$$

In addition, the total route followed by the UAV is calculated based on location information.

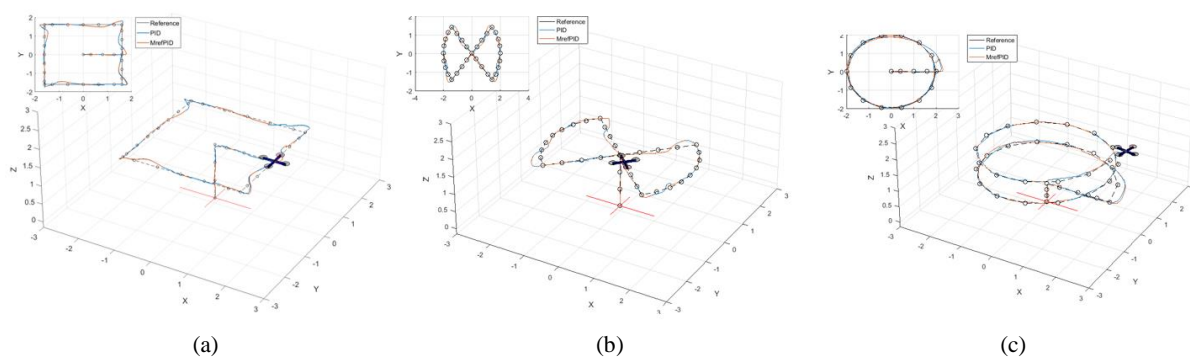


Figure 4. UAV route tracking trajectory (a) rectangle, (b) lemniscate ∞ , (c) spiral.

In this study, route tracking performance of four propeller UAV with PID and adaptive PID controller was investigated. PID, K_p , K_I , and K_D coefficients for X , Y and Z position and roll (ϕ) - pitch (θ) - yaw (ψ) angles and rates of four propeller UAVs are presented in Tab. 2.

The performance of the UAV with adaptive PID control algorithm to follow a rectangular, lemniscate ∞ and spiral trajectory has been investigated on the trajectory shown in Figs. 5-7, respectively. Figs 5-7 also show reference route. In addition, Tab. 3 lists the total path length for PID and adaptive PID controller performance including total route length as well as total distance error as defined in Eq. (22). It has been seen that adaptive PID results much better than PID controller

performance. Adaptive PID total error is about 10% less than PID controller not only for hard turns as in scenario 1 (rectangle), but also for reverse turns as in scenario 2 (lemniscate, ∞). In addition to that adaptive PID shows about 50% better total error compared to PID controller for soft turn - ramp up as in scenario 3 (spiral).

Table 2. PID parameters of UAV.

	X, Y	Z	p, q, r	ϕ, θ	ψ
K_p	0.35	5.89	3.30	4.50	10
K_i	0.25	0.0	0.20	0.12	0.24
K_d	0.35	5.05	0.02	0.17	0.34

Table 3. PID and adaptive PID performance of UAV.

Route	PID		Adaptive PID	
	Route (m)	er(m)	Route (m)	er(m)
Rectangle (16.0m)	18.736	95.509	18.736	85.757
Lemniscate (15.8m)	18.480	100.446	18.405	91.458
Spiral (29.3m)	31.423	189.620	29.943	106.873

Fig. 8 shows the position change X, Y and Z position tracking including yaw angle as well as squared error change for spiral route tracking of both the PID controller and the Adaptive PID controller. Especially for the hard turn at 8-10 sec, Adaptive PID shows much better performance compared to PID controller. It is very important to note that route tracking application should solve hard turn problem. Fig. 9 shows the variation of K_p, K_i, K_d coefficients for adaptive PID controller as in UAV X, Y, Z position and deviation movements. The changes are parallel to the parameters given in Tab. 1.

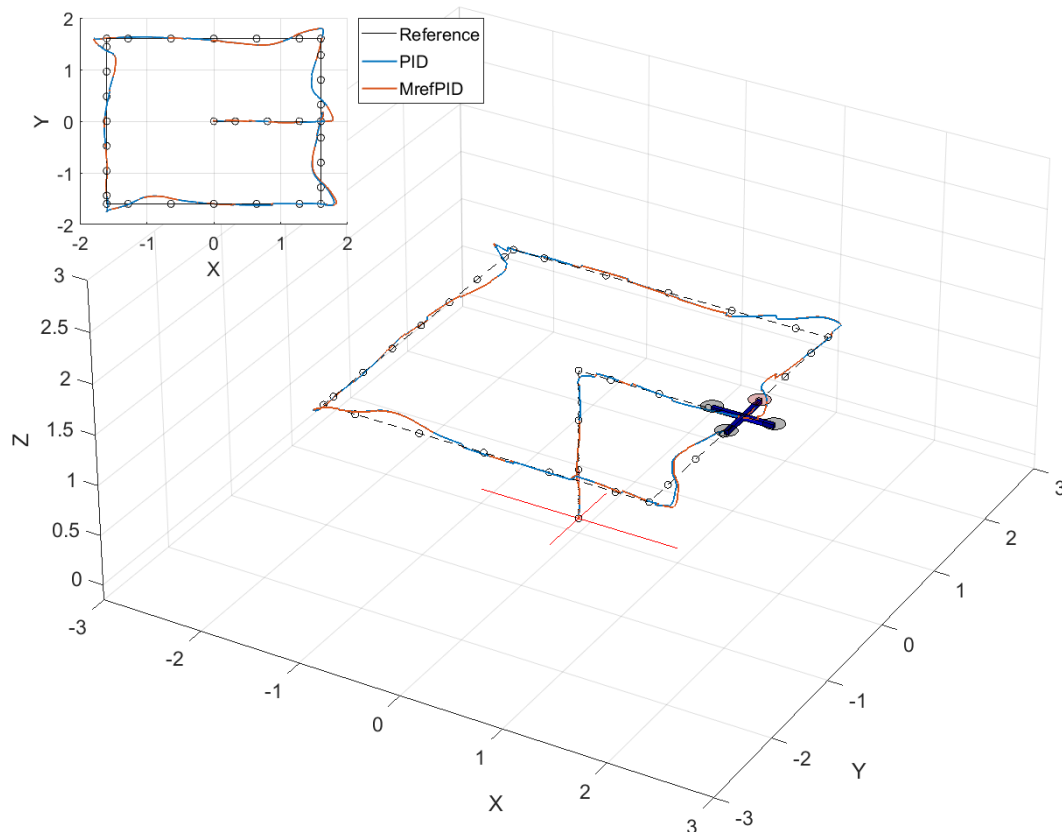


Figure 5. Rectangular route tracking for PID and adaptive PID.

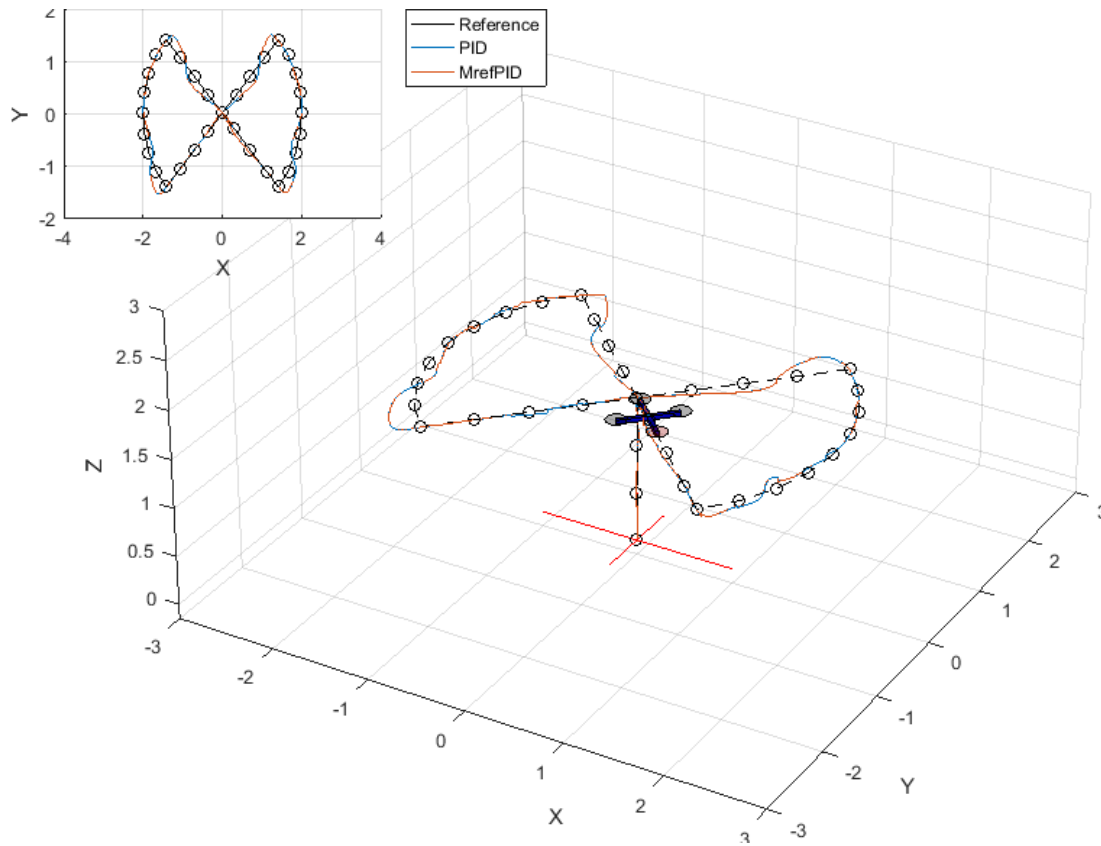


Figure 6. Lemniscate ∞ route tracking for PID and adaptive PID.

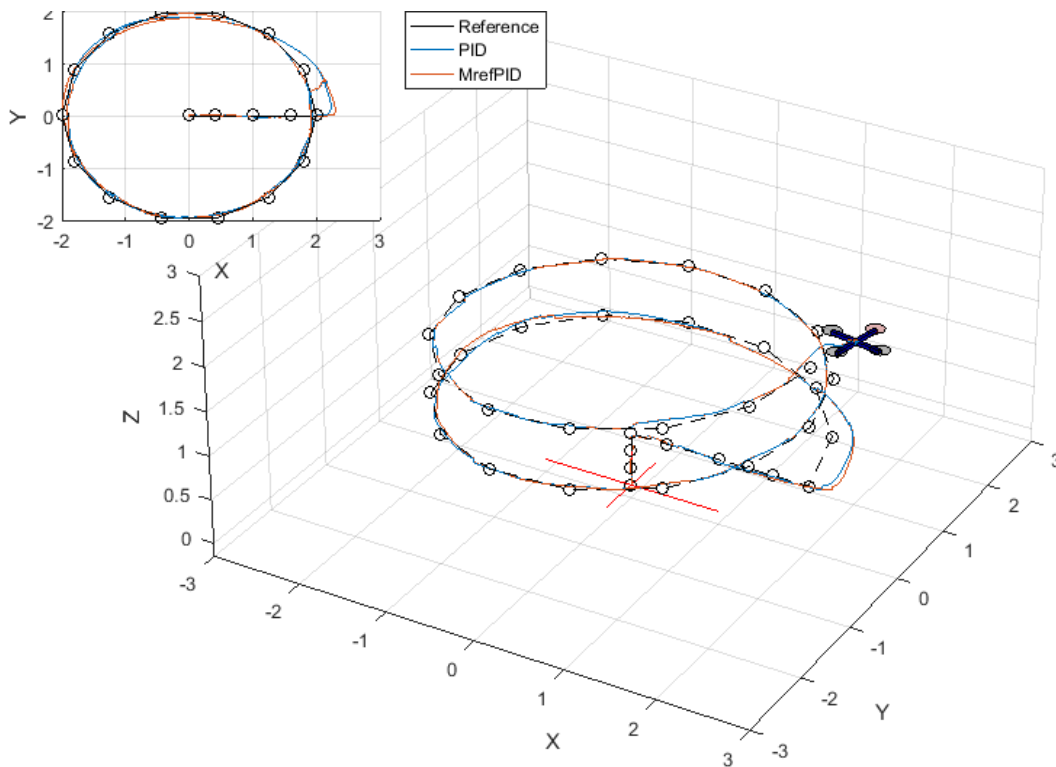


Figure 7. Spiral route tracking for PID and adaptive PID.

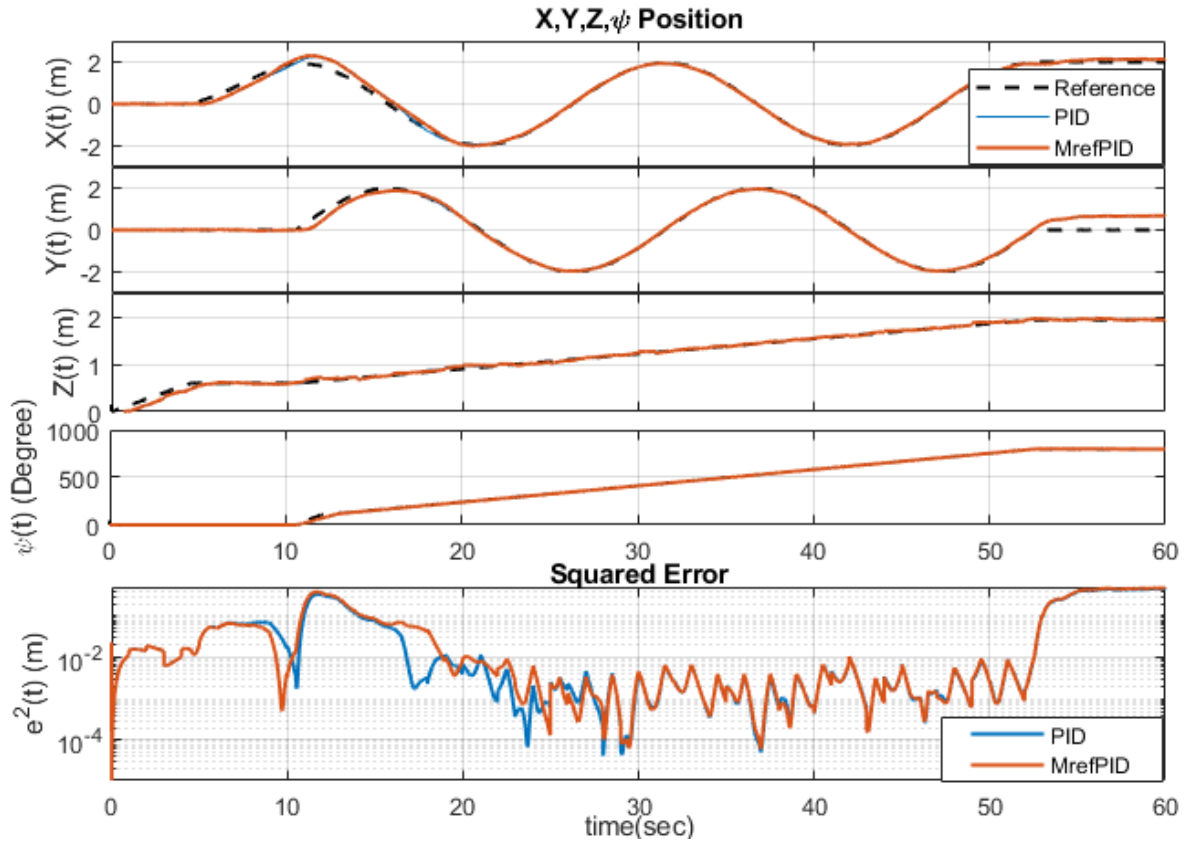


Figure 8. Spiral route tracking X,Y,Z position, yaw angle and square position error for PID and adaptive PID.

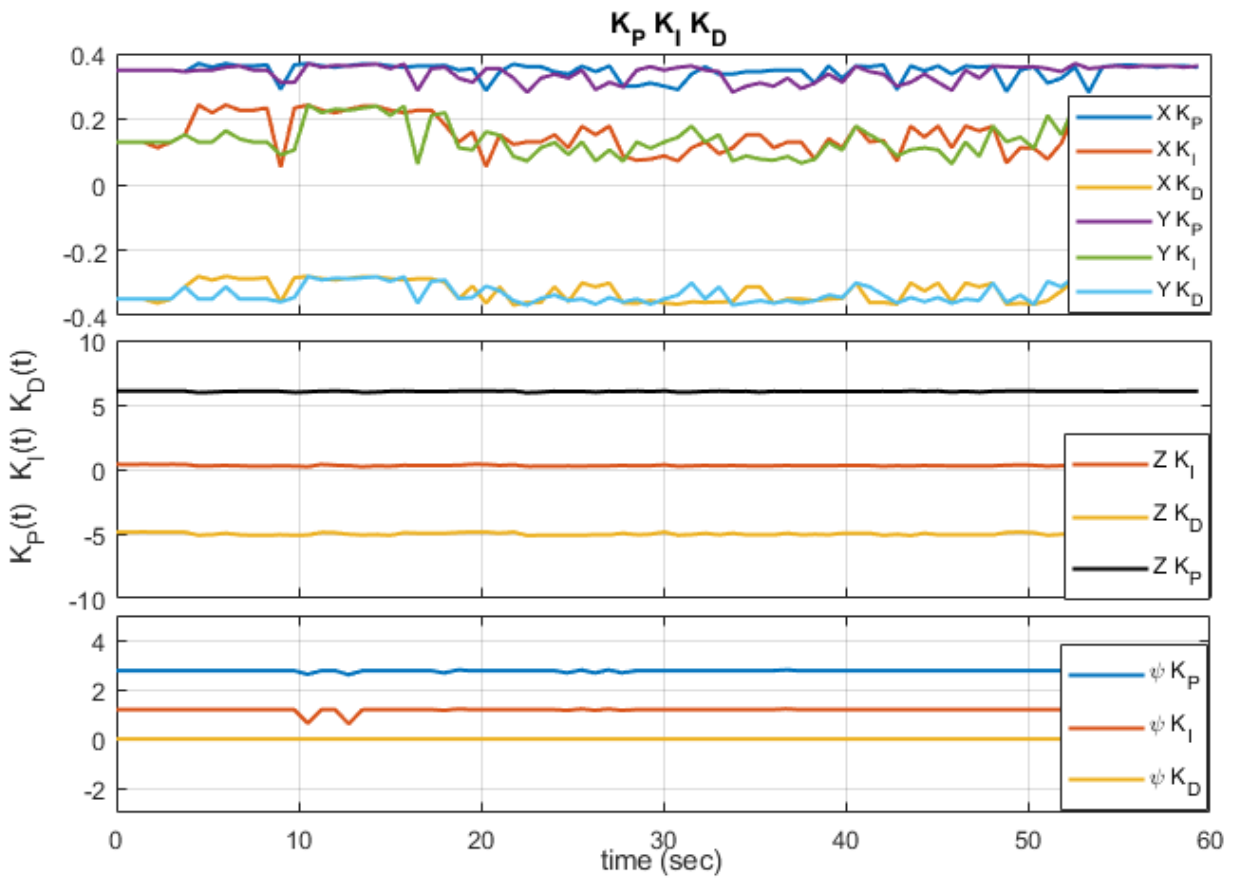


Figure 9. Spiral route tracking PID coefficient change for adaptive PID.

5. Conclusions

In this study, PID and adaptive PID controller performance for route tracking of four propeller UAVs are studied. Performance of both PID and adaptive PID controllers on trajectories with various geometries has been tested. It has been observed that the error rate of the proposed controller for three different trajectories are lower than the PID controller which is used as a reference. In cases of sudden maneuvers, the necessity of adaptive approaches has been demonstrated. In addition, a stable flight was observed when appropriate PID gain values have been obtained for the system. It has been shown that the adaptive PID controller can be used in route tracking applications with high accuracy. In future studies, the performance of the proposed controller will be tested under different external disturbances as well as target detection and tracking applications.

Acknowledgment

This study was supported by Zonguldak Bülent Ecevit University (BAP Project No: 2014-75737790-01). The authors would like to thank Zonguldak Bülent Ecevit University for the support. Preliminary results of this study had been presented in INERS'19 symposium.

References

- [1] Maza, I., Kondak, K., Bernard, M., Ollero, A. (2010). Multi-UAV cooperation and control for load transportation and deployment. *Journal of Intelligent and Robotic Systems*, 1(57), 417-449.
- [2] Altan, A., Aslan, Ö., Hacıoğlu, R. (2018). Real-time control based on NARX neural network of hexarotor UAV with load transporting system for path tracking. *In 2018 6th International Conference on Control Engineering & Information Technology (CEIT)*, İstanbul, Turkey, 1-6.
- [3] Altan, A., Kökal, K., Hacıoğlu, R. (2017). Vektör alan kılavuzu yöntemi ile görsel çizgi takibi için insansız hava aracı üzerindeki yalpanın model öngörülü denetimi. *Karaelmas Science and Engineering Journal*, 7(1), 218-227.
- [4] Tosun, D. C., Işık, Y., Korul, H. (2015). Comparison of PID and LQR controllers on a quadrotor helicopter. *International Journal of Systems Applications Engineering and Development*, 9, 136-143.
- [5] Belge, E., Kaba, H. K., Parlak, A., Altan, A., Hacıoğlu, R. (2020). Estimation of small unmanned aerial vehicle lateral dynamic model with system identification approaches. *Balkan Journal of Electrical and Computer Engineering*, 8(2), 121-126.
- [6] Altan, A., Hacıoğlu, R. (2020). Model predictive control of three-axis gimbal system mounted on UAV for real-time target tracking under external disturbances. *Mechanical Systems and Signal Processing*, 138, 106548.
- [7] Coppejans, H. H., Myburgh, H. C. (2015). A primer on autonomous aerial vehicle design. *Sensors*, 15(12), 30033-30061.
- [8] Selim, E., Uyar, E., Avcı, M. (2013). Quadrocopterin matematiksel modeli ve kontrolü. *Otomatik Kontrol Ulusal Toplantısı (TOK2013)*, Malatya, Turkey, 548-551.
- [9] Hernandez, A., Murcia, H., Copot, C., Keyser, R.D. (2014). Model predictive path-following control of an AR. Drone Quadrotor. *In XVI Latin American Control Conference The International Federation of Automatic Control*, Cancun, Mexico, 618-623.

- [10] Li, J., Li, Y. (2011). Dynamic analysis and PID control for a quadrotor. *In International Conference on Mechatronics and Automation (ICMA)*, Beijing, China, 573-578.
- [11] Zulu, A., John, S. (2014). A review of control algorithms for autonomous quadrotors. *Open Journal of Applied Sciences*, 4, 547-556.
- [12] Tanyer, A., Tatlicioglu, E., Zergeroglu, E. (2017). Model reference tracking control of an aircraft: a robust adaptive approach. *International Journal of Systems Science*, 48(7), 1428-1437.
- [13] Pratama, N., Manggau, F. X., Betaubun, P. (2019). Attitude quadrotor control system with optimization of PID parameters based on fast genetic algorithm. *International Journal of Mechanical Engineering and Technology (IJMET)*, 10(1), 335-343.
- [14] Liu, H., Xi, J., Zhong, Y. (2017). Robust attitude stabilization for nonlinear quadrotor systems with uncertainties and delays. *IEEE Transactions on Industrial Electronics*, 64(7), 5585-5594.
- [15] Larin, V. B., Tunik, A. A. (2016). Synthesis of the quad-rotor flight control system. *In 2016 4th International Conference on Methods and Systems of Navigation and Motion Control (MSNMC)*, Kiev, Ukraine, 12-17.
- [16] Akgun, O., Subasi, E., Turker, T. (2017). A Lyapunov based model reference adaptive control of a quadrotor. *In 2017 10th International Conference on Electrical and Electronics Engineering (ELECO)*, Bursa, Turkey, 1-5.

EFFECT OF WC REINFORCED ON MICROSTRUCTURE AND MECHANICAL PROPERTIES OF CuAlMn ALLOYS PRODUCED BY HOT PRESSING METHOD


Tayfun ÇETİN¹, Mehmet AKKAŞ^{2*}


In this study, the effect of WC reinforcing particles on the microstructure and mechanical properties of CuAlMn and CuAlMn-WC alloy produced by powder metallurgy method was investigated by adding 5 %, 10 % and 15 % by volume WC to CuAlMn alloy. Cu, Al, Mn and WC powders of approximately 99.9 % purity with a grain size of 325 mesh were used in the production of the alloys. The samples were produced by hot pressing method at 900 °C temperatures under 35 MPa pressure for 6 minutes. Microstructure, phase formation, hardness and corrosion properties of the samples were investigated in detail. Scanning electron microscopy (SEM) was used for microstructure analysis and X-ray diffractogram (XRD) was used for phase formation detection. The hardness measurements of the samples were measured by microhardness measuring device. The corrosion tests were performed potentiodynamic polarization curves of the composite materials in 3.5% NaCl solution. As a result, it has been determined that the mechanical properties of WC reinforcing particles added to CuAlMn matrix increase with increasing volume ratio.

Key words: CuAlMn alloys, hot press, mechanical properties, microstructure properties, reinforced WC

1. Introduction

With the rapid development of technology, many new types of materials are being developed and used. These materials are more suitable for today's conditions and their usage is becoming widespread. Metal matrix composite materials have also been studied in recent years and new types of materials are derived. Production method with PM is a method used to produce full or semi-finished products [1]. It has been stated that some composite materials, such as super alloys and hard metals, can only be produced by the PM method, because the melting temperatures of the metals are very high and it is very difficult to reach these temperatures under industrial conditions [2,3,4]. Many different Cu alloys are used in the chemical industry and electro technologies [5-7]. Cu alloys have high corrosion and oxidation resistance in addition to their good thermal resistance and electrical resistance. In addition, copper has a good ductility and toughness [8]. Composites with Cu matrix have high thermal conductivity and electrical conductivity. In addition, the mechanical properties and tribological properties of these composites are good [9-12].

¹ Department of Electricity and Energy, Yüksekova Vocational School of Higher Education, Hakkari University, Hakkari, Turkey, (tayfuncetin@hakkari.edu.tr)  <https://orcid.org/0000-0001-8060-344X>

² Department of Mechanical Engineering, Faculty of Engineering and Architecture, Kastamonu University, Kastamonu, Turkey, (mehmetakkas@kastamonu.edu.tr)  <https://orcid.org/0000-0002-0359-4743>

Metal matrix composites have many positive properties such as high elastic modulus, high strength and reproducibility [13]. In addition, these materials have very good abrasion resistance due to particle reinforcements [14,15]. There is also a lot of research on composites with copper matrix [16]. In a study, the abrasion resistance was improved by adding Ni₃Al particles to the copper matrix [9]. CuCr SiC composite material has been produced and it has been stated that the hardness increases in the examination [17]. In addition, FeMnp and FeCrp were added to the Cu matrix to investigate their microstructure and mechanical properties [18]. By adding different additions to the Cu matrix, its hardness, strength, abrasion resistance and conductivity can be improved [19]. In addition, tensile strength increased up to 4% within the varying Cu matrix ratios; It was observed that after 4% it decreased and the hardness increased with increasing Cu matrix ratio [20].

Although powder metallurgy (PM) is not a newly known process, it was only used as an industrial process in the early 20th century. PM method has been used extensively in different fields since the beginning. As an example to these; tool steels, stainless steels, superalloys, aluminum and titanium alloys, copper and copper alloys, nuclear materials and cermets can be given [1-5,21]. Parts produced by this method have a smoother surface than parts produced by other methods and often do not require secondary treatment. It was determined that approximately 97% of the first material used in mass production with PM was used. Accordingly, the production of the part is cheaper and in the desired composition, and some parts that are difficult to produce and process by other methods are easily produced. By making fluctuations on the value of the punch pressure, it is possible to produce products in various forms in a better quality and in a proper manner [4].

Demand increases for copper (Cu) based alloys, especially Cu-Al-Ni, CuZn-Al and Cu-Al-Mn alloys due to their cheap cost and good shape recall effects and superelasticity in engineering applications [22-24]. Cu-based shape recall alloys have been in great demand after the 1960s and have been used as alternatives to NiTi alloys, because they have good electrical and thermal conductivity [25,26]. Cu based shape remembering alloy systems are in great demand in the practical applications of shape remembering alloys. Because it can be produced both cheaply and easily. However, as the high Al additive to this alloy causes the grain boundaries to weaken, it creates a very fragile alloy. It is important to add new elements to strengthen the Cu-Al alloy with a good ductility [27,28]. The addition of new elements to Cu-Al alloys made this alloy group more useful and attractive. However, in addition to the elementary additive, CuAl based shape recall alloys can improve the performance of the applied heat treatment. Generally, high temperature shape recall alloys are important in the robotics, automotive and aircraft industries. The application temperatures of these alloys should be above 390 K [29,30]. In this study, the effect of heat treatment temperature and heat treatment time on the conversion temperature and crystal structure of CuAlMn alloy, which is a new high temperature shape remember alloy, will be examined. There are some studies in the literature about the production of Cu-Al-Mn alloys with the PM method and the relationship between the microstructure and mechanical properties [31,32]. For example, Yu-Yang Gao et al. [33,34] in their study, they made a characterization study by adding different ratios of SiC to Al-Cu-Mg-Si-Mn composites by using PM method. They determined that the particles were dispersed homogeneously and the tensile strength increased. This has been linked to the formation of precipitates of SiC particles during sintering and post-sintering cooling. Yan et al. In their study, they investigated the change of martensitic phase by adding Ni to Cu-Al-Mn shape memory alloy casting method. They found that when 2% Ni was added, the triple Cu-Al-Mn alloys increased the shape memory from 85% to 92%. Cu-Al-Mn alloys have a high tensile strength. It is used in the production of

machine parts, vehicles, lifting gear, railway wagons in constructions where high strength is required. Strength in Hardened State It has been determined that it reaches the strength of 52 steel [32].

2. Experimental Procedure

In the starting matrix powders, Cu, Al, Mn and WC an average particle size 44 μm were used. The matrix in produced segments that was sintered by hot pressing process. Powder mixtures were weighed by using precision scales and mixing process was applied for 30 minutes by using a turbula mixer (Celmak Group 7T, Turkey). PEG 400 (Polyethylene Glycol) at a rate of 1,5 wt% was added in the powder mixture in order to reduce friction forces during hot pressing and to provide a homogenized mixture. Previously, powders were weighed 20 grams, and then CuAlMn-WC were produced with a pressure of 300 MPa by using double-effect hydraulic press (Dim-Net WP-45SA, Korea). After that, CuAlMn-WC were placed within graphite dies and hot pressed under vacuum atmosphere by a PLC controlled direct hot pressing machine (Zhengzhou Golden Highway, SMVB 80, China) (Fig. 1).



Figure 1. PLC controlled direct hot pressing machine.

Following that production process was completed by applying a sintering to the samples in a furnace (Prothem, PLF 120/27, Turkey) under argon atmosphere at 900 °C and under pressure 35 MPa and for 4 minutes. Composite parameters of production were given in the Tab. 1.

Table 1. Hot pressing production parameters.

Sample	Pressure (MPa)	Temperature (°C)	Time (min.)	Chemical Composition
1				CuAlMn
2	35	900	4	CuAlMn - 5 % WC
3				CuAlMn - 10 % WC
4				CuAlMn - 15 % WC

The produced composite samples were characterized for hardness, optical microscope. Surface of the samples were polished with 200, 400, 600, 800, 1000 and 1200 mesh wet sandpaper by using grinding device (Metkon Forcimat, Turkey). Microhardness of the samples were measured in Vickers

microhardness terms ($HV_{0,1}$) by using 16 second time and 0,1 kg of load. Surface of the samples were etched by a special etcher which consists of 50 gr. ($FeCl_3 - 6H_2O$) + 960 ml. methanol + 200 ml. HCl after polishing and then microstructure investigations were performed. The SEM images and EDS analyzes of the materials were obtained from the “FEI” brand “Quanta FEG 250” in model device at Kastamonu University Central Research Laboratories (Fig. 2a). The XRD analyzes of the samples were taken from “Bruker” brand “D8 Advance” model device at Kastamonu University Central Research Laboratories (Fig. 2b).



Figure 2. (a) FEI QUANTA 250 FEG SEM analyzer, (b) Bruker D8 Advance XRD analyzer.

The hardness measurements of the materials were done by using “SHIMADZU” brand “HMV-G21” model microhardness measurement device (Fig. 3a) under 16 min. waiting time and 100 g load. Corrosion tests of the produced materials were made by “Gamry” brand Potentiostat / Galvanostat device (Fig. 3b).



Figure 3. (a) SHIMADZU HMV-G21 model microhardness measuring device, (b) Reference 3000 Potentiostat / Galvanostat / ZRA device.

3. Results and Discussion

The SEM images of the CuAlMn-WC composites produced by the powder metallurgy method (Fig. 4) were taken and evaluations were made according to the obtained images.

When the SEM images are examined, it is seen that WC particles are distributed homogeneously in the interior of the sample containing CuAlMn. Samples produced are non-cracked and partially porous. As the addition of WC increases, the pore amount decreases and it is seen from SEM

photographs. The homogeneous dispersion may be sufficient due to the sintering temperature [35]. Represents the WC powders are uniformly separated on the CuAlMn in the Fig. 4 [36].

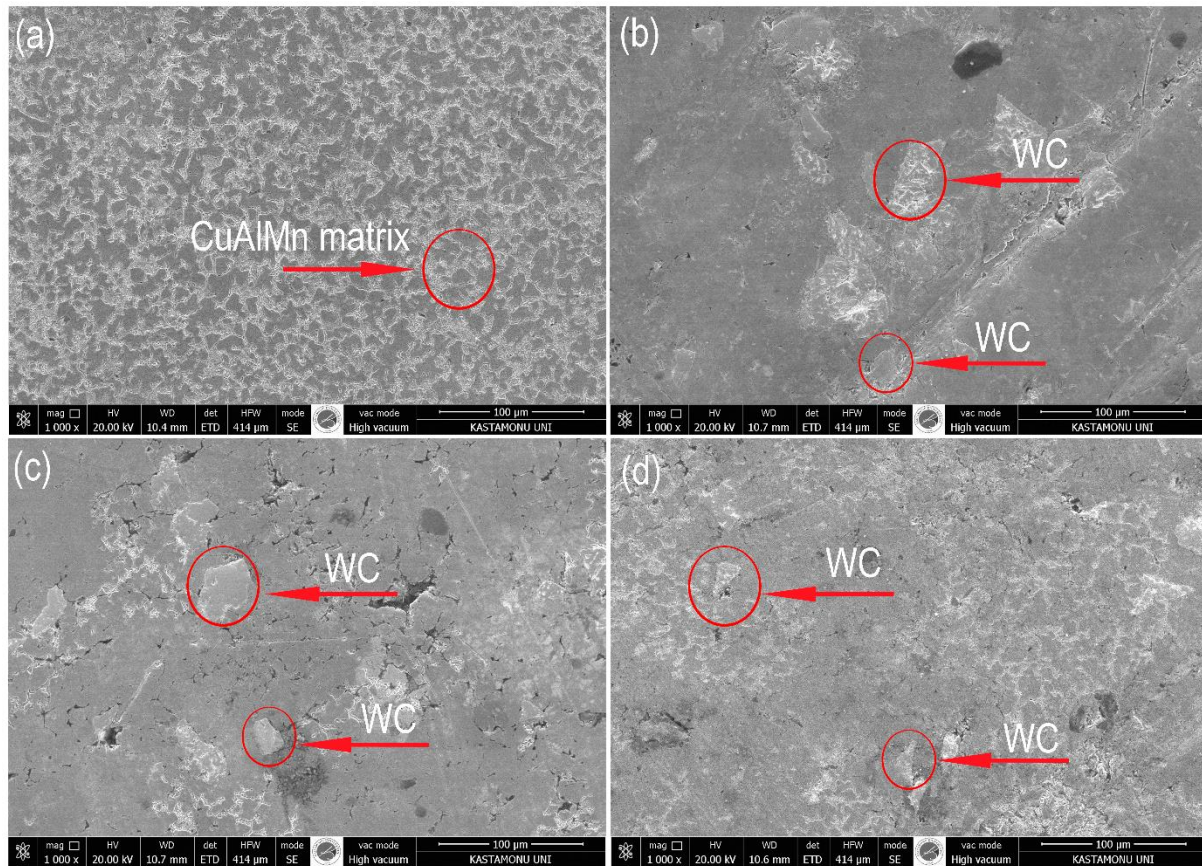


Figure 4. SEM images CuAlMn-WC composites produced: (a) CuAlMn, (b) CuAlMn - 5% WC, (c) CuAlMn - 10% WC and (d) CuAlMn - 15% WC.

Fig. 5 shows hardness as a function of the WC content in the composites.

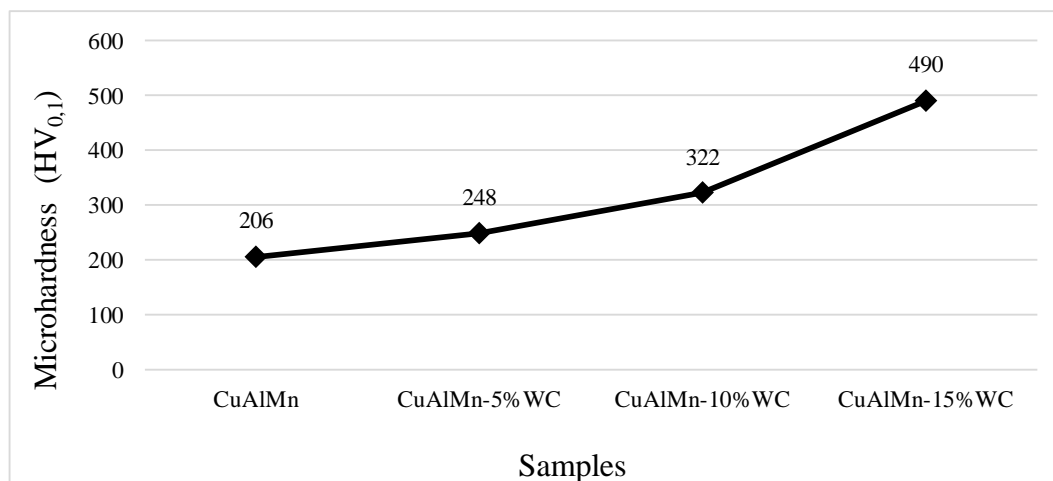


Figure 5. Microhardness graph of samples.

Hardness values were determined by taking the average of six different measurements on each composite. Hardness of the composites increased with increasing WC content. This may be explained by rule of mixture, applied to composite materials [37]. The hardness measurement values were 206 HV_{0.1} for CuAlMn, 248 HV_{0.1} for CuAlMn - 5% WC, 322 HV_{0.1} for CuAlMn - 10% WC and 490 HV_{0.1}

for CuAlMn – 15% WC. They are almost identical in the CuAlMn and CuAlMn – 5% WC hardness of composites by addition of WC. But CuAlMn – 15% WC composite is sharply increased in the hardness increased the amount of WC.

Fig. 6 shows SEM-EDS analysis taken from the samples.

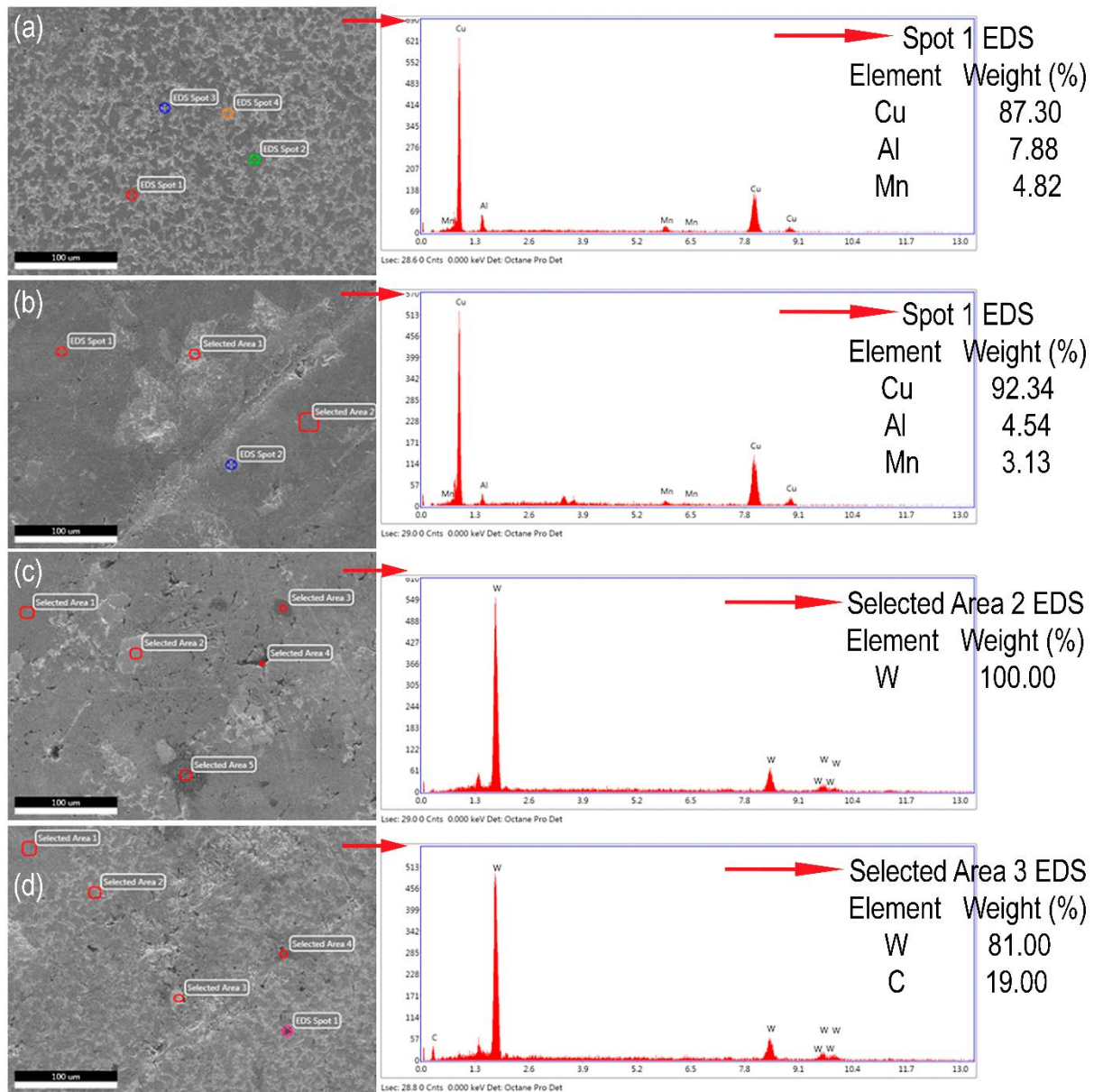


Figure 6. SEM-EDS analysis of the samples.

When the analysis results given in Fig. 6 were examined, it was figured out that the material was CuAlMn and WC. When the analysis results given in Fig. 6 were examined, the peaks of Cu, Al, Mn, W and C that were present also in the samples were clearly seen. The matrix phase acquires a brighter backscattered electrons contrast level in splats where WC dissolution was more pronounced. Fig. 7 shows XRD graphs of the CuAlMn-WC composites produced by hot pressing method.

When the XRD graphs given in Fig. 7 were examined, the peaks of $Al_{77}Mn_{23}$, $Al_5Cu_2Mn_3$, $AlCu_2Mn$, $AlCu_4$, Mn, Al_8Mn_5 , $Cu_{0.4}W_{0.6}$ and WC were determined. In this study, the phases formed are shown by XRD analysis; The formation of other phases has been revealed according to the results of EDS analysis. In their study on the effect of CuAlMn/WC ratio on the plastic deformation in

strengthening mechanism, Ji et al., determined similar peaks [38]. The dominant phases were seen to be $Al_{77}Mn_{23}$, $Al_5Cu_2Mn_3$, $AlCu_2Mn$ and $AlCu_4$ in the graphs. When all peaks were examined, it was found that as WC amount increased in the samples.

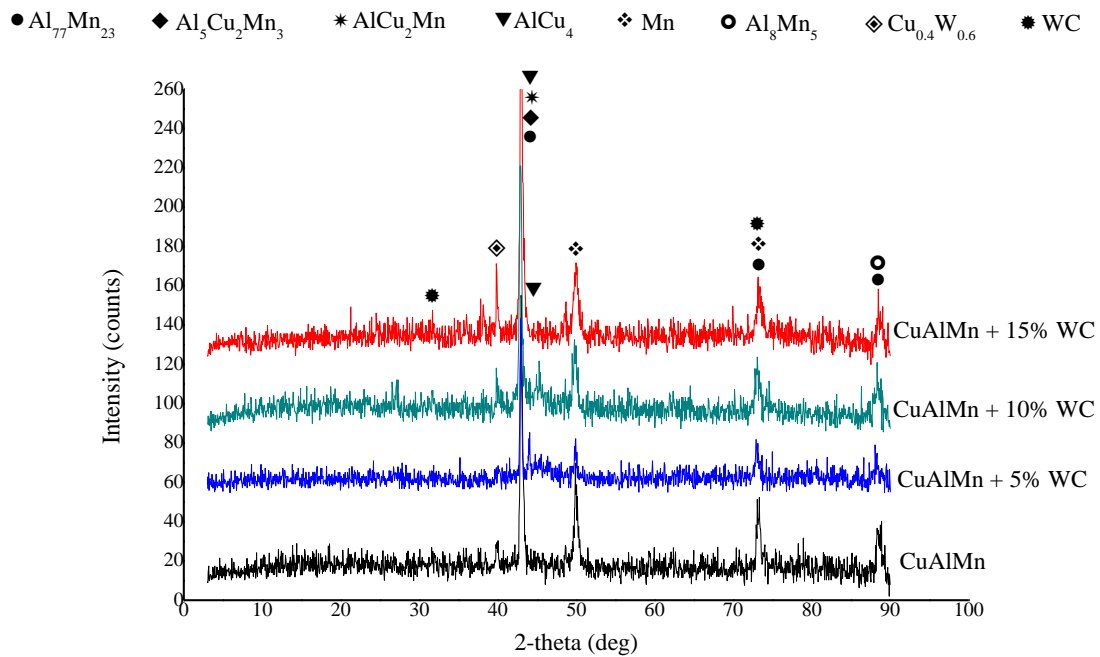


Figure 7. XRD graphs of the samples.

The corrosion tests of the samples were carried out in the prepared 3.5% NaCl solution. Potentiodynamic polarization curves resulting from the experiments are given in Fig. 8.

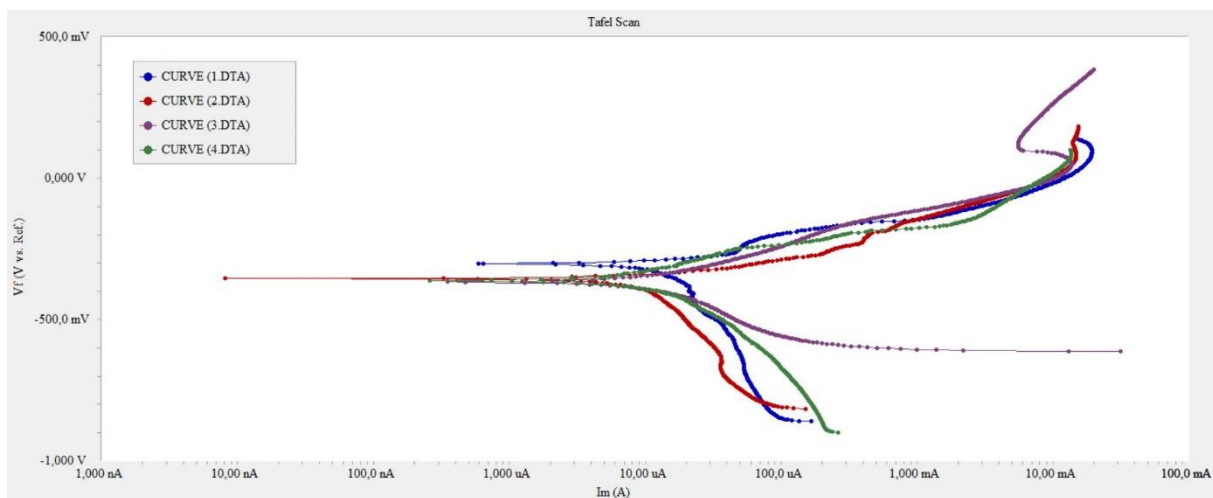


Figure 8. Tafel curves of samples.

The potential was applied to the open circuit potential after -0.5 mV to 0.5 mV. Immersion time of 30 minutes was applied. E_{corr} (corrosion potential), I_{corr} (corrosion current), β_a (anodic tafel curve), β_c (cathodic tafel curve) and corrosion rate were determined from tafel curves. R_p (corrosion resistance) was calculated using Stern and Geary equation (equation 1) [39].

$$R_p = \frac{\beta_a \times \beta_c}{2.303 \times I_{corr} (\beta_a + \beta_c)} \quad (1)$$

The electrochemical results of the samples are given in Tab. 2.

Table 2. Electrochemical results of samples.

Materials	E _{corr} (mV)	I _{corr} (μAcm ⁻²)	β _a (mV)	β _c (mV)	Corrosion rate (mpy)	R _p Corrosion resistance (kΩ.cm ²)
1	-302	16,72	95	512	10,76	2,08
2	-354	21,8	124	759,8	18,54	2,12
3	-367	10,5	127	188	10,23	3,13
4	-391	14,2	142,9	404,9	14,12	3,22

As a result, there is a reaction between Cu, Al, Mn and WC. When the Tab. 2 is examined, the R_p (corrosion resistance) of the sample CuAlMn was 2.08 kΩ.cm², while the value for the sample CuAlMn + 5 % WC was calculated as 3.22 kΩ.cm². It is clear from the data obtained that as the amount of WC in the reinforced increases, the corrosion resistance of the samples increases. Similar results have been found in the literature for composites of reinforced WC [28].

4. Conclusion

The effects of WC on the microstructure and mechanical properties of composites fabricated by hot pressing were investigated.

- Microstructure observation demonstrates a relative homogenous distribution in CuAlMn of WC particulates.
- The hardness measurement values were 206 HV_{0,1} for CuAlMn, 248 HV_{0,1} for CuAlMn – 5% WC, 322 HV_{0,1} for CuAlMn – 10% WC and 490 HV_{0,1} for CuAlMn – 15% WC.
- The analysis of EDS the peaks of Cu, Al, Mn, W and C that were present also in the samples were clearly seen.
- The dominant phases were seen to be Al₇₇Mn₂₃, Al₅Cu₂Mn₃, AlCu₂Mn and AlCu₄ in the XRD graphs.
- It is clear from the data obtained that as the amount of WC in the reinforced increases, the corrosion resistance of the samples increases.

Acknowledgment

This work was supported by Scientific Research Projects Coordination Unit of Hakkari University. Project Number: FM19BAP4.

References

- [1] Yılmaz, S.S. (2004). Demir esaslı T/M parçaların yüzey sertleştirme işlemlerinin fiziksel ve mekanik özelliklerine etkisi. *Doktora Tezi, Celal Bayar Üniversitesi, Manisa, Türkiye.*
- [2] Lawley, A. (1992). Atomization: The Production Of Metal Powders. United States, *Metal Powder Industries.*

- [3] Turan H. and Saritaş, S. (1994). Metal dust production with gas atomization. 6. *International Machine Design and Manufacturing Congress*, Ankara, Türkiye.
- [4] Yılmaz, S.S., Ünlü, B.S. and Varol, R. (2008). Borlanmış ve bilyalı dövülmüş demir esaslı T/M malzemelerinin aşınma ve mekanik özellikleri. *Makine Teknolojileri Elektronik Dergisi*, pp. 7-16.
- [5] Bargel, H.J. (1980). *Werstoffkunde*, VDI-Verlag.
- [6] Tandon, K.N. and Tian, R.Z. (1993). Effect of Pb on the wear behavior of a Cu-Pb alloy. *Scripta Metallurgica et Materialia*, vol. 29, pp. 857- 861.
- [7] Barmouz, M., Asadi, P., Givi, M.K.B. and Taherishargh, M. (2011). Investigation of mechanical properties of Cu/SiC composite fabricated by FSP: Effect of SiC particles' size and volume fraction. *Material Science and Engineering: A*, vol. 528, pp. 1740-1749.
- [8] Barmouz, M., Givi M.K.B. and Seyfi, J. (2011). On the role of processing parameters in producing Cu/SiC metal matrix composites via friction stir processing: Investigating microstructure, microhardness, wear and tensile behavior. *Materials Characterization*, vol. 62, pp. 108- 117.
- [9] Chen, Z. Liu, P., Verhoeven J.D. and Gibson, E.D. (1996). Sliding wear behavior of deformation-processed Cu-15vol.%Cr in situ composites. *Wear*, vol. 195, pp. 214-222.
- [10] Funkenbusch, P.D., Courtney, T.H. and Kubisch, D.G. (1984). Fabricability of an microstructural development in cold-worked metal matrix composites. *Scripta Metallurgica et Materialia*, vol. 18, pp. 1099- 1104.
- [11] Nath, D., Biswas S.K. and Rohatgi P.K. (1980). Wear characteristics and bearing performance of aluminum-mica particulate composite-material. *Wear*, vol. 60, pp. 61-73.
- [12] Saka, N. and Karalekas, D.P. (1985). Friction and wear of particle-reinforced metal ceramic composites. *Proceedings of the International Conference on Wear of Materials*, Canada.
- [13] Muratoğlu, M. and Demirel, M. (2009). Influence of non-standart geometry of plastic gear on sliding velocities. 5. *International Advanced Technologies Symposium*, Karabük, Turkey.
- [14] Alpas A.T. and Zhang, J. (1992). Effect of SiC particulate reinforcement on the Dry Sliding Wear of Aluminum Silicon Alloys (A356). *Wear*, vol. 155, pp. 83-104.
- [15] Chen, R., Iwabuchi, A., Shimizu, T., Shin, H.S. and Mifune, H. (1997). The sliding wear resistance behavior of NiAl and SiC particles reinforced aluminum alloy matrix composites. *Wear*, vol. 213, pp. 175-184.
- [16] Liang, Y.H., Zhao, Q., Zhang, Z.H., Li, X.J. and Ren, L.Q. (2014). Effect of B4C particle size on the reaction behavior of self-propagation high-temperature synthesis of TiC-TiB2 ceramic/Cu composites from a Cu-Ti-B4C system. *International Journal of Refractory Metals and Hard Materials*, vol. 46, pp. 71- 79.
- [17] Yonetken, A., Erol, A. and Kaplan, H. (2015). Microwave sintering and characterization of Cu-Cr-SiC composite materials. *24th International Conference on Metallurgy and Materials Metal 2015*, Brno, Czech Republic.
- [18] Turhan, H., Yildiz T. and Gulenc, B. (2007). Microstructure and mechanical properties of Cu/Fe Mnp and Cu /FeCrp matrix composites produced by powder metallurgy. *Firat University Science and Engineering Magazine*, vol.19, pp. 569-574.
- [19] Callister, W.D. (2007). *Materials Science And Engineering: An Introduction*, John Wiley & Sons.
- [20] Bektaşoğlu A. and Savaşkan, T. (2005). Zn-60Al- (1-5) Cu alaşımlarının kuru sürtünme durumundaki aşınma özelliklerinin incelenmesi. *Mühendis ve Makine*, vol. 46, pp. 31-39.

- [21] Kilic, M., Kirik, I. and Okumus, M. (2017). Microstructure examination of functionally graded NiTi/NiAl/Ni₃Al intermetallic compound produced by self-propagating high-temperature synthesis. *Kovove Mater*, 55, 97-106.
- [22] Wang, C.P., Su, Y., Yang S.Y., Shi, Z. and Liu, X.J. (2014). A new type of Cu–Al–Ta shape memory alloy with high martensitic transformation temperature. *Smart Mater. Struct.* 23, 025018, 1-7.
- [23] Silva C.A. and Lima S.J. (2005). Evaluation of Mechanical Alloying to obtain Cu-Al-Nb Shape Memory Alloy. *Mater. Res.*, 8-2, 169-172.
- [24] Soliman, H.N. and Habib, N. (2014). Effect of ageing treatment on hardness of Cu-12.5 wt% Al shape memory alloy. *Indian J Phys*, 88(8) 803–812.
- [25] Kilic, M., Yenigun, B., Bati, S., Balalan, Z. and Kirik, I. (2019). Effect of Cu addition on porous NiTi SMAs produced by self-propagating high-temperature synthesis. *Materials Testing*, 61(12), 1140-1144.
- [26] Camila, T.A., Rodrigo, E.C., Pedro, C. L., Carina, S.N., Erick, S.M., Murilo, S.S. and Gabriel K.C A. (2015). The effect of Chromium on microstructure of CuAlNi shape memory alloy. *Jun 3rd - 5th 2015*, Brno, Czech Republic, EU.
- [27] Firstov, G.S., Van Humbeeck, J. and Koval Y.N. (2004). High-temperature shape memory alloys Some recent developments. *Mater. Sci. Eng. A*, 378 2–10.
- [28] Liu, N., Li, Z., Xu, G., Feng, Z., Gong, S., Zhu, L. and Liang, S. (2011). Effect of tellurium on machinability and mechanical property of CuAlMnZn shape memory alloy. *Materials Science and Engineering: A*, 528(27), 7956-7961.
- [29] Giordana, M.F., Muñoz-Vásquez, N., GarroGonzález, M., Esquivel M.R. and Zelaya, E. (2015). Study of the formation of Cu-24at.%Al by reactive milling. *Procedia Materials Science*, 9, 262–270.
- [30] Dasgupta, R., Kumar A., Kumar, P., Shahadat, H. and Abhishek P. (2014). Effect of alloying constituents on the martensitic phase formation in some Cu-based SMAs. *J. Mater Res. Technol.* 3(3) 264–273.
- [31] Erden, M.A., Gündüz, S., Türkmen, M. and Karabulut, H. (2014). Microstructural characterization and mechanical properties of microalloyed powder metallurgy steels. *Materials Science and Engineering: A*, 616, 201-206.
- [32] Erden, M.A., Gündüz, S., Karabulut, H. and Türkmen, M. (2016). Effect of vanadium addition on the microstructure and mechanical properties of low carbon micro-alloyed powder metallurgy steels. *Materials Testing*, 58(5), 433-437.
- [33] Gao, Y.Y., Qiu, F., Geng, R., Zhao, W.X., Yang, D.L., Zuo, R. and Jiang, Q.C. (2018). Preparation and characterization of the Al-Cu-Mg-Si-Mn composites reinforced by different surface modified SiCp. *Materials Characterization*, 141, 156-162.
- [34] Yang, Q., Yin, D.Q., Ge, J.Q., Chen, J., Wang, S.L., Peng, H.B. and Wen, Y.H. (2018). Suppressing heating rate-dependent martensitic stabilization in ductile Cu-Al-Mn shape memory alloys by Ni addition: An experimental and first-principles study. *Materials Characterization*, 145, 381-388.
- [35] Liu, J., Chang, L., Liu, H., Li, Y., Yang, H. and Ruan, J. (2017). Microstructure, mechanical behavior and biocompatibility of powder metallurgy Nb-Ti-Ta alloys as biomedical material. *Materials Science and Engineering: C*, 71, 512-519.

- [36] Buytoz, S., Dagdelen, F., Islak, S., Kok, M., Kir, D. and Ercan, E. (2014). Effect of the TiC content on microstructure and thermal properties of Cu–TiC composites prepared by powder metallurgy. *Journal of Thermal Analysis and Calorimetry*, 117(3), 1277-1283.
- [37] Kim, H.S. (2000). On the rule of mixtures for the hardness of particle reinforced composites. *Materials Science and Engineering: A*, 289(1-2), 30-33.
- [38] Ji, X., Wang, Q., Yin, F., Cui, C., Ji, P. and Hao, G. (2018). Fabrication and properties of novel porous CuAlMn shape memory alloys and polymer/CuAlMn composites. *Composites Part A: Applied Science and Manufacturing*, 107, 21-30.
- [39] Stern, M. and Geary, A.L. (1957). Electrochemical polarization I. A theoretical analysis of the shape of polarization curves, *Journal of the electrochemical society*, 104(1), 56-63.

THOROUGH ANALYSIS OF COMBUSTION AND EMISSIONS OF POWER GENERATOR DIESEL ENGINE AT HIGH IDLING OPERATIONS FUELED WITH LOW PERCENTAGE OF DIFFERENT BIODIESEL BLENDS


Selman AYDIN¹

In this study, the ultimate aim is to provide objective scientific proof to promote biodiesel blends in constant areas (official institutions, hospital, school, etc.) as a renewable fuel. For that, biodiesel obtained from animal, vegetable and microalgae oil by a method of transesterification and these biodiesels have been prepared by 10% blended with diesel fuel and has been named respectively as AB10, VB10 and MB10. The biodiesel blends and reference diesel fuel (ULSD) have compared with by obtained combustion and emission values in a diesel engine generator system under cold start, loadless and high idling constant engine speed of 1500 rpm. Experimental results showed that using biodiesel blends in diesel engine generator system had almost parallel cylinder gas pressure (CGP), cumulative heat release (CHR), heat release rate (HRR), knock density (KD) and mean gas temperature (MGT) compared to ULSD fuel operation in this research diesel engine. In addition, CO, NO_x and HC emissions decreased, CO₂ increased compared to ULSD fuel at same experimental conditions.

Keywords: *Cold Start, Loadless, Power Generator Diesel Engine; Biodiesel, High Idling, Combustion*

Abbreviations

ULSD	ultra low sulfur diesel
AB10	10% animal oil biodiesel + 90% ULSD (in vol.)
VB10	10% vegetable oil biodiesel + 90% ULSD (in vol.)
MB10	10% microalgae oil biodiesel + 90% ULSD (in vol.)
HRR	heat release rate, J/CAD
CGP	cylinder gas pressure, bar
CHR	cumulative heat release, J
SOC	start of combustion (CAD)
MGT	mean gas temperature (K)
CAD	crank angle degree
KD	knock density
MGT	mean gas temperature
MBR	mass burning rate
TDC	top dead center

¹ Department of Automotive Engineering, Faculty of Technology, University of Batman, 72060, Batman, Turkey (aydnselman@gmail.com)  <https://orcid.org/0000-0001-9685-9853>

1. Introduction

Continuous depletion of fossil fuels, rising fossil-fuel prices, carbon prices, and the quest for cleaner environment for low carbon fuel these are the reasons why researchers are searching for fossil-fuel alternatives. Clean energy, non-flammable, environmentally friendly and non-toxic are some of the reasons that make biodiesel an acceptable choice for fossil-fuel substitution in the near future [1]. Biodiesel is fast becoming the best option for replacing diesel fuel among many renewable fuels. This is due to their potential for satiating energy demand, rising global warming and greenhouse gasses [2,7]. In addition, biodiesel is distinct from traditional diesel fuel; in any case, it does not contain any kind of undesirable fixations, such as sulphur and polycyclic aromatics. Biodiesel can be used instead of diesel fuel without making any outstanding changes to the engine fuel system components [6,3]. Microalgae are stated to be the alternative source of biomass feedstock for biodiesel that can meet the transport sector's global demand due to superior productivity of biomass and high oil content. Microalgae are capable of producing double biomass in about two days [4,5,10]. For current fuel systems, high engine efficiency should be taken from the biofuel without causing any damage to engine components [8].

Microalgae fuels in a research diesel engine and investigated the factors affecting the in cylinder gas pressure values and maximum in-cylinder pressure change. In this study used diesel fuel, crude microalgae oil and biodiesel based on the results of their study, microalgae oil and biodiesel reduced the performance parameters of engine, as there is an increase on the noise of engine owing to knock density [9]. In a separate analysis by the same team [11], it was demonstrated that the start of injection timings of biodiesel fuels resulted in earlier timings in comparison with diesel fuel owing to its high density and kinematic viscosity.

The purpose in this study of used animal biodiesel, vegetable biodiesel and microalgae biodiesel, which blended ultra-low sulfur diesel fuel (ULSD), was to investigate the possibility and usability of 10 percent biodiesel in a diesel engine generator power at cold start and loadless conditions. The European Union's Renewable Energy Directive, which promotes the use of renewable energy, mandates that at least 10% of the energy resources used in the transportation industry will come from renewable energy sources. Inspired by this idea; three biodiesel blends and ULSD are evaluated and compared, under cold start and loadless conditions of research engine to identify combustion parameters. The ultimate goal is to provide reliable scientific evidence to support biodiesel blending as a renewable fuel in constant areas (official organizations, hospital, education, etc.). Comprehensive experiments have been carried out to evaluate the change in combustion parameters when running the engine with test fuels under cold start, loadless conditions and high idling 1500 rpm in a power generator diesel engine. In addition, under cold start, high idling and unloaded operating conditions, no detailed study has been found in literature on the combustion parameters of AB10, VB10 and MB10 biodiesel blends.

2. Material and Experimental Methods

2.1. Experimental setup and installations

In this study, the animal oil biodiesel (AB) was derived from beef bone marrow by transesterification for the experimental study at the chemical plant in Istanbul (TR), the vegetable oil biodiesel (VB) produced from safflower/canola oil blend was provided from a commercial facility in Kocaeli (TR), and ULSD was purchased in a commercial station in Batman (TR). The aim of various source of biodiesel with ULSD blends was to investigate the possibility and usability in a diesel engine powered generator under cold start, high idling and unloaded operating conditions. So that, experiment fuels were prepared by blending 90% ULSD + 10% animal fat oil biodiesel (AB10), 90% ULSD + 10% safflower/canola biodiesel (VB10) and 90% ULSD + 10% microalga oil biodiesel (MB10). Together with the 10% blends, it produces the best engine performance and can minimize exhaust emissions in comparison with diesel fuel, except NO_x [12]. Thus, biodiesel blend ratios were chosen as 10%. Tab. 1 presents some of the significant chemical and physical characteristics of this fuels.

Table 1. Some of physical and chemical characteristics of ULSD, AB10, VB10 and MB10 fuels.

Parameter / Test fuels	ULSD	AB10	VB10	MB10	EN 14214	ASTM D6751
Lower calorific value, (kJ/kg)	42550	40250	41580	41530	-	-
Viscosity, 40 °C (mm ² /s)	2.959	3.014	3.896	3.968	3.5-5	1.6-6
Diesel index	50.5	52.4	53.8	51.4	51 min	47min

The experimental investigation has been carried out using every one of the ULSD, AB10, VB10 and MB10 experiment fuels in a diesel engine power generator working at cold start, high idling speed of 1500 rpm and loadless. The experimental configuration schematic diagram has viewed in Fig. 1. The aim of various source of biodiesel with ULSD blends was to investigate the possibility and usability in a diesel engine powered generator with high idling operations.

Table 2. Specifications of engine diesel powered electric generator

Engine parameter	Specification
Output power	18 kW
Cooling system	Water cooling
system of Intake	Naturally aspirates
Model	4DW81-23D
Bore x stroke (mm)	85 × 100
Displacement (cm ³)	2400
Cylinders	4
System of combustion	Direct injection
Compression ratio	17:1
Injector nozzles	4
Injection timing	23° BTDC
Injection pressure	400 bar

Together with the 10% blends, it produces the best combustion and can minimize exhaust emissions in comparison with diesel fuel, except NO_x. [12]. Thus, blends of biodiesel were chosen as 10%. Tab. 1 presents some of the significant chemical and physical properties of test fuels.

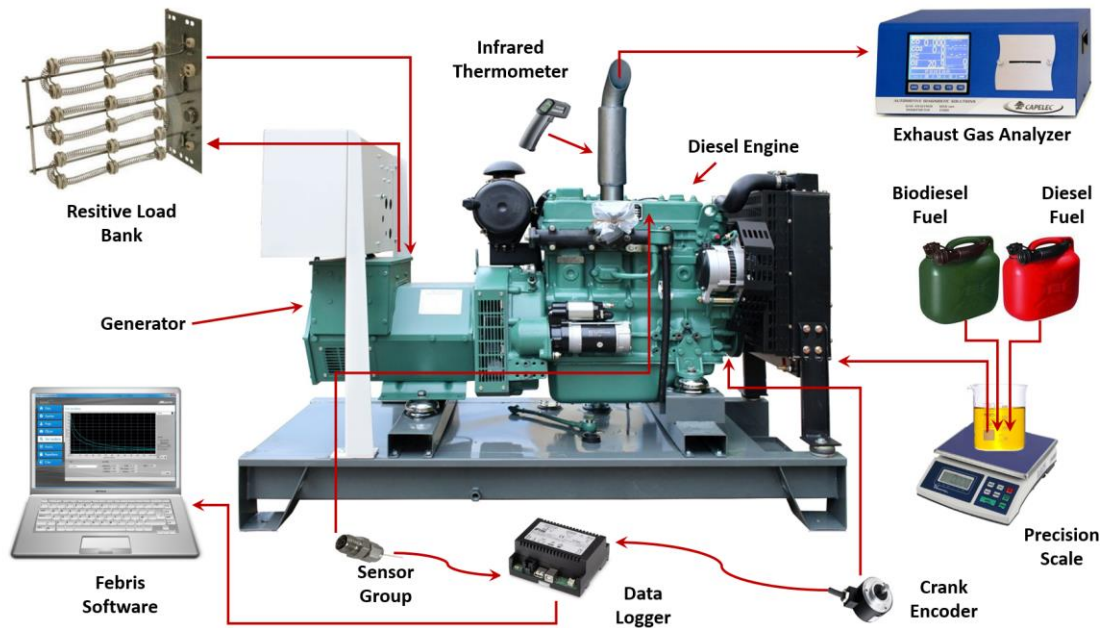


Figure 1. The view of overall experimental configuration

2.2. Methods of Calculation

The parameter of combustion values were obtained by a piezoelectric transducer mounted in the combustion chamber and analyzed by FEBRS combustion software, which allows data to be collected from the cylinder pressure sensor and crank encoder. The obtained and measured by this application is the volume of the cylinder, cylinder gas pressure (CGP), mean piston speed and piston acceleration versus CAD. The CGP was written down for each CAD of 1° and mean of 100 cycles were utilized by the crank encoder. In this work, CGP and other combustion parameters were used to compute knock density (KD), heat release rate (HRR), mean gas temperature (MGT) and total heat release (CHR). By means of software, each CAD of 1° and average of 100 cycles were established for all parameters by equations below:

$$\dot{Q} = \frac{\gamma}{\gamma-1} PdV + \frac{1}{\gamma-1} VdP + Q_w \quad (1)$$

The ratio of specific heats is given in Eq. (2) benefited with the mean gas temperature [13].

$$\gamma = 1.338 - 60 \times 10^{-5}T + 10^{-8}T^2 \quad (2)$$

The cumulative heat release (CHR) was calculated in Eq. (3) [14].

$$\int dQ = \int \left(\frac{\gamma}{\gamma-1}\right) p(dV) + \int \left(\frac{1}{\gamma-1}\right) V(dP) \quad (3)$$

In heat transfer coefficient (HTC) was calculated by using the Eq. (4) [14].

$$h = C_0 V^{-0.06} p^{0.8} T^{-0.4} [c_m + 1.4]^{0.8} \quad (4)$$

The knock density (KD) was given in Eq. (5) and calculated from cylinder gas pressure and mentioned above parameters [15].

$$dp(\theta) = \frac{[86(p_{i-4}-p_{i+4})+142(p_{i+3}-p_{i-3})+193(p_{i+2}-p_{i-2})+126(p_{i+1}-p_{i-1})]}{1188d\theta} \quad (5)$$

3. Experimental Result and Discussion

3.1. Combustion results

In this combustion results section, in cylinder gas pressure (CGP), heat release rate (HRR), knock density (KD), cumulative heat release (CHR) and other significant combustion characteristic depend on crank angle degree (CAD) of power generator diesel engine were examined for ULSD, AB10, VB10 and MB10 test fuels. It can be observed in the Fig. 2 that in CGP and HRR values increased as the experimental engine cold conditions and high idling operations. In order to prevent cyclical differences, the CGP used in the calculation were taken as the average of 100 cycles. The CGP values of loadless cases have occurred after top dead center (TDC). Maximum CGP was occurred at 50.415305 bar in the ULSD test fuel, taken as 9° after TDC. Other hand, under identical experimental conditions, it occurred with 50.265965 bar pressure in AB10 fuel 8 CAD after TDC, with 52.018538 bar pressure in VB10 fuel 9 CAD after TDC and with 52.019738 bar pressure in MB10 fuel 8 CAD after TDC. When in CGP versus on CAD for all test fuels under cold start and loadless conditions were observed, it is seen that every cycle is almost different from each other. There are a many similar results reported in the literature [17-19]. The development of cyclic variations includes a variety of physical and chemical factors [16, 24, 27, 29].

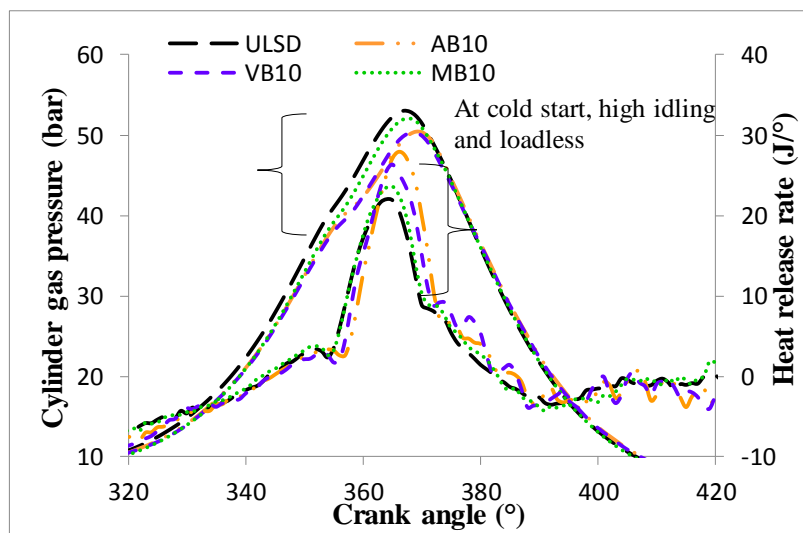


Figure 2. Changing of CGP and HRR curves with CAD at cold start, high idling and loadless conditions

Maximum HRR values were obtained after TDC was between 359°-365° under cold start, loadless and high idling conditions were observed, it is seen in the Fig. 2. The most important parameters affecting the HRR of test fuels are; cetane number, density, viscosity, erasable internal temperature and thermal value. Cetane number, viscosity and density affect the ignition delays of fuels, and as the ignition delay increases, the rate of heat release increases [21-21]. Under cold start, high idling and loadless conditions, maximum HRR for ULSD was obtained as 22.00524 J /CAD after 8° from TDC. Moreover, under identical experimental conditions, maximum HRR for AB10 fuel was measured as 27.891084 J/CAD after 10° TDC, maximum HRR for VB10 occurred as 26.376701 J/CAD after 9° TDC and maximum HRR for MB10 occurred as 23.663952 J/CAD after 9° TDC. Due to the load condition of the experimental engine, a significant difference was found when the HRR values were examined. The HRR values of test fuels were similar under identical experimental conditions. When the CGP and HRR curves were analyzed under same operating conditions, the combustion was delayed for VB10 blend. There are a many similar results reported in the literature [7, 19].

In Fig. 3 are properly inspected, it can be observed that the mean gas temperature (MGT) values have increased due to an increase in CGP at same experiment conditions. The MGT of VB10 fuel showed almost the same combustion behaviour with other fuels during the controlled combustion phase, while it was determined as the fuel that released the lowest temperature, which separates it from the other test fuels during the after combustion phase. The cold research engine is under high idling and loadless, the maximum MGT occurred 1390 K at 374 CAD of engine with AB10 fuel. The MGT increases with the increasing inflammation depending on fuel composition of experimental fuel [23]. The knock density (KD) in diesel engines is that the fuel pumped into the cylinder does not instantly burn, but accumulates and burns unexpectedly, and the in-pressure increases. Thus, this is known as one of the reasons why diesel engines have a high noise level. When the Fig.3 are examined, no KD values has exceeded the acceptable value [22]. As can be observed that KD levels of all the test fuels were obtained at the appropriate values at cold start, high idling and loadless conditions.

Variation of in the mass burning rate (MBR) of ULSD, AB10, VB10 and MB10 test fuels at cold start, high idling and loadless conditions are given in Fig. 4. The MBR is a characteristic calculated from the CGP and volume change of the cylinder in the FEBRIS software based on LabVIEW. This parameter displays the amount of fuel burned at each crank angle over a cycle obtained from the mean of 100 cycles. For all the test blends, MBR values were identical to each other, but it has slight differences. Under same operating conditions VB10, MB10 and AOB10 test fuels have burnt earlier than the ULSD fuel. It is thought that the better evaporation end optimal blends of micro algae, vegetable oil biodiesel and animal fat biodiesel led to this propensity. Values of Heat transfer rate (HTR) depend on crank angel at same operating conditions are present in Fig. 4. As it can be observed in the figure, max. HTR of AB10 and VB10 at these experimental conditions compared to the ULSD and MB10 test fuels are higher.

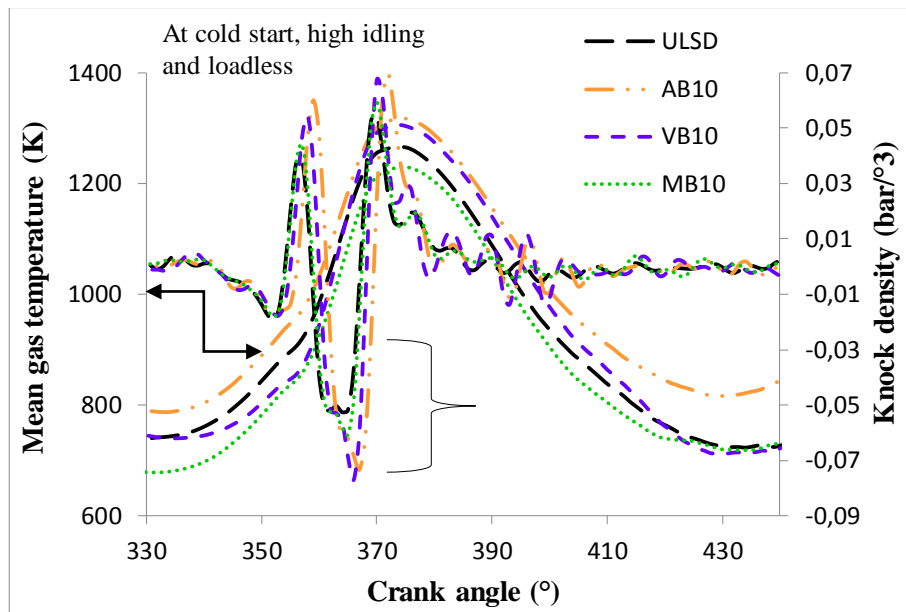


Figure 3. Changing of MGT and KD curves with CAD at cold start, high idling and loadless conditions

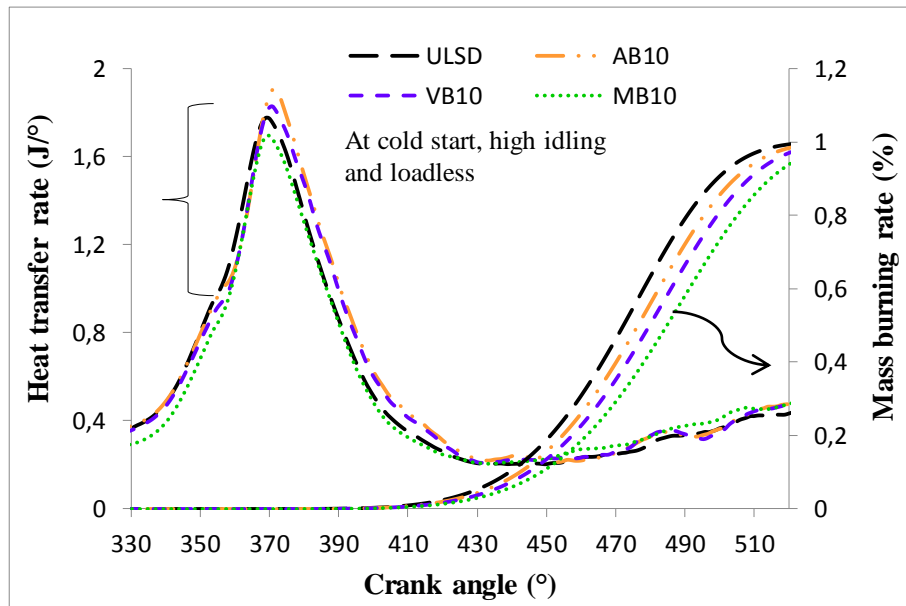


Figure 4. Changing of HTR and MBR curves with CAD at cold start, high idling and loadless conditions

Cumulative heat release (CHR) with depend on CAD for test fuels at cold start and loadless conditions are given in Fig. 5. CHR provides more information about the progress of test fuels combustion in experimental engine and also, CHR is net heat released from chemical energy of the experiment fuels.

In same experimental conditions, maximum CHR values for test fuels were obtained after TDC. The lowest CHR values were obtained VB10 and AB10 at cold start, high idling and loadless conditions. Higher cetane number results in a lower ignition delay and lower fuel to be burned in the phase of premixed combustion. In case of look at Tab. 1, it is seen that the AB10 and VB10 have highest and ULSD have lowest cetane number. Therefore, as AB10 and VB10 fuels are predicted to have a shorter delay in ignition, and thus much more CHR value has been obtained. The higher CHR value of ULSD fuel is only related to the colorific value of the ULSD fuel. The changing of coefficient of heat transfer (CHT) curves with CAD for test fuels are given Fig. 5. The highest coefficient of heat transfer was obtained MB10 and ULSD fuels at cold start and loadless conditions of experimental engine. The increase in heat transfer coefficient is associated with the increase of MGT with engine loads and the cylinder gas velocity.

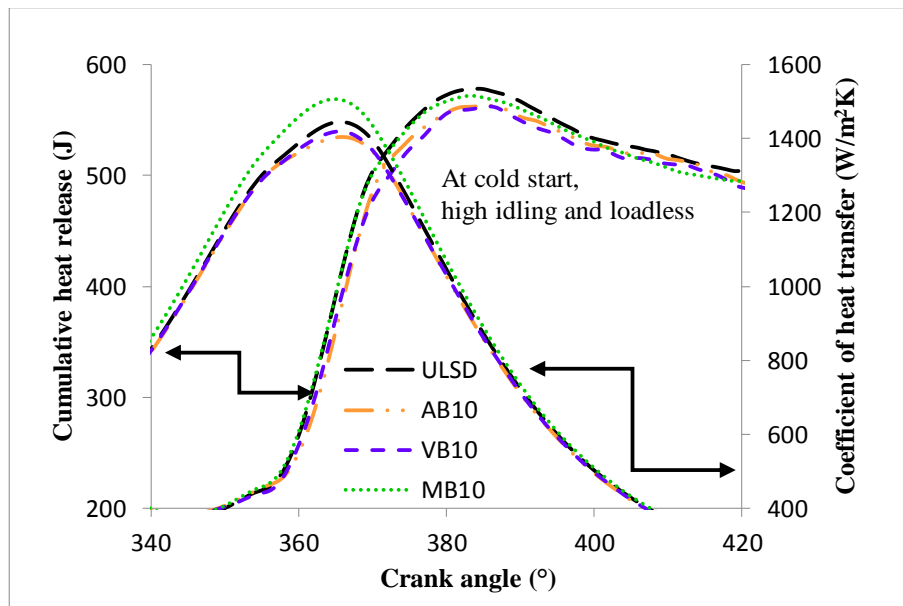


Figure 5. Changing of CHR and CHT curves with CAD at cold start, high idling and loadless conditions

3.2. Emissions results

Changing of CO, CO₂, NO_x and HC emissions of test at cold start, high idling and loadless conditions are presented in Fig. 6A, 6B, 6C, 6D, respectively. In Fig. 6A, CO emissions of AB10, VB10 and MB10 blends were lower than ULSD into power generator diesel engine at cold start, high idling and loadless conditions. The reason may be due to the additional oxygen content in the biodiesel fuel [28]. CO₂ emissions of AB10, VB10 and MB10 blends were higher than ULSD into power generator diesel engine at cold start, high idling and loadless conditions illustrated in Fig. 6B.

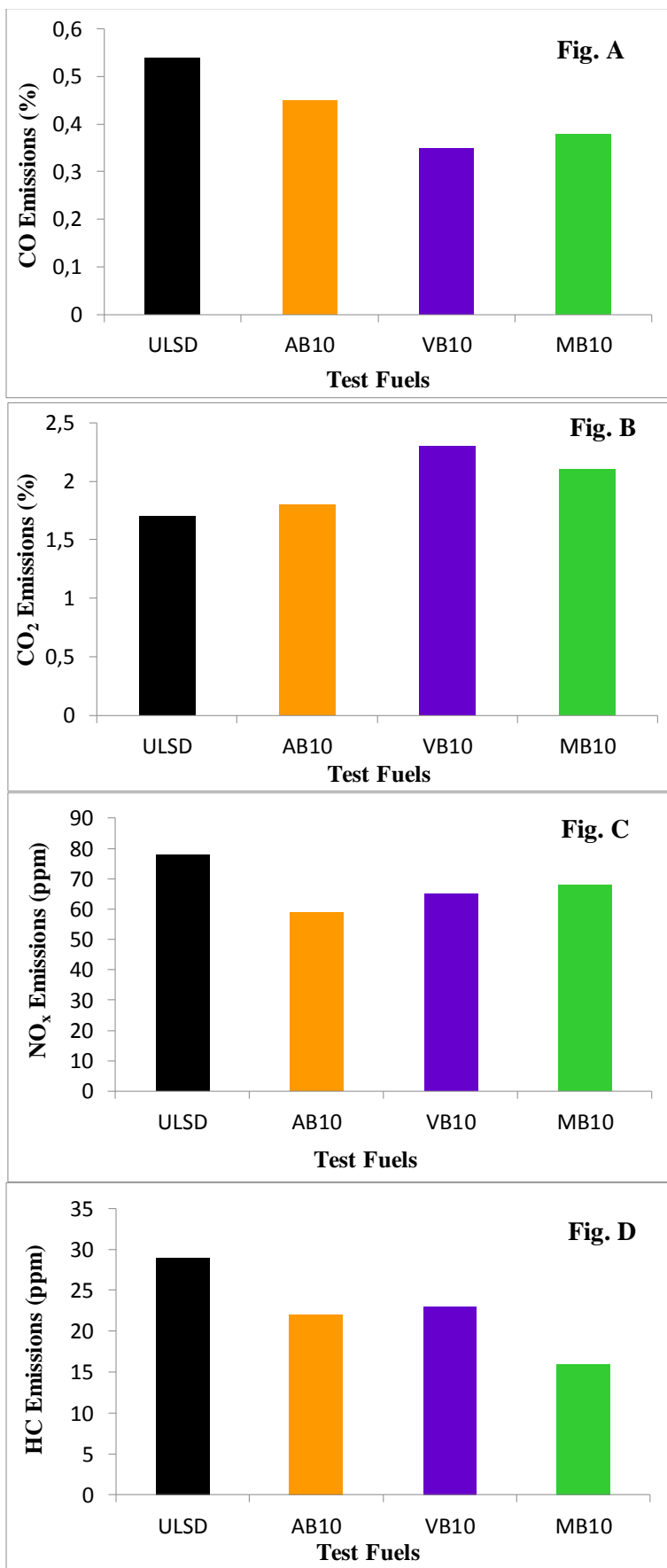


Figure 6. Changing of CO, CO₂, NO_x and HC emissions of test fuels at cold start, high idling and loadless conditions

The reason that may be owing to more efficient combustion of biodiesel blends at this operations condition. So the decline in the value of CO at loadless of experimental engine can be presented as evidence for increases of CO₂ emissions at this conditions. NO_x and HC emissions of test blends were lower than ULSD into power generator diesel engine at cold start, high idling and loadless conditions illustrated in Fig. 6C, 6D, respectively. The consequences of two major factors are produced the NO_x emissions. Firstly, if the temperature of the combustion inside the cylinder is approximately higher than 1600 °C, the nitrogen molecules begin to react with oxygen and as a result NO_x is formed. Secondly, if the reaction time for the above-mentioned condition is reasonable, the amount of NO_x emission will be emitted to the highest level [23].

Conclusions

The effect of AB10, VB10 and MB10 fuels on metrics of combustion in a diesel engine coupled with electrical generator under cold start, high idling and loadless conditions have investigated. This experimental study was carried out under cold start-loadless conditions and constant speed of the generator set. Based on the results obtained from the experiments the following conclusions were concluded:

- * Parameters of combustion such as in-CGP, HRR, and CHR, MGT, MBR, and knock density were partly similar from ULSD fuel. It was identified that the curves were generally parallel to each other; and biodiesel-blended fuel combustion values showed behaviours close to the reference ULSD fuel. In addition, CO, NO_x and HC emissions decreased, CO₂ emissions increased compared to ULSD fuel under cold start-loadless and high idling conditions of the power generator diesel engine.
- * Because of the negative impact of fossil fuels on people and the environment, seeking alternative and cleaner energy sources has become crucial. Some of the alternative biodiesels were analyzed and tested in diesel engine power generator in this study. As the results show, AB10, VB10 and MB10 fuels performed better combustion measures than the ULSD reference. Considering that fossil fuels (gasoline, diesel fuel, oil, and natural gas) will end one day, although biodiesel fuels partially reduce engine performance, it can be used in construction machines requiring high torque.

References

- [1] Sanjid, A., Masjuki, H.H., Kalam, M.A., Ashrafur Rahman, S.M., Abedin, M.J., Palash, S.M., Production of palm and jatropha based biodiesel and investigation of palm-jatropha combined blend properties, performance, exhaust emission and noise in an unmodified diesel engine, *Journal of Cleaner Production*, 65 (2014), 295-303.

- [2] Shahabuddin, M., Liaquat, A.M., Masjuki, H.H., Kalam, M.A., Mofijur, M., Ignition delay, combustion and emission characteristics of diesel engine fueled with biodiesel, *Renew. Sustain. Energy Rev.* 21(2013), 623-632.
- [3] Singh, S.P., Singh, D., Biodiesel production through the use of different sources and characterization of oils and their esters as the substitute of diesel: a review, *Renew. Sustain. Energy Rev.* 14(2010), 200-216.
- [4] Dassey, A.J., Hall, S.G., Theegala, C.S., An analysis of energy consumption for algal biodiesel production: comparing the literature with current estimates, *Algal Res.* 4(2014), 89-95.
- [5] Ahmad, A.L., Yasin, N.H.M., Derek, C.J.C., Lim, J.K. Microalgae as a sustainable energy source for biodiesel production: a review, *Renew. Sustain. Energy Rev.* 15 (2011), 584-593.
- [6] Efe, Ş., Ceviz, M.A., Temur, H., Comparative engine characteristics of biodiesels from hazelnut, corn, soybean, canola and sunflower oils on DI diesel engine, *Renewable Energy*, 119(2018), 142-151.
- [7] Seraç, M.R., Aydın, S., Sayın, C. Comprehensive evaluation of performance, combustion, and emissions of soybean biodiesel blends and diesel fuel in a power generator diesel engine, *Energy Sources, Part A: Recovery, Utilization, and Environmental Effects*, 42(2020),18, 2316-2331.
- [8] Özsezen AN, Çanakçı M., An investigation of the effect of methyl ester produced from waste frying oil on the performance and emissions of an idi diesel engine, *J Facul Eng Architect Gazi Univ.* 23(2008), 2, 395-404.
- [10] Yaşar, F., Evaluation of Renewable Energy Source Algae as Biodiesel, Feedstock, *European Journal of Technique (EJT)*, 9 (2019), 2, 298-311.
- [11] Ozsezen, A.N., Canakci, M., Determination of performance and combustion characteristics of a diesel engine fueled with canola and waste palm oil methyl esters, *Energy Conversion and Management*, 52(2011), 1, 108-116.
- [12] Ong, H.C. Masjuki, H.H., Mahlia, T.M.I., Silitonga, A.S., Chonga, W.T., Yusaf, T., Engine performance and emissions using *Jatropha curcas*, *Ceiba pentandra* and *Calophyllum inophyllum* biodiesel in a CI diesel engine, *Energy*, 69 (2014), 427-445.
- [13] Brunt, M.F.J., Rai, H., Emtage, A.L., The calculation of heat release energy from cylinder pressure data, *SAE Technical Paper* 1998: 981052.
- [14] Hohenberg, GH., Advanced approaches for heat transfer calculations, *SAE Technical Paper* 1979: 790825.
- [15] Checkel, M. and Dale, J., Computerized Knock Detection from Engine Pressure Records, *SAE Technical Paper* 1986: 860028.

- [16] Deverajan, Y., Munuswamy, D. B., & Mahalingam, A., Influence of nano-additive on performance and emission characteristics of a diesel engine running on neat neem oil biodiesel, *Environmental Science and Pollution Research*, 25(2018), 1-6.
- [17] İlkılıç, C., Çilgin, E., & Aydın, H., Terebinth oil for biodiesel production and its diesel engine application, *Journal of the Energy Institute*, 88 (2015), 292-303.
- [18] Çilgin E., Investigation of biodiesel potential of new hybrid of Origanum Sp. Tekin-2017, native to Turkey, *Fuel*, 277(2020), 118180.
- [19] Çelebi, Y., Aydın, H., Investigation of the effects of butanol addition on safflower biodiesel usage as fuel in a generator diesel engine, *Fuel*, 222(2018), 385-393.
- [20] Singh, M., Anjum, F., Yadav, V., Sheikh, M.Y., Mathur, Y.B., Analysis of Combustion on Compression Ignition Diesel Engine fuelled with blends of Neem Biodiesel, *International Research Journal of Engineering and Technology*, 2017, 04.
- [21] Anandavelu, K., Alagumurthi, N., & Saravannan, C. G., Experimental investigation of using eucalyptus oil and diesel fuel blends in Kirloskar TV1 direct injection diesel engine, *J Sustain Energy Environ*, 2(2011), 3.
- [22] Rajput RK. *A textbook of automobile engineering*. Laxmi; 2007.
- [23] Heywood, J. *Internal Combustion Engine Fundamentals*. Macgraw-Hill Book Company, New York, 1988.
- [24] Sayin, C., Gumus, M., and Canakci, M., Effect of fuel injection pressure on the injection, combustion and performance characteristics of a DI diesel engine fueled with canola oil methyl esters-diesel fuel blends, *Biomass and Bioenergy*, 46(2012), 435-446.
- [25] Oumer, A. N., Hasan, M. M., Baheta, A. T., Mamat, R., Abdullah, A. A., Bio-based liquid fuels as a source of renewable energy: A review. *Renewable and Sustainable Energy Reviews*, 88(2018), 82-98.
- [26] Haik, Y., Selim, M.Y.E., Abdulrehman, T., Combustion of algae oil methyl ester in an indirect injection diesel engine, *Energy*, 36 (2011) 1827-1835.
- [27] Kumar, A., Shukla, S. K., & Tierkey, J. V., A review of research and policy on using different biodiesel oils as fuel for CI engine. *Energy Procedia*, 90(2016). 292-304.
- [28] Lapuerta, M., Armas, O., Rodríguez-Fernández, J. Effects of biodiesel fuels on diesel engine emissions, *Prog Energy Combust Sci*, 34(2008), 198–223.
- [29] Aydın, S. Detailed evaluation of combustion, performance and emissions of ethyl proxitol and methyl proxitol-safflower biodiesel blends in a power generator diesel engine, *Fuel*, 270 (2020), 117492.

A STUDY ON THE EXAMINATION OF THE SINTER METALLOGRAPHIC STRUCTURE


Ömer Saltuk BÖLÜKBAŞI^{1*}

Sintering process is carried out domestic and imported iron ore powders, fluxes, coke dust, metallurgical recycling powders and slag forming agents. Nowadays, in order to obtain process and operating parameters that will work with the best sinter quality, extensive researches have been made by iron and steel industry. Sinter quality parameters followed by the sinter blend loaded on the sinter strand and then granulated were examined. We can obtain chemical analysis of the phases by scanning electron microscopy (SEM) technique, but full consistency with images is not always possible and especially SFCA (silico-ferrite of calcium and aluminium) and SFCA-I phases are difficult to distinguish from each other and future studies are required in this field. The mineralogy and microstructure of the sinter plays an important role in determining the physical and metallurgical properties of the iron ore sinter. Mineralogical characterization of sinter phases; it is a complementary tool to conventional physical and metallurgical tests applied to iron ore sinter to evaluate and estimate sinter quality. Measurement techniques used in this study; optical image analysis and X-ray diffraction (XRD), scanning electron microscopy (SEM), energy distribution spectroscopy (EDS), results from raw data converted to autoquan format will be explained on the new studies on the interpretation of the Rietveld system. Depending on the measurement objectives of each technique, the quantification of the crystal phases, the relationship between the measurement results, the chemical composition of the phases and the relations between the minerals, as well as their advantages and disadvantages will be explained.

Key Words: Iron ore sinter mineralogy, agglomeration, crystal structure, SFCA, phase chemistry

1. Introduction

Sinter, which is formed by melting of fine iron ores and fluxes (limestone, dolomite, etc.) at high temperature (950-1350°C), is the main ferrous input material of blast furnace. Iron ores constitute sinter cake compound in SFCA phase compound and in the form of glassy structure. Due to the significant effect of SFCA on sinter quality, it is the most important component of the sinter bond matrix. Sinter reactions become successful by controlling the microstructure and concentration of SFCA during the sintering process. In the current existing sinter plants, quality is monitored on the basis of small basicity (CaO/SiO₂) ratio only. This study will investigate the effect of these four components CaO, Al₂O₃,

¹Department of Metallurgical and Materials Engineering, Iskenderun Technical University, Hatay, Turkey, (osaltuk.bolukbasi@iste.edu.tr)  <https://orcid.org/0000-0002-8862-009X>

Fe_2O_3 , SiO_2 within the sintering process on the hardness, reducibility and efficiency will be investigated and establish an association.

The literature includes studies that qualitatively examined the microstructure of the sinter in general; and its chemical structure, mineralogy, morphology as well as the distribution of different mineral phase structures in the sinter matrix during the sintering process [1, 2, 7]. Sinter mineral formation mainly consists of SFCA, SFCA-I and SFCA-II phases. The key binding phases that provide strength of the material are SFCA and SFCA-I [3, 6, 12, 13]. The formation and contents of these structures vary according to the operational practices (sinter blend used, temperature, basicity, sintering time, etc.). Our study investigates the mineralogical conditions that allow for the formation of SFCA and SFCA-I phase structures which affect quality especially in the internal structure of the sinter. When the sinter blend consisting of iron ore, limestone, coke dust and flux mixture is heated in a sintering machine, dicalcium ferrite ($\text{C}_2\text{F}-2\text{CaO}\cdot\text{Fe}_2\text{O}_3$) structure is formed as the first product at 750-780 °C, and then, iron oxide, SFCA and silicate phases are formed at 1220-1300 °C [4,8,14,15]. With increased sintering temperature, dicalcium ferrites react with hematite to take the form of calcium ferrite ($\text{CF}-\text{CaO}\cdot\text{Fe}_2\text{O}_3$) [5, 10, 16]. Quartz begins to react with the SFCA-I and SFCA form at 1050°C. SFCA-I breaks down between 1220 °C and 1240 °C and takes the form of SFCA [9, 10, 14, 20].

A study by Scarlett et al. (2004) suggests that the phase compositions in the sinter matrix structure consist of iron oxide by 35 to 60%, ferrites (mostly SFCA) by 20 to 45%, glassy phases by more than 10% and dicalcium silicates by more than 10%. They emphasize that the bond phase morphology is typically composed of SFCA phase composition as well as iron oxides and silicates, forming the most important bond phase structure since SFCA has a major impact on the technological properties of the sinter [17, 18, 21]. Cores et al. [19, 25] consider that the technological quality of the sinter depends on the mineral phase form generated during the sintering process, and SFCA is the strongest bond phase affecting the sinter quality. During studies on the effects of ore mixtures of different compositions on sinter quality, it has been observed that the reducibility and cold strength of the sinter depends on the presence of calcium ferrite in the microstructure of the sinter [20, 34]. The said studies also suggest that the form consisting of hematite cores surrounded by SFCA-I is the desired structure for high sinter quality. During the reduction reactions, the porous structure of the acicular SFCA has been proven to provide a wide surface contact to prevent spread of cracks.

Pownceby and Clout (2003) investigated the initiation of mineral compositions of the SFCA phase and the issue that CF_3 ($\text{CaO}\cdot 3\text{Fe}_2\text{O}_3$), CA_3 ($\text{CaO}\cdot 3\text{Al}_2\text{O}_3$) and C_4S_3 ($4\text{CaO}\cdot 3\text{SiO}_2$) or $\text{Fe}_2\text{O}_3-\text{Al}_2\text{O}_3-\text{CaO}$ compounds can be designed to create a link within a planar structure. In the aforementioned study, they observed the SFCA composition encountered in industrial sinter and named the SFCA forms as SFCA, SFCA-I and SFCA-II (dendritic) solid solution series [3,9,10,22]. In their study, Bristow and Waters (1991) state that SFCA affects the grain structure of the sinter matrix by stabilizing a fine porosity during a reduction in the initial reduction phase. They noticed that the SFCA content in the sinter structure has a maximum effect on the increase of reducibility. They studied on the association between the availability of SFCA and hematite in the sinter cake and maximum reducibility [9, 27, 28, 29].

Industrially produced iron ore sinters include two types of SFCA categorized in the literature based on the composition, morphology and crystal structure of the SFCA phase structure in iron ore. SFCA, which is the first type of these phases in the sintered material is found in the composition of $\text{M}_{14}\text{O}_{20}$ stoichiometry and $\text{Ca}^{+2}\cdot 2.3\text{Mg}^{+2}\cdot 0.8\text{Al}^{+3}\cdot 1.5\text{Fe}^{+3}\cdot 8.3\text{Si}^{+4}\cdot 1.1\text{O}^{-2}\cdot 20$, and the second type SFCA-I is found in the composition of $\text{M}_{20}\text{O}_{28}$ stoichiometry and $\text{Ca}^{+2}\cdot 3.18\text{Fe}^{+3}\cdot 15.48\text{Al}^{+3}\cdot 1.34\text{O}^{-2}\cdot 28$ [2,3]. Sinter material differs from chemical composition depending on the raw material used, process conditions and production

conditions. The chemical morphology and element structure of the sintered material, which has a heterogeneous structure, can vary depending on the raw material supply system and process conditions [11-16, 31, 33]. The impact of the SFCA and SFCA-I phases on the formation mechanisms and the formation of a number of sintering parameters have recently been partially done by few studies [19, 23-25, 32]. However, the SFCA phase within the sinter has a significant impact on the improvement of sinter quality parameters such as TI (Tumbler index / cold strength), RDI (Reduction degradation index / hot strength), RI (Reduction index / reduction property) and RUL (Reduction under load) (26, 27, 30).

Sintering plants in the integrated iron and steel plants in our country (İskenderun Iron and Steel Works Co. / İSDEMİR, Ereğli Iron and Steel Works Co. / ERDEMİR and Karabük Iron and Steel Works Co. / KARDEMİR) monitor quality on the basis of small basicity (CaO/SiO_2) ratio only. The total annual sinter production of these plants exceeds 11 million tons. However, what is important in determining the quality in the sintering process is the fact that the changes in ferrite structures, wustite (FeO) and aluminate cannot be monitored since no common monitoring method could be developed yet. By controlling the SFCA (silico-ferrite calcium and aluminium) structure in the sintered structure, this quaternary phase matrix (CaO , Al_2O_3 , Fe_2O_3 , SiO_2) will be taken under control and all parameters that may affect the quality of the process will be examined. All compounds in the sinter matrix must be evaluated individually using the Rietveld method (Fe_2O_3 , Fe_3O_4 , Ca_2SiO_4 , SFCA, SFCA-I) to know the quantitative contents of existing phase structures. Data obtained after determination of SFCA quantity in the sintered material will be associated with other quality parameters monitored (Basicity, RDI, mineralogical, etc.) and performance data coming from blast furnaces to increase the usage efficiency of the sinter and consequently reduce the raw material costs.

2. Material and Method

Sinter is an important blast furnace input material formed by adding 0-10 mm iron ores and fluxes which cannot be charged directly to the blast furnaces and limestone powder, dolomite, olivine, coke dust, return dust and waste materials (chimney dust, steelmaking slag, mill scale, gas cleaning sludge of blast furnace and steelmaking) in certain proportions without being completely melted, which are heated to 950-1350 °C so as to adhere to each other due to superficial melting. The flow chart of a typical industrial sinter plant is displayed in Figure 1. During the sintering process, the combustion that starts in the sinter furnace moves from the surface of the blend laid on the sinter strand to its base, and the surfaces of the particles in the combustion zone reach the melting temperature, and the gangue components form a semi-liquid slag, the moisture in the blend evaporates, the carbonates decompose, the sulphurous compounds oxidize and their sulphur burns away from the system.

The internal structure of the sinter consists of the composition of iron ores in the sintering process, SFCA and dicalcium silicate, and glassy structure. The reactions that occur also regulate the volume fraction of each mineral that may affect the quality of the sinter, thus the performance of the blast furnace. SFCA is considered to be the most important component of the sinter bond matrix since it affects sinter quality significantly if the content of SFCA in sintered iron ore is high. Sinter reactions become successful by controlling the microstructure and concentration of SFCA during the sintering process. In this study, sample variety was provided by producing at different operating parameters with a laboratory type sintering machine in order to be able to perform more rapid test studies from iron ore blends prepared in different compositions. In sinter production, domestic and imported iron ores are mixed with certain proportions of fluxes (limestone, dolomite, etc.) and fuel (coke dust) to produce sinter in the basicity values of 1.6-2.0 (CaO/SiO_2) and at different operating parameters. Ratios of

imported iron powder and domestic iron powder to be used in the sinter blend will vary between 50-70% and between 30-50%, respectively depending on operating and laboratory practices. The content of fluxes to be used in the sinter blend will be in the range of 7 to 9% depending on the acidic compounds such as SiO_2 and Al_2O_3 .

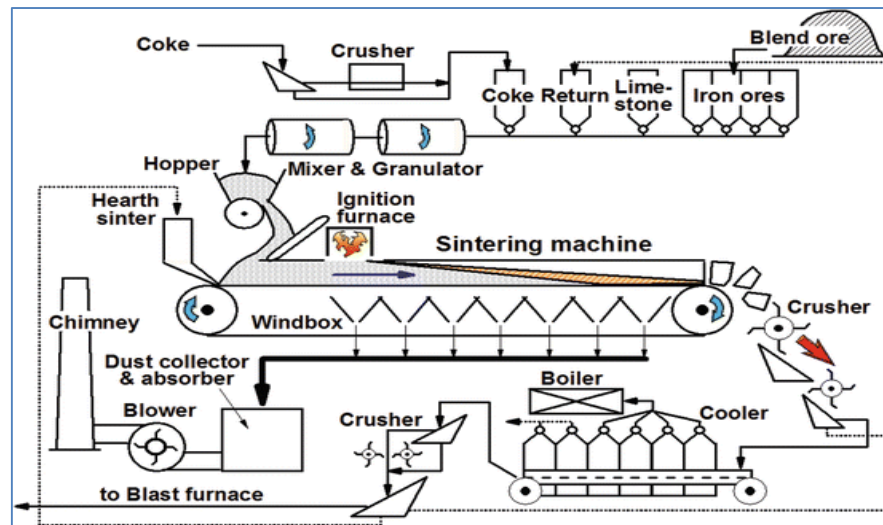


Figure 1. Typical flow chart of industrial type sinter production [35].

Sinter blend samples were prepared in accordance with the following parameters;

- Consumption of coke dust. It will vary between 6% and 7% in the blend depending on the sintering temperature.
- Humidity of the raw material: 7-8%.
- Ignition temperature: 1000~1200 °C, 1 minute ignition negative pressure: 5660 Pa.
- Negative pressure for sinter: 10.850 Pa.

3. Experimental Studies and Comments

3.1. SEM and XRD Studies on Sinter Samples

Given the increasing importance and studies in directing the sinter production quality according to the SFCA content in the sinter phase structure in addition to the existing physical and chemical quality monitoring tests of the sinter, which is an important input material in blast furnace process control; determination of ideal SFCA will help to control all sintering parameters of the sinter, which is the main input material of the blast furnace process in iron and steel plants. Thus, besides the cost advantage to be created by a better process control by charging more stable sinter to the Blast Furnace, a new iron production quality monitoring will be provided for the iron and steel industry on a global scale. Quadruple bond SFCA phase has been accepted as a main parameter in the sintering process by scientists since it significantly affects the technological quality of the sinter including high mechanical hardness (TI, RI and RDI, etc.), but it has not been sufficiently studied yet. Studies conducted on the effects of microstructure and mineral composition on the crack resistance of the sinter noticed that SFCA-I (especially acicular SFCA) is the main material affecting the spreading resistance of cracks. It has been observed that the acicular SFCA type of porous structure provides a greater reaction area in solid-gas contact, thereby increasing the reducibility in the blast furnace, shortening the processing time and saving fuel (metallurgical coke) and time.

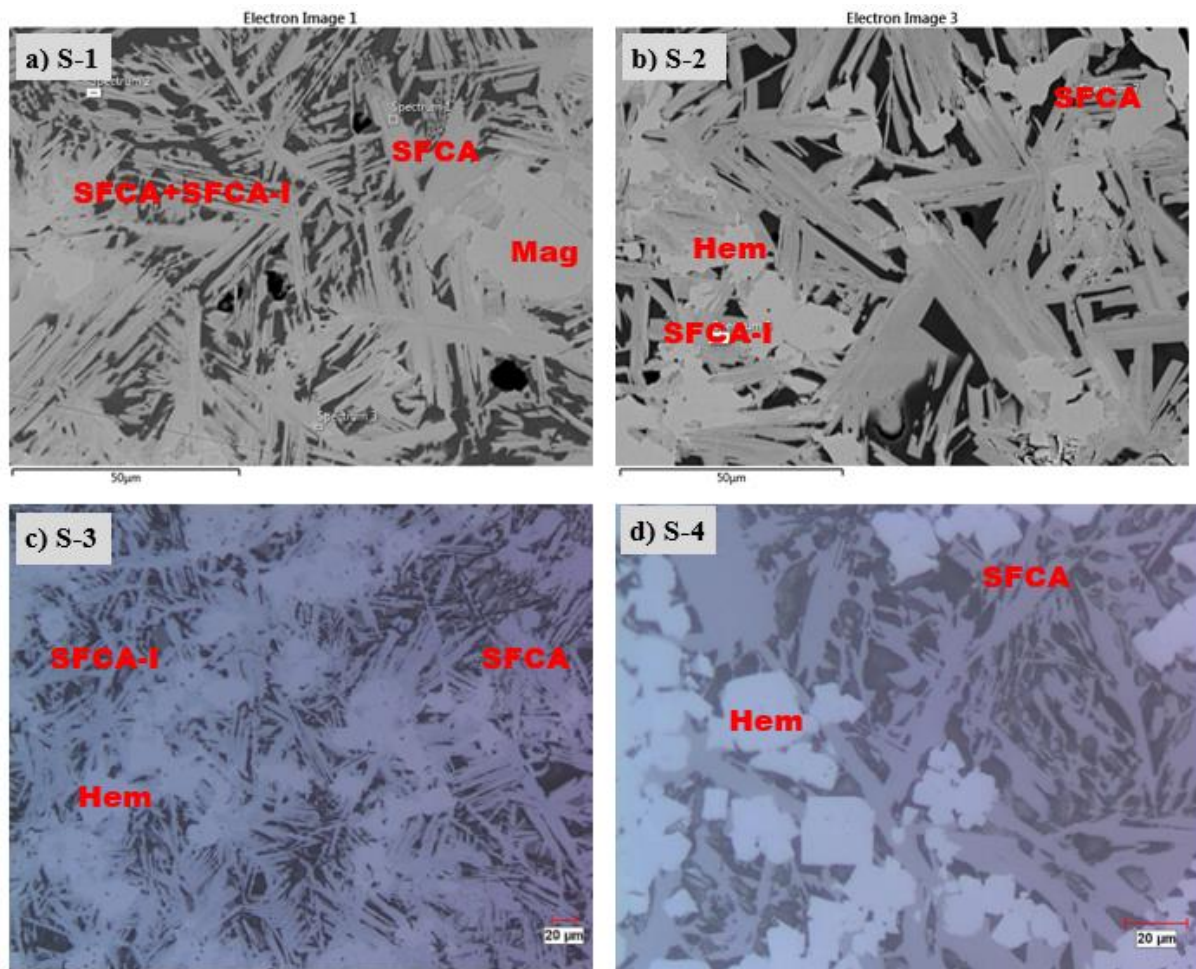


Figure 2. Sinter sample a) S-1 and b) S-2 SEM images, c) S-3 and d) S-4 optical microscope images (Hem: Hematite, Mag: Magnetite, SFCA, SFCA-I (X500))

SEM and optical microscope studies were performed with 500X magnification on sinter samples. The presence of SFCA and SFCA-I phase structures in the sinter matrix varies depending on the sintering temperature, blend ignition time and furnace temperature. The SEM and optical microscope images of the sinter samples are indicated in Figure 2.

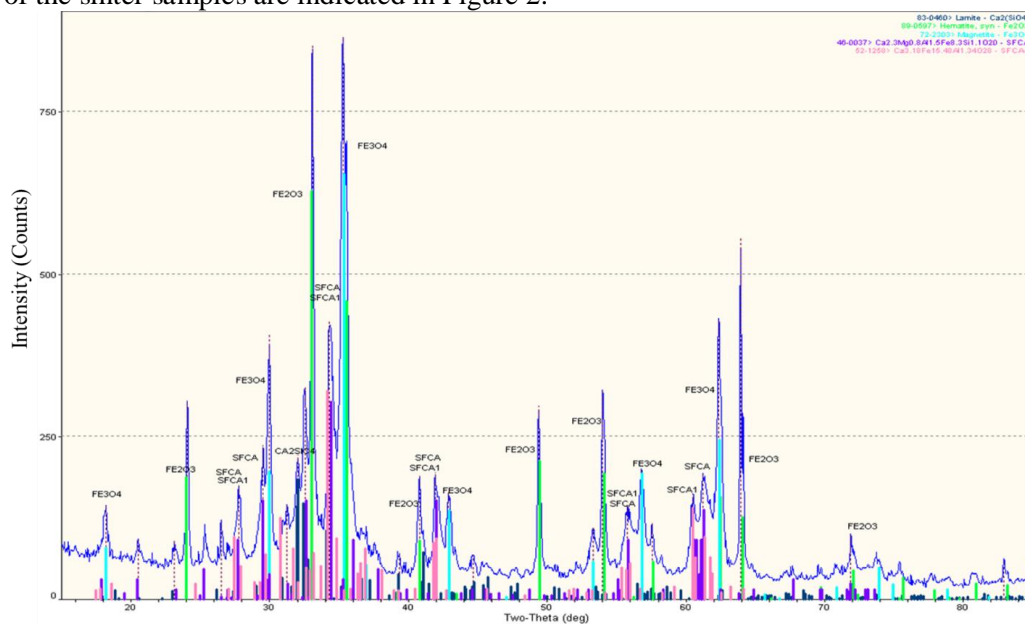


Figure 3. Sinter sample XRD phase analysis diagram.

XRD phase diagram was demonstrated in Figure 3. During the XRD studies conducted, Fe_2O_3 (hematite), Fe_3O_4 (magnetite), FeO (wustite), SiO_2 (quartz), Ca_2SiO_4 (larnite), CaO (lime), and XRD device printouts for SFCA and SFCA-I phases are quantitatively determined with the help of the Rietveld Method. The composition information of SFCA and SFCA-I phases stoichiometrically is demonstrated in Table 1.

Table 1. Stoichiometric composition information of SFCA and SFCA-I phases

	Fe^{+3}	Fe^{+2}	Fe	Al	Ca	Mg	Si	Mn
SFCA ($\text{M}_{14}\text{O}_{20}$)	10.18	0.90	11.08	0.50	1.85	0.17	0.49	0.08
SFCA-I ($\text{M}_{20}\text{O}_{28}$)	14.36	1.72	16.08	0.38	3.48	0.21	0.05	0.38

3.2 The Study of Rietveld Method and Autoquan Program on the Sinter Samples

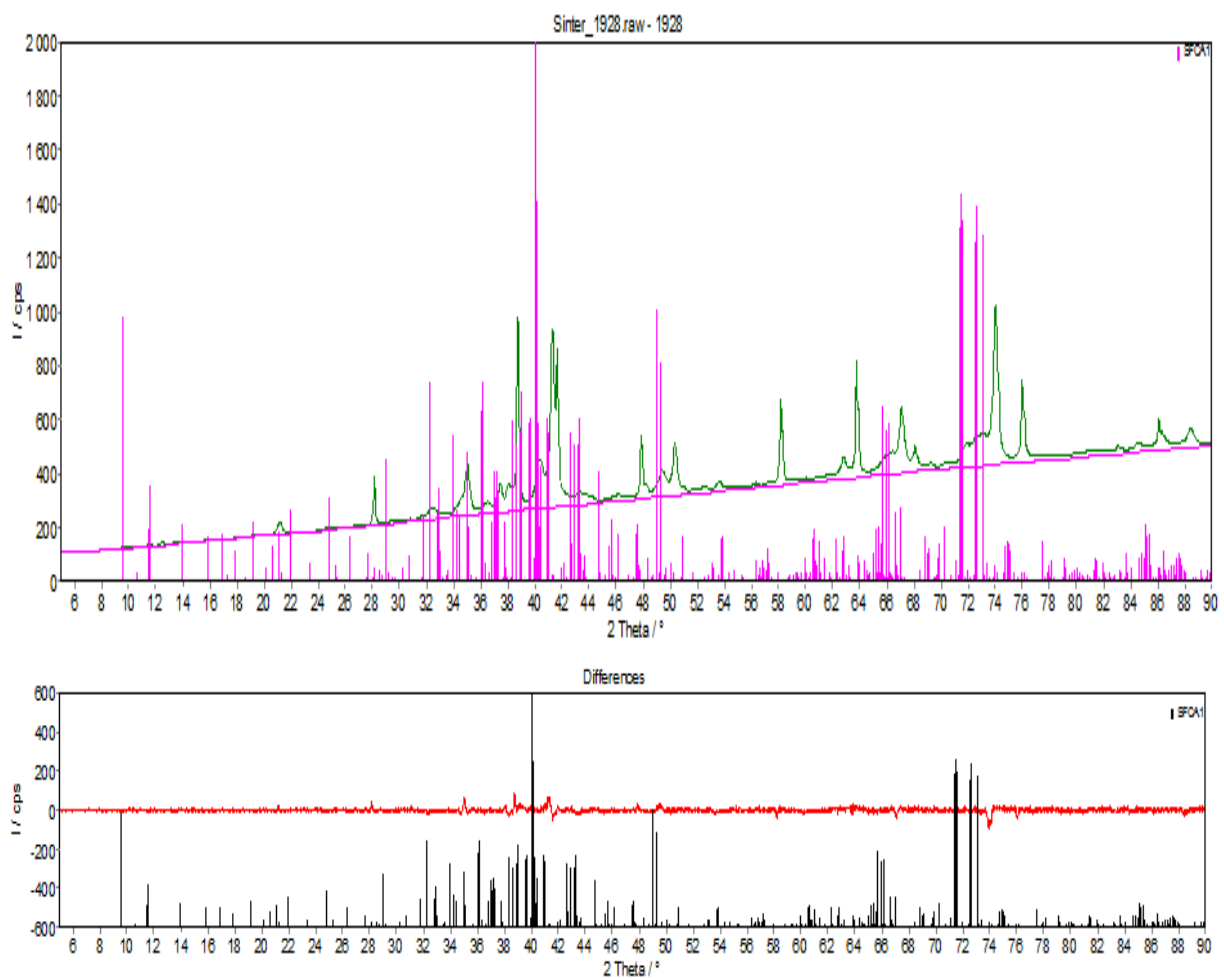


Figure 4. Rietveld (refinement) image of the sinter sample.

The phase structures in the sinter were determined using XRD devices with X-Ray tubes that irradiates Cu K-alpha and Co K-alpha. The scanning process was done between 5-90° at the scanning speed of 2 degree/min. Crystal data phase files with *.XRDML extension of sinter samples is created in XRD device and these files are converted to files with *.RD extension by PANalytical X'Pert Highscore Plus software program. In this file, the files are converted to *.RAW files using ConVX.exe program and opened with the Autoquan program having the crystal data files of the related phases.

Autoquan program and the rietveld method can be used to determine the individual percentage of all phases in the sinter structure. Data on quantitative contents of existing phase structures is obtained from the study conducted by this method. The XRD drawing of a typical sinter material is given in Figure 4. The position of the peaks obtained from the crystal structure of the sinter is shown as a vertical line. For example, the hematite mineral content in the sinter material can be easily identified and measured by XRD with an approximately 12 minute scan. Rietveld image of the sinter sample was indicated in Figure 4. When using powder XRD with mineral compositions obtained by SEM analysis, much information can be obtained about the element distribution in various minerals. The advantage of this method over other methods is to more accurately determine phase contents (%) by using the information content of the diffractogram better.

Before the raw data obtained were evaluated in Autoquan, the conditions of the relevant device were kept available in the device file. This step was important for a proper refinement process. However, the XRD convert program used to convert the raw data format to Autoquan format is given in Figure 5.

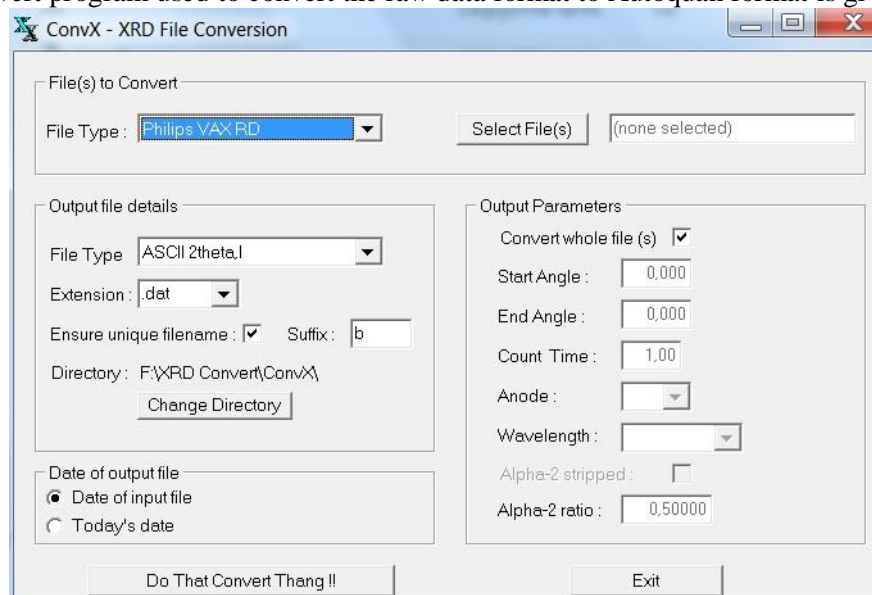


Figure 5. XRD convert program

Figure 5 indicates charts containing the results of quantitative phase measurements using Autoquan with an X-Ray tube that radiates Cu K-alpha and Co K-alpha. Different SFCA values were found in the same samples subjected to Cu K-alpha and Co K-alpha analysis. According to the results obtained with the tube that radiates Cu K-alpha during the investigation of the phase structures of the sinter materials, since the incident ray is absorbed due to the fluorescence and absorption effect, especially in iron-containing materials, the intensity/counts sensitivity values were quite low, so no healthy results could be obtained. In order to determine the phase structures in the sinter, XRD device with X-Ray tube that radiates Co K-alpha, which can make more precise measurements in iron-containing phases, was preferred. After the sample size was grinded to 20 microns, it was scanned at 30 kV and 35 mA in the XRD device. Figure 6 reveals the quantitative (%) sinter phase results of the structures in the internal morphology of the sinter sample, obtained by Rietveld analysis performed via the Autoquan program using XRD device with Cu K-alpha and Co K-alpha radiation on the sinter samples.

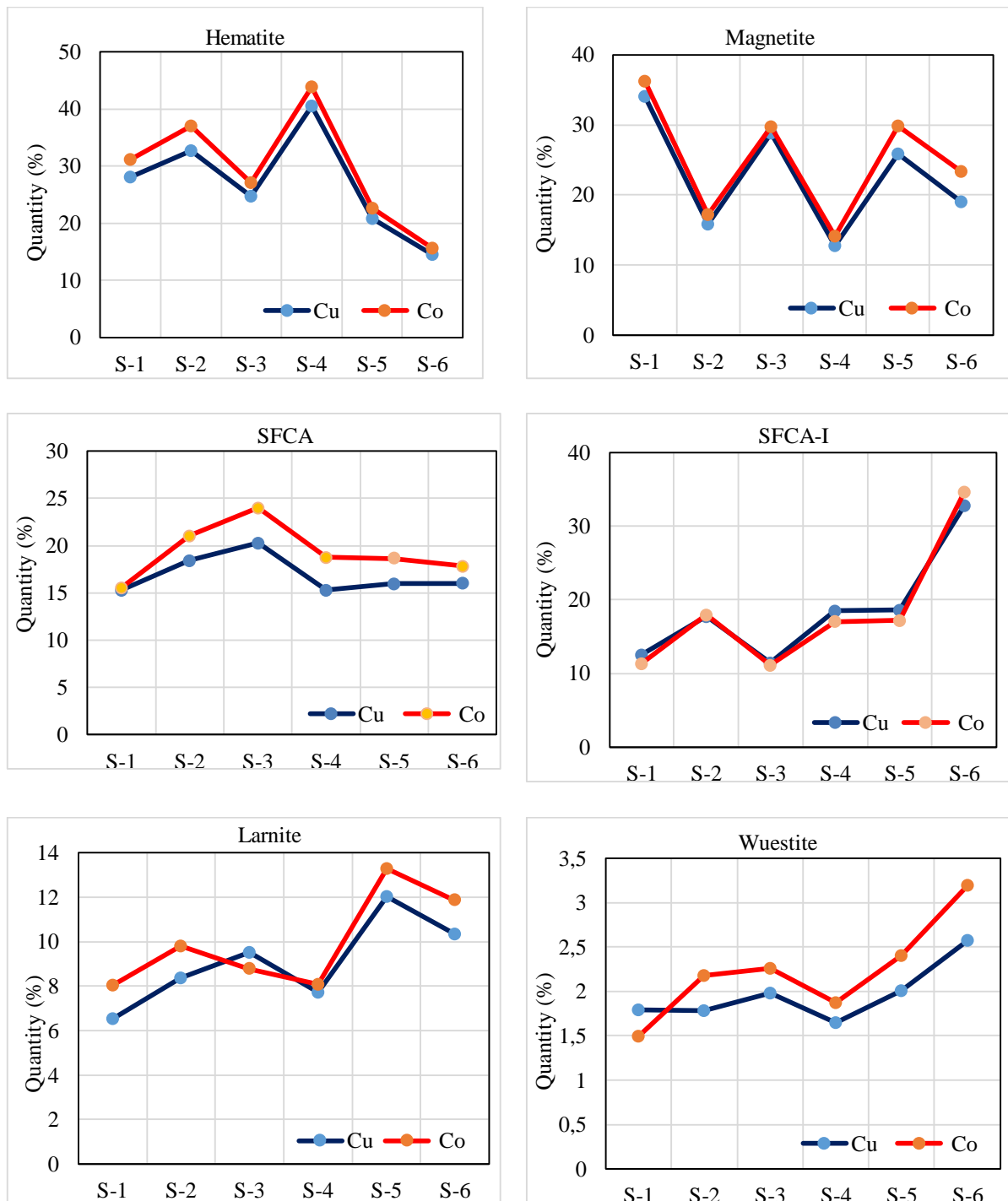


Figure 6. Rietveld analysis quantitative sinter phase results by XRD device with Cu K-alpha and Co K-alpha radiation.

Using the rietveld method, all compounds in the sinter matrix are evaluated individually (FeO, Fe₂O₃, Fe₃O₄, Ca₂SiO₄, SFCA, SFCA-I, etc.) to know about the quantitative contents of the existing phase structures. The Rietveld method utilizes the relative weight ratios of all phase crystals included in the model better and helps the determination of more accurate phase quantities (as %), and results are achieved quantitatively and quickly in a few minutes without the need for standard or calibration [22, 30, 31]. It also facilitates the interpretation of sinter phase data and the regular protection of phases. The Autoquan program supports the analytical listing of SFCA phase results from the sinter sample and

transferring the results to standard applications. Thanks to this program, changes that may occur in the sinter structure or process conditions can be tracked more accurately with the SFCA data.

4. Conclusion

All-important parameters in the sinter material, which affect the quality of the sintering process are examined in order to make the sintering process more stable with a detailed internal structure analysis. The changes shown by the structures within the sinter matrix structure, especially SFCA, SFCA-I and SFCA-II phase structures, which have a great effect on the physical and metallurgical properties of the sinter, depending on the sintering temperature, time, raw material type and basicity are followed by Autoquan program and Rietveld method, and the process and raw material conditions required for the full control of the sinter mineral formation are determined to create more durable sinter production and process monitoring systematics. Within the scope of this study, it will be possible to use the data to be obtained with the XRD device to quantify the phase structures formed in the sinter produced using the related software. In this context, it is important to make a correlation with the physical properties of the material, especially the ones that affect the strength of the material, by following up the ratio of iron oxides formed during the process to the SFCA phase structures. The result of the study is reduction in the return dust contents as a result of the production of high-strength sinter, and the valuation of such fine dusts in the blast furnace to provide significant savings in ore consumption. Utilization of an X-Ray tube that radiates Co K-alpha, which can make more precise measurements in iron-containing phases for investigation of the sinter phase structure, is important due to the fluorescence effect at more intensive values.

Acknowledgements

This manuscript is written with the research study numbered 1059B191401374 supported by 2219 Research Scholarship and Supports Directorate (BİDEB) of The Scientific and Technological Research Council of Turkey (TUBITAK). I am grateful to TUBITAK for assistance.

References

- [1] Zöll, K., Kahlenberg, V., Krüger, H., & Tropper, P. (2018). Investigations on FCAM-III ($\text{Ca}_{2.38}\text{Mg}_{2.09}\text{Fe}^{3+}_{10.61}\text{Fe}^{2+}_{1.59}\text{Al}_{9.33}\text{O}_{36}$): A new homologue of the aenigmatite structure-type in the system $\text{CaO-MgO-Fe}_2\text{O}_3\text{-Al}_2\text{O}_3$. *Journal of Solid State Chemistry*, 258, 307-319.
- [2] Hsieh, L.H., Whiteman, J.A. (1989). Effect of oxygen potential on mineral formation in lime-fluxed iron ore sinter. *ISIJ International*, 29(8), 625-634.
- [3] Kama, M., Miyazaki, T., Ito, K., Hida, Y., Sasaki, M. (1984). Morphological Analysis of Calcium Ferrite and Hematite in Sintered Ore. (Synopsis). *Trans. Iron Steel Inst. Jpn.*, 24(10).
- [4] Liu, D., Loo, C. E., Evans, G. Liu, D., Loo, C. E., Evans, G. (2016). Flow characteristics of the molten mix generated during iron ore sintering. *International Journal of Mineral Processing*, 149, 56-68.
- [5] Pownceby, M. I., & Patrick, T. R. (2000). Stability of SFC (silico-ferrite of calcium) solid solution limits, thermal stability and selected phase relationships within the $\text{Fe}_2\text{O}_3\text{-CaOSiO}_2$ (FCS) system. *European Journal of Mineralogy*, 12(2), 455-468.
- [6] Young, R.A. (1993). *The Rietveld method*, International Union Crystallography, Oxford University Press, Oxford, (Vol. 5, pp. 1-38).
- [7] Dawson, P.R., Ostwald, J., Hayes, K.M. (1984). The influence of the sintering temperature profile on the mineralogy and properties of iron ore sinters. In *AIMM Bull. Proc.* (Vol. 289, No. 5, pp. 163-169).
- [8] Wei, R., Lv, X., Yang, M., Xu, J., You, Z. (2018). Improving the property of calcium ferrite using

- a sonochemical method. *Ultrasonics sonochemistry*, 43, 110-113.
- [9] Ding, X., Guo, X. M. 2016. Study of SiO₂ involved in the formation process of silico-ferrite of calcium (SFC) by solid-state reactions. *International Journal of Mineral Processing*, 149, 69-77.
- [10] De Magalhaes, M.S., Brandao, P. R. G. (2003). Microstructures of industrial sinters from Quadrilatero Ferrifero's iron ores, Minas Gerais State, Brazil. *Minerals Engineering*, 16(11), 1251-1256.
- [11] Scarlett, N.V., Pownceby, M.I., Madsen, I.C., Christensen, A.N. (2004). Reaction sequences in the formation of silico-ferrites of calcium and aluminum in iron ore sinter. *Metallurgical and materials transactions B*, 35(5), 929-936.
- [12] Webster, N. A., Churchill, J. G., Tufaile, F., Pownceby, M. I., Manuel, J. R., Kimpton, J. A. 2016. Fundamentals of silico-ferrite of calcium and aluminium (SFCA) and SFCA-I iron ore sinter bonding phase formation: effects of titanomagnetite-based iron sand and titanium addition. *ISIJ International*, 56(10), 1715-1722.
- [13] Koryttseva, A., Webster, N. A., Pownceby, M. I., Navrotsky, A. (2017). Thermodynamic stability of SFCA (silico- ferrite of calcium and aluminum) and SFCA- I phases. *Journal of the American Ceramic Society*, 100(8), 3646-3651.
- [14] Cai, B., Watanabe, T., Kamijo, C., Susa, M., & Hayashi, M. (2018). Comparison between Reducibilities of Columnar Silico-ferrite of Calcium and Aluminum (SFCA) Covered with Slag and Acicular SFCA with Fine Pores. *ISIJ International*, 58(4), 642-651.
- [15] Webster, N. A., Pownceby, M. I., & Pattel, R. (2017). Fundamentals of silico-ferrite of calcium and aluminium (SFCA) and SFCA-I iron ore sinter bonding phase formation: effects of mill scale addition. *Powder Diffraction*, 32(S2), 85-89.
- [16] Cores, A., Babich, A., Muñiz, M., Ferreira, S., Mochon, J. (2010). The influence of different iron ores mixtures composition on the quality of sinter. *ISIJ International*, 50(8), 1089-1098.
- [17] Pownceby, M.I., Clout, J.M.F. (2003). Importance of fine ore chemical composition and high temperature phase relations: applications to iron ore sintering and pelletising. *Mineral Processing and Extractive Metallurgy*, 112(1), 44-51.
- [18] Bristow, N.J., Waters, A.G. (1991). Role of SFCA in promoting high-temperature reduction properties of iron ore sinters. *Transactions of the Institution of Mining and Metallurgy, Section C*, 100.
- [19] Mumme, W.G., Clout, J.M.F. & Gable, R.W. (1988). The crystal structure of SFCA-I $\text{Ca}_{3.18}\text{Fe}^{3+} 14.66\text{Al}_{1.34}\text{Fe}^{2+} 0.82\text{O}_{28}$, a homologue of the aenigmatite structure type, and new structure type, and new crystal refinements of b -CCF, $\text{Ca}_{2.99}\text{Fe}^{3+} 14.30\text{Fe}^{2+} 0.55\text{O}_{25}$ and Mg-free SFCA, $\text{Ca}_{2.45}\text{Fe}^{3+} 9.04\text{Al}_{1.74}\text{Fe}^{2+} 0.16\text{Si}_{0.6}\text{O}_{20}$. *Neues Jahrbuch Mineralogie-Abhandlungen*, 173(1), 93.
- [20] Mumme W.G. (2003). The crystal structure of SFCA-II, $\text{Ca}_{5.1}\text{Al}_{9.3}\text{Fe}^{3+} 14.30\text{Fe}^{2+} 0.55\text{O}_{48}$, a new homologue of the aenigmatite structure-type, and structure refinement of SFCA, $\text{Ca}_2\text{Al}_5\text{Fe}_7\text{O}_{20}$. Implications for the nature of the. *Neues Jahrbuch für Mineralogie-Abhandlungen: Journal of Mineralogy and Geochemistry*, 178(3), 307-335.
- [21] Bhagat R.P., Chattoray, U., SIL, S.K. (2006). Porosity of sinter and its relation with the sintering indices, *ISIJ International*, 46(11), 1728-1730.
- [22] T. van den Berg and J.P.R. de Villiers: *T. I. Min. Metall. C*, 2009, vol. 118, pp. 214–21.
- [23] Sasaki, M., Hida, Y., (1982). Considerations on the properties of sinter from the point of sintering reaction. *Tetsu to Haganè* 68, 563–571.
- [24] McAndrew, J., Clout, J.M.F., (1993). The nature of SFCA and its importance as a bonding phase in iron ore sinter. In *Proceedings of the 4th China–Australia Symposium on the Technology of Feed Preparation for Ironmaking*, Dampier, pp. 1–15.
- [25] Chaigneau, R. (1994). Fluxed sinter formation and SFCA reduction under Simulated Conditions, PhD Thesis, Delft University Press, p. 12-28.
- [26] Liles, D. C., de Villiers, J. P., Kahlenberg, V. 2016. Refinement of iron ore sinter phases: a silico-ferrite of calcium and aluminium (SFCA) and an Al-free SFC, and the effect on phase quantification by X-ray diffraction. *Mineralogy and Petrology*, 110(1), 141-147.
- [27] Bölükbaşı Ö.S. (2015). Determination of Ideal SFCA (silico-ferrite-calcium-aluminum) Phase

- Structure in Iron Ore Sintering Process, TÜBİTAK Research (1059B191401374) 1. Report Result.
- [28] Ishikawa, Y., Shimomura, Y., Sasaki, M., Toda, H. (1983). Improvement of sinter quality based on the mineralogical properties of ores. *Ironmaking Proceedings*. vol. 42. p. 17-29.
- [29] Hancart, J., Leroy, V., Bragard, A. (1967). A study of the phases present in blast furnace sinter. Some considerations on the mechanism of their formation. *CNRM Metall. Report*, 3-7.
- [30] Patrick, T. R., & Pownceby, M. I. (2002). Stability of silico-ferrite of calcium and aluminum (SFCA) in air-solid solution limits between 1240° C and 1390° C and phase relationships within the Fe₂ O₃-CaO-Al₂O₃-SiO₂ (FCAS) system. *Metallurgical and Materials Transactions B*, 33(1), 79-89.
- [31] Garbers-Craig, P. C., JMA, J. W. (2003). The influence of increased air flow on the spatial variation of iron sinter quality. *Journal of the Southern African Institute of Mining and Metallurgy*, 103(10), 645-650.
- [32] Wei, R., Lv, X., Yang, M., Xu, J., & You, Z. (2018). Improving the property of calcium ferrite using a sonochemical method. *Ultrasonics sonochemistry*, 43, 110-113.
- [33] Scarlett, N. V., Madsen, I. C., Pownceby, M. I., Christensen, A.N. (2004). In situ X-ray diffraction analysis of iron ore sinter phases. *Journal of Applied crystallography*, 37(3), 362-368.
- [34] Kalenga, M.K. (2008). Investigation into the influence of magnesia content, alumina content, basicity and ignition temperature on the mineralogy and properties of iron sinter. Doctoral dissertation, University of Pretoria, Pretoria, Republic of South Africa, 25-27.
- [35] Komarov S.V., Kasai E. (2004). Simulation of sintering of iron ore packed bed with variable porosity. Institute of Multidisciplinary Research for Advanced Materials. Phoenix User Conference, Melbourne, Australia, 25-30.